Unsteady aerodynamic modelling for seakeeping analysis of Floating Offshore Wind Turbines

Vincent Leroy

THESE DE DOCTORAT DE

L'ÉCOLE CENTRALE DE NANTES
COMUE UNIVERSITE BRETAGNE LOIRE

ECOLE DOCTORALE N° 602
Sciences pour l'Ingénieur
Spécialité : *Mécanique des Milieux Fluides*

Par
Vincent LEROY

Aérodynamique instationnaire pour l'analyse de la tenue à la mer des éoliennes flottantes

Thèse présentée et soutenue à Nantes, le 6 décembre 2018
Unité de recherche : Laboratoire d'Hydrodynamique, Energétique et Environnement Atmosphérique (LHEEA), CNRS UMR 6598

Rapporteurs avant soutenance :

Henrik Bredmose   Professeur, DTU Wind Energy (Danemark)
Maurizio Collu   Reader, University of Strathclyde (Royaume-Uni)

Composition du Jury :

Président :   Zhen Gao   Professeur, NTNU (Norvège)
Examinateurs : Henrik Bredmose   Professeur, DTU Wind Energy (Danemark)
               Maurizio Collu   Reader, University of Strathclyde (Royaume-Uni)
               Sandrine Aubrun   Professeur, Centrale Nantes (France)
               Jean-Christophe Gilloteaux Ingénieur de Recherche, Centrale Nantes (France)
Dir. de thèse : Pierre Ferrant   Professeur, Centrale Nantes (France)

Invité
Matias Lynch   Technical Lead Ocean Engineering, INNOSEA (France)

Unsteady aerodynamic modelling for seakeeping analysis of Floating Offshore Wind Turbines

Vincent Leroy

Centrale Nantes
France

December 2018

Résumé

Cette thèse de doctorat s'inscrit dans le cadre de la recherche et développement dans le domaine des énergies marines renouvelables. Les éoliennes offshores sont aujourd'hui au cœur de nombreuses recherches puisqu'elles permettent un accès à une énergie durable, abondante au large de nos côtes. Loin des côtes, la profondeur d'eau impose d'installer ces éoliennes sur des plateformes flottantes ancrées au fond marin afin de limiter les coûts d'infrastructures.

Les éoliennes à axe horizontal sont les plus performantes sur terre (plus hauts coefficients de puissance), elles ont donc été naturellement adaptées pour des applications flottantes. D'autres concepts tels que les éoliennes à axe vertical pourraient toutefois avoir des intérêts pour des applications flottantes puisqu'elles pourraient nécessiter des coûts d'infrastructure inférieurs aux éoliennes à axe horizontal [Borg et al., 2014b]. Cependant, des efforts aérodynamiques s'appliquant aux éoliennes à axe vertical sont très oscillants. De plus, l'axe vertical du rotor et de la génératrice implique intrinsèquement un couple de lacet que seul l'ancrage de la plateforme peut compenser.

Le développement de ces nouvelles technologies impose l'utilisation d'outils de design numérique des structures offshores mélant différents domaines :

- Aérodynamique ;

- Hydrodynamique ;

- Contrôle ;

- Dynamique des structures ;

- ...

Les logiciels courants combinent généralement des logiciels de dimensionnement d'éoliennes terrestres et des logiciels d'étude des systèmes offshore, parfois initialement développés pour l'industrie du pétrole et du gaz. Les solveurs aérodynamiques usités supposent généralement un écoulement stationnaire sur le rotor de l'éolienne. Des modèles semi-empiriques sont alors utilisés pour prendre en compte certains effets instationnaires. Cette approche permet d'obtenir des temps de calculs réduits. Pourtant, rien ne nous permet aujourd'hui d'affirmer que les éoliennes offshores flottantes ont le même comportement aérodynamique que les éoliennes fixes. Au contraire, plusieurs études mettent en évidence le caractère instationnaire des écoulements autour des rotors d'éoliennes flottantes, notamment dans [Sebastian and Lackner, 2013] ou [Jeon et al., 2014].

Cette thèse de doctorat s'intéresse en particulier à l'influences des effets aérodynamiques instationnaires sur la tenue à la mer des éoliennes flottantes. Des éoliennes flottantes à axe horizontal et vertical sont étudiées. Enfin, une étude comparative est menée entre ces deux types de rotors installés sur une plateforme semi-submersible.

Ce manuscrit s'articule comme suit :

- Le chapitre 1 introduit le contexte et les problèmes abordés ;

- Le chapitre 2 parcourt l'état de l'art de la modélisation des éoliennes flottantes, comprenant les théories et les outils numériques disponibles ;

- Le chapitre 3 présente les développements numériques effectués pendant la thèse, et détaille en particulier le travail de couplage entre solveurs ;

- Le chapitre 4 présente un cas d'étude sur une éolienne flottante à axe horizontal et compare les résultats d'un code quasi-stationnaire de référence à l'outil insta-tionnaire développé dans le cadre de la thèse ;

- Le chapitre 5 présente une comparaison entre un solveur aérodynamique quasi-stationnaire développé dans le cadre de la thèse à un solveur instationnaire sur le cas d'une éolienne flottante à axe vertical ;

- Le chapitre 6 se concentre sur la comparaison entre deux topologies d'éoliennes installées sur une plateforme de type semi-submersible : un rotor à axe horizontal et un rotor à axe vertical ;

- Enfin, le chapitre 7 présente les conclusions de la thèse et ouvre sur de potentielles perspectives.

Un résumé de ce travail et des conclusions auxquelles il mène est présenté ci-dessous.

Couplage entre un logiciel de tenue à la mer et un solveur aérodynamique instationnaire

Un nouvel outil de simulation numérique a été développé, couplant le logiciel de tenue à la mer *InWave* [Combourieu et al., 2014], développé par INNOSEA et le labora-toire LHEEA de Centrale Nantes, et le solveur aérodynamique instationnaire *CACTUS* [Murray and Barone, 2011], basé sur la théorie *Free Vortex Wake* (FVW) et développé au laboratoire Sandia, aux USA. Une première vérification est faite, comparant les ré-sultats du logiciel de référence *FAST* (quasi-stationnaire) [Jonkman and Buhl, 2005] et ceux d'*InWave* sur le cas d'une éolienne flottante à axe horizontal supportée par une plateforme de type SPAR. Les résultats sont concordants mais montrent également que le caractère instationnaire de l'écoulement sur le rotor modifie les efforts qu'il subit, ainsi que les mouvements de l'éolienne. Ceci est particulièrement observable lorsque le rotor est fortement chargé (c'est-à-dire quand la vitesse du vent est inférieure ou égale à la vitesse nominale).

Développement d'un simulateur d'éoliennes flottantes à axe vertical

En plus du solveur aérodynamique instationnaire *CACTUS*, un nouveau code quasi-stationnaire basé sur la théorie *Double Multiple Streamtube* (DMS) [Paraschivoiu, 2002] a été entièrement développé pendant la thèse et couplé à *InWave*. Ces codes ont été validés par comparaison à des résultats expérimentaux. Un algorithme de contrôle du couple de la génératrice d'une éolienne flottante à axe vertical a également été développé. Le cas d'une éolienne flottante à axe vertical supportée par une plateforme SPAR a enfin été étudié. Les résultats montrent là aussi que des phénomènes instationnaires impactent les mouvements de l'éolienne lorsque le rotor est fortement chargé.

Caractérisation des effets des phénomènes aérodynamiques instationnaires sur la simulation des éoliennes flottantes

Une méthodologie visant à caractériser les effets de l'aérodynamique instationnaire sur la simulation du comportement des éoliennes flottantes est proposée dans cette thèse de doctorat. Deux solveurs, l'un quasi-stationnaire et l'autre instationnaire, sont comparés au cours des phases suivantes :

- Etude des forces aérodynamiques sur le rotor en rotation autour d'un axe fixe ;

- Simulations entièrement couplées de l'éolienne en mouvements libres, incluant des efforts aérodynamiques, hydrodynamiques, d'ancrage, ... ;

- Etude des forces aérodynamiques sur l'éolienne en mouvements harmoniques imposés et à vitesse de rotation constante du rotor. Les amplitudes et fréquences des mouvements peuvent alors être représentatives des résultats obtenus en simulations entièrement couplées.

Ce dernier point permet notamment de distinguer d'une part les composantes des forces aérodynamiques en phase avec la vitesse de déplacement du rotor (caractérisant l'amortissement aérodynamique), et d'autres part les composantes en quadrature de phase, qui sont les effets de raideur et de masse ajoutée.

A quel point les efforts aérodynamiques instationnaires impactent-ils la simulation de la tenue à la mer des éoliennes flottantes ?

La méthodologie présentée ci-dessus a été appliquée à deux éoliennes flottantes, l'une à axe horizontal et l'autre à axe vertical. Les résultats démontrent que les effets instationnaires d'interaction rotor/sillage sont significatifs lorsque le rotor est fortement chargé. Dans ce cas, les tourbillons dans le sillage proche de l'éolienne sont plus forts et les mouvements de cavalement et tangage de l'éolienne la conduisent parfois à fonctionner dans, ou très proche de son propre sillage. Ceci induit de fortes variations de poussée, impactant la réponse dynamique de l'éolienne flottante. Par exemple, les densités spectrales de puissance de mouvement du flotteur mettent en évidence les différentes estimations du mouvement de tangage aux basses fréquences entre les deux modèles aérodynamiques. Ceci semble être corrélé aux différences d'amortissements aérodynamiques évalués sur les éoliennes en mouvements harmoniques imposés.

Les solveurs quasi-stationnaires parviennent toutefois à correctement capturer le mouvement global du flotteur et devraient obtenir une précision acceptable pour des phases préliminaires de design d'éoliennes flottantes, tant à axe horizontal que vertical. Ils peuvent alors être préférés aux solveurs FVW qui demandent des temps de calculs bien supérieurs.

Quelles sont les performances d'une éolienne flottante à axe vertical par rapport à une éolienne à axe horizontal ?

Une comparaison a été menée entre les deux concepts d'éoliennes flottantes. Le rotor à axe vertical utilisé comporte des pales troposkines et a la particularité, par rapport à d'autres concepts, d'avoir un centre de poussée ainsi qu'un centre de gravité élevés étant donné l'importance de la masse et de la taille de sa tour. Aussi, ce rotor dispose d'un contrôle du couple de sa génératrice mais pas de contrôle d'angle de calage de ses

pales. Ceci induit une poussée aérodynamique très importante pour les vitesses de vent
élevées.

Par opposition, il est non seulement possible de contrôler le couple de l'éolienne
à axe horizontal, mais également l'angle de calage de ses pales, ce qui permet pour
des vitesses de vent élevées de conserver une puissance constante (égale à la puissance
nominale) et de baisser considérablement la poussée aérodynamique exercée sur le rotor.

L'étude montre par la suite que l'éolienne à axe vertical subit de très importants
efforts aux vitesses de vent élevées, induisant de grands déplacements de sa plateforme et
des tensions importantes dans ses lignes d'ancrage. Le moment fléchissant s'appliquant
sur la pièce de transition, au pied de la tour, est également très supérieur sur l'éolienne
à axe vertical. De par la nature des éoliennes à axe vertical, ces efforts sont également
très oscillants. Ces observations impliquent nécessairement un coût plus élevé pour cette
dernière.

D'autres concepts de rotors comportant, notamment, des centres de poussée plus
bas et/ou des possibilités de contrôle de l'angle de calages des pales pourraient toutefois
remettre en cause les conclusions de cette étude.

Abstract

Floating offshore wind turbines give us the opportunity to recover low-carbon and sustainable energy and they have been at the heart of many research and development during the recent years. State-of-the-art simulation tools dedicated to Floating Wind Turbines (FWTs) usually assume a quasi-steady flow on the rotor and their accuracy has been proven on onshore concepts. However, few experimental studies have been performed on FWTs and the accuracy of quasi-steady aerodynamic solver has not been proven yet for such turbines. On the contrary many recent studies emphasize unsteady aerodynamic effects inherent to FWTs that cannot be accounted for with quasi-steady solvers.

Although Vertical Axis Wind Turbines (VAWTs) are less efficient than Horizontal Axis Wind Turbines (HAWTs) in bottom-fixed installations, they may have interesting features for floating applications. For example, it is regularly put forward that the generator (and gearbox, if needed) can be located at the bottom of their tower, lowering the centre of gravity of the structure. Also, the centre of thrust could be lower than on a horizontal axis rotor. This could enhance the stability of FWTs and lower the costs of the substructures. State-of-the-art aerodynamic simulation tools dedicated to VAWTs also assume a quasi-steady flow on the rotor. Here again, this hypothesis would need an accurate validation for floating VAWTs.

During this PhD thesis, an unsteady aerodynamic solver, based on Free Vortex Wake theory, has been coupled to a seakeeping software. Another aerodynamic solver has been specifically developed, based on the quasi-steady Double Multiple Streamtube (DMS) theory, and coupled to the same seakeeping solver. The solvers have been validated on bottom-fixed turbines, either HAWTs or VAWTs, with comparison to experimental measurements.

After describing the numerical developments, the first part of this PhD thesis focuses on the impact of the employed aerodynamic models, either quasi-steady or unsteady, on the seakeeping simulation of FWTs. Several simulations are analysed comparing a reference quasi-steady model to a Free Vortex Wake solver. An innovative methodology is applied to both a floating HAWT and a floating VAWT. The behaviour of the two FWTs is studied in complex sea states, including severe conditions, turbulent wind and misaligned wind and waves. The results show that the unsteady aerodynamic effects can have an impact on the seakeeping of the wind turbines, in particular when the rotors are highly loaded. In that case, strong rotor-wake interactions happen, impacting the thrust on the rotor. For example, the aerodynamic damping can be notably altered, which changes the turbine response amplitude. The strong rotor-wake interactions also alter the mean thrust acting on the turbine which changes its excursion and mean tilt angle. It can be highly critical in design phases: the former changes the mooring mean tensions and the latter can induce large tower base bending moments. However, the study also concludes that quasi-steady solvers could be accurate enough

for early design phases as they seem to correctly compute the global behaviour of the systems, including correct resonance periods, wave excitation responses... A complete validation of the solvers with comparison to large scale FWTs would still be needed.

Eventually, a comparative study is completed between a HAWT and a VAWT, both supported by a semi-submersible platform. The HAWT is the reference NREL 5MW rotor. The VAWT is a 5MW troposkein Darrieus rotor. The comparison is done with several sea-states severities including collinear and non-collinear wind and waves. The VAWTs suffers from a very high aerodynamic thrust at high wind speeds. The loads acting on it and the induced motions are far higher than those of the HAWT, which leads to a lesser performance. Nevertheless, adding blade pitch control to the VAWT could drastically lower the aerodynamic thrust acting on it in severe conditions and perhaps improve the turbine response. Also turbines with lower rotors (H-shaped rotors, for instance) could also have improved performances.

List of publications

Contributions to journals

Two articles submitted, under review:

- Leroy, V., Gilloteaux, J.-C., Lynch, M., Babarit, A., Ferrant, P. (2018). Impact of aerodynamic modelling on seakeeping performance of a Floating Horizontal AxisWind Turbine. **[Submitted to]** *Wind Energy.*

- Leroy, V., Gilloteaux, J.-C., Lynch, M., Babarit, A., Ferrant, P. (2018). Impact of aerodynamic modelling on seakeeping performance of a Floating Vertical AxisWind Turbine. **[Submitted to]** *Wind Energy.*

Contributions to international conferences with peer-reviewed proceedings

- Leroy, V., Gilloteaux, J.-C., Philippe, M., Babarit, A., Ferrant, P. (2017). Development of a simulation tool coupling hydrodynamics and unsteady aerodynamics to study Floating Wind Turbines. OMAE2017-61203. *Proceedings of the ASME 2017 36th International Conference on Ocean, Offshore and Arctic Engineering, OMAE2017, June 25-30, 2017, Trondheim, Norway.*

- Leroy, V., Gilloteaux, J.-C., Combourieu, A., Babarit, A., Ferrant, P. (2018). Impact of the aerodynamic model on the modelling of the behaviour of a Floating Vertical Axis Wind Turbine. *Proceedings of the 15th Deep Sea Offshore Wind R&D conference, Trondheim, Norway, IOP Journal of Science: Conference Series.*

Contributions to national conferences with peer-reviewed proceedings

- Leroy, V., Gilloteaux, J.-C., Philippe, M., Babarit, A., Ferrant, P. (2016). Développement d'un couplage hydrodynamique et aérodynamique instationnaire pour l'étude des éoliennes flottantes à axe vertical. *Actes des 15èmes Journées de l'Hydrodynamique, Nov 2016, Brest, France.*

- Leroy, V., Gilloteaux, J.-C., Philippe, M., Babarit, A., Ferrant, P. (2017). Servo-hydro and unsteady aerodynamic simulation of Floating Vertical Axis Wind Turbines. *Actes du 23ème Congrès Français de Mécanique, 28 Août au 1er Septembre, Lille, France.*

Contributions to seminars and workshops

- Leroy, V., Gilloteaux, J.-C., Philippe, M., Babarit, A., Ferrant, P. (2016). Study on the seakeeping of Floating Vertical Axis Wind Turbines. *12th EAWE PhD Seminar on Wind Energy, 25-27 May 2016, DTU Lyngby, Denmark* [POSTER].

- Leroy, V., Gilloteaux, J.-C., Philippe, M., Babarit, A., Ferrant, P. (2017). Seakeeping study of a Floating Vertical Axis Wind Turbine with a numerical tool based on Free Vortex Wake Method. *13th EAWE PhD Seminar on Wind Energy, 20-22 September 2017, Cranfield University, United Kingdom.*

- Leroy, V., Gilloteaux, J.-C., Lynch, M., Babarit, A., Ferrant, P. (2018). Seakeeping analysis of Floating Wind Turbines: Impact of the aerodynamic model. *Colloque de Recherche Inter-Écoles Centrale (CRIEC).*

- Leroy, V., Leblanc, B. (2018). Senior PhD Workshop: Vertical Axis Wind Turbines. *14th EAWE PhD Seminar on Wind Energy, 18-20 September 2018, Vrije Universiteit Brussel, Belgium.*

Acknowledgement - Remerciements

To start, let me thank the reviewers of this manuscript, Henrik Bredmose and Maurizio Collu, and the other jury members at the defense, Zhen Gao and Sandrine Aubrun. I would like to thank them for their reviews and comments on the manuscript but also for their presence and the interesting discussions at the PhD defence.

Ces trois années de travail de thèse ont été riches et intenses en apprentissage. C'est en bonne partie grâce à l'atmosphère qui règne au laboratoire qu'elles ont été si agréables. Merci donc à tout le personnel du LHEEA pour rendre les échanges si riches, tous domaines confondus.

La thèse est bien souvent un travail solitaire à plancher sur un coin de table ou sur un clavier d'ordinateur, mais j'ai eu la chance d'être remarquablement supervisé. Je remercie très chaleureusement Pierre Ferrant, directeur de thèse, pour son encadrement scientifique. Si Pierre est un expert indéniable de l'hydrodynamique, il est aussi de très bon conseil quand on en vient à parler de variétés de pommes bretonnes et de musique jamaïcaine ! J'ai trouvé auprès d'Aurélien Babarit, co-encadrant, un socle scientifique solide et de précieux conseils méthodologiques sur mon travail de recherche. Merci évidemment pour cela autant que pour toutes nos conversations. Maxime Philippe et Mattias Lynch, ont à tour de rôle encadré ma thèse au sein d'INNOSEA. Je leur suis grandement reconnaissant pour leur disponibilité, leur complémentarité et tout ce que leurs conseils ont apporté à mon travail. Enfin, merci mille fois à Jean-Christophe Gilloteaux, co-encadrant. A son contact j'ai précisé ma pensée, creusé ma réflexion et retrouvé du mordant dans les moments de doute. Merci pour tout, sincèrement.

Côtoyant les aventures d'INNOSEA depuis 2013, j'ai été très heureux de me voir proposer d'effectuer une thèse de doctorat à ses côtés. Ça a été un plaisir constant de travailler, d'échanger et de partager des moments avec toute l'équipe de cette entreprise. Merci à elles et eux ! Je pense en particulier à Marlène, pour son positivisme contagieux, à Pierre-Yves, co-doctorant au LHEEA, et à Violette, encadrante de mon premier stage en énergie des vagues à Penryn (UK) que j'ai retrouvé à INNOSEA. Merci enfin à Samuel, notamment pour ses compétences en informatique. Il a toujours su résoudre mes problèmes de compilation et je lui serai pour cela éternellement reconnaissant !

Merci à l'équipe des doctorants et assimilés du LHEEA et autres laboratoires sur le campus de Centrale Nantes pour les échanges scientifiques et les moments de complicité et de détente (et/ou bien souvent de débat !) autour d'un repas ou d'un café. En particulier, je remercie Marion *Muchette* (camarade Coffee) et Thomas *TCorre* (camarade Rubber) pour tous les moments partagés, les hectolitres de café, et les discussions (plus ou moins intelligentes) à toutes heures du jour et de la nuit. Je n'oublie pas, bien évidemment, Simon, mais aussi Simon, Arnal, Louis, Catherine, mon ami Marco (merci

pour la recette des VRAIES pâtes à la carbonara et je lui souhaite une bonne rémission de la coupe du monde de football 2018), mon compatriote bress'ois Patrick, koâ, et tant d'autres qui m'excuseront de ne pas les nommer !

Me lancer dans cette aventure aurait été bien vain sans le soutien infaillible de mes amis qui ont su me porter et ont dû me supporter tout au long de ma thèse. Mes pensées vont donc à Marie-Louise, qui n'est plus là mais sans qui je ne serai pas où je suis ; à mes amis d'enfance, de lycée, de prépa, de Centrale (dont l'équipe amatrice de charcuterie fine, bien entendu), de l'excellente équipe *Loisir* de la Laetitia Handball, de Brest, de Nantes et du Festival du Bout du Monde (avec un clin d'œil tout particulier à Elena qui se trouve à la croisée de plusieurs de ces univers).

Le soutien permanent de mes proches est évidemment essentiel et je remercie du fond du cœur toute la tribu pour leur soutien infaillible : mes parents, ma Dr. sœur, mes grands-parents (trugarez deoc'h, tudoù-kozh, poezhus eo bet ho kalonekaat !) ainsi que toute ma famille et belle famille. Je terminerai par Iris qui, en plus de partager ma vie et de m'éblouir, a su m'aider, me supporter, me comprendre et m'encourager en toutes circonstances !

Bonne lecture.

Abbreviations

AC	Actuator Cylinder
AD	Actuator Disk
AL	Actuator Line
AOA	Angle Of Attack
BE	Blade Element
BEM	Blade Element Momentum
CAPEX	Capital Expenditure
CFD	Computational Fluid Dynamics
CM	Centre of Mass
COG	Centre of Gravity
DLC	Dynamic Load Case
DLL	Dynamic Link Library
DMS	Double Multiple Streamtube
DOF	Degree of Freedom
FWT	Floating Wind Turbine
FVW	Free Vortex Wake
GDW	Generalized Dynamic Wake
HAWT	Horizontal Axis Wind Turbine
HDB	Hydrodynamic Database
LCoE	Levelized Cost of Energy
LES	Large Eddy Simulation
MBL	Minimum Breaking Load
OPEX	Operational Expenditure
PVW	Prescribed Vortex Wake
QS	Quasi-Static
RANS	Reynolds-Average Navier-Stokes
STD	Standard Deviation
TLP	Tension Leg Platform
TSR	Tip Speed Ratio
VAWT	Vertical Axis Wind Turbine
WEC	Wave Energy Converter

Contents

List of Figures

List of Tables

Chapter 1

Introduction

Contents

Figure 1.1 – Annual onshore and offshore wind installations in the EU (from [Fraile and Mbistrova, 2018]).

1.1 Offshore wind: foreword

The idea of converting wind energy into electricity appeared in the late XIXth century [Rapin and Noël, 2010]. Today, this sector is expanding at high speed as many countries aim at reducing their fossil-based electricity production share. The global cumulative installed wind capacity has for instance grown from 59GW in 2005 up to 238GW in 2011 [Islam et al., 2013]. It almost reached 500GW in 2016 [Fried, 2017]. Today's trend is to install wind turbines off the shore. Pushing turbines offshore allows to access to a resource of better quality (stronger and less varying winds), but also to avoid visual pollution and thus ease the social acceptance of those turbines. Installed systems are then transported by boat, which permits bigger rotors than onshore.

The capacity factor of onshore wind turbines is increasing with the progress in engineering and the better knowledge of the resource. Also, the political will to develop renewable energy eases the access to better wind resource. For instance, in ranged from 25% to 50% in the US in 2013 [Moné et al., 2015]. The capacity factor of installed offshore wind turbines in the EU ranges from 29% to 48% [T. and Mbistrova, 2018]. The highest monthly capacity factor for offshore wind power reached 67.9% in Germany in February 2017. Figure 1.1 shows the annual onshore and offshore wind installations in the European Union (EU) from 2005 to 2017. One can see that the offshore share is increasing each year.

Offshore turbines get also bigger and bigger: the first 11 commercial rotors to be installed offshore in 1991 had a 37m diameter (Bonus B37, 450kW [Rapin and Noël, 2010]), today's rotors almost reach 180m diameter and are planned to exceed 250m by 2020 [Islam et al., 2013]. The wind turbines are eventually being pushed further offshore where the wind resource is more abundant, but in deeper seas where bottom-fixed foundations are no longer possible. The first offshore floating wind farm was thus installed in October 2017 in Scotland (Hywind Scotland).

New challenges emerge: the sea is a violent environment with stronger winds and waves, offshore operations and maintenance are complex, ... Also, the offshore wind energy industry needs to lower its Levelized Cost of Energy (LCoE) if it wants to be competitive on the energy market. To do so, it is essential to optimise the energy conversion of Floating Wind Turbines (FWTs) and to reduce the costs of the structures and installations. Many improvements are thus expected in our knowledge about such systems and their behaviour at sea.

Figure 1.2 – Three types of platforms for FWTs (graphic by Josh Bauer, NREL).

1.2 Floating offshore wind turbine technologies

1.2.1 Floating support platforms

If the water depth exceeds 50m, bottom-fixed structures supporting the turbines are usually too expensive. Floating platforms have hence been developed to carry Floating Wind Turbines (FWTs). Platforms and mooring concepts coming from the Oil and Gas industry such as SPAR, Semi-Submersible, barge, or Tension-Leg Platform (TLP) platforms have been adapted to support Floating Wind Turbines (FWTs). Three of of these platform types are presented in figure 1.2 (from the left to the right: SPAR, Semi-Submersible and TLP).

Every platform has its pros and cons. A SPAR platform is stabilised by its low centre of mass compared to its centre of buoyancy but has a very large draft. Its reduced water plane area reduces the waves loads compared to other types of platforms. It is usually moored with soft catenary mooring lines and has a pitch natural period around 30s. The semi-submersible and barge platforms have a large metacentric height and are stable thanks to their spread water plane area. They are usually moored with catenary mooring lines. Having a higher hydrostatic stiffness than the SPAR, their pitch natural period is usually smaller and near 20s. FWTs based on SPAR, semi-submersible or barge platforms can usually be assembled at the harbour or close to the shore and towed to the wind farm site. Eventually, the TLP platform is stabilised by its taut mooring system (usually cables) and a large positive buoyancy. Its stiff mooring system induces very short natural periods in pitch and heave, usually below 5s. A TLP is hence more difficult to transport and install as the fully assembled turbine is not stable without its moorings.

For instance, a stability triangle is represented in figure 1.3. Each contribution to the stability: ballast, buoyancy and moorings are represented in respectively red, green and blue arrows. The shorter the arrow, the more important its contribution. The SPAR platform is for example stabilised with its ballast and is located in the lower left
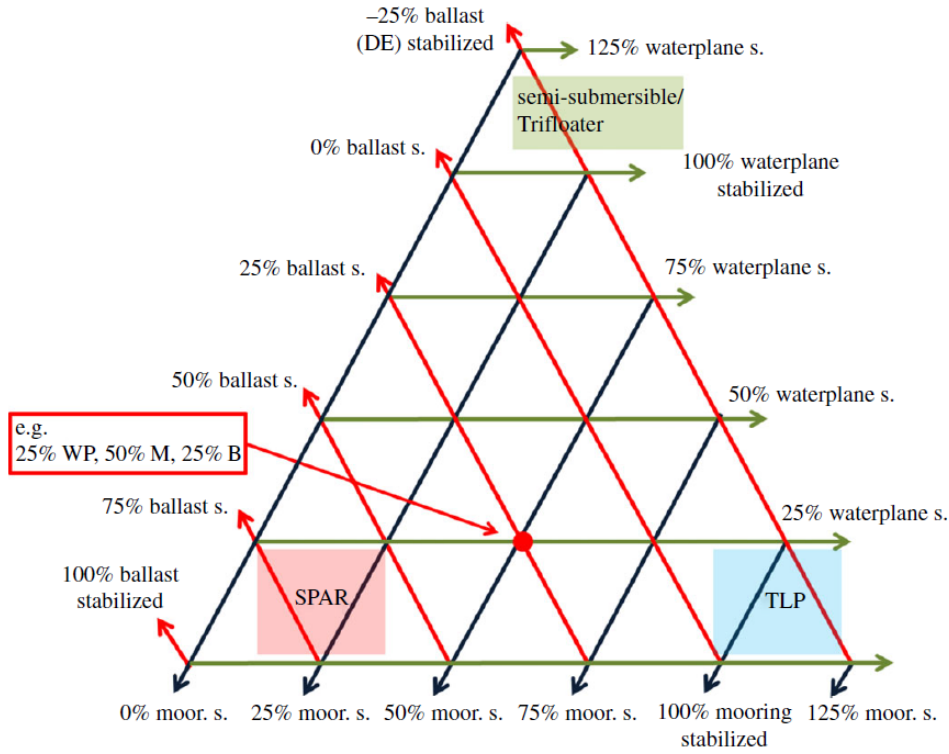
Figure 1.3 – Platform stability triangle (from [Borg and Collu, 2015a]).

angle of the triangle. The red dot in the center of the figure shows another example of a random platform stabilised 25% with its buoyancy (or water plane area), 50% with its moorings and 25% with its ballast.

The choice of a platform depends a lot on the site's environmental conditions (depth, waves, current, wind), but also on the rotor and tower design, mooring choices and anchoring possibilities. Engineers must then design cost-efficient solutions, keeping natural periods outside the environmental excitation frequencies. An analysis of the dynamics and economics of several FWTs is for example presented in [Wayman, 2006].

1.2.2 Floating Horizontal Axis Wind Turbines

Horizontal Axis Turbines (HAWTs), which were more efficient than Vertical Axis Wind Turbines (VAWTs) in onshore applications, have first been studied for offshore floating installations. Rotors' topologies are similar to those installed onshore: mostly three-bladed and rotating around a horizontal axis. However, their structural design depends on the offshore environment and on the motions of the platform. For instance, the tower and the blades can experience substantial oscillating loads due to the motions of the platform.

Offshore wind turbines are also much bigger than onshore turbines. Compared to a 100m diameter 3MW onshore turbine, offshore rotors under development grow up to more than 200m diameter for a 10 to 20MW rated power.

Notably, the *Floatgen* wind turbine (EU Project FP7) is the first FWT installed in France 2018. The barge platform designed by IDEOL supports a 2MW three-bladed HAWT shown in figure 1.4.

Figure 1.4 – Installation of the *Floatgen* wind turbine ©Centrale Nantes/ABOVE ALL.

1.2.3 Floating Vertical Axis Wind Turbines

In 1926, Georges Darrieus, a French engineer, filed the first patent related to a Vertical Axis Wind Turbines (VAWT) [Darrieus, 1931]. It is illustrated in figure 1.5. The Darrieus lift-driven VAWT concept has been for instance at the heart of many research at the Sandia National Laboratories (USA) from the 1970's to the 1990's [Sutherland et al., 2012]. It was shown to be less efficient for bottom-fixed applications than the Horizontal Axis Wind Turbines (HAWTs): the measured optimal power coefficients C_p of a VAWT and of a HAWT are respectively approximately 0.4 and 0.45.

However, as presented in [Borg et al., 2014b], VAWTs are not sensible to the wind direction and can have lower mechanical parts (generator, gearbox, if needed). Also, depending on the designs, the center of thrust and of gravity can be lower than that of a HAWT. It enhances the turbine's stability and can hence reduces the costs of the substructure. Also, the lower mechanical parts simplifies the installation and mainte-nance operations, which reduces operational costs as well. This is illustrated in figure 1.6, from [Borg et al., 2014b].

A vertical axis rotor has a very different behaviour from that of a HAWT. First, the thrust and torque is highly oscillating. As presented in [Cheng, 2016], this can induce oscillations in the dynamic behaviour of the turbines and cyclic loadings can lead to fatigue rupture. The rotor experiences an oscillating side force which can lead to unusual transverse motions compared to a HAWT. Finally, the counter torque of the generator induces oscillations in yaw of the whole system. The mooring system provides the restoring torque and additional tensions are hence induced in the mooring lines.

It is also relevant to mention that the industrial network of onshore and offshore HAWTs is now wide (including large companies such as *Siemens*, *VESTAS*, ...). However VAWTs are still at R& D stage and projects are often being carried out by smaller developers.

Different concepts of Floating VAWTs have been developed in the last years. For instance, *DeepWind* [Paulsen et al., 2014] is a 5MW floating VAWT presented in figure 1.7, aimed at reaching 20MW once upscaled. It consists in a 2-bladed troposkien rotor (or Φ-shaped) mounted on a SPAR buoy. The Centre of Gravity (COG) is low as

Dec. 8, 1931.   G. J. M. DARRIEUS   1,835,018
TURBINE HAVING ITS ROTATING SHAFT TRANSVERSE
TO THE FLOW OF THE CURRENT
Filed Oct. 1, 1926
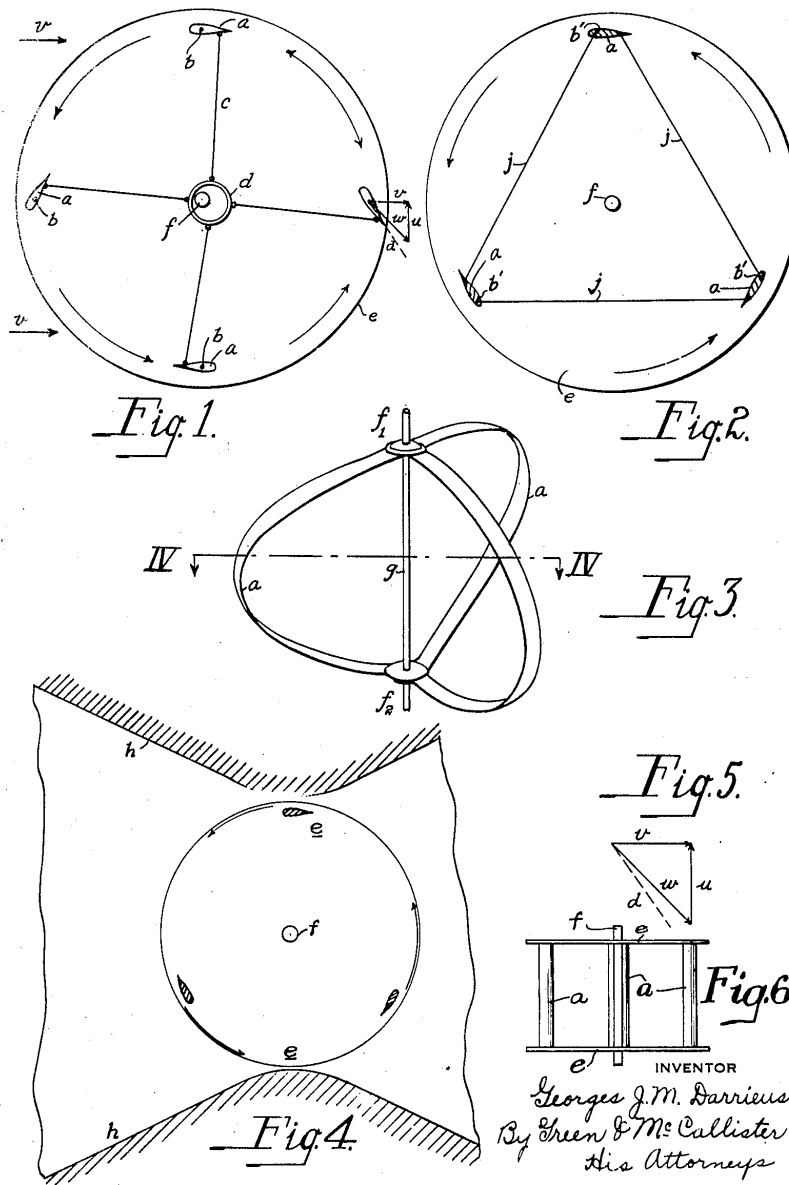
Figure 1.5 – Patent from Georges Darrieus on a VAWT. Prority date: 1925 [Darrieus, 1931].
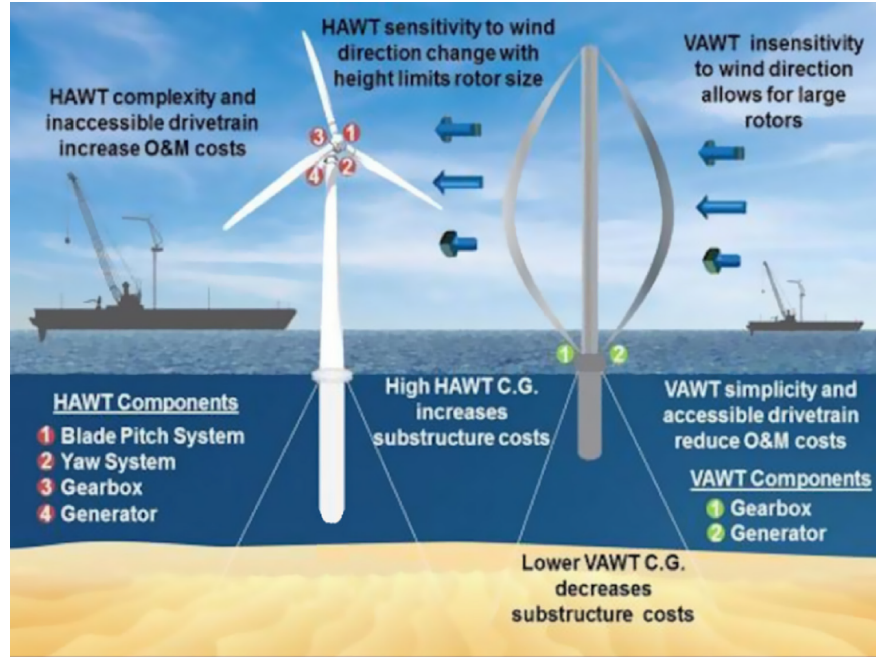
Figure 1.6 – Conceptual comparison: HAWT vs. VAWT (Graphic from Sandia National Laboratories).

the whole electrical part is at the bottom of the SPAR. *Nenuphar* [1] combines a semi-submersible floater with twin counter-rotating straight-bladed rotors (or *H*-shaped) as presented in figure 1.8. This concept allows to bypass several of the presented issues concerning floating VAWTs, such as oscillating side force, and counter generator torque. Eolfi is leading another project with several industrial partners on another 5MW floating VAWT called *SpinFloat*, presented in figure 1.9. It has straight blades which eases the dynamic blade pitch control to enhance the energy conversion and is also supported by a semi-submersible floater.

1.3 Modelling Floating Wind Turbines

1.3.1 Modelling needs and challenges

An accurate modelling is essential for analysis and design phases of FWTs. Numerical studies can be performed, alongside with experimental campaigns on reduced scale models.

Experimental works carried out on FWTs raise several issues:

- Experimental modelling of FWTs are very expensive as it needs wind tunnel and/or wave tanks, which are complex and expensive facilities. Also, generating a good wind field in a wave tank is very difficult;

- Downscaling a wind turbine is complicated as both Reynolds and Froude numbers need to be respected in either aerodynamic and hydrodynamic parts;

- Motions and loads can be difficult to measure accurately.

---

[1]The firm *Nenuphar* entered liquidation in April 2018

Figure 1.7 – DeepWind VAWT (from [Vita et al., 2011]).

Figure 1.8 – The TWINFLOAT concept by Nenuphar ©2015 NENUPHAR.

Figure 1.9 – The SPINFLOAT concept by Eolfi ©2014 ASAH LM/GustoMSC.

Many uncertainties can be at stake when testing small-scale prototypes. An uncertainty analysis is for example presented in [Robertson, 2017] about the testing of a HAWT supported on a semi-submersible platform in a wave tank with a wind generation device. As presented, the uncertainties are sometimes difficult to evaluate and still need more knowledge and experience in this type of testing.

To study and design FWTs, it is hence essential to develop reliable numerical tools that are able to simulate the system's behaviour at sea, including its different components and sub-systems (rotor, gearbox, generator, tower, platform, mooring system, dynamic cable, ...) in various environmental conditions. As presented in [Matha et al., 2011], numerical simulation of FWTs is very challenging as the physical phenomena to include are numerous. Also, state-of-the-art aerodynamic and structural design tools commonly used for bottom-fixed turbines may not be appropriate for FWTs. In harsh environmental conditions, for example, the large motions of the platform may have a strong impact on the aerodynamics of the rotor. Couplings between physical phenomena may be very important and complex. Hydrodynamics, aerodynamics, structural dynamics... and their interactions must therefore be accurately represented. Eventually, thousands of simulations need to be run on long durations to verify compliance of the systems with the industry standards. A compromise between CPU cost and accuracy is thus expected, even if the very fast recent progress in computational science allows now for more complex numerical models than before.

The Research and Development in offshore floating wind turbines hence faces on the one hand the need to implement accurate coupled numerical models and on the other hand the difficulty to implement and validate them due to a lack of experimental data on large-scale FWTs.

1.3.2 Previous studies on the seakeeping of Floating Wind Turbines

1.3.2.1 Studies on Floating Wind Turbines at the LHEEA Laboratory

Previous PhD theses have been realised in the LHEEA Laboratory of Centrale Nantes about FWTs. For instance, M. Philippe [Philippe, 2012] developed a coupling between the state-of-the-art code *FAST* [Jonkman and Buhl, 2005] and the hydrodynamic linear potential flow theory-based solver *NEMOH*. The study particularly focuses on the hydrodynamic model of a semi-submersible platform supporting a HAWT. The model includes linear radiation loads, non-linear Froude-Krylov forces and eventually quadratic drag forces on the slender elements of the platform. On the aerodynamic side, the coupling uses the Blade Element Momentum (BEM) model used in *FAST*, assuming a steady and inviscid flow on the rotor.

The thesis of A. Courbois [Courbois, 2013] designed an experimental facility consisting of a wind generation device in the Centrale Nantes wake tank so that FWTs could be tested at model scale with wave and wind induced loads. Experimental results on a semi-submersible floating HAWT are then compared to Philippe's model [Philippe et al., 2013]. It shows a good agreement on the hydrodynamic model in decay tests and regular waves tests without aerodynamic loads. But the agreement on the pitch motion, strongly influenced by the aerodynamic loads, is poor in regular waves and constant wind. This may come on the one hand from downscaling issues inducing errors in the aerodynamic loads, and on the other hand from the aerodynamic model that may not accurately represent the couplings between the motions of the platform and the aerodynamic loads. Especially, unsteady effects induced by the motions may be at stake.

1.3.2.2 Previous studies on floating HAWTs

The numerical modelling of floating HAWTs has been extensively studied in the last decade. The following tends to briefly describe the state of the art of the modelling of floating HAWTs.

A state of the art of the numerical simulation tools developed for FWTs was presented in 2011 in [Cordle and Jonkman, 2011]. Many of those codes use hydrodynamic, structural and mooring models developed for the offshore Oil & Gas industry such as *SIMO-RIFLEX* for example. Others such as *ADAMS* use more general codes developed to study structural dynamics in various industrial projects. Models developed to study FWTs consist most of the time of a seakeeping analysis numerical tool coupled to an aerodynamic solver. Aerodynamic tools used in the onshore wind research and industry have been primarily used. They are based on the BEM method with added semi-empirical models to account for unsteady and viscous effects, described in [Schepers, 2012] for instance. These corrections have been calibrated for onshore wind turbines and have not been validated for floating wind turbines up to now.

The OC3 [Jonkman and Musial, 2010] and OC4 [Robertson et al., 2014b] projects present a benchmarking of FWTs simulation tools focusing on a 5MW HAWT respectively supported by a SPAR platform and a semi-submersible platform. More than 20 software developers have contributed to the benchmarking but all numerical aerodynamic solvers involved use BEM or Generalised Dynamic Wake (GDW) theory-based solvers. The solvers show a reasonable agreement, especially on the motions of the platform but large discrepancies can be observed on the mooring and tower base loads for instance. The OC4 project especially showed some discrepancies in the results because of the variety of hydrodynamic models implemented for the semi-submersible platform.

The OC5 project is ongoing and focuses on experimental validation of the models developed within the OC4 project. Experimental measurements are confronted to numerical results of the semi-submersible HAWT in [Robertson et al., 2017]. Given the level of uncertainty on the measurements [Robertson, 2017], it is however difficult to conclude on the quality of the agreement of the numerical solvers with the observed physics.

Errors in the numerical solvers presented above may partly come from the aerodynamic models. The BEM assumes a steady flow on the rotor and the GDW assumes a lightly loaded rotor. However unsteady aerodynamic phenomena may happen on a FWT, especially when its rotor is highly loaded. For example, [Sebastian and Lackner, 2013] showed through a frequency domain analysis that a wide range of oscillations frequencies (including the natural frequencies of the FWTs) may induce unsteady loadings that cannot be accounted for in BEM methods. Also, [Jeon et al., 2014] and [Shen et al., 2018b] use Free Vortex Wake (FVW) methods to emphasize unsteady vortices generated in the near wake of the rotor as it moves. These vortices can induce unsteady loadings and alter the wake induction.

These unsteady loading and induction variations are induced by the inherent rotor-wake interaction and by the motions of the platform. Coupled simulation tools accounting for unsteady aerodynamic loading are hence necessary in order to investigate whether or not they have a substantial impact on the dynamic behaviour of the FWTs in seakeeping analyses.

1.3.2.3 Previous studies on floating VAWTs

Previous studies have been conducted on the subject of floating VAWTs. A non-exhaustive list of such studies which are relevant references for this PhD thesis is presented in the following.

In his PhD thesis at DTU Wind Energy (Denmark) Vita [Vita et al., 2011] designed the DeepWind floating VAWT with the design tool *HAWC2* including a Double Multiple Streamtube (DMS) solver to compute the aerodynamic loads (see chapter 2). A 5MW baseline design is presented in detail, focusing on several aspects: aerodynamics, control, hydrodynamics, blades structure and generator design. A cost model for the DeepWind VAWT is finally presented.

Many research has also been run on the topic of floating VAWTs by Borg et al. A review of the interests of offshore floating VAWTs has been published [Borg et al., 2014b] [Borg et al., 2014a] [Borg and Collu, 2015b], presenting several aspects such as aerodynamic models, hydrodynamics, moorings and structural dynamics. A coupled model, *FloVAWT* [Collu et al., 2013] has been developed, coupling a linear potential hydrodynamic solver to a DMS aerodynamic solver. Amongst other studies, Borg et al. studied the response of VAWTs based on various floaters [Borg and Collu, 2014]. It particularly illustrates differences in the mooring design requirements for a VAWT, compared to a HAWT. The static and dynamic behaviours of a floating VAWTs and a HAWTs [Borg and Collu, 2015a] were also compared, highlighting the oscillating dynamic behaviour of a VAWT. It also emphasizes its lower centres of thrust and gravity which reduces the cost of the substructures.

In his PhD thesis at NTNU (Norway), Wang [Wang, 2015] developed a new coupled method for floating VAWTs, *Simo-Riflex-DMS* (see chapter 2), and studied the dynamic response of such systems (including structural dynamics). In particular, a study has focused on the use of a hydrodynamic brake to mitigate the yaw response of the floater during an emergency shut-down.

During his PhD thesis at NTNU (Norway), Cheng [Cheng, 2016] followed the work of Wang and developed *Simo-Riflex-AC*, coupling an Actuator Cylinder theory-based aerodynamic solver to *Simo-Riflex* (see chapter 2). Amongst many other aspects, Cheng et al. published studies on the effects of either the number of blades [Cheng et al., 2017b] or the support structure concept [Cheng et al., 2015] on the behaviour of a floating VAWT. Those studies consider structural and mooring dynamics and thus highlight specific design issues for VAWTs coming from highly oscillating behaviour. However, as for the other studies presented in this part, the aerodynamic model is quasi-steady. The validity of this assumption has not been validated and the impact of unsteady aerodynamics has not been investigated up to now.

1.4   Aims and scope of this PhD

Stemming from fixed onshore and offshore wind developments, quasi-steady aerodynamic models are widely used in research and in the industry to study both Floating Horizontal and Vertical Axis Wind Turbines. Because of the wave and wind induced motions, the accuracy of these models may be questionable. As presented in section 1.3.2.2, the importance of unsteady aerodynamics in the calculation of aerodynamic loads acting on FWTs has been evaluated in previous research but some questions still need to be answered:

- How to quantify the impact of unsteady aerodynamics on FWTs simulations?

- To what extent do unsteady aerodynamic loads alter the simulation of the sea-keeping of FWTs?

- Which aerodynamic model is the most appropriate to simulate the behaviour of FWTs in complex environmental conditions?

The latter also addresses the need for a compromise between accuracy and efficiency of the models, depending of the level of accuracy needed in one or other phase of the design of a FWT.

Lower the cost of energy has become a priority in the offshore wind Research and Development. It is not only important to improve the design process of FWTs, we must also question the relevance of the FWTs concepts. The renewed interest for floating VAWTs raises questions about their cost and relevance to install such systems offshore.

- How does a floating VAWT behave at sea compared to a HAWT?

- What are the performances of a floating VAWT compared to a HAWT?

This PhD thesis *Unsteady aerodynamic modelling for seakeeping analysis of Floating Offshore Wind Turbines* addresses these questions and is structured as follows.

First, chapter 2 describes our actual knowledge and current methods on the simulation of FWTs. State-of-the-art simulations tools are described, covering several aerodynamic models. Hydrodynamic models, mooring modelling theories and control methods are explained.

A new simulation tool has been developed during this PhD thesis, coupling hydrodynamic, aerodynamic, mooring modelling and control for FWTs. The software *InWave* [Combourieu et al., 2014], developed at INNOSEA and Centrale Nantes, has been coupled to two aerodynamic solvers: a quasi-steady Double Multiple Streamtube

(DMS) solver and *CACTUS* [Murray and Barone, 2011], an unsteady Free Vortex Wake (FVW) solver. During this PhD thesis, the DMS solver has been developed and *CACTUS*, which was initially developed by the Sandia National Laboratories (USA), has been improved and adapted for the coupling with *InWave*. The developments realised during this PhD thesis and the involved theories are extensively described in chapter 3. The validation of the implemented tools is also presented.

Chapter 4 shows the first application of the developed codes on the case of a floating HAWT. It compares *InWave* to the state of the art quasi-steady code *FAST* [Jonkman and Buhl, 2005]. The test case is the NREL 5MW HAWT supported by the OC3Hywind SPAR platform as defined in [Jonkman, 2010]. The study shows a good agreement between the two solvers but also emphasizes the impact of unsteady aerodynamic loadings on the seakeeping of a floating HAWT when the rotor is highly loaded. Nevertheless, the results obtained with the quasi-steady seem to accurately describe the global behaviour of the turbine, which could be enough for early-stage design phases.

Chapter 5 focuses on the seakeeping of a floating VAWT consisting of a two-straight-bladed rotor based on a SPAR platform. It tends to quantify the impact of unsteady aerodynamic modelling when simulating the behaviour of such a structure at sea. The unsteady Free Vortex Wake solver is then compared to the in-house DMS solver developed during this PhD thesis. Similarly to chapter 4, the study shows that, when compared to a quasi-steady aerodynamic solver, unsteady aerodynamic loading influence the simulation of the seakeeping of a floating VAWT when the rotor is highly loaded. The DMS solver however shows encouraging results that could be sufficient for early-stage design phases of floating VAWTs.

Eventually, chapter 6 shows a comparison between floating Horizontal and Vertical Axis Wind Turbines. The comparison involves the NREL5MW HAWT and a 2-bladed troposkian rotor supported by the DeepCWind semi-submersible platform [Robertson et al., 2014a]. The aim is to compare the seakeeping performance and power production of these two turbine concepts in several complex sea-states. The study indicates that the VAWT needs to improve and develop new control laws in order to mitigate its motion in over-rated wind speeds and steep sea-states.

This PhD thesis was made possible thanks to the collaboration of the LHEEA Laboratory (Centrale Nantes/CNRS), INNOSEA and the ANRT (*Association Nationale de la Recherche et de la Technologie*). It started in November 2015.

Chapter 2

State of the art of the numerical Modelling Of Floating Wind Turbines

Contents

Figure 2.1 – Unsteady aerodynamics for a Floating HAWT.

2.1 Aerodynamics

2.1.1 Overview of the aerodynamic models used for FWTs

2.1.1.1 Floating Wind Turbine aerodynamics

A floating wind turbine is subjected to an even more unsteady flow than a bottom-fixed turbine. As presented in figure 2.1, the sources of unsteady phenomena are numerous:

- The inflow is turbulent and unsteady: it includes a boundary layer with different scales of vortices, it interacts with the waves and can thus vary in velocity and direction;

- The rotor generates unsteady vortices and interacts with its wake;

- Dynamic stall can occur on the blades;

- If used, the blade pitch control also induces lift and drag variations;

- The tower generates vortices and creates a shadow-effect;

- The motions of the whole structure depends on the hydrodynamic loads, mooring, and aerodynamics and thus induce unsteady relative wind velocities at the rotor. In particular, the aerodynamic thrust can result in a strong tilt angle of the turbine, resulting in a skewed flow configuration. Also, the pitch motion can induce strong rotor-wake interactions.

Considering the aerodynamics of FWTs, these phenomena may result for instance in strong variations of Angle Of Attack (AOA) on the blade, oscillations in blade loading resulting in fatigue rupture...

Different levels of complexity exist amongst the aerodynamic models used for wind turbines rotors [Van Kuik, 2018]. Some of them model the full rotor with its detailed geometry in a real viscous flow. These Computational Fluid Dynamics models require to mesh accurately the blade section from its leading edge to its trailing edge with sufficiently fine cells to correctly calculate the boundary layer effects in order to correctly model the pressure field around the rotor. They can be very complex to implement and have a very high CPU cost. Such numerical models are thus rarely used to model entire turbines in large time and space scales. Other models consider the blade geometry in an inviscid flow, which lowers the CPU cost.

Other theories do not consider the exact blade section and its interactions with the flow but only use tabulated aerodynamic data to model the effects of the blade geometry. These models use the assumption of the Blade Element theory. The lift and drag coefficients acting on a blade section are obtained as a function of the AOA. The fluid around the rotor can be either viscous or inviscid which strongly impacts the CPU cost. Such inviscid models with low CPU costs are widely used for engineering purposes.

A non-exhaustive list of models used for wind turbines aerodynamics is presented in this part, starting from the simplest fluid models to the most complex ones. More details on rotor aerodynamics can be for example found in [Van Kuik, 2018].

2.1.1.2 Froude-Rankine Actuator Disk

The *Actuator Disk* or Froude-Rankine theory has been widely used to study propellers and wind turbines. It is for instance used coupled with Blade Element theory (described in part 2.1.1.3) in the *AeroDyn* code [Moriarty and Hansen, 2005], developed at the National Renewable Energy Laboratory (NREL, USA). It considers an actuator disk in a streamtube as presented in figure 2.2.

This theory is based on the assumptions of:

- potential flow (inviscid, incompressible and irrotational);

- steady and axial flow.

When passing through the actuator disk, the flow experiences a pressure drop (in the case of a wind turbine) from p_u to p_d. The thrust force on the disk and the wind speed through the disk can be computed applying Bernoulli's theorem on both sides of the actuator disk and the conservation of the momentum through the rotor. The thrust and the power are obtained as a function of an induction factor a defined as $a = \frac{U_\infty - U_d}{U_\infty}$, U_d being the velocity through the disk.

The fluid velocity at the disk is then equal to:

$$U_d = U(1 - a) \tag{2.1}$$

And the velocity in the wake, at the outlet is equal to:

$$U_w = U(1 - 2a) \tag{2.2}$$

The thrust coefficient is finally defined as:
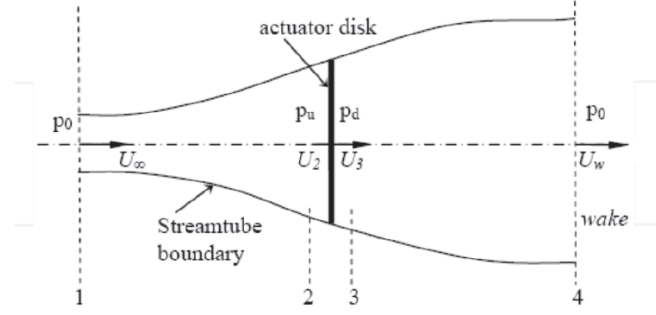
Figure 2.2 – Froude-Rankine Actuator Disk in a streamtube (from [Kulunk, 2011]).
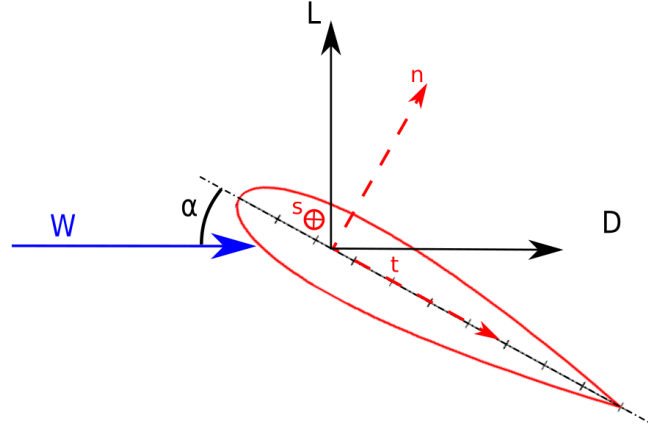
Figure 2.3 – Blade Element in 2D flow.

$$C_T = 4a(1 - a) \tag{2.3}$$

And the power coefficient as:

$$C_P = 4a(1 - a)^2 \tag{2.4}$$

More details about the equations are given in appendix A.1.

2.1.1.3 Blade Element theory

For a given blade divided into a number elements in the span-wise direction, the Blade Element theory assumes that each element experiences a two-dimensional flow in its normal and tangential directions. The loads on a blade element is then in the same plan, as shown in figure 2.3. This assumption neglects the flow in the span-wise direction of a blade and allows to use tabulated aerodynamic coefficients:

- C_L: lift coefficient;

- C_D: drag coefficient;

- C_M: moment coefficient.

These coefficients can be either determined with experimental measurements or obtained with viscous or potential flow solvers. In the following, the moment coefficient

is neglected. Sometimes, to model a VAWT for example, the aerodynamic coefficients need also to be known on wide intervals like $[-180^o, +180^o]$. Extrapolation is then needed. Two main methods can be outlined: Montgomerie's [Montgomerie, 2004] and Viterna's [Viterna and Corrigan, 1982]. The lift L and the drag D forces on the blade elements are then respectively given as follows:

$$L = \frac{1}{2}\rho W S_{BE} C_L(\alpha, R_e) \tag{2.5}$$

$$D = \frac{1}{2}\rho W S_{BE} C_D(\alpha, R_e) \tag{2.6}$$

Where S_{BE} is the surface of the blade element. A numerical model that uses Blade Element assumption does not consider the flow diversion with the blade geometry, but assumes the forces are concentrated on a lifting line and computes the lift and the drag forces directly as a function of the local flow velocity W, the Reynolds number R_e and the AOA α on the blade element.

2.1.1.4 Models based on tabulated polar data

Several models use the Blade Element theory with various degrees of complexity for the flow modelling.

The most common models are the *Momentum* models. They use Froude-Rankine theory coupled to the Blade Element theory. For HAWTs, the *Blade Element Momentum* uses one actuator disk at the rotor plane. It is detailed in [Kulunk, 2011] and [Moriarty and Hansen, 2005]. It assumes an axial, steady and inviscid flow on the rotor. The induction factor of the actuator disk equations must be solved so that the thrust on the disk equals the thrust force on the blades obtained through Blade Element Theory. A tangential induction factor is also introduced so that the torque coefficient C_Q converges as well in both theories. This theory has been widely used to study HAWTs, either bottom-fixed or floating, and is for instance implemented in the wind turbine design tool *FAST* [Jonkman and Buhl, 2005]. It however shows some limitations at high TSRs when the rotor strongly interacts with its wake or when the turbine is tilted because the rotor is in a skewed flow. Semi-empirical models such as Glauert's corrections (presented in [Moriarty and Hansen, 2005]) can be added to the model's equations to account for these effects.

Equivalent theories for VAWTs can be derived in several forms as detailed for example in [Paraschivoiu, 2002]: *Single Streamtube* (SS), *Multiple Streamtube* (MS) or *Double Multiple Streamtube* (DMS) theories. They are also based on the conservation of the momentum in a quasi-steady flow. The SS method assumes that the actuator disk representing the rotor rotor is entirely contained in one streamtube. The MS theory extends this model with many adjacent and independent streamtubes, all passing through the actuator disk representing the rotor. This allows to have a distribution of different induction factors on the rotor projected surface. At last, the DMS theory considers that the streamtubes of the MS theory pass through two subsequent actuator disks: the first one representing the upwind half of the blades and the second one on the downwind side. The DMS theory will be detailed in part 3.6.2. The main difference between HAWTs and VAWTs being that a VAWT blade passes both upwind and downwind of the rotor center.

The *Actuator Cylinder* theory (AC) has also been derived from the actuator disk theory for VAWTs. It is similar to Froude-Rankine theory but considering the whole surface swept by the rotor blades. For a straight-bladed VAWT, it would thus be a
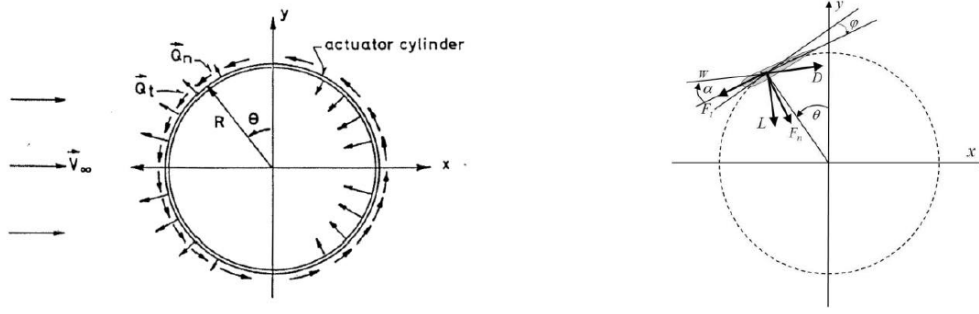
Figure 2.4 – Actuator Cylinder representation (from [Madsen, 1982]).

cylinder. The AC theory has been first introduced in [Madsen, 1982] and then improved in [Cheng, 2016]. It lies on the equations of Euler for an inviscid and incompressible flow and on the conservation of mass. It also uses the Blade Element theory and tabulated aerodynamic coefficients to compute blade loads. In figure 2.4 is represented an actuator cylinder surface on the left. On the right is plotted a blade segment with its loadings at a given instant.

The *Free Vortex Wake* (FVW) has first been applied to a full three-dimensional Darrieus VAWT in [Strickland et al., 1979]. This theory also assumes an inviscid fluid but models the wake induction in a different way. The lift forces on the blades generate vortices. At each time step, these vortices are shed and advected in the wake. By vorticity, they induce velocities in the whole fluid domain, including at the rotor inflow. This induction can be computed with the Biot-Savart law. Vortex filaments also interact with each other. If this interaction is ignored, the vortex filaments are advected at a constant wake speed. The method is then called *Prescribed Vortex Wake* (PVW). More detail about this theory is given in part 3.6.1.

A similar approach can be used in the *Actuator Disk* theory (AD). Following Froude-Rankine Actuator Disk theory. The flow around the rotor is solved with a RANS solver but the loads on the blades and the reaction effects on the fluid is computed with an actuator disk and/or a complete and more accurate Blade Element Momentum code.

The *Actuator Line* theory (AL), introduced by [Sørensen and Shen, 2002], is an unsteady three-dimensional flow model. It considers rotor blades as actuator lines immersed in a viscous flow that can be computed with a RANS solver. This theory uses the incompressible Navier-Stokes equations described below:

$$\frac{\partial \mathbf{U}}{\partial t} + \mathbf{U} \cdot \nabla \mathbf{U} = -\frac{1}{\rho} \nabla p + \nu \nabla^2 \mathbf{U} + \mathbf{f} \tag{2.7}$$

$$\nabla \cdot \mathbf{U} = 0 \tag{2.8}$$

Where the force on the blades f is computed with the Blade Element Theory.

An important limitation of these numerical models is that using tabulated aerodynamic coefficients assume that the flow on the blades is quasi-steady. However, AOA variations can result in a hysteresis in the aerodynamic loads that is difficult to account for with tabulated aerodynamic coefficients. Also, these tables can be either measured in wind tunnel tests or computed using CFD solvers or potential flow solvers such as XFOIL [Drela, 1989]. But for VAWTs, for example, the AOA on the blade is always varying and variations are particularly strong at low TSRs and they may enter stall at each revolution. The used aerodynamic coefficients thus have a very important impact on the computed behaviour of the turbine [Marten et al., 2017].
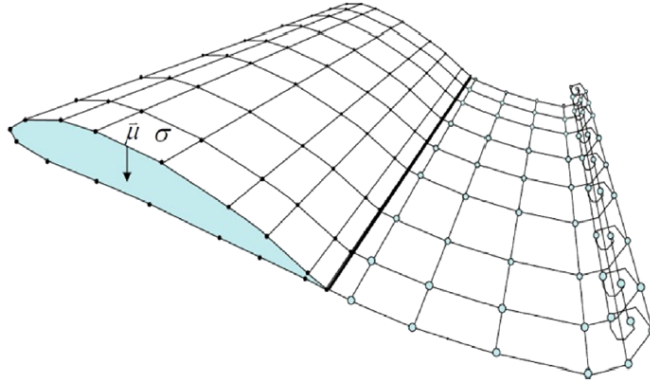
Figure 2.5 – Discretization of a blade in panels including potential sources and panels (from [Borg et al., 2014b]).

2.1.1.5 Models based on exact blade section geometry

Other methods, such as Panels Free Vortex Wake, consider the accurate geometry of the blade but in a potential flow, as presented in [Shen et al., 2018a] for HAWTs or [Ferreira, 2009] for VAWTs for example. The surface of the foil is meshed and "covered" with potential flow sources or doublets. The calculation method is similar to the hydrodynamics Boundary Element Method and improves the modelling of dynamic inflow as presented in [Shen et al., 2018b]. The induction of the wake is then computed in a similar way to Free Vortex Wake Theory, presented in part 3.6.1. A picture presenting a meshed blade portion is displayed in 2.5. Viscous phenomena such as dynamic stall cannot be computed in this theory, however they can be accounted for with semi-empirical models integrated to the solvers.

The most accurate way to model a wind turbine rotor is to calculate the flow around it by solving the Navier-Stokes equations. The complex viscous and possibly compressible flow around the rotor can be computed with different solvers. First of all, the *Reynolds Average Navier-Stokes* equations (RANS), or URANS (for *unsteady* RANS), use an approximation of turbulence at all scales. The *Large-Eddy Simulations* (LES), or an equivalent *Variational Multiscale* (VMS) (implicit LES), uses an additional term to approximate the small scales of turbulence. Only the large scales of turbulence have thus to be computed and the simulations must be run on a much finer mesh and time step. CPU cost is higher than for RANS models. Finally, a *Direct Navier-Stokes* solver (DNS) can be used to compute all scales of turbulence but the mesh can then rapidly reach a very high number of nodes and elements and CPU cost is extremely high. No particular assumption has however to be made on the flow. A comparison of RANS, LES and DNS simulations on a turbulent jet is shown in figure 2.6a. These solvers can accurately model viscous phenomena such as dynamic stall. However, compared to engineering models, both spatial and temporal discretization have to be very small and this increases the CPU cost. A screenshot of a 25 million-element fluid domain mesh for a full FWT problem modelled with an Arbitrary Lagrangian–Eulerian Variational Multicale (ALE-VMS) formulation is displayed in figure 2.6b. Today, the most complex theory used to model FWT aerodynamics is LES (or equivalent) but it is only at an early stage for now (as presented in [Yan et al., 2016], for instance). RANS solvers have been adapted for floating wind turbines (as presented in [Quallen and Xing, 2016], for instance) but they are still too expensive to be used in engineering purposes.

(a) DNS (left), LES (middle) and RANS (right) simulations of a turbulent jet (from [Maries et al., 2012]).

(b) Full FWT mesh for a LES (from [Yan et al., 2016]).
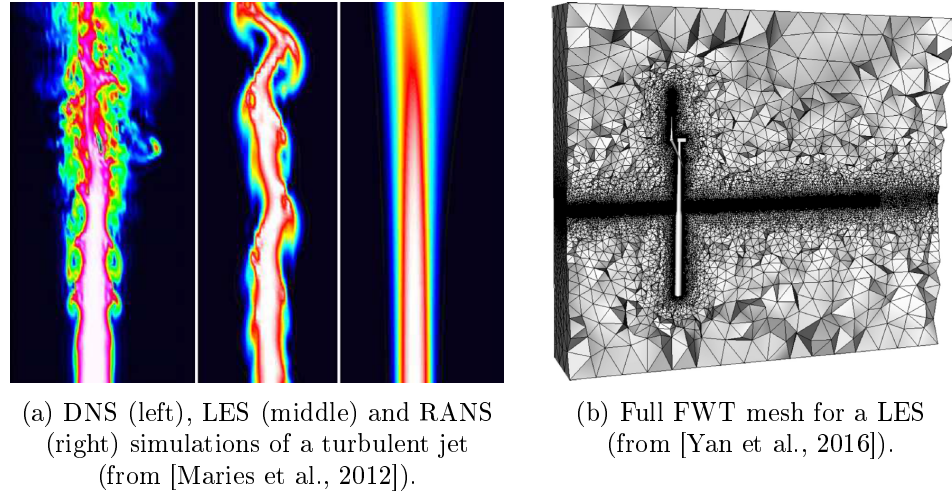
Figure 2.6 – CFD models for FWTs.

2.1.2 Semi-empirical corrections

2.1.2.1 Semi-empirical dynamic inflow models

Momentum models assume a steady flow, which implies that the induced velocity follows instantaneously a change in time in the force coefficient. The wake is hence assumed to be at an equilibrium at each time step. However, given a sudden change in the blade pitch of wind speed, the induced velocity can be lagged before reaching its equilibrium. Several models have been developed to account for this lag in the blade loads when the blade pitch is suddenly changed. They are called dynamic inflow models.

Dynamic inflow models have been developed from experimental measurements on test wind turbines. They can be added to BEM codes to account for unsteady induced velocity effects. For instance, in figure 2.7, is illustrated the effect of dynamic inflow on the induced velocity in a BEM code. The dashed line representing the quasi-steady model steps instantaneously with the blade pitch angle (blue line). The effect of the dynamic inflow is to lag the induced velocity as presented on the continuous black line. More details about those models are available in [Schepers, 2012].

2.1.2.2 Semi-empirical dynamic stall models

When a blade enters stall beyond a certain AOA (about 15° if static, depending on the Reynolds number) the flow can be detached from the blade and the lift decreases rapidly. Then, the flow reattaches if the AOA decreases. Depending on the AOA range, the stall angle can be delayed, and the flow reattachment can also be delayed. This phenomena has for example been accurately described in [Jumper et al., 1987].

Semi-empirical models are sometimes used to improve numerical models that do not inherently account for this phenomena. For instance, the Free Vortex Wake model presented in part 2.1.1.4 assumes a potential flow and uses tabulated aerodynamic coefficients to compute the loads on the blades. It cannot inherently account for viscous phenomena. However, it is possible to use a dynamic stall model to account for dynamic stall.

Several models exist. It can be here pointed out that some models, such as *Gormont-Berg* or *Boeing-Vertol* presented in [Paraschivoiu, 2002], account for stall delay depending on the AOA range, by changing the lift and power coefficient as a
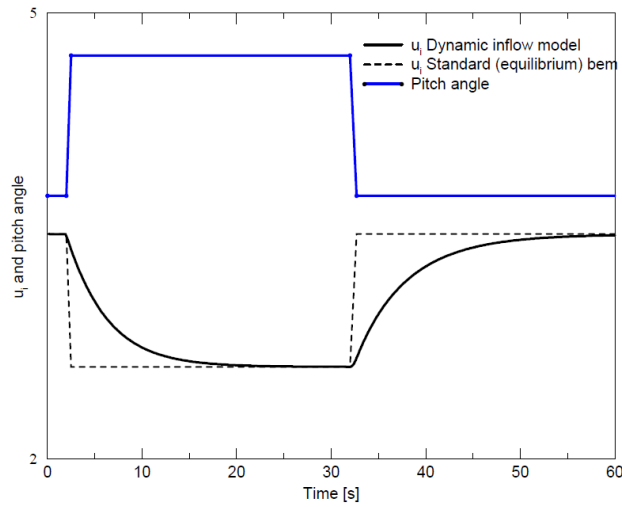
Figure 2.7 – Qualitative induced velocity in response to pitch angle step (from [Schepers, 2012]).

function of the AOA, of the AOA range and of empirical constants. The *Leishman-Beddoes* model [Leishman and Beddoes, 1989] tries to describe the physical phases of the stall phenomena: leading edge vortex build-up, vortex shedding, full stall, and flow reattachment. It may be more accurate but may also be more difficult to tune as it lies on more empirical constants to describe each phase.

2.1.3 Quasi-steady vs. Unsteady aerodynamic models

Amongst models based on Blade Element theory, some assume a steady flow (BEM or DMS theories, for instance) and others consider an unsteady flow (FVW theory). Quasi-steady solvers have been widely used for bottom-fixed applications as they show a very good compromise between CPU cost and accuracy. However, they have been shown to be unable to correctly capture some unsteady phenomena in the rotor aerodynamics that are inherent to FWTs. Previous studies have focused on this matter, particularly for HAWTs.

The wind thrust can lead to a significant tilt angle of a FWT, putting the rotor in a skewed flow configuration. Usually, BEM codes are known to be less accurate in a skewed flow as they miss the uneven distribution of the induction factor on the rotor. The FVW theory inherently accounts for those phenomena. It is shown in [Blondel et al., 2016] that a FVW is far more able than a BEM code to predict the loads acting on a rotor in this kind of configuration. An improved yaw model for a BEM method is however presented in [Blondel et al., 2017] and compared to a FVW and CFD Actuator Line (AL) models for a yawed HAWT. This improvement lies on many empirical constant and is hence difficult to calibrate but shows a good agreement with experimental measurements.

A frequency domain study presented in [Sebastian and Lackner, 2013] suggests that quasi-steady models cannot well predict important aerodynamics loads induced by platform motions. For example, for a HAWT based on a SPAR platform, the pitch and the yaw of the platform would induce unsteady aerodynamic loadings. Similarly, [Jeon et al., 2014] concludes that the creation and convection of the tip vortex on the blades

plays an important role on the aerodynamics of a floating HAWT especially when the rotor is moving in the wind direction. For example, [Tran and Kim, 2015] showed with advanced unsteady CFD smulations that the gap distance between advected tip vortices vary consequently when the turbine experiences a pitch motion, which could alter the loads on the rotor. Those vortices are inherently accounted for in FVW methods but can only be included in BEMs or DMSs by using semi-empirical models. [Shen et al., 2018b] for instance emphasises the tip vortex instability on a HAWT in imposed pitch motions. The impact of this unsteady phenomenon on the aerodynamic loads of a FWT has however not been investigated.

Eventually, [Bayati et al., 2016] presents a comparison between *AeroDyn* (BEM code) and experimental measurements on a HAWT submitted to imposed surge and pitch motion. It is shown that *AeroDyn* is unable to entirely reproduce the load variations due to the motions of the rotor, which induce unsteady aerodynamic phenomena.

Focusing on a land-based VAWT, [Blondel and Cathelain, 2017] shows in a benchmarking study that the dynamic stall models play a very important role as soon as the blades experience a strongly varying angle of attack. But both AC and FVW models here show a good agreement if stall models are not used. Also, the FVW seems to obtain better results than a Multiple Streamtube code when focusing on a pitching airfoil, due to its accurate description of the wake.

2.1.4 Summary of the aerodynamic models

Table 2.1 is a comparison of the previously mentionned aerodynamic models.

2.2 Hydrodynamics and hydrostatics

Two main state-of-the-art theories are used by engineers to study floating systems at sea. The choice mostly depends on the size of the system compared to the incident waves. To describe the size of a body compared to the waves, the Keulegan-Carpenter number KC is defined as follows:

$$KC = \frac{2\pi A}{D} \tag{2.9}$$

Where A is the wave amplitude and D is the dimension of the system.

2.2.1 Morison equation

For a large KC ($KC > 10$), the flow may be separated because the body is slender. Viscous effects are thus important. The Morison equation may be applied to compute the hydrodynamic forces acting on the body. It was originaly used for oscillating forces on slender cylinders. It thus assumes motions in oscillating flows. A slender body is divided into several elements and the Morison equation gives the hydrodyamic forces on each elements as follows [Faltinsen, 1990]:

$$\mathbf{F}_{hydro}(t) = \underbrace{\rho(1 + C_a)V\dot{\mathbf{u}}(t)}_{a} - \underbrace{\rho C_a V\dot{\mathbf{v}}(t)}_{b} + \underbrace{\frac{1}{2}\rho C_d A|\mathbf{u}(t) - \mathbf{v}(t)|(\mathbf{u}(t) - \mathbf{v}(t))}_{c} \tag{2.10}$$

Where ρ is the volumetric mass of the fluid, C_a is the added mass coefficient (giving the inertia coefficient as $C_m = 1 + C_a$), $\mathbf{u}(t)$ and $\mathbf{v}(t)$ are respectively the fluid and the

Table 2.1 – Comparative table of the aerodynamic models used for Wind Turbines.

Name	Fluid model	Loads	Wake	Corrections	Complexity	CPU cost
BEM - DMS	Inviscid Incompressible Steady	Momentum balance Blade Element	Implicit	Dynamic inflow Dynamic stall Skewed flow Highly loaded Tip/hub losses	+	+
AC	Inviscid Incompressible Steady Two-dimensional	Momentum balance Blade Element	Explicit	Dynamic stall	++	++
Vortex Wake	Potential	Lifting line (+ BE)	Explicit	Dynamic stall	++	++
		Lifting surface	Explicit	Dynamic stall	+++	+++
CFD Method	Misc. Fluid domain mesh	Momentum methods: Actuador Disk/Line + BE	Explicit	Misc.	++++	++++
	Misc. Full mesh	Pressure field on blade mesh	Explicit	Misc.	+++++	+++++

body element velocities and C_d is the drag coefficient. V is the volume of the element, and A is its projected area in the fluid velocity direction. The terms marked a, b and c are respectively the Froude-Krylov force, the added mass term (for a moving body) and the drag force.

This formula shows good accuracy for slender bodies and is easy to apply as it only needs two empirical constants C_a and C_d that depend on the Reynolds number R_e.

2.2.2 Potential flow theory

For a smaller KC ($KC < 2$), the flow will be fully attached to the body. Viscous effects are negligible and the flow is assumed potential (inviscid, isovolume and irrotational).

The hydrodynamic and hydrostatic loads F_H on a floating structure can be naturally calculated by integrating the unsteady fluid pressure acting on its wet surface S_B.

$$\mathbf{F}_H = \iint_{S_B} p\mathbf{n}dS \tag{2.11}$$

Where $\mathbf{n}$ is the normal vector oriented towards the outside of the body.

The pressure p in the fluid can be expressed as a function of the velocity potential ϕ as expressed in Bernoulli-Lagrange equation:

$$p = p_0 - \rho g z - \rho\frac{\partial\phi}{\partial t} - \frac{1}{2}\rho(\nabla\phi)^2 \tag{2.12}$$

The first aim of potential flow theory is then to calculate the velocity potential to compute the hydrodynamic loads. The equation of motion then writes:

$$\mathbf{M}\frac{d\mathbf{X}^2(t)}{dt} = \mathbf{F}_H + \mathbf{F}_{other} \tag{2.13}$$

Where:

- $\mathbf{M}$ is the (6x6) generalized mass matrix;

- $\mathbf{F}_{other}$ is any other force (induced by current, wind, moorings... if needed).

The Hydrodynamic force acting on the body can be decomposed into zero, first and superior orders components:

$$\mathbf{F}_H = \mathbf{F}_H^{(0)} + \mathbf{F}_H^{(1)} + \mathbf{F}_H^{(2)} + \mathbf{F}_H^{(3)} + ... \tag{2.14}$$

Where $F^{(0)}$ corresponds to the force at the equilibrium position or to a constant force (current drag, for instance). $F^{(1)}$ is the first order approximation of the wave forces, at the same frequencies. It is described in section 2.2.2.1. $F^{(2)}$ is then the second order force deriving from second order elements of equation 2.12. Its effects are described in section 2.2.2.2.

Following the same trend, the velocity potential and the free-surface elevation (used in equation 2.14) are also decomposed into fist and higher orders components:

$$\phi = \phi^{(0)} + \phi^{(1)} + \phi^{(2)} + \phi^{(3)} + ... \tag{2.15}$$

$$\eta = \eta^{(0)} + \eta^{(1)} + \eta^{(2)} + \eta^{(3)} + ... \tag{2.16}$$

The following does not describe the resolution of the involved equations, but how the forces are decomposed and how the equation of motion of a floating system is solved.

2.2.2.1 Linear potential flow theory

In a first approximation, only the first order terms can be kept in equation 2.12, using the potential decomposed in equation 2.15 and the free surface elevation in equation 2.16. The forces are then linearised and the equation of motion write:

$$\mathbf{M}\frac{d\mathbf{X}^2(t)}{dt} = \mathbf{F}_{HS} - \iint_{S_B} \rho\frac{\partial\phi^{(1)}}{\partial t}\mathbf{n}dS + \mathbf{F}_{other} \tag{2.17}$$

Linear potential flow theory is detailed for example in [Faltinsen, 1990] and [Molin, 2002]. The body is considered to have small-amplitude oscillations around its equilibrium position and the free-surface elevation is assumed to be very small: $\eta << O(1)$. This section focuses on the first order loads and describes the method used for seakeeping computations.

Where $\mathbf{F}_{HS}$ is the hydrostatic force (described in section 2.2.4.

Linear theory is usually solved in frequency domain considering an Airy wave propagating with a frequency ω and an amplitude A.

The velocity potential is decomposed in three components:

$$\phi = \phi_I + \phi_D + \phi_R \tag{2.18}$$

Where:

- ϕ_I is the incident wave potential computed with Airy theory [Faltinsen, 1990];

- ϕ_D is potential of the wave diffracted wave, assuming a fixed rigid body;

- ϕ_R is the potential of the radiated wave as the body moves, ignoring the incident wave.

The wave forces is thus decomposed in three independent components:

- Froude-Krylov force $\mathbf{F}_{FK}$: induced by the undisturbed and unsteady pressure field in the incident wave;

- Diffraction force $\mathbf{F}_{diff}$: force applied by the wave diffracted by the body;

- Radiation force $\mathbf{F}_{rad}$: force applied to the body by the radiated wave.

The Froude-Krylov force is computed by integrating the unsteady pressure p_I on the wet body surface S_{B_0} (the index 0 corresponding to the equilibrium position), associated with a regular Airy wave propagating at the free surface:

$$\mathbf{F}_{FK} = \iint_{S_{B_0}} p_I\mathbf{n}dS \tag{2.19}$$

p_I can be obtained analytically in Airy waves theory deriving the incident wave potential ϕ_I. It is also possible to compute non-linear Froude-Krylov loads on a wind turbine platform as presented in [Philippe, 2012] by integrating the incident wave pressure field on the instantaneous wetted surface. This can have an impact in steep waves when experiencing large motions.

In the same way, the linear diffraction and radiation forces $\mathbf{F}_{diff}$ and $\mathbf{F}_{rad}$ are computed as:

$$\mathbf{F}_{diff} = \iint_{S_{B_0}} p_{diff}\mathbf{n}dS \tag{2.20}$$

$$\mathbf{F}_{rad} = \iint_{S_{B_0}} p_{rad}\mathbf{n}dS \tag{2.21}$$

Where the pressures p_{diff} and p_{rad} are obtained by solving the potential flow field, either ϕ_D or ϕ_R, around the wet body surface with specific boundary conditions corresponding to either incident waves or body motions. This is done by using a potential flow solver such as *Nemoh* [Babarit and Delhommeau, 2015] or *WAMIT* [Lee, 1995] for instance. In those solvers, the Froude-Krylov and diffraction forces are often summed up to form the excitation force $\mathbf{F}_e$. The radiation loads are decomposed as the sum of an added mass term and of a linear damping term, expressed as a function of motion frequency:

$$\mathbf{F}_{rad}(\omega) = -\mathbf{M}_a(\omega)\ddot{\mathbf{x}}(\omega) - \mathbf{B}(\omega)\dot{\mathbf{x}}(\omega) \tag{2.22}$$

Where $\mathbf{x}$ is the vector representing the body position and rotation ($\mathbf{x} = 0$ at static equilibrium position), with 6 dimensions, $\mathbf{M}_a$ is the added mass matrix and $\mathbf{B}$ is the radiation linear damping matrix. In linear theory, the system is considered to response at the same frequency as the incident wave. Therefore in frequency domain, the equation of motion of a floating body takes the form:

$$(\mathbf{M} + \mathbf{M}_a(\omega))\ddot{\mathbf{x}}(\omega) + \mathbf{B}(\omega)\dot{\mathbf{x}}(\omega) + \mathbf{K}_h\mathbf{x}(\omega) = \mathbf{F}_e(\omega) \tag{2.23}$$

Where $\mathbf{K}_h$ is the hydrostatic stiffness matrix.

In time domain, however, a memory effect in the generated waves has to be accounted for. This is accomplished by computing convolution products with impulse responses of excitation and radiation loads, respectively $\mathbf{K}_e$ and $\mathbf{K}_{rad}$. The equation of motion shall thus be written as by Cummins [Cummins, 1962]:

$$\begin{aligned}(\mathbf{M} + \mathbf{M}_{a\infty})\ddot{\mathbf{x}}(t) + \int_0^t \mathbf{K}_{rad}(\tau)\dot{\mathbf{x}}(t - \tau)d\tau + \mathbf{K}_h\mathbf{x}(t) \\ = \int_{-\infty}^{+\infty} \mathbf{K}_e(\tau)\eta(t - \tau)d\tau + \mathbf{F}_{other}\end{aligned} \tag{2.24}$$

Where:

- $\mathbf{M}_{a\infty}$ is the added mass matrix at infinite motion frequency

- $\mathbf{K}_{rad}$ is the radiation impulse response

- $\mathbf{K}_e$ is the excitation impulse response

- η is the free-surface elevation

- $\mathbf{F}_{other}$ is any other force (induced by current, wind, moorings... if needed)

2.2.2.2 Second order effects

In order to perform a more accurate hydrodynamic in steep waves, it is possible to include second order terms from equation 2.14 as detailed in [Molin, 2002].

In regular waves of angular frequency ω and amplitude A, the second order force $F^{(2)}$ appear at zero or double frequency 2ω and its amplitude is proportional with $\epsilon^2 = (kA)^2$, where k is the wave number. In irregular waves, the second order force will act on the floating body at frequencies $\omega_i - \omega_j$ and $\omega_i + \omega_j$, where i and j are indices of the wave spectrum. The second order force hence covers a much larger range of frequencies than the first order force which only acts at the wave frequencies. It can then alter the system response in steep waves. Focusing on floating wind turbines, the drift forces can alter the mean position of the system. Also, the $\omega_i - \omega_j$ frequencies can induce low frequency oscillations impacting notably the mooring loads.

In particular, the semi-submersible platforms can be sensible to low-frequency forces induced by second order effects. TLPs can however be sensible to high frequency second order induced effects.

As presented in chapter 3, only first order loads are however considered in this PhD thesis. The hydrodynamic solver involved cannot compute the second order forces.

2.2.3 Added Morison drag and hybrid formulations

2.2.3.1 Formulation

For intermediary KC (in $[2, 10]$), either Morison equation or linear potential theory alone may not be appropriate. Therefore, a hybrid formulation can be chosen for bodies including both large and slender parts compared to the typical wavelength. For example, several types of geometries can be found on the well-known OC4 DeepCWind semi-submersible platform [Robertson et al., 2014a]. As presented in figure 2.8, this semi-submersible contains very slender braces with high KC on which the Morison formulation shall be applied. It also contains wide columns and an intermediary pile on which the Keulegan-Carpenter number would be low or intermediary depending on the wave amplitudes. It can hence be chosen to apply Morison formula on the braces and potential flow theory to the large columns.

However, a quadratic drag term coming from Morison equation is systematically added in time domain to the main columns and central pile to account for viscous effects:

$$\mathbf{D}(t) = \frac{1}{2}\rho C_d A |\mathbf{u}(t) - \mathbf{v}(t)|(\mathbf{u}(t) - \mathbf{v}(t)) \tag{2.25}$$

Where $\mathbf{u}$ and $\mathbf{v}$ are defined as in section 2.2.1. Additionally, a vertical drag term can be added to account for the viscous effects on the heave plates at the bottom of the three large columns. This kind of hydrodynamic modelling is detailed in [Philippe, 2012] for example.

2.2.3.2 Differences between implementations

Depending on the models, some differences can appear. The linear potential theory assumes small amplitude motions of the body. However, questions raises on the application of the added Morison drag as the body and the free surface move.

For example, on the first hand, in *Hydrodyn* [Jonkman et al., 2014] used in *FAST* [Jonkman and Buhl, 2005], strip elements are defined underwater at the equilibrium
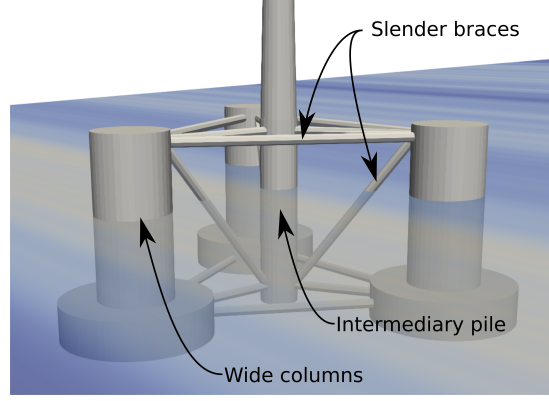
Figure 2.8 – OC4 DeepCWind platform
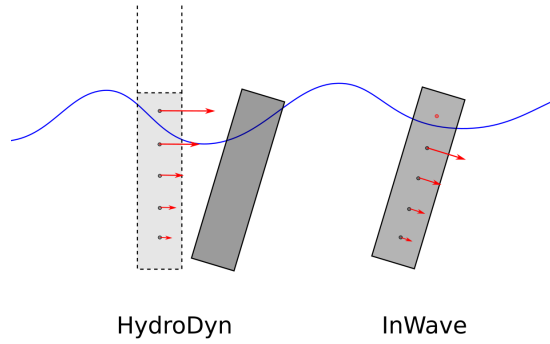
Figure 2.9 – Different ways to apply Morison drag in a hydrodynamic model

position of the whole system at still water. Then, as the body moves during a simulation, drag forces are computed on these elements taking $\mathbf{u}$ at the position of each element at its equilibrium position. On the other hand, in *InWave*, presented in this study (see chapter 3), it has been chosen to compute $\mathbf{u}$ at the instantaneous position of each element, and to only apply drag forces to elements under the free-surface only. Therefore, the force can be asymmetric as the wave passes: elements situated in the upper part are sometimes in the water and sometimes above a trough. These approaches are presented on a scheme in figure 2.9.

This difference between to models can lead to consequential differences in the computed motions as it will be shown in chapter 4.

2.2.4 Linear and non-linear hydrostatics

The linear hydrostatic loads are represented as a linear spring inducing a restoring force:

$$\mathbf{F}_{HS} = -\mathbf{K}_h \mathbf{x}(t) \tag{2.26}$$

The hydrostatic stiffness matrix $\mathbf{K}_h$ is computed as presented in [Faltinsen, 1990] and $\mathbf{x}(t)$ is the instantaneous position vector. It is a function of the water plane area, of the weight of the body and the positions of the gravity and buoyancy centres. This approach assumes small amplitude motions around the equilibrium position. Depending on the geometry, for a sphere for example, the water plane area changes very fast as soon as the body heaves. In some cases, it can be preferable to use non-linear hydrostatics.

This approach consists in integrating the hydrostatic pressure p_{HS} field acting on the wetted part of the body:

$$\mathbf{F}_{HS_{NL}} = \iint_{S_{B_{wet}}} p_{HS} \mathbf{n} dS \tag{2.27}$$

Where $\mathbf{n}$ is vector normal to the surface, oriented towards the outside of the body. For a given mesh, it thus requires to re-mesh the wetted surface of the body or to compute the exact position of the underwater mesh cell. It hence has a higher CPU cost.

2.3 Moorings

2.3.1 Mooring numerical modelling challenges

The numerical modelling of the moorings is a key issue for the design of floating systems. When simulating mooring systems, the main criteria that must be kept in mind are:

- Maintaining the platform at a given mean position with limited maximum excursions depending on the export cable requirements;

- Respect the Minimum Breaking Load (MBL), including a safety factor. The tension T in a line must always stay lower than the MBL divided by a safety factor γ: $T \leq \frac{MBL}{\gamma}$;

- For catenary mooring lines with drag-embedded anchors: no vertical force must be applied to the anchor. Otherwise, the anchor might be dug out. This condition can also be to always have a portion of line laying on the seabed. Which can be written as the condition $l - l_s > 0$, where l and l_s are respectively the total length of line, and the length carried up from the seabed (see figure 2.10. Depending on the anchor type, other conditions may be applied;

- And others... [DNV, 2013a]

For a mooring system design, thousands of load cases are to consider, including extreme, operational and fatigue cases. The criteria above are always to consider. More details and information can be found in the standards [DNV, 2013b] or [DNV, 2013a].

Depending on the load cases, the numerical models used to compute the mooring lines tensions could impact not only the tension values but also affect the motions of the platform and therefore the aerodynamics of the rotor as well. But here again the matter lies in a compromise between accuracy, implementation complexity and CPU cost.

2.3.2 Quasi-static models

2.3.2.1 Linear mooring stiffness

In linear theory, the motions of the system are assumed small so the mooring can be considered as a linear spring. The mooring restoring force is then:

$$\mathbf{F}_m(t) = -\mathbf{K}_m \mathbf{x}(t) \tag{2.28}$$

Where $\mathbf{K}_m$ is the mooring stiffness matrix ($6*6$) and $\mathbf{x}$ is the position vector ($\mathbf{x} = 0$ at the static equilibrium position). The mooring load is thus very simple to compute but
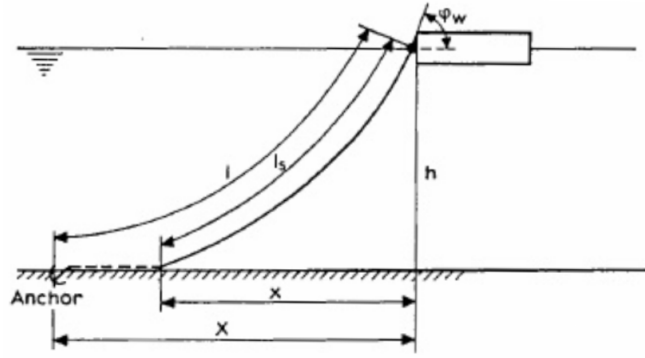
Figure 2.10 – Static mooring line with symbols (from [Faltinsen, 1990]))

the loads become inaccurate as soon as the motion amplitude increases. The mooring behaviour is very non-linear in reality and is experiences drag and added mass loads due to the presence of the water.

2.3.2.2 Non-linear quasi-static mooring models

The quasi-static mooring model assumes that the mooring line is in a static position between the anchor and the instantaneous position of the fairlead at each time-step. The tension is computed by solving the loads and positions of each line elements, only considering the weight of the element and Archimedes force. The equations are detailed in [Faltinsen, 1990]. This model is non-linear and accounts for the variations in line weight depending on the length of line carried by the floater (noted l_s on 2.10) but does not include neither the hydrodynamic loads, inertial effects nor internal damping that could be of importance. Depending for calm sea-states, with small motions of the floater, this model could be satisfying. But lines dynamics can be essential to compute in some cases.

2.3.3 Use of dynamic models for floating wind turbines

Dynamic models are the most precise mooring numerical models. They are thus more complex to implement and make computation time more expensive. Different theories are presented in [Masciola et al., 2014].

Dynamic mooring models can account for hydrodynamic loads (drag and vortex induced vibrations), inertial effects, internal damping or line/seabed friction. There are three main models:

- Lumped-mass (LM);

- Finite Element Analysis (FEA);

- Finite Differences (FD).

The LM methods divides a line in a given number nodes containing the mass of the line. Two nodes are connected with an element that models the internal forces as a spring and damper system as shown in figure 2.11. Line bending forces at a node can also be accounted for. The mooring dynamics is solved as a linear system, but here the mass matrix is strictly diagonal. It is thus very easy and quick to inverse. This lumped-mass assumption shows good accuracy as long as torsional effects can be
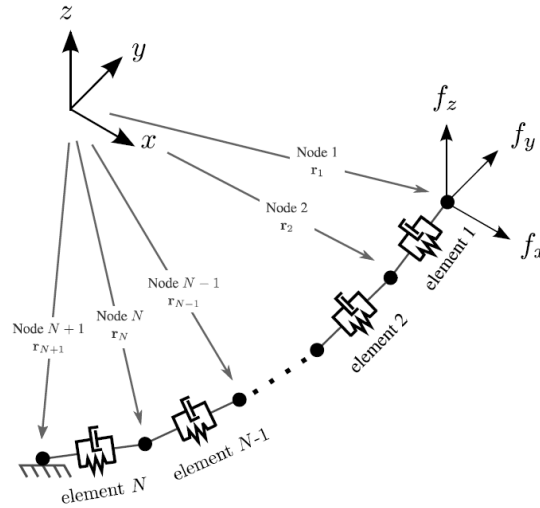
Figure 2.11 – Lumped-mass representation (from [Masciola et al., 2014])

neglected. Also, coupling terms might miss if a one node is connected to more than two elements (as in a net, for instance).

The FEA model applies the Finite Element Method (FEM) to the lines, discretized in a number of elements. Compared to the LM model, the mass matrix is no longer diagonal. Also, the FEA model allows more complex boundary conditions and internal or external force discretization.

The DS model is similar to the FEA model, except it replaces FEM piece-wise gradients by gradients approached by time and space first-order difference functions computed over two or three cable elements. This method can show as good accuracy as FEA models but has numerical instability issues. It is thus rarely used in simulation tools.

2.3.4 Dynamic vs Quasi-static mooring modelling

Either mooring line dynamics and loads applied to the lines can be very important to consider especially in severe sea states, as presented in [Masciola et al., 2013b] for example. Those can only be accounted for in dynamic models. Although mooring dynamics is essential to correctly predict mooring force standard deviation and extreme loads, quasi-static models could be accurate enough in some cases.

For instance, [Cevasco et al., 2017] showed that QS models are sufficient to compute the heave and yaw motions and mooring forces of a floating VAWT on a semi-submersible platform with comparison to a Lumped-Mass model. While it also correctly predicts the mean surge mooring force, the QS under-estimates its standard deviation. The study also shows that QS mdoels over-estimate the pitch mooring forces and motions, but from a design point of view, this is better than under-estimation. Eventually, [Cevasco et al., 2018] shows that a good agreement is obtained between QS and the dynamic model at low frequencies of the wind turbulence frequency range. In this study, a QS model will be used, knowing that some outputs will be over-estimated but assuming that the global behaviour of the mooring is well simulated.

2.4 Control

2.4.1 Expected behaviour of a wind turbine

Wind turbines usually need to be controlled in order to maximise the generated power without letting it exceeding the nominal power of the generator. The power of a turbine is equal to the product of the generator rotational speed ω_{gen} with the generator torque Q_{gen}. It can also be computed as a function of the rotor speed ω_{rotor}, the rotor torque Q_{rotor} and the drive-train efficiency η_{dt}:

$$P_{gen} = Q_{gen} \cdot \omega_{gen} = \eta_{dt} \cdot Q_{rotor} \cdot \omega_{rotor} \qquad (2.29)$$

A gearbox is sometimes used. γ_{gb} is then the multiplication factor between the generator rotor and the turbine rotor rotational velocities:

$$\omega_{gen} = \gamma_{gb} \cdot \omega_{rotor} \qquad (2.30)$$

A description of the turbine behaviour can be given as follows as a function of the wind speed U_∞:

- **Region 1:** Below the start-up wind speed, $U_\infty < U_{start-up}$: the generator torque is zero and no energy is extracted. The wind can be used to accelerate the rotor for start-up.

- **Region 2:** Below the rated wind speed, $U_{start-up} < U_\infty < U_{rated}$: the wind turbine rotates at its optimal TSR λ_{opt} at which the power is maximum for the incident wind. A wind turbine operates in this region most of the time, but stronger winds may occur.

- **Region 3:** Above the rated wind speed, $U_{rated} < U_\infty < U_{cut-out}$: the wind turbine operates at its nominal power to avoid generator damage or failure. The TSR and C_p thus decrease as the wind grows bigger.

- Above the cut-out wind speed, $U_{cut-out} < U_\infty$: the wind is too powerful so the turbine is stopped and the blades are oriented so that the drag is minimal.

These regions are presented on a simplified power curve of the NREL 5MW wind turbine [Jonkman et al., 2009] in 2.12. Linear transition zones can be also created to smooth the transitions from a regime to another one. They can be called regions $1\frac{1}{2}$ and $2\frac{1}{2}$ [Jonkman et al., 2009]. The wind speed can be measured with LiDARs they are expensive and their measurements are still difficult to process if they are installed on floating and moving support structures. Generally, if the wind speed is not directly known on a site, the control law is made as a function on the rotational velocity which can be easily and accurately measured with a sensor on the turbine.

2.4.2 Means to control the output power

On the one hand, the generator torque can be controlled by mitigating the electro-magnetic flux. An example of control law is given for the well-known NREL 5MW HAWT in [Jonkman et al., 2009]. An equivalent strategy of generator control for a VAWT is presented in [Merz and Svendsen, 2013] [Svendsen and Merz, 2013] for example.
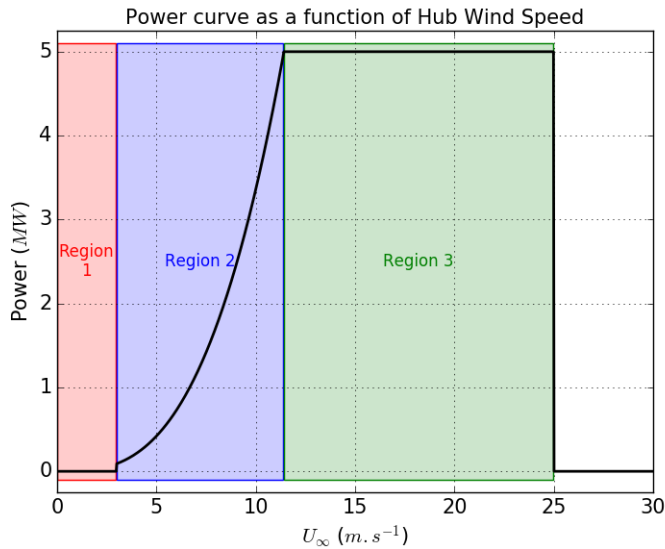
Figure 2.12 – NREL 5MW wind turbine power curve

To slow down the wind turbine and to decrease the rotor torque, it is also possible to reduce the aerodynamic lift acting on the blade. This can be done through blade pitching, which decreases the angle of attack on the blades. The blade pitch control can be individual or collective. Inividual control can for instance be used to orient a turbine in yaw by decreasing the thrust on one side of the rotor. Pitching the blades however requires dedicated actuators. For a HAWT, an actuator is located for each blade in the hub. This strategy is accurate but the actuators must be sufficiently fast, especially for yaw control (only a few seconds response time). For a VAWT, it can be technically difficult to pitch the blades depending on their shape. VAWTs are thus sometimes simply *stall-regulated*. However, research has been done on this field on H-HAWTs as presented in [Paraschivoiu et al., 2009] or [Bayati et al., 2018] for instance. Some of these projects are still undergoing.

Another way to control the lift on the blades is to control the flow with air or plasma jets as presented in [Aubrun et al., 2017]. This is not addressed in this study as it is not at an industrial level of readiness yet.

Additional questions have been raised for FWTs with the land-based HAWTs control laws. Indeed, the slow time response created a phenomenon of *negative damping* in region 3. Control laws have thus been adapted as presented in [Jonkman et al., 2009].

2.5 Structure dynamics

The first assumption that can be made is to consider rigid bodies. The flexibility of the floater components, tower, shaft and blades is thus neglected. In some models (in *FAST* [Jonkman and Buhl, 2005], for example), the blades and tower flexibility can be modelled with a beam approach. The blades or tower are divided into several elements with respectively different flap-wise and edge-wise stiffness (for the blades) or fore-aft side-side stiffness (for the tower). This method gives accurate results but does not consider all structural degrees of freedom.

Modal approaches can also be used to find the structural modes of a wind turbines. They are widely used in design processes. The aim is then to keep resonance frequencies

out of the excitation frequency ranges.

The most complete model used in time domain consists in using the Finite Element Method. This last theory leads to higher CPU costs but is more accurate. It also allows to consider the platform deformation.

A comparison of rigid and flexible floating VAWTs models is presented in [Wang et al., 2016] with a DMS aerodynamic solver. It shows that structural flexibility does not significantly affect the mean values of the global motions of the platform or the tower base bending moment. However, the standard deviations and maximum values of the fore-aft tower bending moment and the pitch motion can be affected and underestimated with a rigid model, which also induces differences in the mooring lines tensions. Therefore, fatigue calculations would be needed if a rigid model is used to dimension a floating VAWT. Concerning the pitch response in the frequency domain, differences between rigid and flexible models are particularly significant at low wind speed. This is induced by strong differences in the aerodynamic damping between rigid and flexible models when the aerodynamic loads are predominant compared to waves induced loadings.

2.6 Existing numerical tools for Floating Wind Turbines

This part presents a non-exhaustive list of codes used to simulate and design FWTs.

2.6.1 Floating Horizontal Axis Wind Turbines

The *FAST* [Jonkman and Buhl, 2005] (standing for *Fatigue, Aerodynamics, Structures and Turbulence*) open-source code has been developed at the NREL. It includes several modules focusing on different parts of the turbine's physics. *AeroDyn* [Moriarty and Hansen, 2005] [Jonkman et al., 2016] is its aerodynamic solver. It uses either the Boundary Element Method (BEM) or on the Generalized Dynamic Wake theory (not studied in this project) and can account for complex turbulent wind fields generated with *TurbSim* [Jonkman, 2009]. It also includes *HydroDyn* [Jonkman et al., 2014] to compute the hydrodynamic loads on the platform, using either linear potential theory or Morison equation (see part 2.2). Bodies can be considered either rigid or flexible in the time-domain mechanical solver *ElastoDyn* [Jonkman and Buhl, 2005] and both generator torque and blade pitch angle can be controlled in the *ServoDyn* module. Eventually, both quasi-static and dynamic mooring models can be used by FAST, respectively *MAP++* [Masciola et al., 2013a] and *MoorDyn* [Hall, 2017].

HAWC2 [Larsen and Hansen, 2013] is a wind turbine design tool developed at the Danish Technical University (DTU). Several aerodynamic models have been implemented in HAWC2, including BEM for HAWTs. Hydrodynamics is computed using Morison's equation, but linear potential flow can also be used for bigger bodies if HAWC2 is plugged onto an external hydrodynamic solver. Bodies can be flexible and the structure's dynamics is solved using a multi-body formulation. As many other tools, connections allow to plug other modules onto HAWC2 to include several controllers, for instance.

SIMO-RIFLEX-AeroDyn [Ormberg and Bachynski, 2012] has been developed at SINTEF Ocean (Norway) to study FHAWTs. On the one hand, *SIMO* is a time-domain simulation tool to study motions of multibody systems. It computes the hydrodynamic forces acting on the bodies using linear potential flow theory (including second order loads) or Morison force. On the other hand, *RIFLEX* has been developed for slender

hydrodynamic bodies such as mooring lines or dynamic export cables. Beam or bar elements but also finite elements can be used to solve the system's dynamics. Eventually, *AeroDyn* [Moriarty and Hansen, 2005] uses the BEM theory to compute the aerodynamic loads on the rotor.

Other commercial tools are developed in France such as *DeepLinesWind* [Le Cunff et al., 2013] [Perdrizet et al., 2013], developed by Principia and IFPEN (France), coupling a sea-keeping software with an aerodynamic solver based on BEM method. A finite-element solver is used to compute the structures, mooring lines and export cable dynamics. Hydrodynamic loads can be either computed using potential linear theory (first and second order loads) or Morison theory.

2.6.2   Floating Vertical Axis Wind Turbines

Following the developments made on the FHAWTs, *HAWC2* has been coupled to an Actuator Cylinder model to compute the behaviour of a FVAWT [Madsen et al., 2013]. *HAWC2* has been presented in part 2.6.1.

In the same manner, *SIMO-RIFLEX* presented in part 2.6.1 has been coupled to both a DMS model [Wang, 2015] and an Actuator Cylinder model to form *SIMO-RIFLEX-DMS* and *SIMO-RIFLEX-AC*. A comparison between *HAWC2* and *SIMO-RIFLEX-AC* on a VAWT is presented in [Koppenol et al., 2017]. Differences between the two codes come from different implementations and corrections of the AC theory when the rotor is highly loaded.

FloVAWT [Collu et al., 2013] has been developed at Cranfield University (United Kingdom). A DMS solver computes the aerodynamics on the rotor and linear potential flow theory is used on compute the hydrodynamics. The mooring lines can be accounted for using either a quasi-static solver (*MAP++* [Masciola et al., 2013a]) or a dynamic lumped-mass theory-based solver (*MoorDyn* [Hall, 2017]). Up to now, there has been no development on the generator or blade pitch angle control.

The code *QBlade* [Marten et al., 2015] is being developed at TU Berlin. The aerodynamics can be computed through either DMS theory or a FVW code. At the moment, the release version does not account for platform motions, but a link has been made with the *FAST* framework, allowing for complete simulation of a FVAWT.

All the models presented in the above can use dynamic stall models such as Gormont-Berg, Boeing-Vertol or Leishman-Beddoes.

2.6.3   Experimental and hybrid testing for validation

Coupled models used to simulate the seakeeping of FWTs are difficult to validate. Loads are difficult to reproduce on small-scale prototypes. These tests are expensive as they need large and complex facilities as presented in [Courbois, 2013] whose experimental campaign carried out on a floating HAWT is presented in figure 2.13. On such a small-scale FWT, the Reynolds number on the blades and the Froude number for the hydrodynamic loads may not be accurately conserved in downscaling. It is thus hard to validate numerical coupled models with such tests as presented in [Philippe et al., 2013].

Hybrid experimental-numerical research (Software In the Loop (SIL) or Hardware In the Loop (HIL)) is also ongoing consisting in a small-scale wind turbine rotor based on a controlled moving platform in a wind tunnel. Such experiments have for example been carried out in Politecnico di Milano, Italy [Bayati et al., 2016]. The hydrodynamic part is then accounted for numerically and the motions of the platform are reproduced
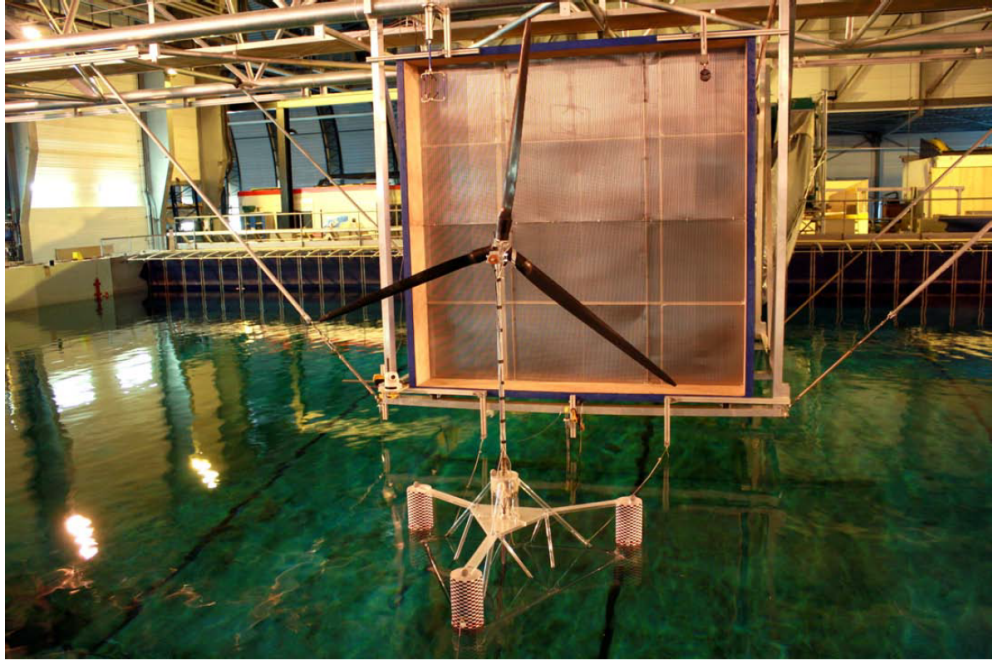
Figure 2.13 – Small-scale tests in a wave tank with a wind generation facility (from [Courbois, 2013])

with a motorised support structure. The inverse can also be performed in a wave tank as done in [Chabaud, 2016] at NTNU, Norway: actuators can be installed on a small-scale floating platform to account for aerodynamic loads acting on a numerically modelled rotor. In each one of these approaches, half of the fluid domain is computed with a numerical tool. Additionally to the difficulties of small scale experimental modelling, a simulation software, either hydrodynamic or aerodynamic, is used with its uncertainties and errors.

Eventually, large-scale prototypes are expensive and only very few have been installed up to now. For instance, the *WindFloat* project [Roddier et al., 2017] was installed in 2011 on the northern Portugal Atlantic coast (see figure 2.14. It represented an overall CAPEX of 21M€and was decommissioned 5 years later in 2016. There are hence few experimental data that can be used to validate simulation tools.

2.6.4 Need for new simulation tools dedicated to Floating Wind Turbines

As presented in parts 2.6.1 and 2.6.2, most coupled codes developed for simulating FWTs use quasi-steady aerodynamic models. They are fast but their accuracy has not been proved yet because of expensive and scarce experimental campaigns. Also, as mentioned in part 2.1.3, several studies have proved that quasi-steady aerodynamic models miss unsteady phenomena that could have a substantial impact on the seakeeping of the FWTs. New coupled models using more complex aerodynamic solvers are hence needed for their verification and further investigation about the seakeeping of FWTs. In particular, the impact of the unsteady aerodynamic loads unduced by the motions of the FWTs on the seakeeping has to be investigated.

Figure 2.14 – Full-scale testing in the WindFloat project (from [Roddier et al., 2017])

Chapter 3

Development of coupled models for Floating Wind Turbines

Contents

Figure 3.1 – Screenshot of a floating articulated Wave Energy Converter (WEC) simulation with *InWave*, inspired from the Langlee Wave Power$^{\text{TM}}$system

3.1 *InWave*: Overview

This chapter presents the numerical tools that have been developed and used for this PhD thesis. Several coupled solvers are presented. *InWave* is a seakeeping code developed by INNOSEA and Centrale Nantes. It was initially developed as a design tool for Wave Energy Converters (WEC) as its multi-body algorithm presented in section 3.3 is very convenient for floating articulated bodies. For example, a simulation of a multi-body WEC inspired by the Langlee Wave Power system$^{\text{TM}}$is presented in figure 3.1.

In the context of this PhD work, two aerodynamic solvers have been coupled to *InWave*: *CACTUS*, an unsteady aerodynamic FVW theory-based solver developed at Sandia National Laboratories, and a new in-house DMS theory-based solver which has been specifically developed. Control algorithms were eventually added in order to control the generator torque or the pitch of the blades.

All solvers have been coupled in a modular framework. Each module is presented in the following and the coupling adopted strategy is finally presented in section 3.2.

3.2 Coupling strategy

The different modules have been coupled in a modular framework allowing for more flexibility in the independent development of each module. A scheme representing the coupling is presented in figure 3.2.

At each time step the solvers exchange information. For instance, the multi-body solver sends the position and velocity of the rotor blade elements to the aerodynamic solver. In return, the loads acting on them are sent to the multi-body solver to solve the equation of motion. The aerodynamic module has its own pre-processing environment (to generate the rotor geometry, for instance) and handles the wind.

The control and aerodynamic modules have been coupled to *InWave* during this PhD work. They are presented in the following. The coupling between *InWave* and *MAP++* already existed beforehand.
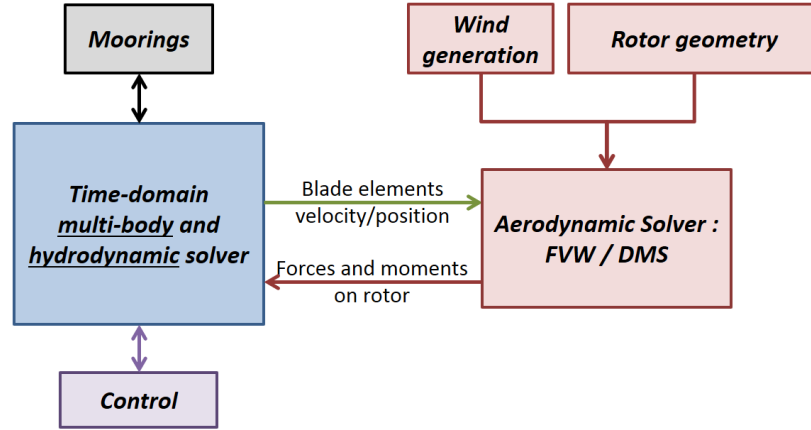
Figure 3.2 – Modular framework of *InWave*

The aerodynamic module can use several solvers, which are presented later. A unique multi-body mechanical solver can be used.

InWave is implemented in $C++$ and compiled into an executable file. All the other modules are implemented in *fortran90* and compiled into separate DLLs.

3.3   Multi-body algorithm

InWave [Combourieu et al., 2014] has been developed at INNOSEA and the LHEEA laboratory of Centrale Nantes since 2013. It is a seakeeping software based on a multi-body algorithm.

The multi-body algorithm is inspired from [Rongère and Clément, 2013]. It can describe a number of bodies linked with each other with various links. The kinematic tree is described as an open tree-structure as illustrated in figure 3.3. The algorithm imposes the following statements:

- The base is indexed 0 and can have 0 to 6 Degrees of Freedom (DoFs);

- Any succeeding body is linked to its direct ancestor by a one-DoF joint (either rotation or translation);

- A body can have only one ancestor (open tree structure, a closed kinematic loop of bodies cannot be modelled here);

- A body can have several successors.

There is thus up to 6 DoF for the base, and one additional DoF per succeeding body. DoFs can be deactivated (or blocked) during simulations. In figure 3.3, one can see 7 bodies, linked with each other with 6 joints for a total of 12 DoFs (including 6 for the floating base).

A frame R_j is attached to each body j as described in [Combourieu et al., 2014]. A rotation matrix ${}^i\mathbf{R}_j$ is then defined between the frames of a body j and its ancestor's indexed i. Note that following this notation, the rotation matrix transporting a vector from the frame R_i to the frame R_j writes : ${}^j\mathbf{R}_i = ({}^i\mathbf{R}_j)^T$. A vector $\mathbf{x}$ defined in R_i is written ${}^i\mathbf{x}$.
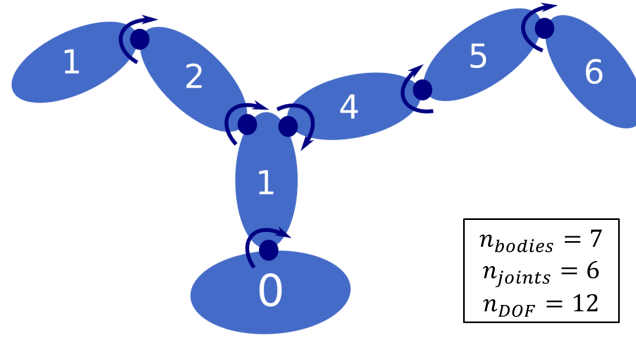
Figure 3.3 – Kinematic tree of a multi-body system in *InWave*

The reference fixed frame is called R_e and its origin is located on the free surface mean elevation. The equation of motion is solved in the base's frame R_0.

Considering relative DoFs allows to limit the number of unknowns in the equation of motion (compared to a fully Cartesian coordinate system) and hence to enhance the software performances. Such a model is convenient for a FWT as it can for example include the following DoFs:

- 6 degrees of freedom for the floating platform, including the tower;

- The nacelle yaw orientation around the tower (in the case of a HAWT);

- The hub or rotor rotation about its rotation linked to the nacelle.

Generator torque is then treated as an internal torque, and control laws can easily be implemented. In the case of a HAWT, blades could also be considered as individual bodies in rotation with the hub (blade pitch degree of freedom) and be themselves divided in a number of bodies to model blade flexibility. At it is today, flexible bodies cannot be included in *InWave* so the rotor and hub are considered as one single rigid body rotating with its shaft. Blade pitch control is accounted for in the aerodynamic solver only and does not alter the inertias.

3.4 Hydrodynamics

3.4.1 Hydrodynamic loads in *InWave*

InWave can account for linear and non-linear hydrostatics. Both theories are presented in section 2.2.4.

InWave is coupled to the Boundary Element Method solver *Nemoh* [Babarit and Delhommeau, 2015], developed at Centrale Nantes. It is open-source (Apache license) and here integrated within *InWave*'s procedure as presented in section 3.8.

Nemoh is used to compute the hydrodynamic loads in compliance with the linear potential flow theory (see section 2.2). *Nemoh* computes the Froude-Krylov force, the diffraction force and the radiation loads decomposed into added mass and radiation damping. The Hydrodynamic Database (HDB) is computed when the floating system is at a static equilibrium. It is then used in time domain simulations to compute hydrodynamic loads as presented in section 2.2.

Non-linear Froude-Krylov forces can be considered in *InWave*. The Morison equation can be used, or only Morison quadratic drag can be added on bodies. In time-domain, the Morison equation loads are computed on the body at its instantaneous position accounting for the wave kinematics at this position as presented in section 2.2.3.2.

InWave can include either regular or irregular waves, and a ramp can be imposed to the free surface elevation in order to mitigate the transient effects.

3.4.2 Linear potential flow theory in a non-linear equation of motion

The linear potential flow theory assumes small motions of the floating bodies around their equilibrium position. Small rotations are hence expected and the rotation matrix from the body-linked frame to the reference fixed frame is often linearised. This matrix uses the classical Cardan angles in the sequence yaw ψ, pitch θ and roll φ. Assuming small angles, the rotation matrix from the base's frame (body 0) to the reference fixed frame (referenced e) is hence classically approximated as presented in equation 3.1, with $C_\varphi = \cos(\varphi)$ and $S_\varphi = \sin(\varphi)$:

$$
{}^e\mathbf{R}_0 = \begin{bmatrix} C_\psi C_\theta & -S_\psi C_\varphi + C_\psi S_\theta S_\varphi & S_\psi S_\varphi + C_\psi S_\theta C_\varphi \\ S_\psi C_\theta & C_\psi C_\varphi + S_\psi S_\theta S_\varphi & -C_\psi S_\varphi + S_\psi S_\theta C_\varphi \\ -S_\theta & C_\theta S_\varphi & C_\theta C_\varphi \end{bmatrix} \approx \begin{bmatrix} 1 & -\psi & \theta \\ \psi & 1 & -\varphi \\ -\theta & \varphi & 1 \end{bmatrix} \quad (3.1)
$$

In *InWave*, the equation of motion is non-linear. The rotation matrix is then kept as on the left side of equation 3.1.

The equation of motion is solved in the base's frame R_0. The hydrodynamic loads are computed following linear potential flow theory in the R_e frame, and then transported to the base's frame R_0. Using a non-linear rotation matrix in large motions can lead to strong couplings between degrees of freedom.

In particular, *InWave* computes the radiation loads as follows. The radiation impulse response is defined in R_e: ${}^e\mathbf{K}_{rad}(t)$. The velocity vector is defined in the base's frame R_0: ${}^0\dot{\mathbf{x}}(t)$. The Cummins equation is hence written as presented in equation 3.2:

$$
{}^0\mathbf{F}_{rad} = ({}^0\mathbf{R}_e) \int_0^t {}^e\mathbf{K}_{rad}(\tau) \cdot ({}^e\mathbf{R}_0) \cdot {}^0\dot{\mathbf{x}}(t - \tau)d\tau \quad (3.2)
$$

3.5 Moorings

InWave can use a linear mooring stiffness, but a non-linear mooring model is also available.

The quasi-static mooring solver *MAP++* [Masciola et al., 2013a] is coupled to *InWave*. In some cases, it would be preferable to use a dynamic mooring solver as presented in section 2.3 but a more accurate mooring module has not been implemented in *InWave* yet.

MAP++ is compiled in a Dynamic Link Library (DLL) and called from *InWave* at each time step to compute the mooring quasi-static restoring force.

3.6 Aerodynamics

This part presents the two aerodynamic solvers that have been coupled to *InWave* as part of this PhD work. The Free Vortex Wake (FVW) solver *CACTUS* [Murray and
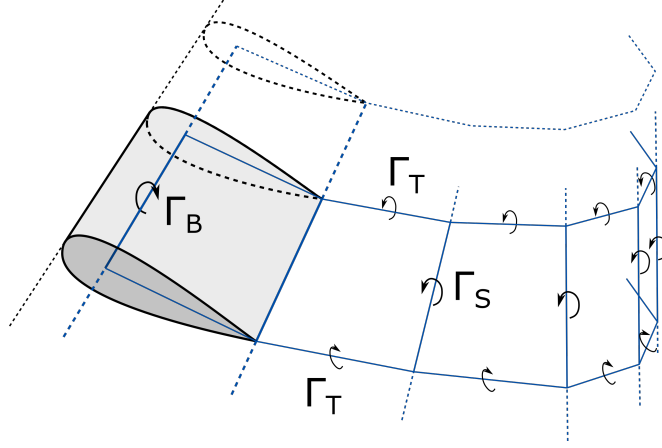
Figure 3.4 – FVW's representation of vortices

Barone, 2011] has been developed at Sandia National Laboratories. It is presented in part 3.6.1. The Double Multiple Streamtube (DMS) solver has been developed at Centrale Nantes in the context of this PhD thesis and is presented in part 3.6.2. The two solvers have been loosely-coupled to *InWave* in a modular framework.

3.6.1 Free Vortex Wake solver

3.6.1.1 Free Vortex Wake theory

The Free Vortex Wake theory is a Lagrangian approach that assumes a potential flow (inviscid, incompressible and irrotational). It computes the wake induction by modelling vortex filaments created on the blades and shed in the wake as shown in figure 3.4. This part presents the theory and the equations of the model. Blade Element theory is also used (see section 2.1.1.3) which allows to compute the blade loads using the 2D lift coefficient C_L and drag coefficient C_D.

The calculations in time domain are divided in several phases:

1. Calculation of the fluid velocity;

2. Calculation of the vortices;

3. Vortex shedding;

4. Advection of the wake.

Calculation of the fluid velocity: The fluid velocity vector $\mathbf{U}$ on the blade element includes:

- The free stream velocity $\mathbf{U}_{fs}$;

- The relative velocity induced by the motion of the blade element $\mathbf{U}_{motion}$;

- The velocity induced by the vorticity (including wake and blade vortices) $\mathbf{U}_{ind}$.
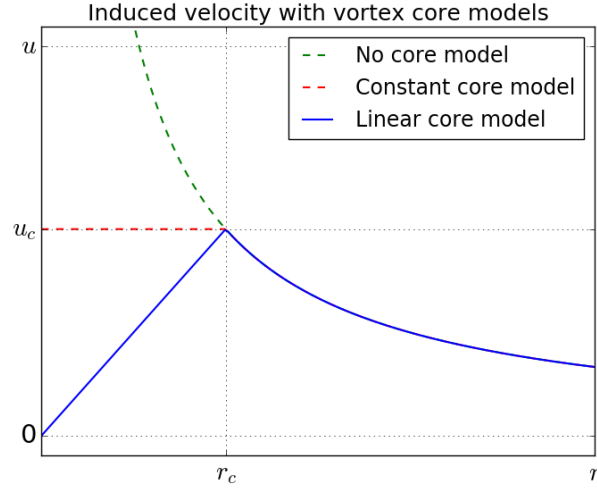
Figure 3.5 – Core models for the FVW theory

It is written as:

$$\mathbf{U} = \mathbf{U}_{fs} + \mathbf{U}_{motion} + \mathbf{U}_{ind} \tag{3.3}$$

$\mathbf{U}_{ind}$ is the velocity induced by the vortices in the wake. As illustrated in figure 3.4, the vortex lattice is composed of vortices created by each blade element:

- The bound vortex Γ_B created on each element inducing the lift force;

- The trailing vortices Γ_T induced by velocity discontinuity in the wake lattice;

- The span-wise vortices Γ_S induced by bound vortex variations (i.e. lift variations).

The calculation of these vortices is detailed later.

$\mathbf{U}_{ind}$ is calculated by application of the Biot-Savart on each vortex filament in the wake and on the blade. The velocity induced at a point P by each vortex filament i induces a velocity $\mathbf{u}_i$ given by the Biot-Savart law shown in equation 3.4 [Murray and Barone, 2011]:

$$\mathbf{u}_i = \frac{\Gamma_i}{4\pi} \frac{\mathbf{r}_1 \wedge \mathbf{r}_2}{|\mathbf{r}_1 \wedge \mathbf{r}_2|^2} (\mathbf{r}_1 - \mathbf{r}_2) \cdot \left(\frac{\mathbf{r}_1}{|\mathbf{r}_1|} - \frac{\mathbf{r}_2}{|\mathbf{r}_2|} \right) \tag{3.4}$$

Where $\boldsymbol{\Gamma_i}$ is the vortex strength vector of the vortex filament i (bound, trailing or span-wise) and $\mathbf{r}_1$ and $\mathbf{r}_2$ are the vectors pointing from the two ends of a vortex filaments to that point P.

To avoid a singularity on a vortex line (when $\mathbf{r}_1 \wedge \mathbf{r}_2 = \vec{0}$), vortex core models can be used. For instance, if the distance to the vortex filament is smaller than the core radius r_c, the induced velocity can be either computed as constant inside the core and equal to a maximum velocity u_c or increasing linearly with the distance as presented in figure 3.5.

Calculation of the vortices: Similarly to Prandtl's lifting line theory, a bound vortex is located at the quarter of the airfoil's chord and generates the lift force. Trailing vortices are then formed along the blade element's tangential vector. At each time-step a span-wise vortex is shed in the wake, closing the vortex structure as presented in figure 3.4.

The bound vortex's strength Γ_B is computed using the Kutta-Joukowski law presented in equation 3.5.

$$L = \rho U \Gamma_B \tag{3.5}$$

Where L is the blade element lift force, ρ the fluid density and U the aforementioned fluid velocity on the blade element. The lift force can also be computed with the blade element theory, giving:

$$L = \frac{1}{2} \rho c s U^2 C_L \tag{3.6}$$

Where, c and s are respectively is the blade element chord and span. Combining equations 3.5 and 3.6 gives the bound vortex as a function of the fluid velocity U and the lift coefficient C_L:

$$\Gamma_B = \frac{1}{2} c s U C_L \tag{3.7}$$

Vortex shedding: As the bound vortex strength Γ_B varies, the span-wise shed vortex strength Γ_S must be equal to the opposite of the time variation of the bound vortex strength as required by Kelvin's circulation theorem [Katz and Plotkin, 1991]. In a given region consisting of the same fluid particles in an incompressible and inviscid flow, this theorem writes for a circulation around a close contour:

$$\frac{D\Gamma}{Dt} = 0 \tag{3.8}$$

To balance the blade's bound circulation variation, the span-wise shed vortex strength is then written as:

$$\Gamma_S = \Gamma_B(y, t - dt) - \Gamma_B(y, t) \tag{3.9}$$

Where y is the coordinate of the blade element along the blade span.

Following Helmholtz's second theorem [Katz and Plotkin, 1991], a vortex filament cannot end in a fluid and must either extend to the boundaries of the domain or form a closed filament. The trailing vortex strength can thus be written as the span-wise variation of the bound vortex:

$$\Gamma_T = \Gamma_B(y, t) - \Gamma_B(y - dy, t) \tag{3.10}$$

Resolution: The bound vortex strength Γ_B depends on the fluid velocity U, which depends on the velocity induced by the vortices (wake vortices and bound vortex). Iterations are thus needed to converge towards a final value of the bound vortex strength repeating:

1. The velocity calculation with Biot-Savart law

2. The bound vortex calculation with the Kutta-Joukowski condition

3. The shed and trailing vortex strength calculation with Kelvin's and Helmholtz's theorems

Once these iterations on Γ_B have converged, the lift and drag loads on the blade elements are computed using Blade Element theory. The velocity on the tower, hub or struts can also be computed directly as the Biot-Savart law can be used at any position.

Advection of the wake: At the end of a time-step, the vortices are advected in the wake at the local flow velocity which includes the free-stream velocity and the velocity induced by every other vortex in the wake. According to Kelvin's circulation theorem, the vorticity of those shed closed vortex lines remains constant.

The calculation of the wake vortex filaments velocities increases a lot the CPU time. Indeed, the velocity of each vortex filament end includes the velocity induced by every other vortex filament. Therefore, differently from the FVW theory, the Prescribed Vortex Wake (PVW) keeps constant the velocity of a vortex filament as it is advected. The wake self-induction and dynamics are thus not accounted for. Models are also currently investigated to fasten the FVW methods. For example, [Boorsma et al., 2018] simplifies the far wake of the rotor by skipping vortices in the Biot-Savart calculations.

Calculation convergence: Vortices are created and advected at each time step. Several aspects are hence to consider to ensure a convergence of the calculation of a FVW model:

- The time step needs to be small enough so that the aerodynamics is accurate;

- The rotor blades need to be discretised in a sufficient number of blade elements;

- The wake needs to be long enough (a sufficient number of advected vortices need to be considered) so that the induction is accurately calculated.

A transient in the aerodynamic loads can be observed while the wake reaches a sufficient length. The wake can be truncated after a sufficient length is reached. The higher the TSR, the stronger the rotor-wake interaction. The maximum wake length has then to be very large in high TSR simulations. Also, at a given TSR, the wake vortices are advected faster if the wind speed is high. The more expensive simulations to run are hence the simulation at low wind speed and high TSR.

Other features: The FVW theory is known for being accurate for unsteady aerodynamic loads acting on low-solidity rotors, independently of the TSR. Although span-wise circulation cannot be computed in the Blade Element theory, the FVW theory accurately calculates skewed flow configurations as the wake asymmetry and deviation are inherently accounted for. However, the inviscid flow model needs to be corrected with semi-empirical models to account for viscous phenomena (see part 2.1.2.2).

3.6.1.2 *CACTUS* FVW solver

CACTUS (standing for Code for Axial and Cross-flow TUrbine Simulation) [Murray and Barone, 2011] is a FVW theory-based solver that has been developed at the Sandia National Laboratories. It is open source and released under BSD licence. The code is flexible and can work as well for HAWTs as for VAWTs. It has been chosen amongst

other solvers because of its BSD license which allows for integration in a commercial software such as *InWave*.

The solver also includes a flow-curvature model (used for VAWTs) and an added-mass model. Dynamic stall semi-empirical models are included: Boeing-Vertol and Leishman-Beddoes (see part 2.1.2.2). This version of *CACTUS* has been validated on fixed horizontal and vertical axis rotors, with and without dynamic stall models [Murray and Barone, 2011] [Michelen et al., 2014]. Originally, *CACTUS* could compute the aerodynamic loads on blades and struts rotating at constant speed around a fixed axis.

The solver has been improved and adapted during this PhD thesis:

- The motion of the platform is accounted for (added velocity and position);

- The rotor velocity can be variable and is input at each time step;

- Blade pitch angle can be controlled and changed at each time step;

- Complex turbulent wind fields can be accounted for, using Taylor's frozen turbulence hypothesis (as presented in [Jonkman, 2009]);

- The code has been parallelized with *OpenMP* to lower the computation times;

- Wake visualization has been added using *Paraview*.

3.6.2 Double Multiple Streamtube solver

This section presents the Double Multiple Streamtube (DMS) aerodynamic solver that has been developed and coupled to *InWave* during this PhD work.

3.6.2.1 Double Multiple Streamtube Theory

The DMS theory has first been introduced by Paraschivoiu [Paraschivoiu, 2002]. It derives from the momentum theories used for HAWTs, but assumes two subsequent actuator disks in the flow direction. The present model can account for velocities induced by the motion of the platform and for a rotor tilt angle. It has been mainly inspired by the work of K. Wang presented in [Wang, 2015].

The DMS theory assumes a steady, inviscid and incompressible flow. The first numerical models [Paraschivoiu, 2002] developed for lift-driven VAWTs were based on the same assumptions. For instance, the Single Streamtube (SS) approach couples the Blade Element theory with a momentum balance on both sides of an actuator disk representing the turbine. However this model leads to a uniform induction. Multiple Streamtube models allow a more accurate description of a non uniform induction factor on the rotor projected area. A large number of independent streamtubes with an actuator disk are modelled on the projected area of the rotor. Froude-Rankine and Blade Element equations are solved independently in those streamtubes. However, these models ignore the effect of the upwind half of the rotor on the downwind half.

Finally, Paraschivoiu split those independent streamtubes with an upwind disk and a downwind disk. The effect of the upwind induction on the downwind aerodynamics is then accounted for. On the left hand side of figure 3.6 is a scheme of the projected area of a Darrieus VAWT, facing the wind direction. On the top right hand side is a view from the above showing a line swept by a blade element, crossing twice a streamtube. On the lower right hand side, one can see the two subsequent actuator disks.
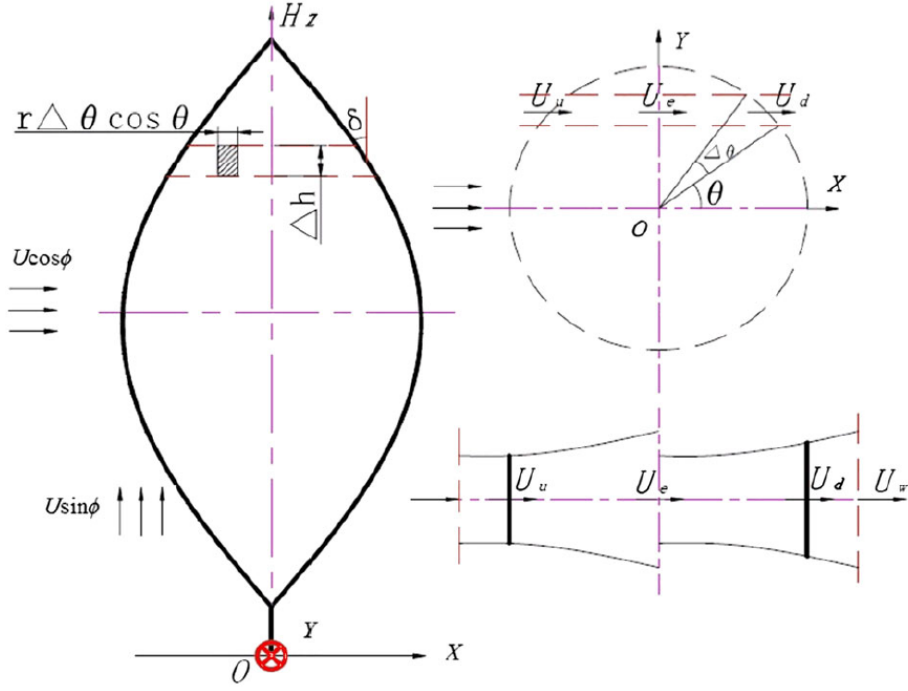
Figure 3.6 – DMS model for a Darrieus turbine (from [Wang, 2015])

Let us first define the platform-based base $(\mathbf{x}, \mathbf{y}, \mathbf{z})$. This base is following the equatorial plane of the rotor $(\mathbf{x}, \mathbf{y})$. It is calculated so that the relative wind velocity $\mathbf{U}$ stays in the platform vertical plane $(\mathbf{x}, \mathbf{z})$.

At any point of the FWT, the velocity induced by the platform motion is included in $\mathbf{U}$:

$$\mathbf{U} = \mathbf{U}_\infty - \mathbf{U}_{platform} \qquad (3.11)$$

Where $\mathbf{U}_\infty$ and $\mathbf{U}_{platform}$ are respectively the free-stream and the platform motion velocity at the considered point. The velocity induced by the platform rotations may not be uniform on the rotor depending on the streamtube height. $\mathbf{U}$ is therefore computed for each streamtube. A change in $\mathbf{U}$ also induces a change in the $(\mathbf{x}, \mathbf{y}, \mathbf{z})$ base orientation.

The following parameters are then defined:

- θ is the angular position of a blade element ($\theta = 0$ when the blade is downwind, aligned with the tower);

- r is the horizontal distance between the blade element and the tower (here $r = R_{max}$ at the equatorial position);

- δ is the angle of the blade element tangent with the vertical plane;

- Δh is the height of one streamtube;

- ϕ is the tilt angle of the rotor.

The projected area of a streamtube is then:

$$A_s = r\Delta\theta|\cos\theta|\Delta h \tag{3.12}$$

In this model adapted from [Wang, 2015], a correction is implemented for a ϕ tilt angle of the rotor. ϕ is the angle between the relative velocity vector $\mathbf{U}$ and the equatorial plane of the rotor.

$$\mathbf{U} = \begin{pmatrix} U\cos\phi \\ U\sin\phi \end{pmatrix} \tag{3.13}$$

Where $U = \|\mathbf{U}\|$. The tilt angle ϕ is hence computed as the angle between the angle of $\mathbf{U}$ with the equatorial plane as:

$$\phi = \arcsin\left(\frac{\mathbf{U}\cdot\mathbf{z}}{U}\right) \tag{3.14}$$

Momentum equations As it is presented in [Wang, 2015], the vertical component of the velocity within the downwind zone is assumed to be negligible in the complex turbulent wake of the upwind half of the rotor. The vertical velocity is thus considered for the upwind part only. Also, only an axial (i.e. horizontal) induction has to be considered.

Following the *Wind Energy Handbook* [Burton et al., 2001], Glauert's model for the yawed rotors is applied to the upwind part, meaning the axial thrust coefficient acting on the upwind actuator disk is defined as a function of the tilt angle ϕ and of the upwind induction factor a_u:

$$C_{T_u} = 4a_u\sqrt{(\cos\phi - a_u)^2 + \sin^2\phi} \tag{3.15}$$

On the downwind disk, the thrust coefficient is defined similarly to the Froude-Rankine actuator disk theory presented in section 2.1.1.2 as a function of the induction factor a_d:

$$C_{T_d} = 4a_d(1 - a_d) \tag{3.16}$$

The momentum equations presented in section 2.1.1.2 are then adapted and the following velocities are defined in the streamtubes for the tilted rotor (see figure 3.6):

- U_u and V_u are the horizontal and vertical velocities at the upwind actuator disk;

- U_e is the velocity at the "equilibrium", i.e. at the upwind streamtube outlet and downwind streamtube inlet;

- U_d is the velocity at the downwind actuator disk;

- U_w is the velocity at the outlet of the downwind steamtube.

These velocities are then respectively equated as follows in equations 3.17 to 3.21.

$$U_u = (\cos\phi - a_u)U \tag{3.17}$$

$$V_u = U\sin\phi \tag{3.18}$$

$$U_e = U(\cos\phi - 2a_u) \tag{3.19}$$
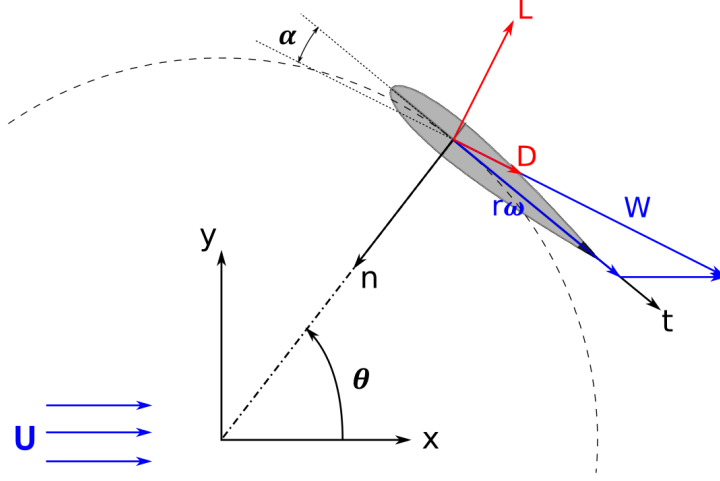
Figure 3.7 – Blade element frame and relative velocity

$$U_d = (1 - a_d)U_e = (1 - a_d)(\cos\phi - 2a_u)U \tag{3.20}$$

$$U_w = (1 - 2a_d)U_e = (1 - 2a_d)(\cos\phi - 2a_u)U \tag{3.21}$$

The momentum variations at each upwind and downwind disk can then be equated as presented in equations 3.22 and 3.23

$$\Delta I_u = \frac{1}{2}\rho A_s U^2 C_{T_u} \tag{3.22}$$

$$\Delta I_d = \frac{1}{2}\rho A_s U_e{}^2 C_{T_d} \tag{3.23}$$

Blade Element equations Blade Element theory is presented in section 2.1.1.3. The fluid velocity on the blade element is used to compute the aerodynamic loads. This velocity is obtained by addition of several rotations:

- θ is the blade element angular position around the tower and $\dot{\theta} = \omega$;

- δ is the angle of the blade element tangent with the vertical plane of the rotor;

- β is the pitch angle of the blade element ($\beta = 0$ unless blade pitch control is active).

A simplified 2D scheme (ignoring δ and β) is presented in figure 3.7. The tangential and normal vectors $\mathbf{t}$ and $\mathbf{n}$ are presented. We here define de blade element frame $(\mathbf{s}, \mathbf{t}, \mathbf{n})$, where $\mathbf{s}$ is the span-wise vector of the considered blade element.

Decomposing the motion of the blade element following the several rotations leads to the following fluid velocity on the blade element, defined in the $(\mathbf{s}, \mathbf{t}, \mathbf{n})$ frame, for the upwind half:

$$\mathbf{W}_u = \begin{pmatrix} 0 \\ -\cos\beta(U_u\sin\theta + r\omega) - \sin\beta(U_u\cos\theta\cos\delta + V_u\sin\delta) \\ \sin\beta(U_u\sin\theta + r\omega) - \cos\beta(U_u\cos\theta\cos\delta + V_u\sin\delta) \end{pmatrix} \tag{3.24}$$

53

On the down-wind half, the relative fluid velocity on a blade element is:

$$\mathbf{W}_d = \begin{pmatrix} 0 \\ -\cos\beta(U_d\sin\theta + r\omega) - U_d\cos\theta\cos\delta\sin\beta \\ \sin\beta(U_d\sin\theta + r\omega) - U_d\cos\theta\cos\delta\cos\beta \end{pmatrix} \tag{3.25}$$

The angle of attack, either upwind or downwind, is then calculated as follows:

$$\alpha = tan^{-1}\Big(\frac{\mathbf{W}\cdot\mathbf{n}}{\mathbf{W}\cdot\mathbf{t}}\Big) \tag{3.26}$$

The loads acting on a blade element can then be computed as a function of the induced velocities following blade element theory as presented in section 2.1.1.3. The tangential and normal force coefficients (directed along $\mathbf{t}$ and $\mathbf{n}$) can be equated as presented in equation 3.27 as a function of the angle of attack and drag and lift coefficients C_D and C_L. These coefficients are computed as a function of the angle of attack α and of the Reynolds number R_e

$$\begin{cases} C_t = -C_D\cos\alpha + C_L\sin\alpha \\ C_n = C_D\sin\alpha + C_L\cos\alpha \end{cases} \tag{3.27}$$

Projecting C_t and C_n in the $(\mathbf{x}, \mathbf{y}, \mathbf{z})$ frame gives the following force coefficients on the main axes:

$$\begin{cases} C_x = -C_t(\cos\beta\sin\theta + \sin\beta\cos\delta\cos\theta) + C_n(\sin\beta\sin\theta - \cos\beta\cos\delta\cos\theta) \\ C_y = C_t(\cos\beta\cos\theta - sin\beta\cos\delta\sin\theta) - C_n(\sin\beta\cos\theta + \cos\beta\cos\delta\sin\theta) \\ C_z = -\sin\delta(C_t\sin\beta + C_n\cos\beta)) \end{cases} \tag{3.28}$$

The thrust force in a streamtube corresponds to the stream-wise force f_x produced by N_b blades in the streamtube area swept by the rotor. An individual blade element spends a fraction $\frac{\Delta\theta}{2\pi}$ of a revolution in a streamtube. Therefore, the average thrust force in the direction of the streamtube from the blade element theory can be expressed as follows for either upwind or downwind halves of the rotors:

$$f_x = \frac{N_b\Delta\theta}{2\pi}\frac{1}{2}\rho\frac{c\Delta h}{\cos\delta}W^2 C_x \tag{3.29}$$

Where c is the blade element chord and $\frac{c\Delta h}{\cos\delta}$ is the blade element surface. The thrust coefficient acting on the blade element in the streamtube (upwind or downwind) is thus calculated from the blade element theory as follows:

$$C_{T_{BE}} = \frac{f_x}{\frac{1}{2}\rho A_s U^2} = \frac{N_b c}{2\pi}\frac{W^2}{U^2}\frac{C_x}{r|\cos\theta|\cos\delta} \tag{3.30}$$

The DMS resolution hence consists in finding the induction factor to equate $C_{T_{BE}}$ and C_{T_u} upwind or C_{T_d} downwind. Each streamtube can be solved independently and the downwind induction depends on the upwind induction.

Iterations are then made trough equations 3.15 or 3.16 and 3.30 until the induction factor is converged, for each streamtube, upwind and downwind.
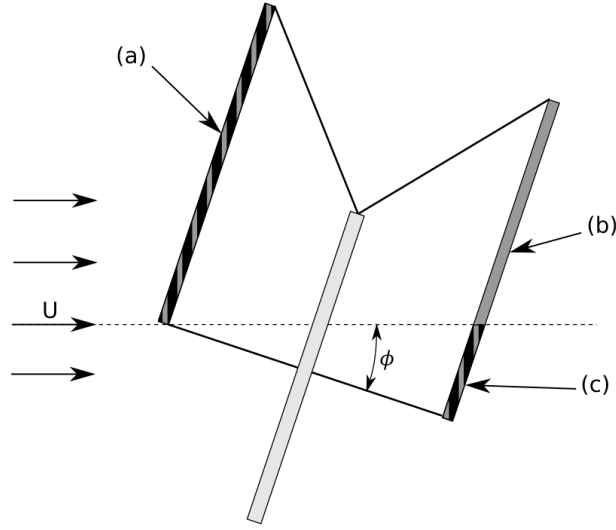
Figure 3.8 – Impact of the skew angle on the downwind induction of a tilted VAWT

Skew correction Additionally to the skew correction in the computation of the upwind induction, the downwind induction can be corrected as follows for a ϕ skew angle. Mertens et al. [Mertens et al., 2003] showed that the skew angle of the rotor altered the power coefficient. Also, a certain skew angle allows to improve the performance of the rotor. Mertens et al. modified a Multiple Streamtube model to account for the rotor skew angle defining a downwind zone that is not impacted by the upwind induction as presented in figure 3.8. On the figure, zone (a) is the upwind zone. Zone (b) is the downwind zone in the wake of the upwind zone, with a $\mathbf{U}_e$ inflow velocity. However zone (c) is not impacted by the upwind half of the rotor and its inflow velocity is $\mathbf{U}$.

This model has been adapted and implemented in the DMS solver in order to account for the tilt angle of a floating VAWT. It is validated in section 3.9.

3.6.2.2   Implementation and algorithm

The DMS solver has been implemented in *fortran90* in the *CACTUS* framework. The theory presented in section 3.6.2.1 has been implemented following the algorithm presented in figure 3.9.

At each time-step, *InWave*'s multi-body solver computes the position and velocity of the platform and rotor. Using these inputs, the DMS solver computes the needed angles and velocities for each streamtube: θ, ϕ and $\mathbf{U}$. A double-disk streamtube is then defined for each blade element. The iterations between the momentum conservation equations and the blade element equations are then performed until convergence of the induction factors of each independant streamtube. A bisection algorithm is used to converge towards the correct induction factor.

If a blade element is upwind (see figure 3.10a), the iterations between momentum conservation and Blade Element theory in a streamtube are performed only upwind. If the considered blade element is downwind (see figure 3.10b), the downwind iterations are performed once the upwind induction factor is converged.

The calculation in each streamtube is performed independently, in parallel using *OpenMP*.
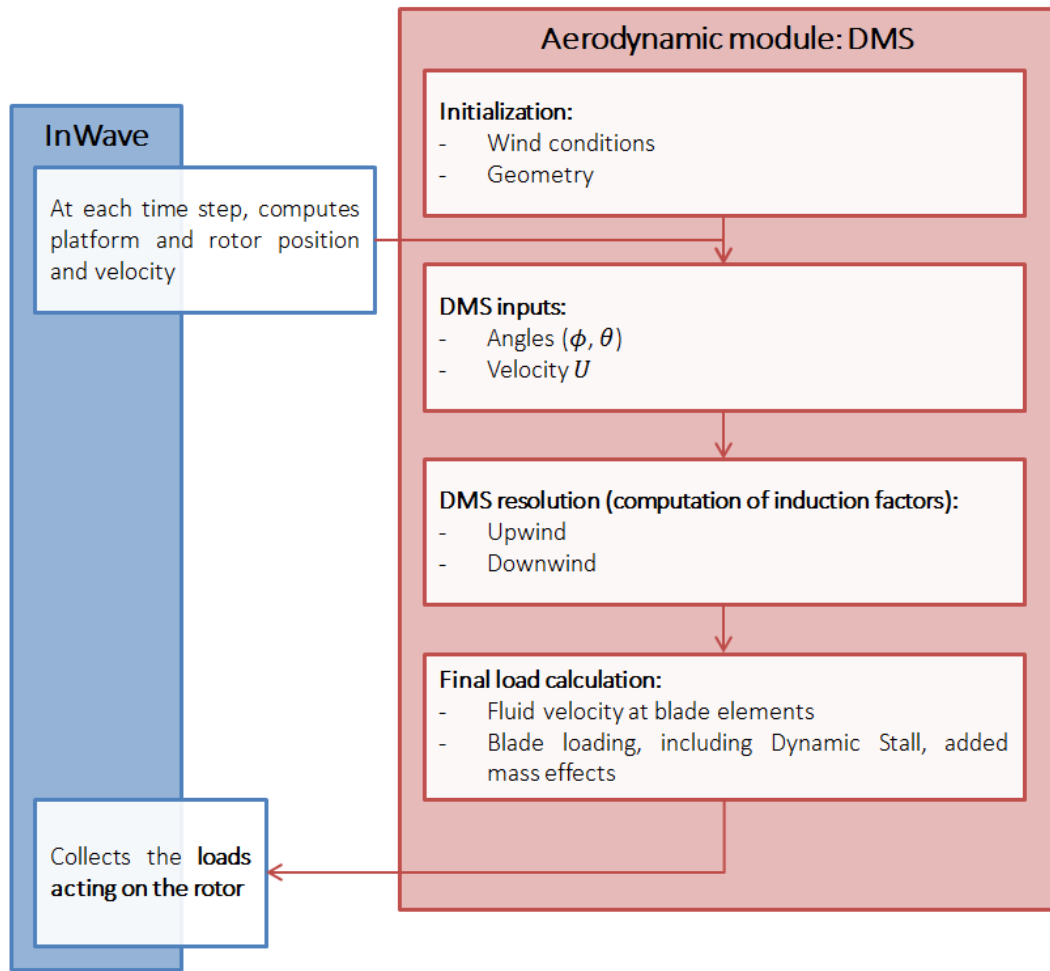
Figure 3.9 – Process followed by the Double Multiple Streamtube aerodynamic solver

(a) Upwind blade element   (b) Downwind blade element
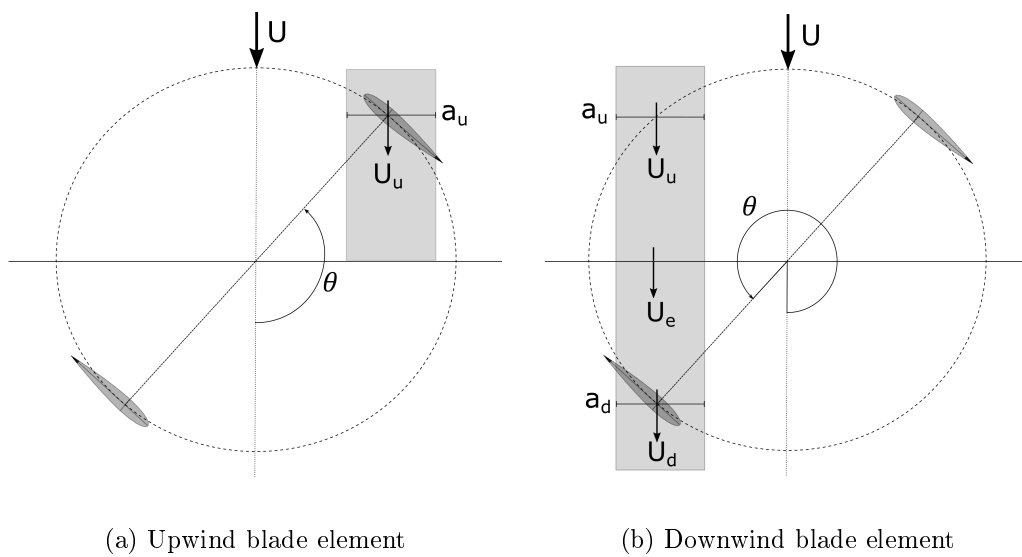
Figure 3.10 – Actuator disks for upwind and downwind blade elements

Once each induction factor is converged, the final load computation is performed. Blade Element theory is used, and Boeing-Vertol or Leihsman-Beddoes dynamic stall models can be used (presented in section 2.1.2.2).

Eventually, the total aerodynamic loads acting on the rotor are sent to the multi-body algorithm for the time-domain dynamic resolution.

3.7 Control

3.7.1 For HAWTs

For HAWTs, *InWave* uses the control algorithm presented by the NREL for the NREL 5MW turbine [Jonkman et al., 2009]. Compiled in a DLL, it has been coupled to *InWave* following the coupling architecture presented in section 3.2.

The algorithm computes the generator torque and the blade pitch angle optimising the power extraction. For above-rated wind speed, the control algorithm tends to not exceed the nominal power.

3.7.2 For VAWTs

A control algorithm has been specifically implemented for VAWTs and coupled to *In-Wave*. It follows the algorithm presented in [Merz and Svendsen, 2013] and modified in [Cheng, 2016] to compute the generator torque for the *DeepWind* rotor [Paulsen et al., 2014]. [Cheng, 2016] shows an improvement of this controller by decreasing the rotational speed of the rotor above the rated wind speed in order to keep the output power constant at the rated value. The resulting control law is represented in figure 3.11. The optimal TSR is aimed by the controller for wind speeds up to when the rated rotational speed Ω_N is reached. The wind speed is then equal to V_{Ω_N}. The rotational speed is kept constant until the rated wind speed V_N. For above-rated wind speed, the rotational speed decreases.

This control algorithm has been adapted and is presented in figure 3.12. In this version, the reference rotor rotational speed is always given as a function of the wind speed. The torque of the generator is computed using a PID corrector (in the present study, the gain K_D of the differentiator is zero as given in [Merz and Svendsen, 2013]) regulating the rotational speed. A notch filter is used to filter the $2p$ frequency from the low-pass filtered measured rotational speed ω in order to avoid such fluctuations in the generator torque. The notch frequency is kept constant in a simulation and is defined as a function of the mean wind speed using the look-up table giving the control law $\omega = f(U)$.

The reference rotational speed is defined from the low-pass filtered wind speed at the reference height.

More details about the filters gains and time constants are given in [Merz and Svendsen, 2013].

3.8 Methodology - Procedure

The *InWave* methodology is summed up in the following:

1. **Hydrostatic equilibrium research:** the equilibrium position of the system is computed. Only non-linear hydrostatic loads are accounted for, with an additional artificial damping to converge rapidly towards the equilibrium position.
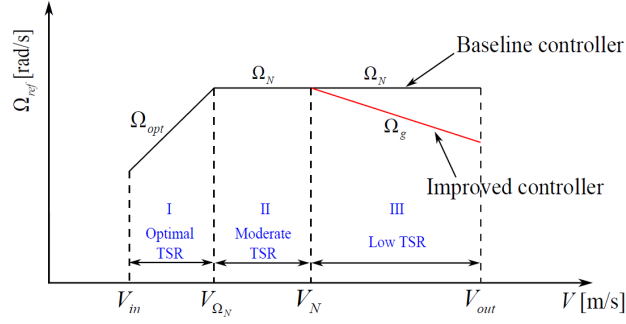
Figure 3.11 – Control law of the rotor rotational speed as a function of the wind speed (from [Cheng, 2016])
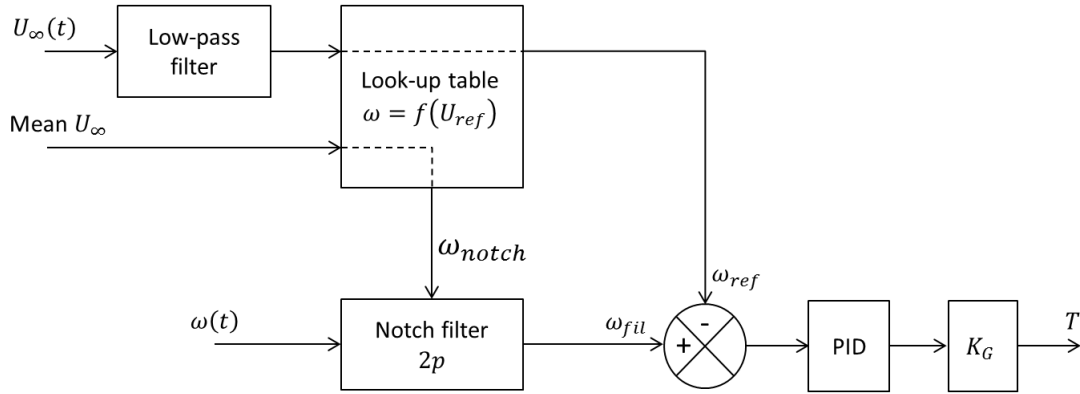
Figure 3.12 – Control algorithm used for floating VAWTs

2. **Hydrodynamic Database (HDB):** the linear potential flow solver *Nemoh* is used to compute the hydrodynamic loads acting on the wet bodies. Inline with linear potential flow theory, those computations are run on the meshes at their equilibrium position.

3. **Dynamic time-domain simulation:** dynamic simulations can then be run in time domain using an RK4 or Adams-Moulton integration schemes. The two aerodynamic models can be used, and the wind can be oriented in any direction around the turbine. Still water, regular or irregular waves can be considered. A ramp can be considered for the wave generation in order to mitigate the transient effects.

The post-processing and visualization are performed outside this procedure within a python library that has been developed.

3.9   Verifications and validations

InWave has been verified with comparisons to other numerical investigations on WECs [Combourieu et al., 2014] [Leroy et al., 2014] and validated with comparisons to experimental results [Combourieu et al., 2015]. The following describes verifications and validations done concerning the latest development during this PhD work.

More verification work on a FWT is presented in chapter 4.
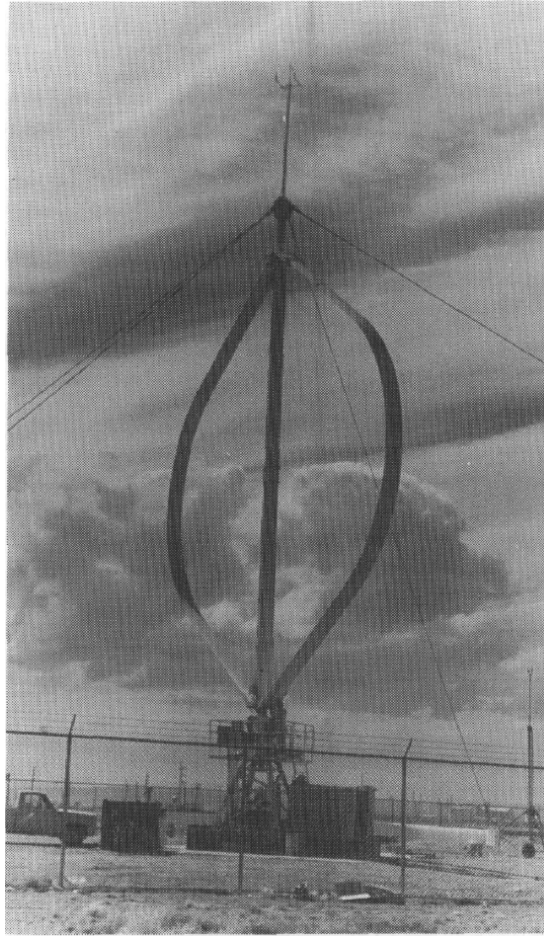
Figure 3.13 – SANDIA/DOE 17-m research turbine, Albuquerque, New Mexico (from [Akins et al., 1986])

3.9.1 Validation on the SANDIA 17m VAWT

The SANDIA National Laboratories performed measurement campaigns on large scale VAWTs. The studied turbine is the 17m diameter turbine presented in figure 3.13. The turbine is formed of two troposkein blades with a NACA 0015 profile and a $0.612m$ chord. The heigth to diameter ratio is equal to 1.0.

3.9.1.1 Power curve

First, the aerodynamic power is computed at different wind speeds with a constant rotational speed of $42.2RPM$. The measurements on the SANDIA 17m VAWT are available in [Allet and Paraschivoiu, 1995]. Computations have been run with both aerodynamic models DMS and FVW, with and without the Leishman-Beddoes dynamic stall model.

The convergence of the two aerodynamic solver is ensured in term of:

- Number of elements in the blades;
- Length of the time-step;
- Length of the wake in the FVW solver.

(a) Without dynamic stall

(b) With dynamic stall
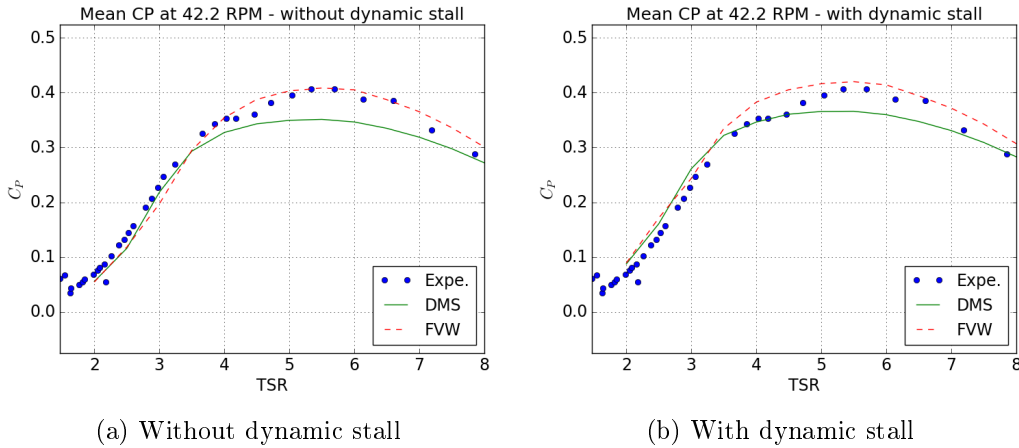
Figure 3.14 – Power coefficient of the SANDIA 17m VAWT

The power coefficient is plotted as a function of the TSR in figure 3.14 and compared to measurements from the SANDIA. Both cases (with and without dynamic stall) are presented. One can see a good agreement of the numerical models with the measurements on the SANDIA. The shape of the curve is well reproduced, with a maximum at the correct TSR.

The DMS solver tends to underestimate the maximum power without dynamic stall. The agreement on the mean power coefficient is then better with the Leishman-Beddoes model.

On the contrary, the lift delay induced by dynamic stall hence tends to overestimate the power coefficient with the FVW solver. Both cases however show a good agreement with the measurements.

3.9.1.2   Torque coefficient along a revolution

The torque acting on a 2-bladed vertical axis rotor is fluctuating at the $2p$ frequency. It is essential to capture this oscillations, in both aerodynamic torque and thrust. [Akins et al., 1986] presents the torque measurements made on the 17m SANDIA VAWT along a revolution at several TSRs. The rotor rotates at $50.6RPM$ and three TSRs are presented here: 2.5, 3.0 and 4.0. These computations were not performed at higher TSR with the FVW solver because of a too high CPU cost at high TSR.

The two aerodynamic models, DMS and FVW have been compared to the experimental results and to Akins et al. DMS model. The latest incorporates a Boeing-Vertol dynamic stall model.

Computations have been run with and without Leishman-Beddoes dynamic stall model. The aerodynamic torque is plotted in $kN.m$ as a function of the rotor azimuth on half a revolution, either without dynamic stall in figure 3.15 or with Leishman-Beddoes dynamic stall in figure 3.16.

The dynamic stall is particularly important at low TSR when the angle of attack on the blade varies with a large magnitude. It is therefore surprising to see a better agreement, especially at low TSR, without the dynamic stall in both aerodynamic models in figure 3.15. The results show a better agreement with the experimental measurements than Akins's et al. DMS model.

As mentioned in section 3.9.1.1, the lift delay induced by the dynamic stall model seems overestimated. The agreement with dynamic stall is then poorer and the torque

amplitude is overestimated with both the DMS and the FVW model at the three presented TSRs.

Dynamic stall models such as Leishman-Beddoes are highly sensitive to the foil polars, as detailed in [Marten et al., 2017]. Because of a lack of experimental data, the polars C_L and C_D used in this study are computed with the inviscid solver *Xfoil*. The stall region is thus poorly estimated. It would then be necessary to accurately calibrate the polars and the semi-empirical constants used in the dynamic stall model.

Eventually, it is also essential to question the accuracy of the measurements, which were made in real turbulent flow conditions. Consequently, we estimate the accuracy of both models as acceptable for our study.

3.9.2 Validation on a tilted VAWT

A validation of the skew model used in the DMS is finally done using the study of [Mertens et al., 2003]. This latest study measured the power extracted by a small-scale tilted VAWT in a wind tunnel. The model is $2.2m$ diameter and $0.5m$ height. It has two straight blade with a $0.08m$ chord using a NACA 0018 profile. The wind speed is $7m.s^{-1}$ and the rotational speed is controlled to cover a broad range of TSRs. The tilt angles goes from 0° to 60°.

The results of the DMS models developed in the present PhD work have been compared to measurements and numerical results of Mertens et al. No dynamic stall model has been used in this study.

Figure 3.17 shows the optimal TSR λ_{opt} divided by the optimal TSR without skew angle $\lambda_{opt_{\phi=0}}$. In figure 3.18 is the maximum CP divided by the maximum CP without skew angle. The results show a good agreement with the experimental measurements, and in particular a much better agreement than the Multiple Streamtube model of Mertens et al. Apparently, the DMS solver is appropriate for such a skew correction.

3.10 Conclusions

The simulation tool *InWave* has been adapted for the simulation of FWTs. Two aerodynamic solvers have been coupled to *InWave*'s multi-body and hydrodynamic solver:

- The FVW solver *CACTUS*: developed and validated for fixed turbines (HAWTs and VAWTs) by the SANDIA National Laboratories;

- A new DMS solver, developed on purpose at Centrale Nantes and INNOSEA.

Dynamic stall models can be used in both aerodynamic solvers: Boeing-Vertol and Leishman-Beddoes. In particular, the Leishman-Beddoes model will be used in the following of this study.

The solvers have been used to model the 17m SANDIA Darrieus VAWT. The mean power coefficient as a function of the TSR and the torque variation along a rotor revolution have been computed and compared to experimental measurements. Some simulations were not completed at high TSR with the FVW solver because of a too-high computational time. However, complete power curve have already been studied by the SANDIA with *CACTUS* [Murray and Barone, 2011].

The agreement with the experimental measurement is good. In particular, the agreement on the mean power coefficient is better with the Leishman-Beddoes dynamic

(a) $TSR = 2.5$
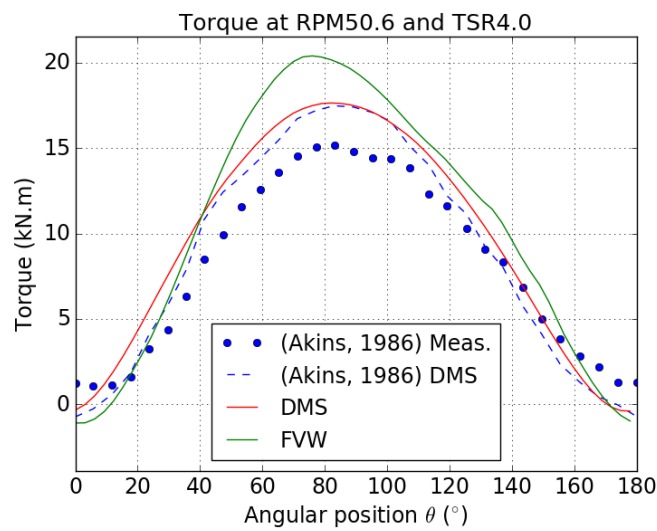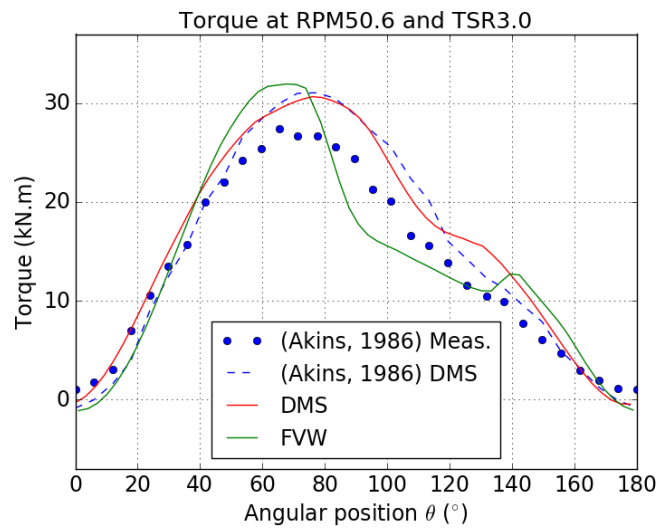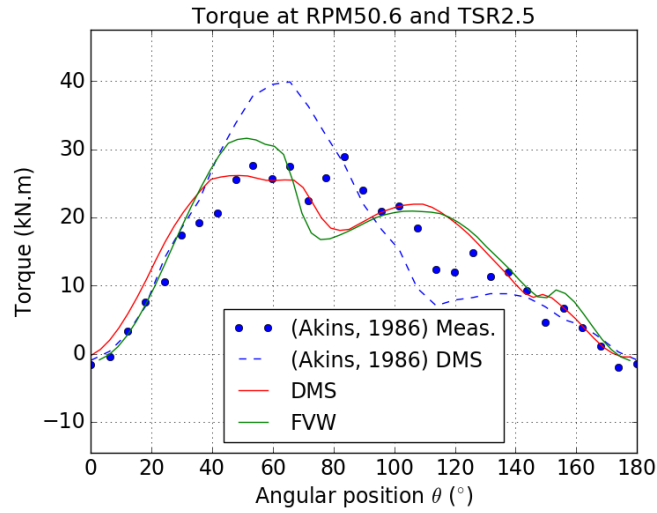
(b) $TSR = 3.0$

(c) $TSR = 4.0$

Figure 3.15 – Rotor torque validation without dynamic stall
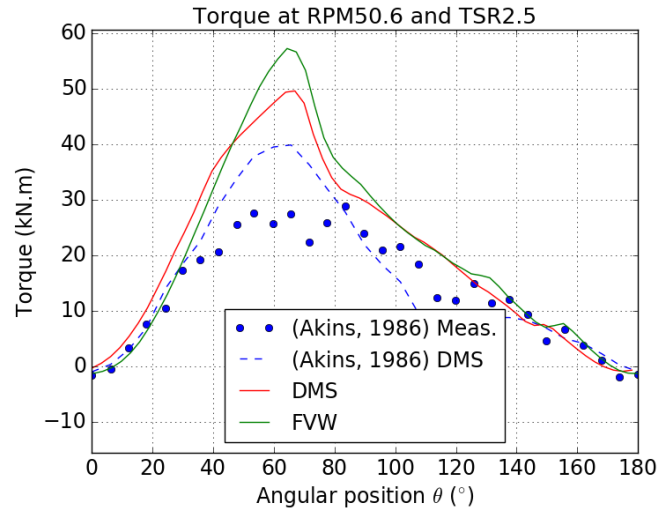
(a) $TSR = 2.5$
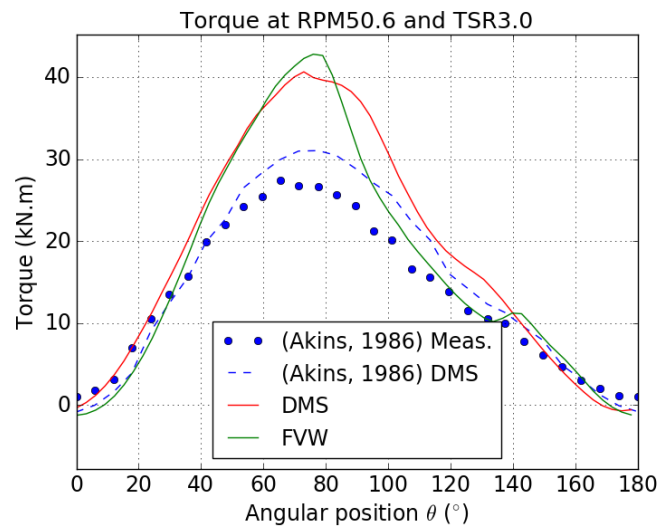
(b) $TSR = 3.0$
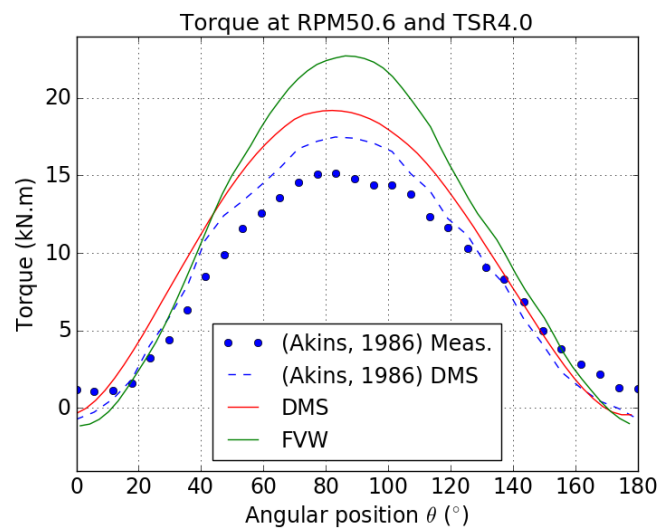
(c) $TSR = 4.0$

Figure 3.16 – Rotor torque validation with dynamic stall
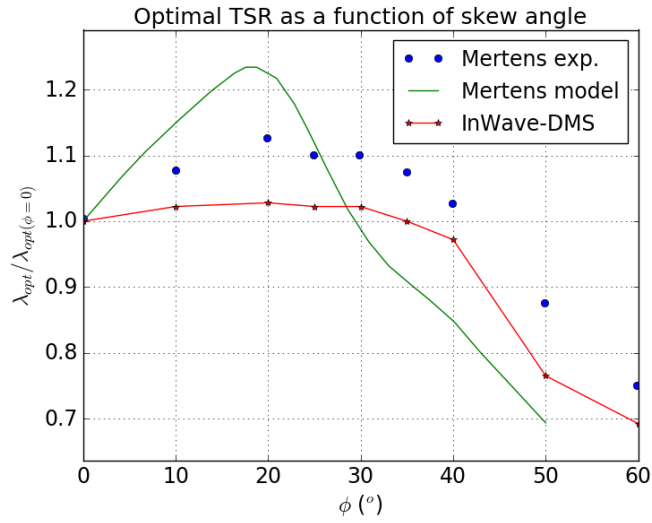
Figure 3.17 – Optimal TSR as a function of the tilt angle
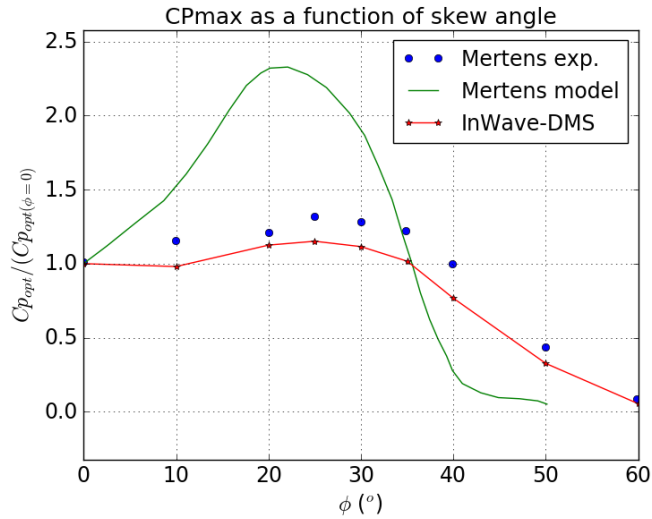
Figure 3.18 – Optimal power coefficient as a function of the tilt angle

stall model, as presented in section 3.9.1.1. However, the torque fluctuations presented in section 3.9.1.2 are more accurately computed without dynamic stall.

In both cases and with both aerodynamic solvers, the agreement is acceptable.

A control algorithm for HAWTs has been coupled to *InWave*. Finally, a control algorithm dedicated to floating VAWTs has been implemented and coupled to *InWave*.

A verification of the full servo-hydro-aerodynamic coupling has been performed on a HAWT and is presented in chapter 4.

Chapter 4

Dynamic response of a Floating Horizontal Axis Wind Turbine: impact of the aerodynamic model

Contents

4.1   Introduction

The simulation of Floating Wind Turbines is challenging because it covers several fields: hydrodynamics, aerodynamics, control, mooring modelling, structural analysis, ... As presented in chapter 2, several coupled simulation tools have been developed taking into account these phenomena. For the design and optimization of FWTs, engineers must run thousands of simulations. Hence, design tools that are both fast and accurate are needed.

A state of the art of the numerical simulation tools developed for FWTs was presented in 2011 in [Cordle and Jonkman, 2011]. Models developed to study FWTs consist most of the time either of a seakeeping analysis numerical tool coupled to an aerodynamic solver or an onshore wind turbine design tool to which an offshore module is added. Aerodynamic tools used in the onshore wind research and industry have been primarily used. They are based on the Blade Element Momentum (BEM) method with added semi-empirical models to account for unsteady and viscous effects, described in chapter 2. These corrections have been calibrated for onshore wind turbines and and few validation work has been conducted [Driscoll et al., 2016].

Part of the OC3 [Jonkman and Musial, 2010] and OC4 [Robertson et al., 2014b] projects present a benchmarking of FWTs simulation tools focusing on a 5MW HAWT respectively supported by a SPAR platform and a semi-submersible platform. More than 20 software developers have contributed to the benchmarking but all numerical aerodynamic solvers involved use BEM or Generalised Dynamic Wake (GDW) theory-based solvers. The solvers show a reasonable agreement, especially on the motions of the platform but large discrepancies can be observed on the mooring and tower base loads for instance. Experimental measurements are confronted to numerical results of the semi-submersible HAWT in [Robertson et al., 2017]. Given the level of uncertainty of experimental measurements [Robertson, 2017] and of small scale testing, it is however difficult to conclude on the quality of the agreement of the numerical solvers with the observed physics at full-scale.

State-of-the-art quasi-steady aerodynamic models such as BEM used to design bottom-fixed turbines may not be accurate enough to compute the aerodynamics of a FWT's rotor because of the motions of the floating platform. Indeed the 6 Degrees of Freedom (DOFs) of the floating platform induce unsteady phenomena in the aerodynamics of the rotor. The importance of unsteady aerodynamic loads acting on FWTs has been highlighted in section 2.1.3. For example, the advection of the tip vortex is altered by the rotor motions and impacts the induction. When the rotor moves in the downstream direction, it strongly interacts with its wake and with the tip vortex. Moreover, [Bayati et al., 2016] showed experimentally that aerodynamic loads on a pitching wind turbine cannot be accurately predicted by a BEM method. In particular, the added aerodynamic damping in pitch was over-estimated by the BEM.

The present chapter focuses on the impact of the aerodynamic model, either quasi-steady or unsteady, on the seakeeping of a FWT in the case of a Horizontal Axis Wind Turbine (HAWT). The dynamic response of a FWT from the reference code *FAST* [Jonkman and Buhl, 2005] is compared to the results from, *InWave-FVW*. The case studies include the NREL 5MW rotor [Jonkman et al., 2009] OC3Hywind SPAR platform-supported FWT [Jonkman, 2010] in aligned and misaligned wind and waves. Important differences appear as the importance of unsteady aerodynamic phenomena increases. Differences between the models are detailed by analysing the aerodynamic loads acting on a surging and pitching turbine in imposed motions. This allows a
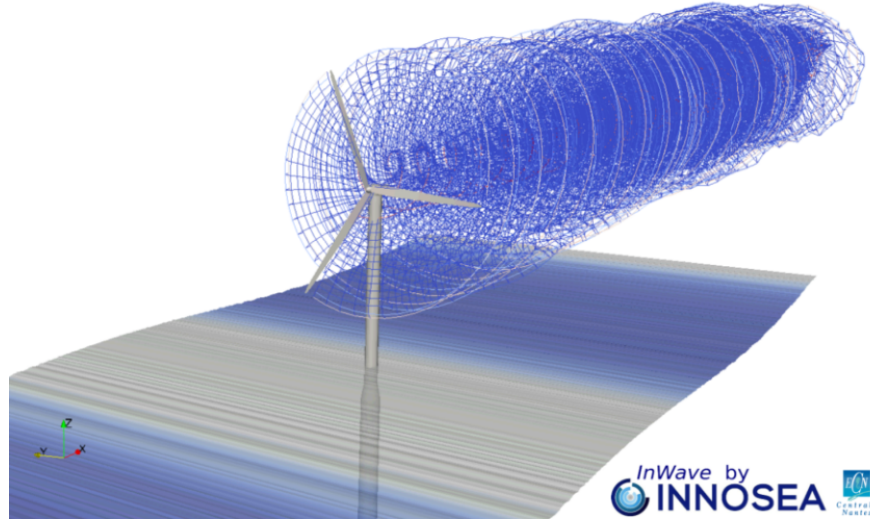
Figure 4.1 – Screenshot of a simulation with *InWave-FVW*

better understanding of the dynamic loads involved, including aerodynamic stiffness, added mass and damping. In particular, it is highlighted that the BEM seems to miss important phenomena when the turbine operates at high Tip Speed Ratio (TSR).

4.2 Study case and methodology

4.2.1 Study case

In the following, the study focuses on the case study of Phase IV of Offshore Code Comparison Collaboration project (OC3), which is the OC3Hywind SPAR platform supporting the NREL 5MW HAWT. A screenshot of a simulation of this system with *InWave-FVW* is presented in figure 4.1.

The SPAR buoy is 120m draft. It is moored with 3 catenary lines with 2-point line fairlead connections (delta-line connections) (see figure 4.2). The mooring loads are computed with *MAP++* considering the three main lines and the delta lines are accounted for by including an additional $98340kN.rad^{-1}$ stiffness in yaw [Jonkman, 2010]. The rotor is $63m$ radius. The generator torque and the blade pitch are controlled by the control algorithm presented in [Jonkman et al., 2009]. The hub is at $90m$ height with a 5° shaft tilt. The effect of the tower on the aerodynamics is not modelled. The main parameters of the floating system are defined in [Jonkman and Musial, 2010]. They are recalled in table 4.1. In this study, the waves propagate in the x direction. The wind direction angle with the x axis is denoted θ_w as shown in figure 4.2. The wind and waves directions are not necessarily aligned. The reference for the displacements is the equilibrium position O obtained in still water without wind. It is located at the waterline and shown in figure 4.2.

All bodies, including the tower, the blades and the rotor shaft are assumed rigid as *InWave* cannot simulate flexible bodies so far.

4.2.2 Aerodynamic models

In this chapter, *InWave-FVW* (Free Vortex Wake) and *InWave-PVW* (Prescribed Vortex Wake) are compared with the reference open-sources code *FAST*. *FAST* uses the
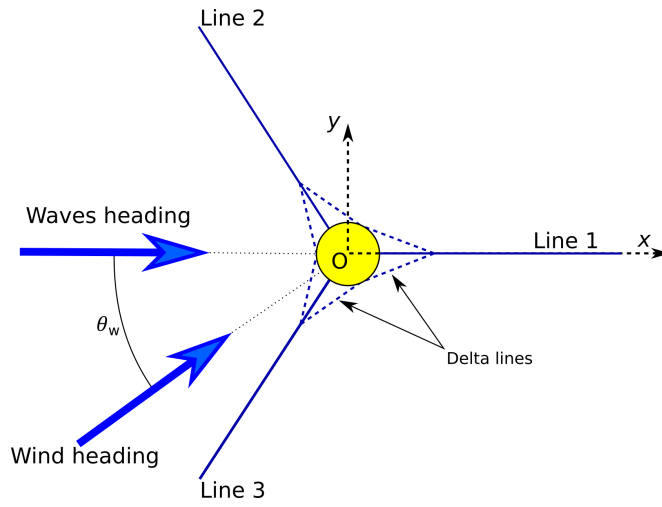
Figure 4.2 – OC3 mooring system

Table 4.1 – Main parameters of the floating system

Water depth	$320m$
Draft	$120m$
Platform diameter	$9.4m$
Platform, tower and nacelle mass	$7956t$
Rotor mass	$110t$
Rotor radius	$63m$
Hub height	$90m$
Shaft tilt	5°
Rated wind speed	$11.4m.s^{-1}$
Rated rotational speed	$12RPM$
Fairleads depth	$-70m$
Lines length	$902.2m$
Lines linear mass	$77.066kg.m^{-1}$
Line axial stiffness	$384.243MN$
Line diameter	$0.09m$
Surge resonance period	$125s$
Heave resonance period	$31s$
Pitch and roll resonance period	$30s$
Yaw resonance period	$8.25s$
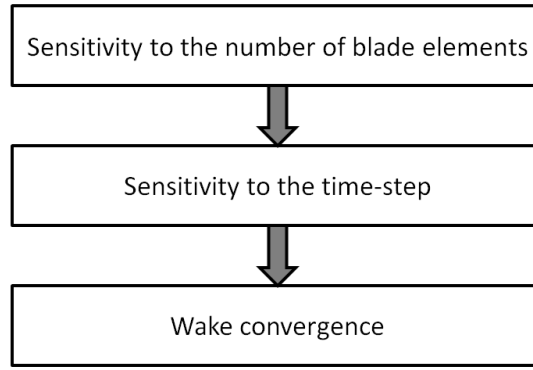
Figure 4.3 – Convergence study process

Blade Element Momentum (BEM) solver *AeroDyn* (version 15) [Jonkman et al., 2016] which assumes a steady flow as presented in section 2.1. This version of *AeroDyn* does not include the Generalized Dynamic Wake (GDW) model [Moriarty and Hansen, 2005]. The use of the BEM is preferable for this study because the GDW can be unstable when the rotor is highly loaded. The same polars C_L and C_D are used in all models. They are computed with *Xfoil* [Drela, 1989].

First, convergence of the calculations is verified in term of:

- Number of blade elements

- Time-step length

- Length of the wake (for PVW and FVW solvers)

The CPU cost of the simulations increases with a large number of blade elements, a short time step and a long wake. However, the increase of those parameters improve the accuracy of the calculations.

The process is described in figure 4.3. This process is followed at the rated wind and rotational speeds as it is a critical high TSR simulation, for which the computational time is acceptable.

First, several simulations are run with different numbers of blade elements: 19, 30 and 40. The obtained power coefficient is plotted in figure 4.4a. The time-step used in this calculation is $0.2s$. One can see that the results obtained with 30 and 40 blade elements are almost superimposed. Taking the results with 40 elements as a reference, the relative difference with the value of C_P at $30s$ obtained with 30 elements is 0.26% versus 2.7 with 20 blade elements. 30 elements are hence enough for an acceptable accuracy (the BEM solver uses 18 blade elements per blade).

Then, with the selected rotor, simulations are run with several time-steps using a RK4 integration scheme: $0.4s$, $0.2s$ and $0.1s$. The obtained power coefficient is plotted in figure 4.4b. One can see a good agreement between the three solutions (the relative difference is always below 0.5%).

The same time step length sensitivity investigation is followed for the hydrodynamic time-domain solver. A time step of 0.2 is needed for convergence. This will be the time step used in the following calculations.

Eventually, to verify the wake is sufficiently long in the vortex solvers, simulations are run with no wake limit on a fixed turbine. The wake grows progressively until a constant induction is obtained. The wake length can be characterised in term of

(a) Calculation sensitivity to blade discretisation

(b) Calculation sensitivity to time-step
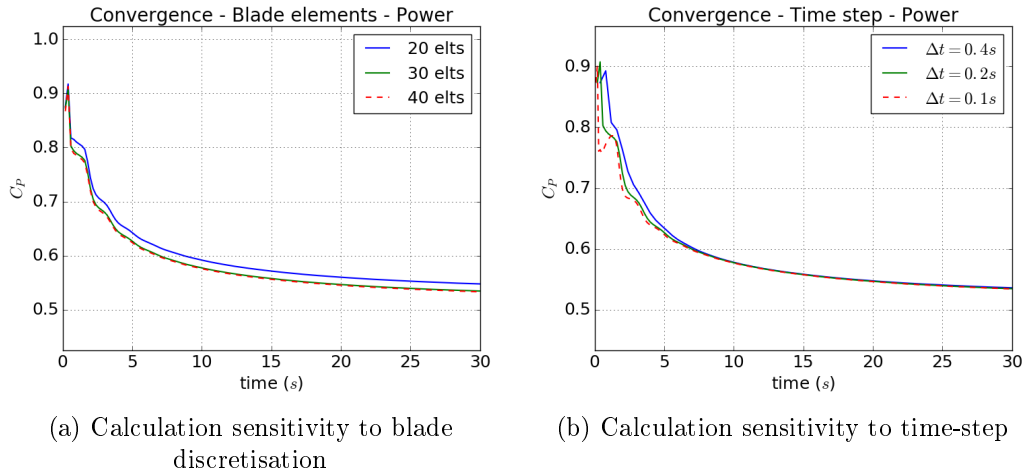
Figure 4.4 – Convergence study: number of blade elements and time-step
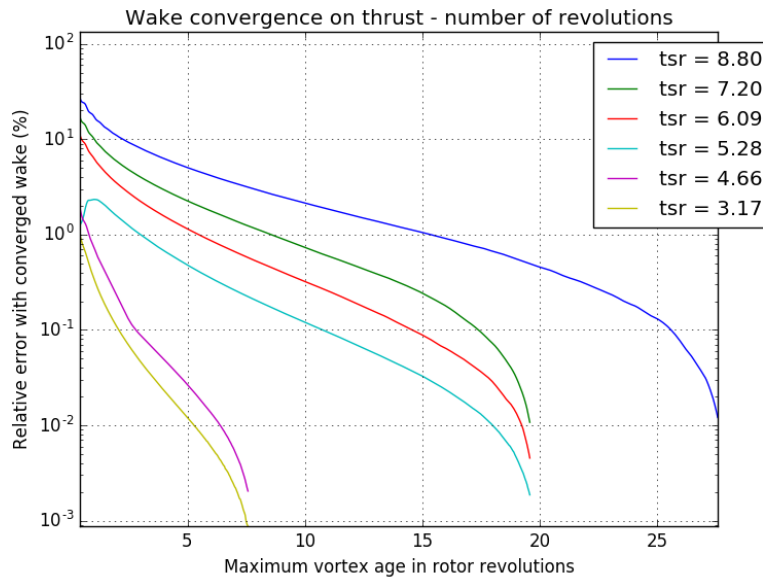
Figure 4.5 – Wake convergence as a function of rotor revolutions

geometrical length and of vortex age: the furthest vortex is the oldest vortex generated by the rotor.

For example, the relative difference between the instantaneous thrust coefficient and the final thrust coefficient is plotted as a function of the number of rotor revolutions in figure 4.5 for several simulations run at different TSRs. One can see that the needed wake length grows with the TSR. When the rotor is loaded, a long wake is needed. At low TSR, the wake be shorter.

In the simulations, it is hence ensured that a sufficiently long wake is considered. It has a very strong impact on the CPU cost of the FVW solver. Indeed, as explained in chapter 3, the wake needs to be advected at the local wind speed including the vorticity of all the vortices. If the wake is long, this phase takes a very long time (more than 99% of the simulation time with $CACTUS$).
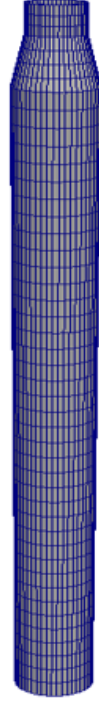
Figure 4.6 – Hydrodynamic mesh of the SPAR buoy

4.2.3 Hydrodynamic model

We ensure that the mesh of the SPAR used for the linear potential flow hydrodynamic calculation contains a sufficient number of cells (2400 cells) to compute accurate hydrodynamic loads. A picture of the mesh is shown in figure 4.6.

Morison drag on the platform is also taken into account. The drag coefficient is $C_D = 0.6$, following [Jonkman, 2010]. Eventually, as presented in section 4.2.2, a time-step sensitivity study is done and a time-step of $0.2s$ is chosen. The hydrodynamic impulse response is $30s$ long.

In *FAST*, the Morison drag is computed on the platform elements below $z = 0$, accounting for the fluid velocity field at their equilibrium position. On the contrary, *InWave* computes the viscous drag on the elements below the free surface elevation $(z < \eta(t, x, y))$ considering the fluid velocity at their instantaneous position. This was discussed in section 2.2.3.2 of chapter 2.

4.2.4 Load cases

The system is studied in several load cases proposed in the OC3 project [Jonkman and Musial, 2010]. The load cases are presented in table 4.2. Finally, the load cases 7 and 8 are considered with non-collinear wind and waves with a $\theta_w = 45^o$ wind heading angle.

The turbine is considered rigid in all solvers.

Table 4.2 – Load cases of the OC3 project

Load Case	Analysis	Wind Conditions	Wave conditions
1	Equilibrium position	Air density $= 0$	Still water
2	Decay	Air density $= 0$	Still water
3	Time-series	Air density $= 0$	Airy wave: $H = 6m, T = 10s$
4	PSD	Air density $= 0$	JONSWAP wave spectrum: $H_s = 6m, T_P = 10s$
5	Time-series	Steady, uniform, no shear: $U_\infty = 8m.s^{-1}$	Airy wave: $H = 6m, T = 10s$
6	Time-series	Steady, uniform, no shear: $U_\infty = 18m.s^{-1}$	Airy wave: $H = 6m, T = 10s$
7	PSD	Turbulent, Kaimal spectrum: $U_\infty = 11.4m.s^{-1}$	JONSWAP wave spectrum: $H_s = 6m, T_P = 10s$
8	PSD	Turbulent, Kaimal spectrum: $U_\infty = 18m.s^{-1}$	JONSWAP wave spectrum: $H_s = 6m, T_P = 10s$

(a) Thrust coefficient (b) Power coefficient
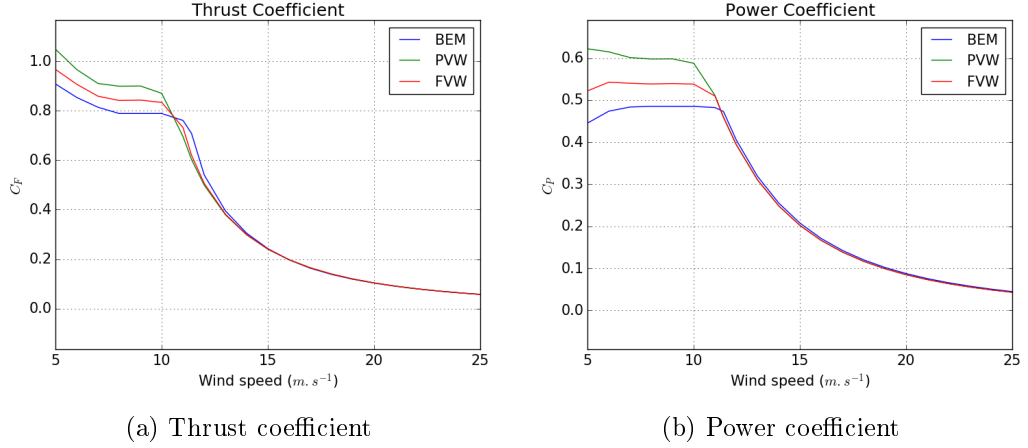
Figure 4.7 – Results for the fixed NREL 5MW HAWT

4.3 Results and discussion

4.3.1 Bottom fixed turbine

Let us consider the case of the bottom-fixed NREL 5MW rotor. The results from *FAST* (BEM) are compared to those from *InWave* computed with both PVW and FVW theories. Skewed flow correction (used in *FAST*) and dynamic stall models are disabled in this part to only focus on the effect of the induction. The generator torque and blade pitch angles are controlled by the same algorithm. The turbine is considered rigid in all solvers. The inflow wind U_∞ is constant and uniformly distributed, ranging from 5 to $25 m.s^{-1}$ in different simulations.

The thrust coefficient acting on the rotor and the aerodynamic power coefficient are plotted as function of the wind speed in figure 4.7. The increase of the thrust coefficient at low wind speeds ($U_\infty < 8 m.s^{-1}$) directly comes from the control law of the generator torque [Jonkman et al., 2009].

Although the three aerodynamic models show a good agreement, differences can be observed at low wind speeds when the rotor is operating at high TSR (above 7). At low wind speed, the relative difference between the thrust forces computed with the BEM and the FVW solvers is about 7.7%. As the torque is slightly different at a same rotor speed, the torque controller induces differences in the rotor speed and thus between the thrust forces. The overestimation of the power coefficient at low wind speeds by the vortex methods compared to the BEM causes the controller to pitch the blades at lower wind speeds with the FVW and PVW. It substantially reduces the thrust force at the rated wind speed $U_\infty = 11.4 m.s^{-1}$. Consequently, the thrust coefficient of the BEM at the rated wind speed is 12% larger than that of the FVW.

Concerning the PVW model, one can see that the agreement with the FVW model is good at high wind speeds (greater than $12 m.s^{-1}$). However, the agreement is poorer for the lower wind speeds and the power coefficient exceeds the Betz limit. It is because the rotor is highly loaded and the wake self-induction is important in these wind conditions. The advection of the vortex filaments at constant shedding speed leads to errors in the computation of the induction at the rotor. Above $15 m.s^{-1}$, the agreement between the three models is better and all computed forces superimpose perfectly.

(a) Surge decay test

(b) Heave decay test
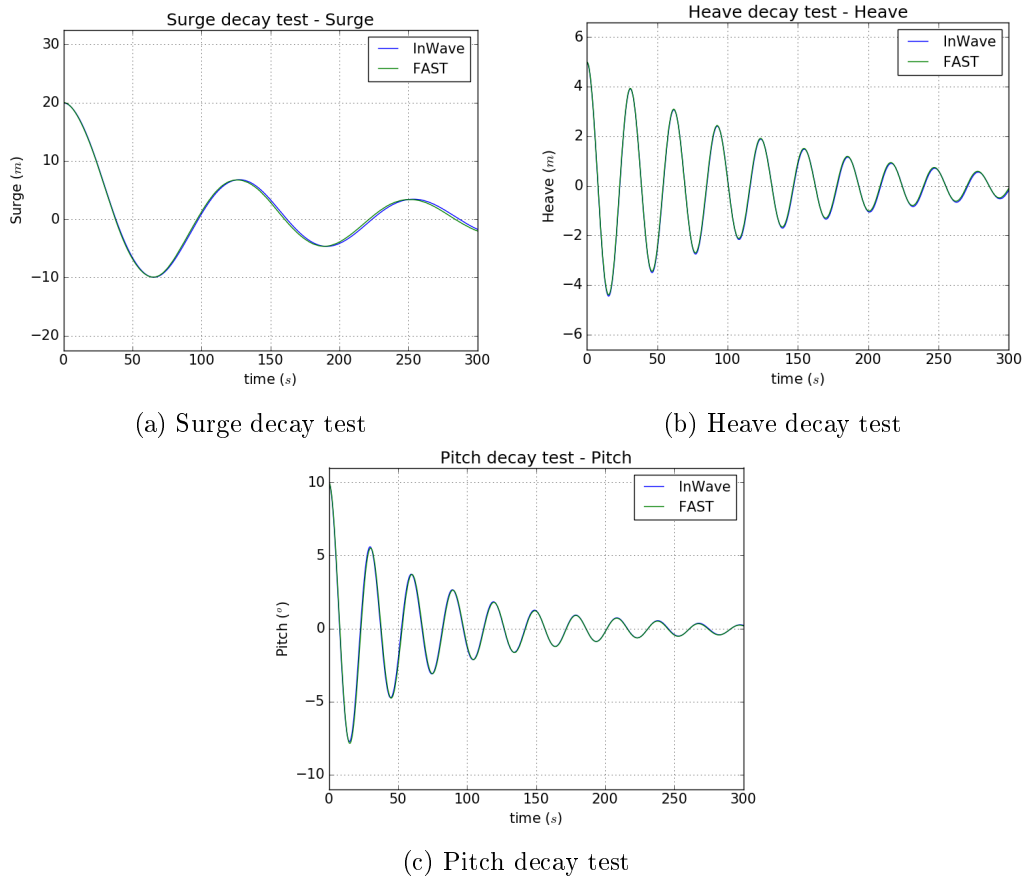
(c) Pitch decay test

Figure 4.8 – Decay tests of the floating HAWT

4.3.2   Free floating wind turbine

4.3.2.1   Without aerodynamic loads

Decay tests: Surge, heave and pitch decay tests are first performed to verify the hydrodynamic model and the system's natural frequencies. Aerodynamic loads and the rotation of the rotor are not considered. The initial surge, heave and pitch in the separated decay tests are respectively $20m$, $5m$ and 10°. The results are shown in figure 4.8. The agreement between *FAST* and *InWave* is very good.

Regular and irregular waves: Simulations are also run with regular and irregular waves without aerodynamic loads. Time series and PSDs of the pitch motion of the wind turbine in irregular waves are for example presented in figure 4.9 (DLC 4 of table 4.2). The agreement of the PSDs is very good at wave frequencies. A peak is observed at the pitch natural frequency. It comes from the viscous drift induced by the implementation of the viscous drag loads in *InWave* (see section 4.2.3). The agreement is perfect if we do not account for the drag loads.

4.3.2.2   Regular waves and constant wind

Simulations are run with regular waves. The regular wave is $3m$ amplitude and $10s$ period. The wind is constant and uniformly distributed at two wind speeds: $U_\infty = 11.4m.s^{-1}$ and $18m.s^{-1}$. Leishman-Beddoes dynamic stall correction model is used in

(a) Pitch time series

(b) Pitch PSD
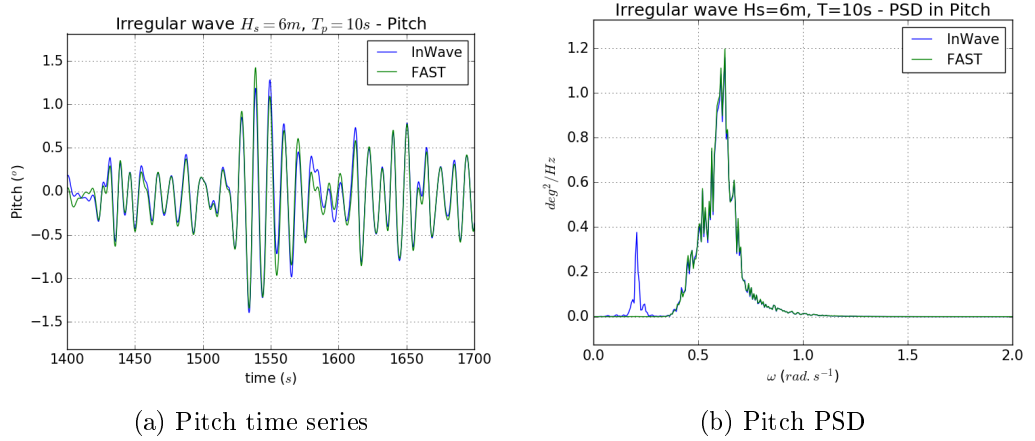
Figure 4.9 – Results of a simulation with irregular waves without aerodynamics

the three aerodynamic solvers. A skew correction from [Pitt and Peters, 1980] is used in the BEM. The generator torque and the collective blade pitch angle are controlled by the control module. Transient effects are ignored and only the periodic steady state is studied. The results from *FAST* are compared to the results from both *InWave-PVW* and *InWave-FVW*. The mean values and amplitudes of the resulting oscillations in platform pitch motion, power coefficient and blade pitch angle at both wind speeds are plotted in figure 4.10. No phase shift between the three responses is observed.

One can see that the solvers show a good agreement at high wind speed. Here the rotor is operating at low TSR. The amplitude of variation of the power coefficient is however small in *FAST*. At low TSR, the PVW and FVW solvers agree perfectly. At lower wind speed, at the rated TSR, the agreement is poorer. In particular, the amplitude of the power coefficient oscillations is much smaller in *FAST*. Also, the mean value is smaller than observed on a bottom-fixed turbine.

The mean platform pitch at $U_\infty = 11.4 m.s^{-1}$ is similar with the three solvers but the thrust computed on the bottom-fixed wind turbine in section 4.3.1 was 12% larger with the BEM than with the FVW solver. The large motions of the turbine at the rated wind speed induce substantial variations in the relative wind speed at the rotor hub, consequently inducing torque and thrust variations. The controller then has a strong effect on the turbine response as it pitches the blades. Similar platform pitch responses are obtained between the three solvers but the blade pitch angle shows large discrepancies at the rated wind speed in both mean value and variations as shown in figure 4.10c. The agreement between the three solvers is much better at lower TSR when $U_\infty = 18 m.s^{-1}$.

4.3.2.3 Floating wind turbine in collinear irregular waves and turbulent wind

Simulations are run in irregular waves and turbulent wind. The irregular waves are described by a JONSWAP spectrum defined by a $H_s = 6m$ significant height, a $T_p = 10s$ peak period and a $\gamma = 3.3$ peakness factor as proposed in the OC3 project. For a given JONSWAP spectrum, one can define the steepness of the irregular waves as $\epsilon = \frac{H_s}{\lambda}$, where λ is the wavelength. The wave steepness of this spectrum is then $\epsilon = 3.8\%$. The input waves have the same amplitudes and phases in both *FAST* and InWave solvers.

Two hub-height mean wind speeds are considered in this study: $U_\infty = 11.4$ and

(a) Power coefficient

(b) Platform pitch

(c) Blade pitch angle
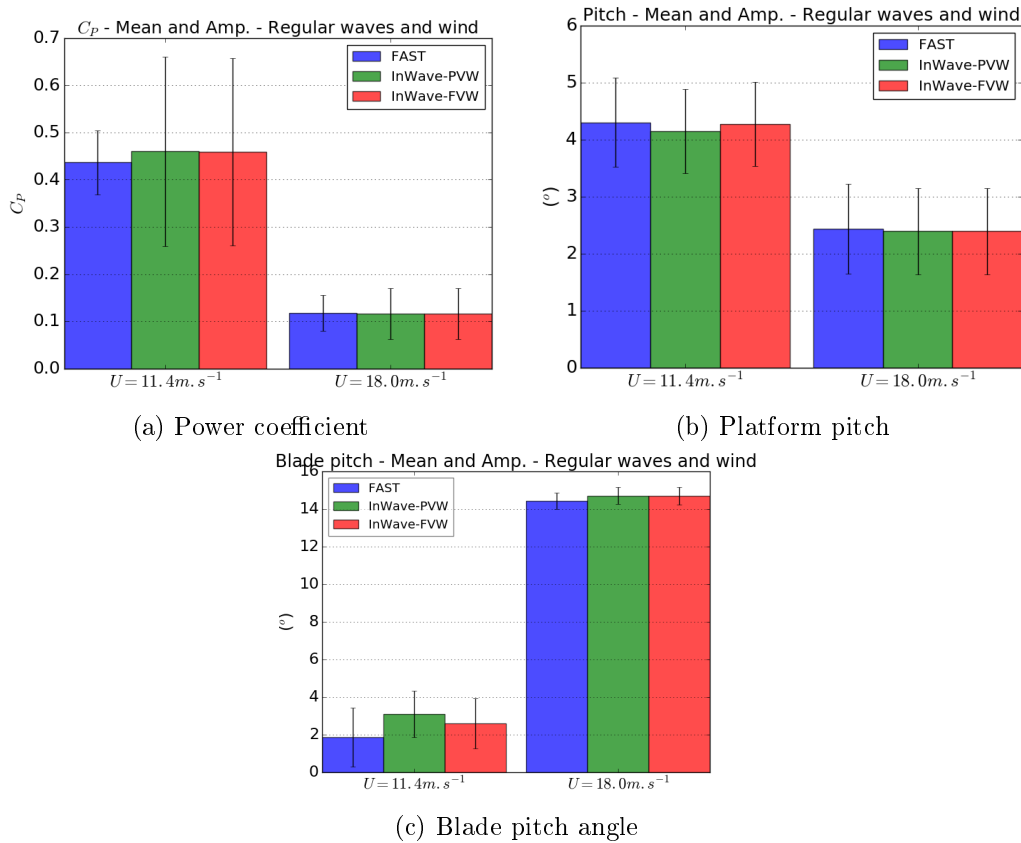
Figure 4.10 – Regular waves results for the floating HAWT

$18.0m.s^{-1}$ (respectively corresponding to TSRs of 7 and 4.4). Turbulent wind fields based on a Kaimal spectrum with a 8.5% turbulence intensity are generated using *TurbSim* [Jonkman, 2009] and used in both codes. The wind profile is calculated with a power law. Leishman-Beddoes dynamic stall correction model is used in the three aerodynamic solvers. The generator torque and the collective blade pitch angle are controlled by the control module. Simulations are run for $5000s$ in order to correctly capture the low-frequency responses and the first $1200s$ are ignored when computing the PSDs so that all transient effects are avoided.

The turbine's motions occur mostly in the (xOz) plane (surge, heave and pitch DOFs). Only the pitch motions time series and PSDs are presented in figure 4.11 and in figure 4.12. In each following figure, the high TSR simulation is on the left and the low TSR is on the right. One can see in figure 4.11 that the three different solvers give three different time series for $U_\infty = 11.4m.s^{-1}$ (i.e. high TSR), although the environmental conditions (wind and wave time series) are the same. Also, as presented in section 4.3.2.2, the blade pitch control may reduce the differences between the dynamic responses of the FWT. In contrast, the results are very similar at $U_\infty = 18m.s^{-1}$ (i.e. low TSR).

Figure 4.12 shows the PSD for the two wind speeds. At high TSR (on the left hand side), one can see that there is a good agreement between the three solvers at wave frequencies (around $\omega = 0.62rad.s^{-1}$) but there are significant differences at low and pitch resonance frequencies responses (respectively around $0.05rad.s^{-1}$ and $0.17rad.s^{-1}$). At low TSR (right hand side in figure 4.12), the three approaches are in good agreement. Especially, both vortex codes results are superimposed. Similar conclusions can be ob-

(a) $U_\infty = 11.4 m.s^{-1}$ (b) $U_\infty = 18.0 m.s^{-1}$
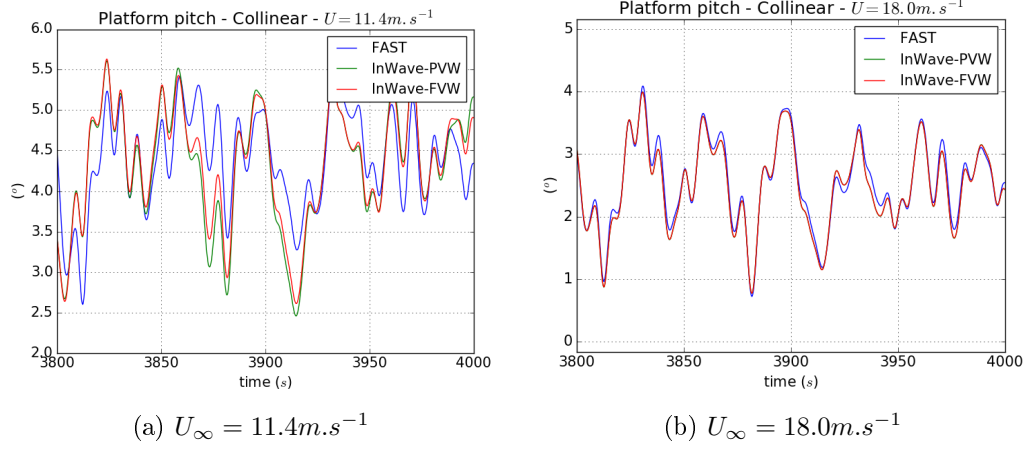
Figure 4.11 – Platform pitch time series in collinear wind and waves

(a) At $U_\infty = 11.4 m.s^{-1}$ (b) At $U_\infty = 18.0 m.s^{-1}$
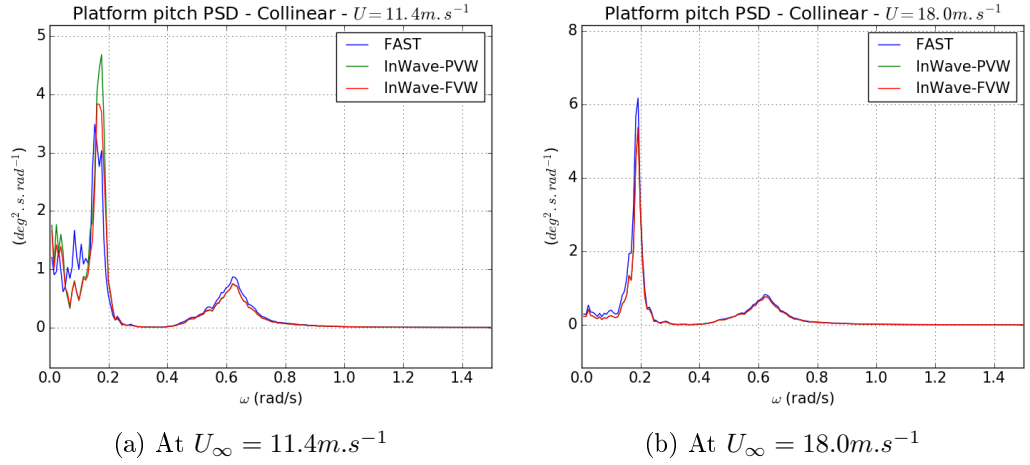
Figure 4.12 – Platform pitch PSD in collinear turbulent wind and irregular waves

tained for the other DOFs, the aerodynamic loads and mooring tensions [Leroy et al., 2017].

On the PSDs in figure 4.12, it is noteworthy that the pitch resonance frequency is slightly altered by the wind speed. It is due to the mean wind thrust. Indeed, a high thrust (for $U_\infty = 11.4 m.s^{-1}$ for example) pushes the turbine further in surge and increases the mooring tension and stiffness, which reduces the pitch resonance frequency compared to the one obtained with a lower wind thrust (as for $U_\infty = 18 m.s^{-1}$ for example). The pitch resonance frequency thus moves from $0.2 rad.s^{-1}$ at $U_\infty = 18 m.s^{-1}$ to $0.17 rad.s^{-1}$ at $U_\infty = 11.4 m.s^{-1}$.

4.3.3 Wind turbine aerodynamic loads in imposed motions

4.3.3.1 Methodology

In order to better understand the effect of the aerodynamic models and to explain the differences between the results presented in section 4.3.2, aerodynamic simulations are run on the wind turbine in imposed motions. It is chosen to impose a sinusoidal motion to the base of the turbine. A methodology is presented to choose the motion amplitude and frequency. Significant motion amplitudes have been chosen in order to represent
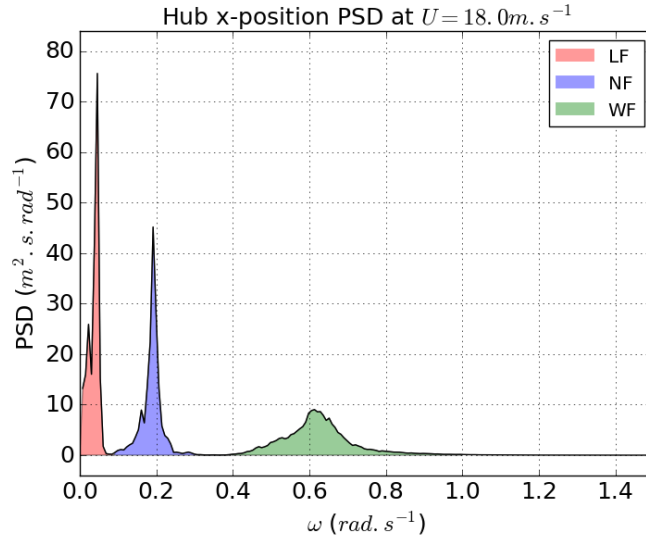
Figure 4.13 – Low (red), natural (blue) and wave (green) frequency response domains in a pitch motion PSD. The mean wind speed is $U_\infty = 18.0 m.s^{-1}$

the motions observed in irregular waves and turbulent wind. This sinusoidal motion must account for the impact of couplings between surge and pitch on the wind velocity at the hub.

Power Spectral Densities (PSDs) of the hub displacement are computed from the dynamic response of the FWT presented previously. In particular, the PSD of the hub motion in the wind direction is decomposed into three regions as presented in figure 4.13: one at low frequency (corresponding to the surge resonance frequency, induced by the mooring stiffness only) here called LF, one around the pitch natural frequency (NF) and one at wave frequencies (WF).

For each of the three domains, we define a corresponding representative single-harmonic motion of the wind turbine. Its frequency is set equal to the peak frequency of the domain. The significant surge motion amplitude A_s is obtained by matching the energy of the single-harmonic motion to the energy in the domain:

$$A_s = \sqrt{2 \int_{\omega_{min}}^{\omega_{max}} S_f(\omega) d\omega} \tag{4.1}$$

Where: S_f is the motion PSD and ω_{min} and ω_{max} are the frequency bounds of the considered response domain.

Sinusoidal surge and pitch motions are imposed to the wind turbine for steady wind conditions with $U_\infty = 11.4$ and $18.0 m.s^{-1}$. For the pitch imposed motion, we choose to rotate the turbine around the reference point $(0, 0, 0)$. The significant pitch amplitude is then calculated so that the hub displacement is equivalent to that imposed in surge: $A_p = \tan^{-1}(\frac{A_s}{h})$, where A_p is the significant pitch amplitude and h is the hub height. The platform pitch oscillates from 0 to $2 * A_p$, the mean value is hence A_p. The mean tilt angle of the rotor is smaller than in coupled simulations, which reduces the impact of the skew model used in the BEM. However, the unsteady effects induced by the rotor tilt variations can be simulated.

The rotor rotational speed is kept constant at the rated speed of $12.1 RPM$ and the blade pitch angle is kept constant at the two wind speeds at respectively 0° and

Table 4.3 – Imposed motions: frequencies

Response	Frequencies ($rad.s^{-1}$)
Low frequency: LF	$\omega_{LF} = 0.05$
Pitch natural frequency: NF	$\omega_{NF} = 0.17$
Wave frequency: WF	$\omega_{WF} = 0.63$

Table 4.4 – Imposed motions: amplitudes

Surge (m)	$U_\infty = 11.4 m.s^{-1}$	$U_\infty = 18.0 m.s^{-1}$
LF	$A_{LF} = 2.99$	$A_{LF} = 1.46$
NF	$A_{NF} = 1.66$	$A_{NF} = 1.73$
WF	$A_{WF} = 1.18$	$A_{WF} = 1.19$
Pitch (^{o})		
LF	$A_{LF} = 1.90$	$A_{LF} = 0.93$
NF	$A_{NF} = 1.06$	$A_{NF} = 1.10$
WF	$A_{NF} = 1.07$	$A_{WF} = 0.76$

14.92^o [Jonkman et al., 2009]. The dynamic stall correction models are disabled for this analysis in order to only compare the induction models. Note that *FAST* was adapted in order to allow the platform motions to be imposed. The dynamic stall is disabled in all solvers, but in *FAST*, *AeroDyn* uses a skew correction. The skewed flow is inherently accounted for in the PVW and FVW solvers.

The imposed motion frequencies are described in table 4.3. Motion amplitudes for surge and pitch at the two studied wind speeds are presented in table 4.4.

The surge oscillation impacts the velocity at the hub while the pitch oscillation impacts both the velocity and the skew angle of the rotor.

4.3.3.2 Surge imposed motions

Results for the pitch natural frequency and wave frequency imposed surge motions are respectively presented in figure 4.14 and figure 4.15. The TSRs at $U_\infty = 11.4$ and $18.0 m.s^{-1}$ are respectively 7 and 4.4.

Let us call U_{dyn} the oscillating part of the wind velocity at the hub and U_{rel} the relative velocity at the hub. One can write:

$$U_{rel} = U_\infty + U_{dyn} \tag{4.2}$$

The thrust variation is plotted as a function of the dynamic velocity at the hub following the methodology presented in [Bayati et al., 2016]. In this representation of the oscillating thrust $\Delta Thrust = f(U_{dyn})$, the slope of the elliptic curve corresponds to the aerodynamic damping, in-phase with the velocity whereas the hysteresis area is correlated with quadrature-phase phenomena which are aerodynamic added mass and stiffness. However, the differences between mean loadings in the three different models cannot be represented following this methodology as only the dynamic loadings are plotted.

The aerodynamic stiffness corresponds to the thrust variation induced by changes in the position of the turbine. Here, the aerodynamic thrust varies with skew angle variations. The damping is in-phase with the velocity of the turbine and opposed to the motion. It comes from variations in the angle of attack on the blades of the rotor,

Table 4.5 – Damping coefficients in imposed surge motions (in $kN/(m.s^{-1})$), with relative differences to the FVW solver solution

U_∞ $(m.s^{-1})$	freq.	BEM	PVW	FVW
11.4	NF	83.3 ($+6.2\%$)	77.0 (-1.9%)	78.4
18	NF	77.0 (-3.6%)	79.9 ($+0.1\%$)	79.9
11.4	WF	83.2 ($+3.4\%$)	77.8 (-3.3%)	80.5
18	WF	77.0 (-8.8%)	84.4 ($+0.1\%$)	84.4

inducing fluctuations in the lift force. The aerodynamic added mass induces thrust variations with the acceleration of the turbine.

Regarding the low frequency, their motion amplitudes are very different at the two wind speeds as can be seen in table 4.4. It is thus difficult to compare the induced aerodynamic loads variations, which is why they are not presented in the following. In the absence of dynamic inflow and stall models, neither aerodynamic added mass nor stiffness is computed in the BEM in surge motions. The oscillation of the BEM's aerodynamic load is quasi-steady and thus fully in phase with the surge velocity.

The damping coefficients (slopes of the ellipses) are presented in table 4.5 with the relative differences with the FVW results.

At natural frequency motion, in figure 4.14, the two vortex solvers are in good agreement. The aerodynamic damping computed by the BEM code is 6.2% greater than by the FVW solver for the high TSR and 3.6% smaller for the low TSR. Also, quadrature-phase effects are very low at natural pitch frequency in comparison to those at wave frequency. At low TSR, both vortex solvers are in perfect agreement. Indeed, the wake dynamics is less important when the rotor is lightly loaded.

Similar conclusions can be drawn for the wave frequency motion in figure 4.15, except that the added mass and stiffness effects computed by the vortex solvers appear to be greater as can be seen in natural frequency imposed motions.

4.3.3.3 Pitch imposed motion

The aerodynamic loads variations on the rotor in pitch motions at pitch natural frequency and wave frequency are plotted respectively in figure 4.16 and in figure 4.17. At both wind speeds, the computed aerodynamic damping is similar to that obtained in surge motions, but more quadratic effects are observed, particularly with the BEM solver. Indeed, the pitch of the rotor induces an aerodynamic stiffness in the quasi-steady aerodynamic force. The calculated damping coefficients are presented in table 4.6 with the relative differences with the FVW results.

At the pitch natural frequency motion, the agreement between both vortex theories is good. The aerodynamic damping at low wind speed is slightly lower with the PVW than with the FVW (2.4% relative difference) but they agree perfectly at high wind speed. As observed with the surge motion, the damping computed with the BEM is greater at low wind speed (5.3% relative difference with the FVW solver) and smaller at high wind speed (-5.3% relative difference). Eventually, quadrature-phase effects are greater at both wind speeds with the BEM.

At the wave frequency in figure 4.17, the aerodynamic loads in the BEM are mostly in-phase with the velocity while the added mass and stiffness computed in the vortex solvers are more important, especially at high wind speed. Here again, the damping

(a) $U_\infty = 11.4 m.s^{-1}$ (b) $U_\infty = 18.0 m.s^{-1}$
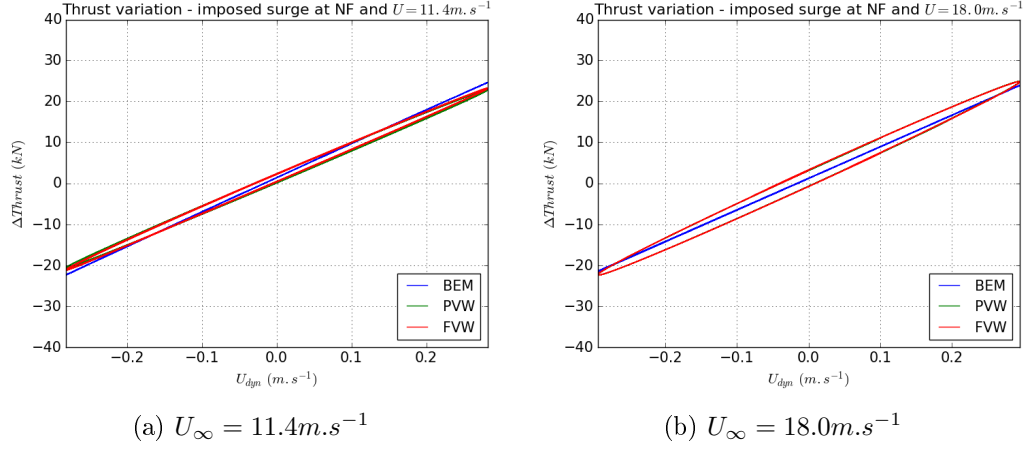
Figure 4.14 – Oscillating aerodynamic loading in natural frequency imposed surge motion

(a) $U_\infty = 11.4 m.s^{-1}$ (b) $U_\infty = 18.0 m.s^{-1}$
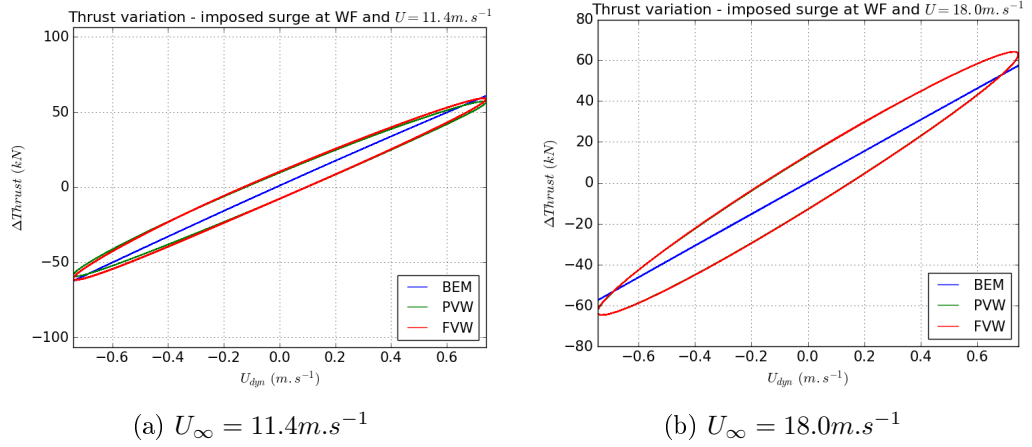
Figure 4.15 – Oscillating aerodynamic loading in wave frequency imposed surge motion

Table 4.6 – Damping coefficients in imposed pitch motions (in $kN/(m.s^{-1})$), with relative differences to the FVW solver solution

U_∞ $(m.s^{-1})$	freq.	BEM	PVW	FVW
11.4	NF	83.7 (+5.3%)	77.5 (−2.4%)	79.5
18	NF	76.4 (−5.3%)	80.7 (+0.1%)	80.7
11.4	WF	83.4 (+3.5%)	78.1 (−3.1%)	80.6
18	WF	76.3 (−9.8%)	84.6 (+0.1%)	84.6

computed by the BEM is slightly greater at low wind speed (3.5% relative difference with the FVW solver) and smaller at high wind speed (9.8% relative difference).

4.3.3.4 Discussion

The dynamic loads computed by BEM, PVW and FVW solvers have been compared for the case of the NREL 5MW rotor with imposed surge and pitch motions. The inherent dynamic inflow in both vortex codes leads to strong differences in comparison to the dynamic loadings computed with the BEM quasi-steady model. Here the com-

(a) $U_\infty = 11.4 m.s^{-1}$

(b) $U_\infty = 18.0 m.s^{-1}$
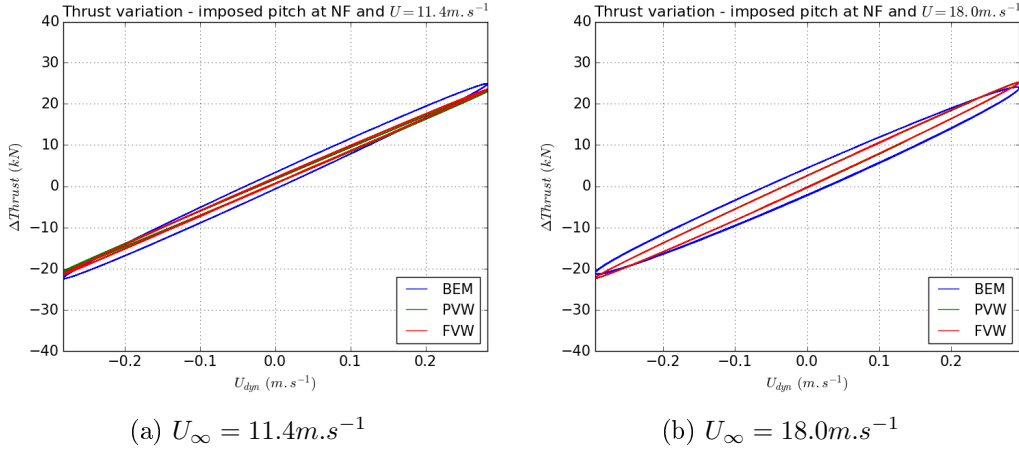
Figure 4.16 – Oscillating aerodynamic loading in natural frequency imposed pitch motion

(a) $U_\infty = 11.4 m.s^{-1}$

(b) $U_\infty = 18.0 m.s^{-1}$
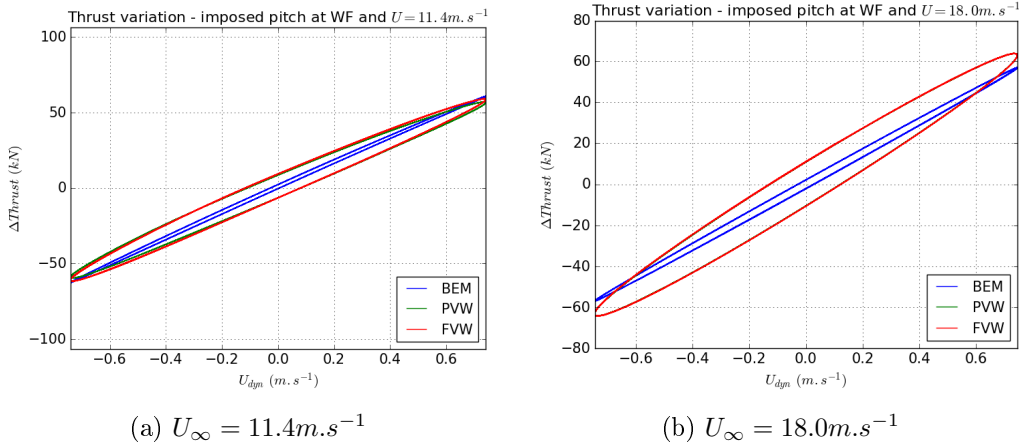
Figure 4.17 – Oscillating aerodynamic loading in wave frequency imposed pitch motion

puted aerodynamic damping is impacted by the wind speed rather than by the degree of freedom of the rotor, either surge or pitch, and can differ with the three solvers. Discrepancies are also observed on the aerodynamic stiffness and the added mass. As the rotor moves downstream, the relative wind speed decreases. The rotor then operates at even higher TSR and hence strongly interacts with its wake, as presented in [Shen et al., 2018b] and [Tran and Kim, 2015]. This can lead to highly unsteady phenomena that are not accounted for in the BEM method.

The PVW theory accounts for strong rotor-wake interaction but does not include wake dynamics. At low TSR, the wake dynamics is less important as the rotor is lightly loaded. The PVW and FVW solvers have hence very similar behaviours and loads are superimposed at $U_\infty = 18 m.s^{-1}$. Small differences in the computed aerodynamic damping have been observed at high TSR when $U_\infty = 11.4 m.s^{-1}$ but the main difference between PVW and FVW methods at high TSR here remains the mean load presented in section 4.3.1. Greater differences between dynamic loadings may however be observed for greater rotor motions when wake dynamics impacts the induction.

The exposed differences can lead to discrepancies in the response of the FWT: a higher damping can lead to a lower motion response, and differences in the quadrature-

phase loads can alter the resonance frequencies. As presented previously, the FWT's mass and inertias, the hydrodynamic, mooring and mean aerodynamic loads are dominant and determine the system's resonance frequencies but the aerodynamic loads variations can alter the amplitude of the responses.

In coupled simulation, at high TSR, lower peak amplitude at the pitch resonance frequency was observed in the pitch response PSD computed by *FAST*. On the contrary, the response at low TSR was higher with the BEM solver used in *FAST*. This correlates with the differences between the aerodynamics computed by the three aerodynamic solvers observed in imposed NF platform motions. Nevertheless, not only the aerodynamic damping observed in imposed motions can impact the motion amplitude. The peak aerodynamic loads due to dynamic stall or wind turbulence also alter the motion of the turbine. Differences between the hydrodynamic models were also emphasized in section 4.2.3. At wave frequency, the response does not correlate with the observed aerodynamic damping as hydrodynamic wave loads are dominant at this frequency range.

It is eventually important to highlight that it is difficult to state at this stage which model is the most accurate as experimental measurements would be required.

4.3.4 Floating wind turbine in misaligned irregular waves and turbulent wind

The case of a $\theta_w = 45^o$ wind heading angle with respect to the wave propagation direction is eventually considered. In this case, the FWT moves significantly in all 6 degrees of freedom. The Morison drag loads push the FWT in the wave propagation direction while the wind thrust pushes and tilts the turbine in the $\theta_w = 45^o$ direction. The FWT hence reaches a position at which the mooring loads are no longer symmetric. The nacelle is yawed in the wind direction. As yaw control is not implemented, there is no relative motion between the nacelle and the platform during a simulation.

The roll motion here corresponds to the rotation around the x axis, the wave heading direction. In misaligned wind and wave conditions, this degree of freedom can be significantly excited by the wind. Also, couplings between degrees of freedom and asymmetric mooring loads induce roll motions at wave frequencies. In the following, the roll and pitch motion responses are presented. The roll and pitch time series are respectively plotted in Figure 14 and Figure 15. The roll and pitch PSDs are plotted in Figure 16 and Figure 17.

Significant differences between the codes appear for the roll and pitch time series in figure 4.18 in figure 4.19 for the low wind speed (high TSR, on the left hand side of the figures). However, there is good agreement for the higher wind speed (lower TSR).

A poor agreement is observed at low and pitch/roll natural frequencies (below $\omega = 0.25 rad.s^{-1}$) on the PSDs at $U_\infty = 11.4 m.s^{-1}$ in figure 4.20 and figure 4.21. The roll and pitch responses at natural frequency of both vortex solvers are much greater than that of the BEM. It may be explained by the lower aerodynamic damping observed in these solvers at natural frequency imposed motion. The difference between the two vortex solvers at the resonance peak is also significant.

The three codes show a better agreement at low TSR (on the right hand side of the figures). In particular, the PVW and the FVW codes have superimposed PSDs. A difference with the BEM code is however visible at the pitch and roll resonance frequency: the PSDs from *FAST* tend to have a more important pitch response in roll and pitch than those from *InWave*, which was also visible on the pitch in collinear wind

(a) $U_\infty = 11.4 m.s^{-1}$

(b) $U_\infty = 18.0 m.s^{-1}$
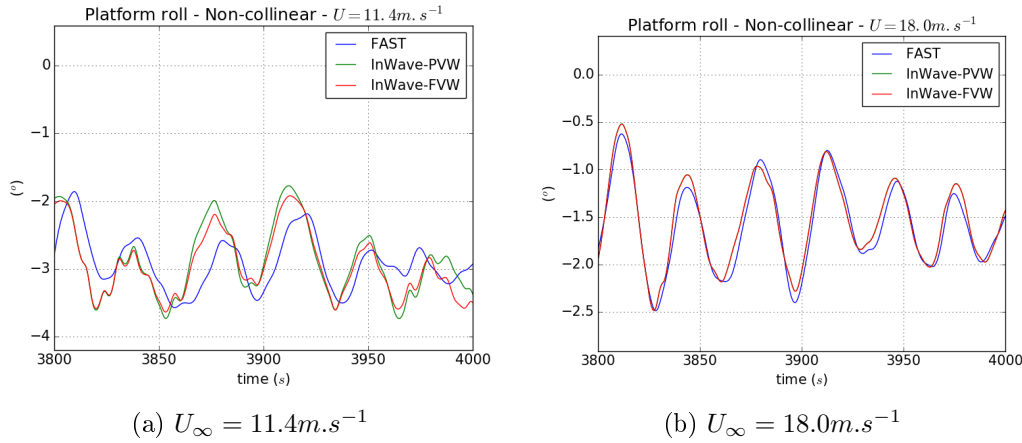
Figure 4.18 – Platform roll time series in non-collinear wind and waves

(a) $U_\infty = 11.4 m.s^{-1}$

(b) $U_\infty = 18.0 m.s^{-1}$
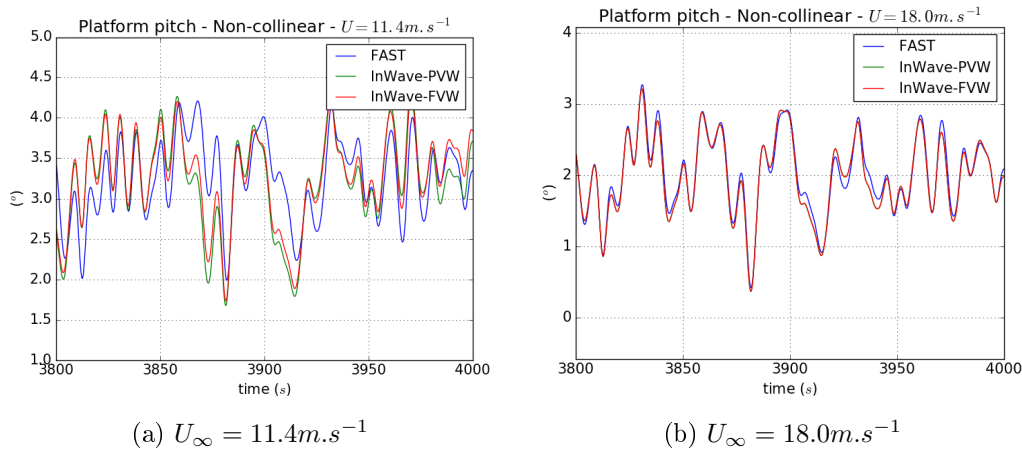
Figure 4.19 – Platform pitch time series in non-collinear wind and waves

and waves. The aerodynamic damping in this region was shown to be smaller with the BEM in section 4.3.3.

4.3.5 Impact of the sea state on the Floating Wind Turbine performances

The seakeeping of the FWT is finally simulated in a set of several sea states to compare the results of *FAST* and *InWave-FVW* in other environmental conditions. The PVW solver is not studied here as it previously showed no interest compared to the formers: it does not seem more accurate than the BEM but requires larger computation times. The studied sea states are inspired by [Cheng, 2016]. They are given in table 4.7. The irregular wave steepness ϵ is also given in the table. The wind is generated using a Kaimal spectum. The wind and wave directions are collinear. No wind speed below $8 m.s^{-1}$ has been studied because of too long computation times needed by the FVW solver.

The simulations are run over 3600s with the same aerodynamic and hydrodynamic models as previously. Leishman-Beddoes dynamic stall model is used in both *FAST* and *InWave-FVW*. The first 1200s of the resulting time series are ignored to avoid any transient effect.

(a) $U_\infty = 11.4 m.s^{-1}$ (b) $U_\infty = 18.0 m.s^{-1}$
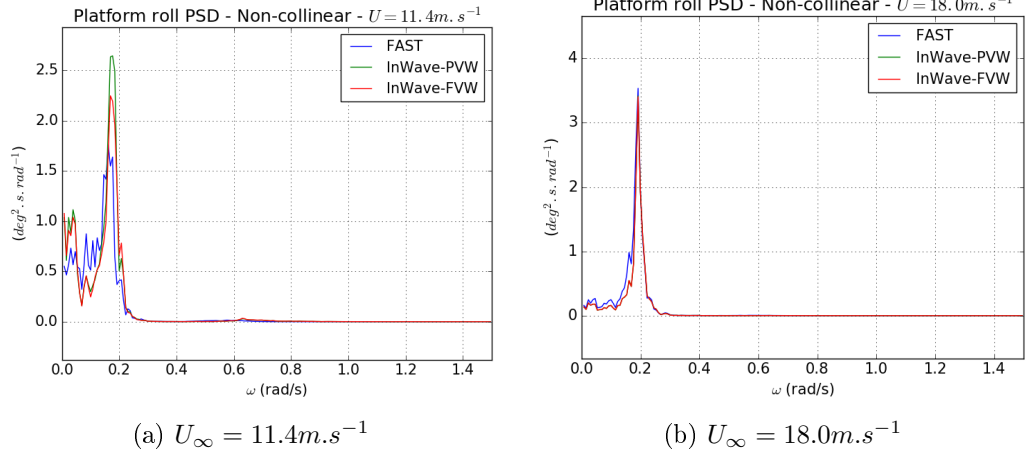
Figure 4.20 – Platform roll PSD in non-collinear wind and waves

(a) $U_\infty = 11.4 m.s^{-1}$ (b) $U_\infty = 18.0 m.s^{-1}$
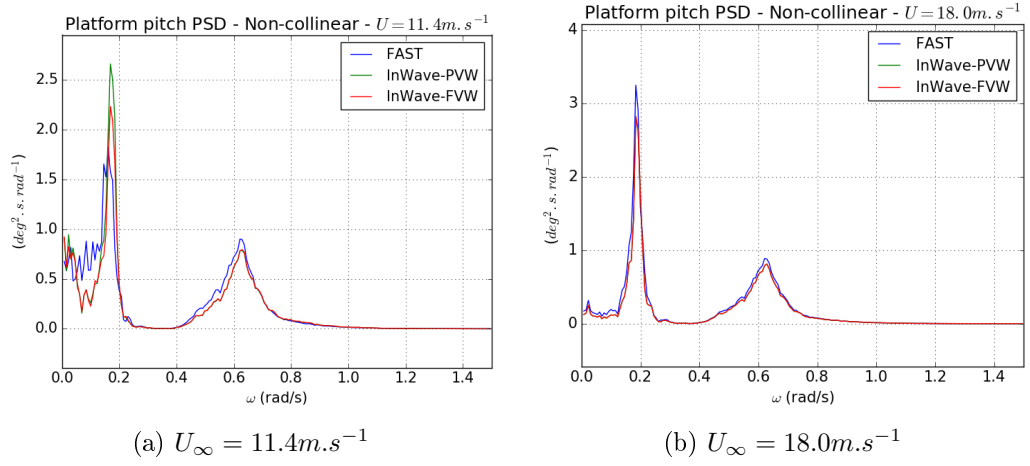
Figure 4.21 – Platform pitch PSD in non-collinear wind and waves

Table 4.7 – Load cases for the floating HAWT in several environmental conditions

DLC	U_∞ $(m.s^{-1})$	H_s (m)	T_p (s)	ϵ
1	8	2.568	9.084	2.0%
2	11.4	3.139	10.0885	2.0%
3	14	3.62	10.29	2.2%
4	18	4.44	10.66	2.5%
5	22	5.32	11.06	2.8%
6	25	6.02	11.38	3.0%

4.3.5.1 Floating Wind Turbine motions and loads

The motions of the turbine is first studied and the responses from *FAST* and *InWave-FVW* are compared. The pitch motion PSDs from all DLCs are computed and compared in figure 4.22. The pitch motion is critical as it induces a skewed flow on the rotor and strongly alters the relative wind speed on the blades.

First, the importance of the wave frequency response increases with the wave height and steepness. The low frequency response in all PSDs come from the aerodynamic loads. Large differences can be observed at those frequencies between *FAST* and *InWave-FVW*. The figures follow the observations made in the previous sections: the FVW solver tends to compute higher low-frequency responses at high TSRs (low wind speeds) and lower responses at low TSRs. The PSDs have globally a better agreement at low TSRs. Similar conclusions are obtained with the other DOFs.

The mean values and STDs of the platform pitch motion are also studied and plotted in figure 4.23a. It is clear that the agreement between mean values and STDs improves when the TSR decreases. At $U_\infty = 8m.s^{-1}$ for instance (DLC 1), there is a 10% relative difference between the mean values of *FAST* and *InWave-FVW* while the agreement is almost perfect at high wind speeds.

It is also interesting to study the ratio between the aerodynamic forces on the hydrodynamic excitation forces $\frac{F_{aero}}{F_{hydro}}$ to measure the importance of each type of loading in the response of the FWT. This ratio is calculated with *InWave*'s outputs. Only the absolute value of the linear hydrodynamic excitation force F_e is accounted for in F_{hydro}. This ratio is plotted for all DLCs in figure 4.23b. We can see that the blade pitch control (active in DLCs 3, 4, 5 and 6) mitigates the importance of the aerodynamic loads. Strong differences between the responses computed with *FAST* and *InWave-FVW* are observed when the aerodynamic loads are almost as important as hydrodynamic loads. The two solvers have very similar results when the rotor is lightly loaded.

The tower base bending moment is also studied as it is a critical design criteria for FWTs: the transition piece which links the tower with the platform is designed to withstand very important loads. In this study, the tower base loads torsors have been calculated with the two solvers from the wind thrust, gravity loads and inertial loads from the platform motions. The last is computed from the acceleration of the platform and the inertia matrix of the top-side group: $\{rotor + nacelle + tower\}$.

The force torsor representing the loads of the tower (indexed 1) on the platform (indexed 0) is $\{\mathcal{T}_{(1/0)}\}$ and can be written as presented in equation 4.3. The tower base reference point is called O_1, and G_1 is the gravity center of the top-side group. e references to the global inertial frame.

$$\{\mathcal{T}_{(1/0)}\}_{O_1} = \{\mathcal{T}_{aero.}\}_{O_1} + \{\mathcal{T}_{gravity}\}_{O_1} + \{\mathcal{T}_{inertia}\}_{O_1} \tag{4.3}$$

Where the torsors are computed as follows:

$$\{\mathcal{T}_{aero.}\}_{O_1} = \left\{ \begin{array}{c} \overrightarrow{F_{aero}} \\ \overrightarrow{M_{aero}}(O_1) \end{array} \right\} \tag{4.4}$$

$$\{\mathcal{T}_{gravity}\}_{O_1} = \left\{ \begin{array}{c} \overrightarrow{P} \\ \overrightarrow{O_1G_1} \wedge \overrightarrow{P} \end{array} \right\} \tag{4.5}$$

$$\{\mathcal{T}_{inertia}\}_{O_1} = - \left\{ \begin{array}{c} m_1 \frac{d}{dt} \left(\overrightarrow{V(O_1)_{(0/e)}} \right) \\ I_1(O_1) \frac{d}{dt} \left(\overrightarrow{\Omega_{(0/e)}} \right) \end{array} \right\} \tag{4.6}$$

(a) DLC 1

(b) DLC 2

(c) DLC 3

(d) DLC 4

(e) DLC 5

(f) DLC 6
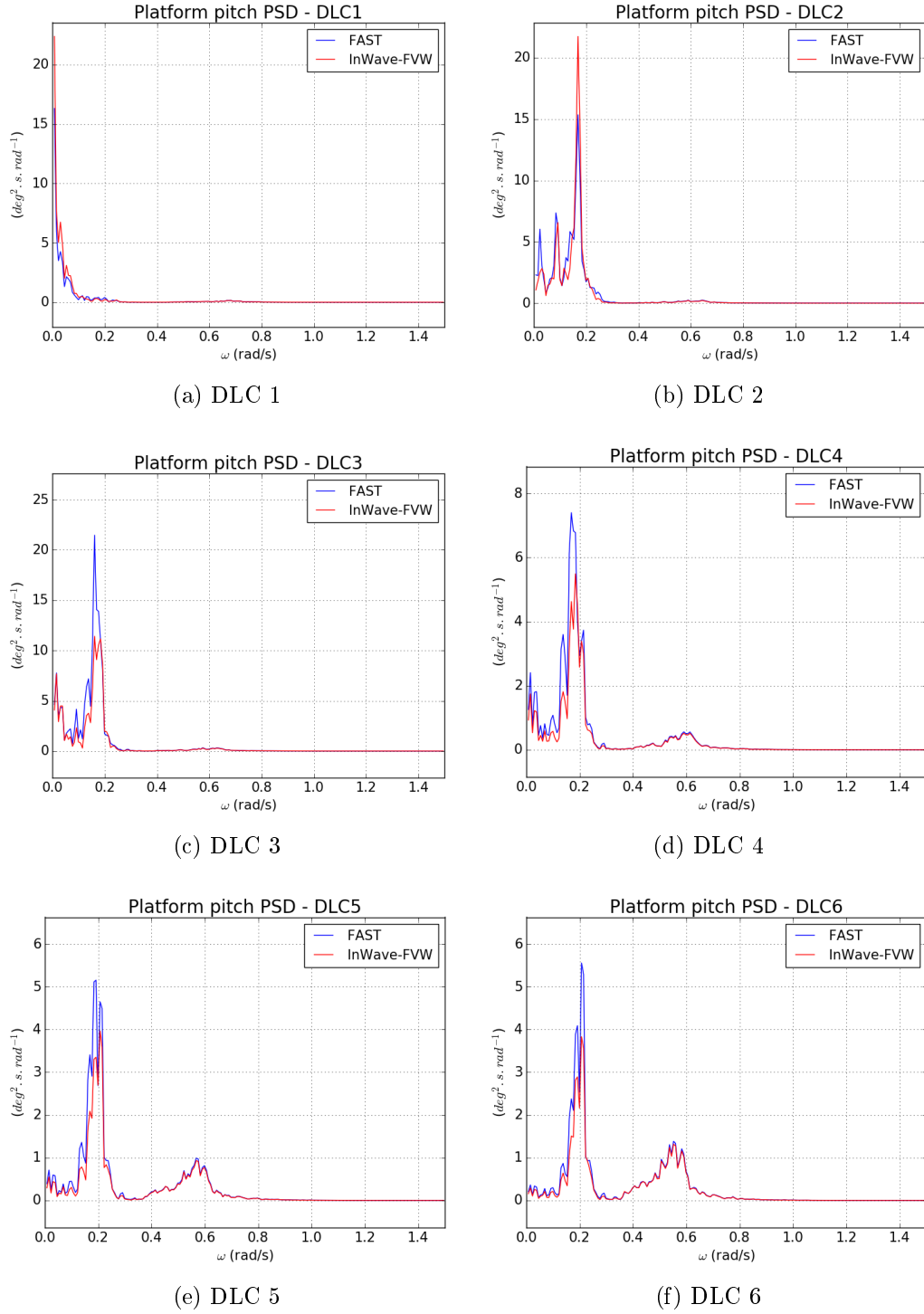
Figure 4.22 – Platform pitch PSDs in all 6 DLCs

(a) Mean pitch and STDs
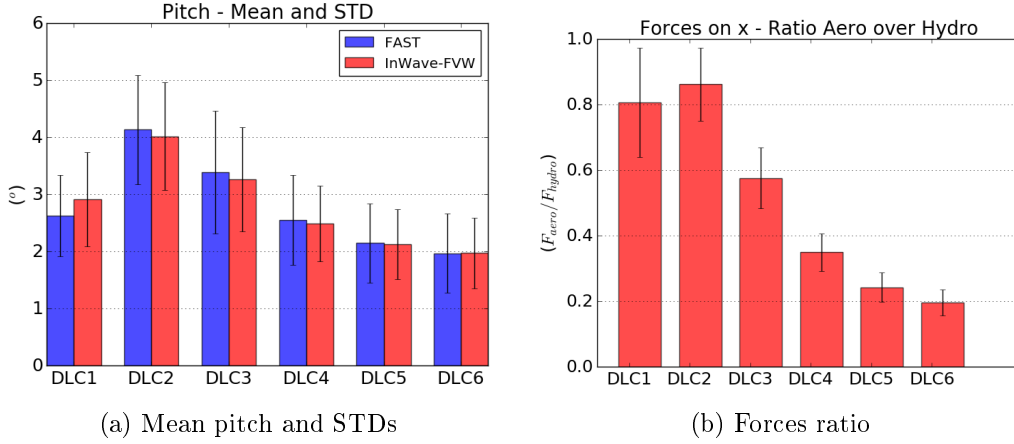
(b) Forces ratio

Figure 4.23 – Mean motions and forces ratio

$\overrightarrow{F_{aero}}$ refers to the aerodynamic thrust, and $\overrightarrow{M_{aero}}(O_1)$ to its moment in O_1. $\overrightarrow{P}$ is the weight vector, m_1 is the mass and $I_1(O_1)$ is the inertia matrix in O_1 of the top-side group.

The fore-aft tower base bending moment PSDs have been computed for all DLCs and are plotted in figure 4.24. One can see, as for the platform pitch PSDs, that the agreement is better at high wind speeds. Also, the loads harmonics at wave frequencies get more and more important as the sea state severity grows. This is especially due to the larger motions of the platform, inducing very large inertial loads at the tower base. Also, the aerodynamic loads are much lower than the wave loads in severe DLCs, as presented before.

At below-rated wind speeds (DLCs 1 and 2), the BEM solver seems to greatly underestimate the low frequency loads at the tower base. This could lead to dramatic design problems. At over-rated wind speeds, the BEM solver overestimates the PSD amplitude at low-frequency compared to the FVW solver. With these rougher sea-states, using the BEM solver would probably lead to conservative designs: this increases the cost of the structures but reduces the risks.

To illustrate this conclusion, the mean values, standard deviation and maximum values of the tower base bending moment are plotted in figure 4.25. The mean value and STD in DLC1 are smaller with *FAST* than with *InWave*. At other DLCs, *FAST* overestimates the mean and STD values. The maximum tower base bending moment is smaller with *FAST* at below-rated and rated wind speeds while larger at over-rated wind speeds.

4.3.5.2   Impact of the sea state on the wind turbine power curve

Finally, the extracted power is computed for each DLC and compared to the reference bottom-fixed turbine (computed with *FAST*) in turbulent wind fields. Power curves are plotted in figure 4.26a. Differences between the mean power at low wind speeds still come partly from the generator torque controller: small differences in torques computed by the two solvers induce larger differences in rotational speed and thus on aerodynamic power, as presented in section 4.3.1. The STDs are also plotted on each curve. The ratio between the STD and the mean power $\sigma/\bar{P}$ is plotted in figure 4.26b, emphasizing the importance of both wind turbulence and platform motion on the wind turbine power. The mean power is not altered at high wind speeds, but the motions of the turbine

(a) DLC 1

(b) DLC 2

(c) DLC 3

(d) DLC 4

(e) DLC 5

(f) DLC 6
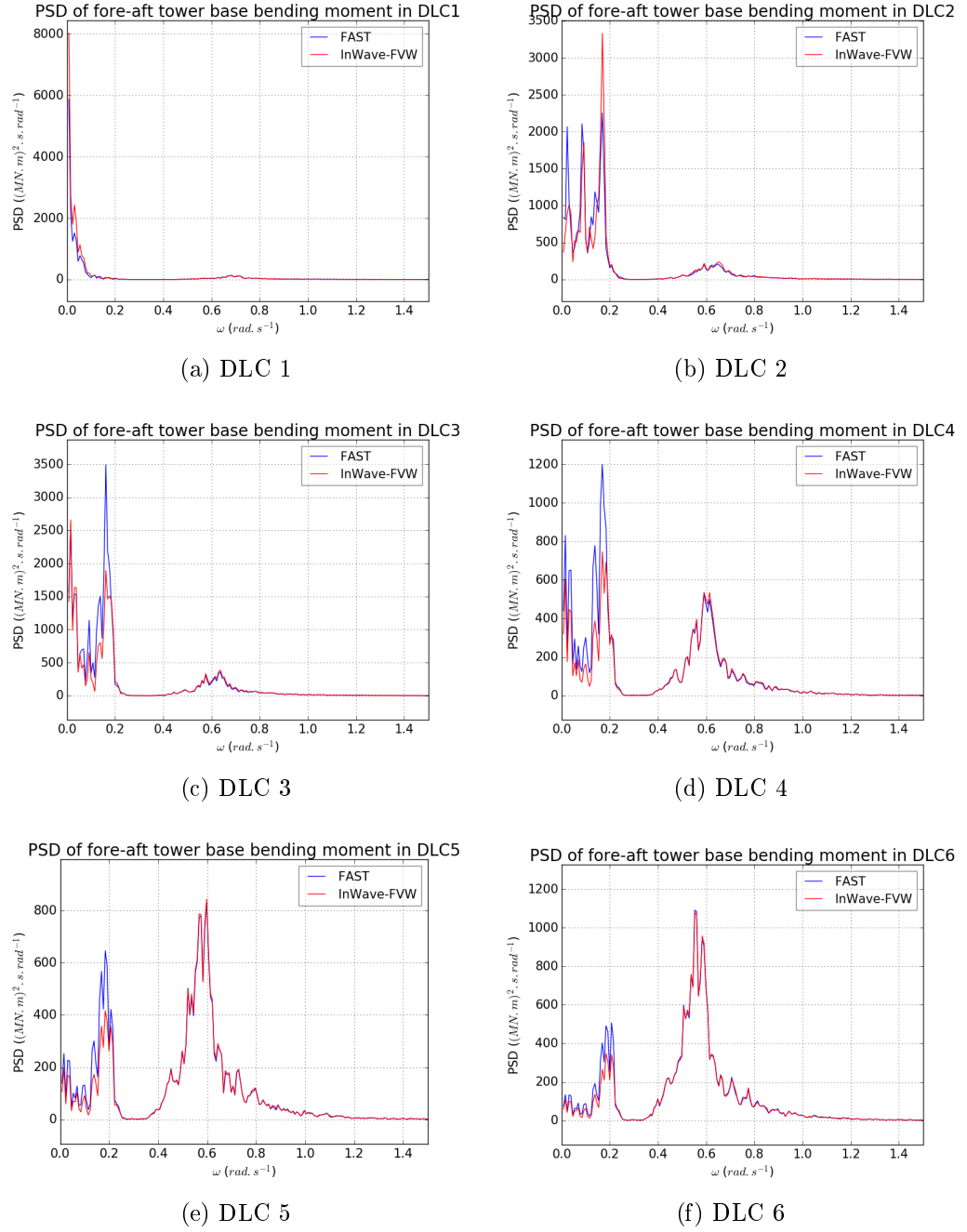
Figure 4.24 – Tower base bending moment PSDs in all 6 DLCs

(a) Mean and STD
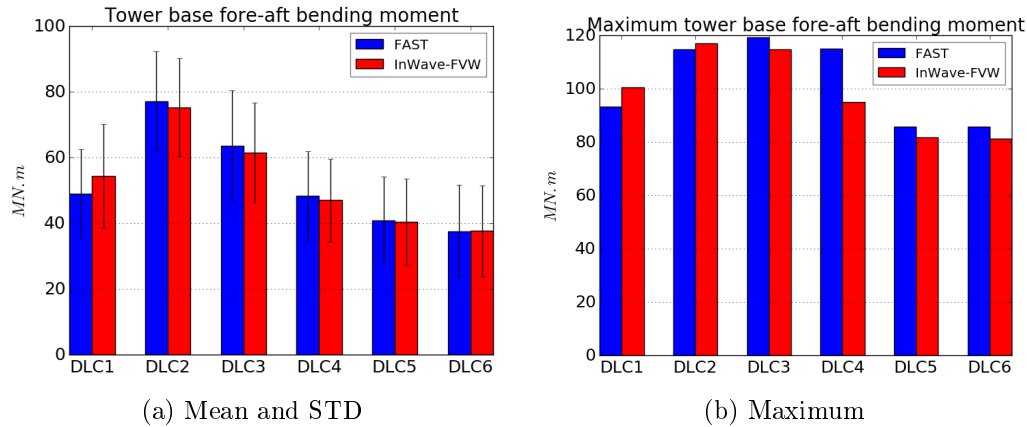
(b) Maximum

Figure 4.25 – Tower base bending moment : mean, STD and maximum values

(a) Power curve (bottom-fixed and floating)

(b) STD over mean power ratio
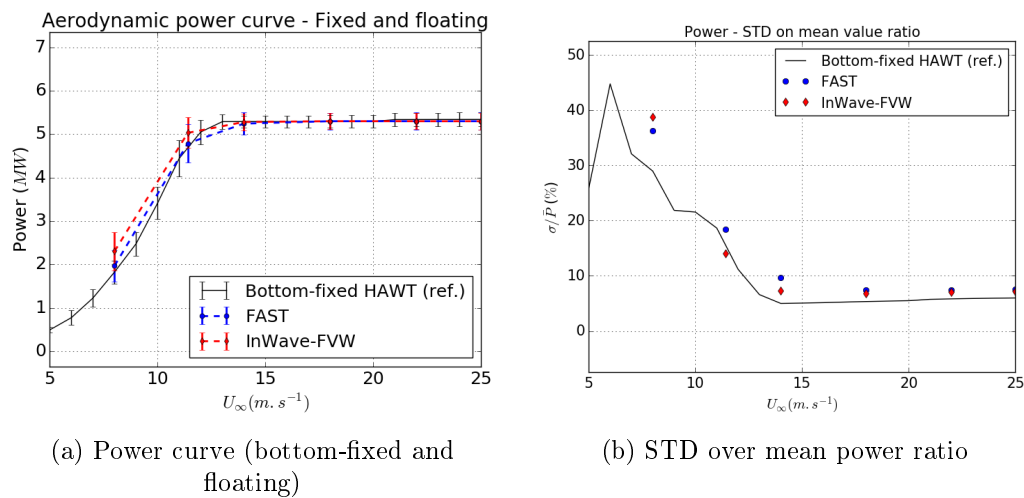
Figure 4.26 – Generated power: comparison between fixed and floating turbines

induce slightly larger variations. At lower wind speeds, the wind turbulence induces a larger wind variation compared to the mean wind speed. Also, in this region where the wind loads are more important compared to the hydrodynamic loads, larger power variations are observed on the FWT. As it could be expected, the differences between the BEM and the FVW solver are larger at low wind speeds. The influence of the rotor control law would also need to be investigated.

4.4 Conclusion

This chapter compared three different aerodynamic solvers for coupled seakeeping analysis of a floating Horizontal Axis Wind Turbine. The aerodynamic solvers are the quasi-steady Blade Element Momentum (BEM) method, the Prescribed Vortex Wake (PVW) method and the Free Vortex Wake (FVW) method. The first is implemented in *FAST* while the two others are implemented in *CACTUS* which was coupled to *InWave*. The wind turbine is the NREL 5MW rotor. The aerodynamic models were compared in the following cases:

1. Bottom-fixed turbine

2. Coupled hydro-aerodynamic simulations of the FWT based on the OC3Hywind SPAR platform

3. Turbine in imposed surge and pitch motions

In bottom-fixed applications, the three solvers show very similar results at high wind speed (i.e. low TSR) but differences are visible on the thrust forces at low wind speeds (i.e. at the nominal, high TSR). At the rated wind speed, motion PSDs of the floating HAWT modelled with the BEM, PVW and FVW solvers were compared. A very good agreement was obtained at high wind speed, but different results were observed in the low wind speed simulation. In particular, different resonance amplitudes were observed at low frequency and pitch natural frequencies. These differences have been shown to come mostly from the aerodynamic models. Indeed, aerodynamic simulations of the turbine following prescribed motions showed different aerodynamic damping, stiffness and added mass induced by the motions of the turbine. Small differences were obtained in the coupled simulations at the wave frequencies as the wave loads seem to be predominant on this frequency range.

More precisely, the study shows that PVW and FVW have very similar results at low TSR. However, the wake dynamics induced by the large platform motions and the wake self-induction seem to play an important role in the determination of the rotor induction at high TSR. The BEM and the PVW methods seem to miss important unsteady aerodynamic phenomena occurring at high TSR when the platform is moving with large motions. In misaligned wind and wave condition, the motion of the rotor is even more complex as more platform degrees of freedom are excited. As suggested in [Shen et al., 2018b] and [Jeon et al., 2014], this complex motion occurring at high TSR induces highly unsteady phenomena in the wake dynamics and in the rotor/wake interactions. Eventually, they strongly impact the rotor aerodynamic loads and thus the motions of the FWT especially at low frequency motions for which the wave loads are not dominant. A similar study could also be done with other types of platforms: a barge or semi-submersible supported turbine could experience larger motions which could alter the aerodynamic loads.

A set of other sea states was finally simulated. The results emphasize the conclusions above. The tower base bending moments were also computed (PSDs, mean values, STDs and maxima). It appears that *FAST* underestimates the bending moment at high TSR (rated and below-rated wind speeds) compared to *InWave-FVW*. At over-rated wind speeds, the quasi-steady solver leads to an overestimation of this moment. If the use of the BEM solver may be less accurate, it may however lead to more conservative designs (inducing higher costs but lower risks). Also, the comparison of the aerodynamic power curves of the floating wind turbine computed with *FAST* and *InWave-FVW* showed that the BEM computes larger oscillations in the power extracted by the rotor.

Despite the differences at low frequencies, the global behaviour of the turbine is well modelled with the three solvers: the resonance peaks in the motion PSDs are located at the same frequencies and the responses at wave frequencies are very similar. This can give confidence in BEM solvers used for pre-design phases, compared to FVW solvers which have a very high computational cost. The FVW shall obtain more accurate results than the two other solvers at high TSR but further experimental studies are needed for a complete validation.

Chapter 5

Dynamic response of a Floating Vertical Axis Wind Turbine: impact of the aerodynamic model

Contents

5.1 Introduction

State of the art models used to compute the aerodynamic loads on VAWTs, such as the Multiple Streamtube (MS) method by [Merz, 2012], the Double Multiple Streamtube (DMS) method by [Paraschivoiu, 2002], or the Actuator Cylinder (AC) method by [Madsen, 1982] assume a steady flow on the rotor (see section 2.1). As the floating platform moves, unsteady aerodynamic phenomena may happen on the rotor. Strong rotor-wake interaction can occur at high Tip Speed Ratio (TSR) and the motions of the turbine can induce complex wake dynamics which can impact the induction on the rotor. In particular, a floating VAWT may operate at higher TSR and in its own wake when the turbine moves in the wind direction. For example, [Lei et al., 2017a] and [Lei et al., 2017b] present the CFD simulation results for a three-bladed VAWT in imposed surge and pitch motions. They emphasize the strong rotor-wake interactions when the rotor moves downstream into its own wake. In large pitch motion amplitudes, stronger and fluctuating blade-tip vortices are created which strongly impacts the loads and power of the rotor. These effects are neglected by the MS and DMS method and may have an impact on the seakeeping of the floating turbine as shown in [Leroy et al., 2018]. The AC theory explicitly models the wake, but it also assumes a steady flow.

In order to address this issue, *InWave* and its three aerodynamic solvers have been used to compute the dynamic response of a floating VAWT in several environmental conditions. The study includes the DMS solver, the Prescribed Vortex Wake (PVW) solver and the Free Vortex Wake (FVW) solver, presented in chapter 3. Following the methodology presented on a floating HAWT in chapter 4, the importance of the unsteady nature of the aerodynamic loads on the seakeeping of a floating VAWT is here investigated on a 2-bladed H-shaped 5MW VAWT rotor mounted on a SPAR platform.

First, the models are compared on a bottom-fixed VAWT, and then the dynamic responses of the FWTs are compared in irregular waves and turbulent wind. Eventually, simulations on the rotors with imposed sinusoidal surge and pitch motions are run in order to improve the understanding of the differences between the aerodynamic models. The study shows that the models agree well at high wind speeds but the DMS codes seems to miss important phenomena at lower wind speed when the rotor is highly loaded and strongly interacts with its wake. This leads to substantial differences in the computed motions of the floating platform.

5.2 Presentation of the numerical models

5.2.1 Aerodynamic models

Among the various numerical models suitable for the simulation of VAWTs, we choose to compare a state-of-the-art DMS method with a PVW and a FVW theory-based solver. This choice was motivated by the need to assess numerical models which offer the best compromise between accuracy and CPU time consumption. These codes consider the blades as lifting lines and use tabulated lift and drag coefficients.

On the one hand, several momentum models inspired by the Blade Element Momentum model used for horizontal axis rotors have been proposed, for instance by Merz [Merz, 2012] or Paraschivoiu [Paraschivoiu, 2002]. The former derives from the Multiple Streamtube approach defined by Strickland [Strickland, 1975] with additional dynamic inflow and stall models. The latter consists in a Double Multiple Streamtube (DMS) model, considering two subsequent actuator disks per streamtube. The downwind part of the rotor is thus impacted by the induction of the upwind half of the rotor. The DMS

theory however ignores the effects of the downwind half on the upwind half's aerodynamics. These models are quasi-steady, apart from the possibly added dynamic inflow and stall models, and do not explicitly model the wake effects.

On the other hand, the wake induction can be computed explicitly in other models. The Actuator Cylinder (AC) has been for instance presented by Madsen [Madsen, 1982]. The vertical axis rotor is here considered as an actuator surface representing the surface swept by the blades. The Euler equation is solved in the fluid domain inside the rotor and in the wake. However, this theory is quasi-steady and is difficult to extend to 3D flow and only a 2D flow is usually considered in horizontal slices of the rotor. An AC solver has been compared to a DMS solver in [Cheng et al., 2017c] and the two codes show a good agreement on a floating VAWT's dynamics.

Eventually, the vortex wake theories, presented in section 3.6.1, are unsteady and are particularly interesting because they inherently account for the dynamic inflow, skewed flow and wake dynamics. Dynamic stall models can be added to each of these models.

5.2.2 Studied case

The studied floating VAWT is inspired from [Cheng, 2016]. The H-shape two-bladed rotor geometry and mass properties are described in table 5.1. The $39m$ radius rotor is supported by the OC3Hywind SPAR platform [Jonkman, 2010] which has been slightly adapted to carry this rotor. The blades use a NACA 0018 profile. The same polars C_L and C_D are used in all models. They are computed with *Xfoil* [Drela, 1989].

The geometry and mass properties of the platform are described in table 5.2. The SPAR buoy is 120m draft. It is moored with 3 catenary lines with 2-point lines fairlead connections (delta-line connections) at the fairleads (see figure 5.1). The mooring loads are computed with $MAP++$ considering the three main lines and the delta lines are accounted for by adding an additional $98340kN.rad^{-1}$ stiffness in yaw [Jonkman, 2010]. The linear potential hydrodynamic loads are computed using the hydrodynamic coefficients calculated by *Nemoh*. The mesh of the SPAR contains 2400 panels (same mesh as in chapter 4). Morison drag on the platform is taken into account with a $C_D = 0.6$ drag coefficient, following [Jonkman, 2010].

The FWT is presented in figure 5.2. The blades and tower are assumed rigid. Natural periods are determined after performing decay tests without neither aerodynamic loads nor rotation between the platform and the rotor.

Following the process described in section 4.2.2, it is ensured that the time-step is sufficiently small for calculation convergence. Also, the blades are described with a sufficient number of blade elements and the wake length is large enough for induction convergence. The needed wake length depends on the TSR. Each blade is discretized into 20 elements and a time-step of $0.1s$ is used.

The control algorithm presented in section 3.7.2 is used to control the generator torque.

5.3 Results and discussion

5.3.1 Bottom-fixed VAWT

A first study is done on the bottom-fixed H-shaped two-bladed VAWT. Simulations were run at constant speed, without shear layer, from $U_\infty = 5$ to $25m.s^{-1}$. The generator torque is computed with the control module and can alter the rotor rotational speed.

Table 5.1 – Rotor geometry and mass properties

Rated power	$5MW$
Rotor radius	$39m$
Height (from tip to tip)	$80m$
Chord	$4.05m$
Tower top height	$79.78m$
Airfoil profile	$NACA0018$
Cut-in, rated, cut-out wind speed	$5, 14, 25m.s^{-1}$
Rated rotational speed	$1.08rad.s^{-1}$
Optimal Tip Speed Ratio (TSR)	3.5
Mass (including blades, tower and shaft)	$350.1tons$
Water clearance (height of low blade tip)	$39.78m$

Table 5.2 – Modified OC3Hywind SPAR platform properties

Water depth	$320m$
Draft	$120m$
Platform mass, including ballast and generator	$7712tons$
Vertical position of the platform COG	$-89.76m$
Surge, sway natural period	$128s$
Heave natural period	$31s$
Roll, pitch natural period	$23.2s$
Yaw natural period	$9.8s$
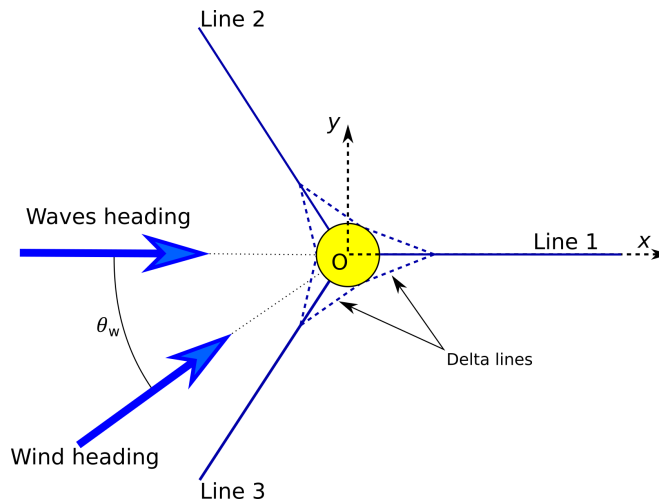
Figure 5.1 – OC3 mooring system
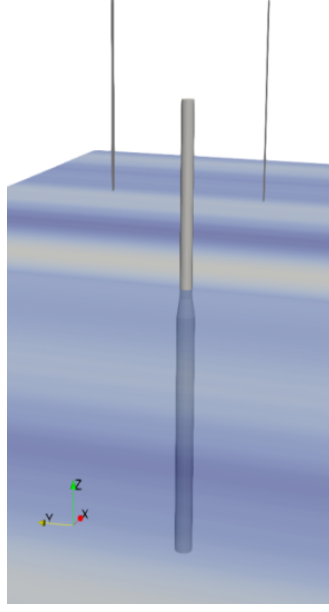
Figure 5.2 – Screenshot of the H-shaped rotor on the OC3Hywind SPAR platform

The Leishman-Beddoes dynamic stall model is used. The power and thrust coefficient are presented in figure 5.3. The rotational speed and the TSR are presented in figure 5.4. One can see that the PVW theory seems to over-estimate the power coefficient at below-rated wind speed (it reaches $C_P = 0.54$). The thrust coefficient also looks over-estimated by the PVW solver at high TSR (i.e. low wind speed) compared to the other models. This must come from an overestimation of the velocity deficit in the rotor wake by the PVW (i.e. over-estimation of the induction). There is a 12% maximum relative difference between the DMS and the FVW solvers. Here the rotor operates at the optimal TSR of 3.5, which is where the induction is at its highest. Momentum methods such as the DMS can be less accurate in these conditions because of strong rotor-wake interaction. There can be flow recirculation due to large vortices, especially at the tip of the blades. Those vortices are not accounted for in the DMS.

As the wind increases, the TSR decreases and the agreement between the solvers improves on both power and thrust coefficients. Very similar results can be observed at above-rated wind speed.

5.3.2 Coupled simulations: collinear irregular waves and turbulent wind

Coupled simulations were carried out in order to compare the DMS, PVW and FVW aerodynamic solvers. The simulations were run with irregular waves described by a JONSWAP spectrum defined following the sea-state defined in chapter 4 by a peak period $T_p = 10s$, a significant wave height $H_s = 6m$ and a peakness factor $\gamma = 3.3$. The same random wave phases are used in each simulation.

Turbulent wind is included at two mean wind speeds: $U_\infty = 12m.s^{-1}$ and $U_\infty = 18m.s^{-1}$. The reference height for the wind speed is $89m$. With the studied rotor, these wind speeds respectively correspond to TSRs of 3.5 and 2. The turbulent wind fields are generated with *TurbSim* [Jonkman, 2009] using a Kaimal spectrum with a 8.5%

(a) Power coefficient

(b) Thrust coefficient
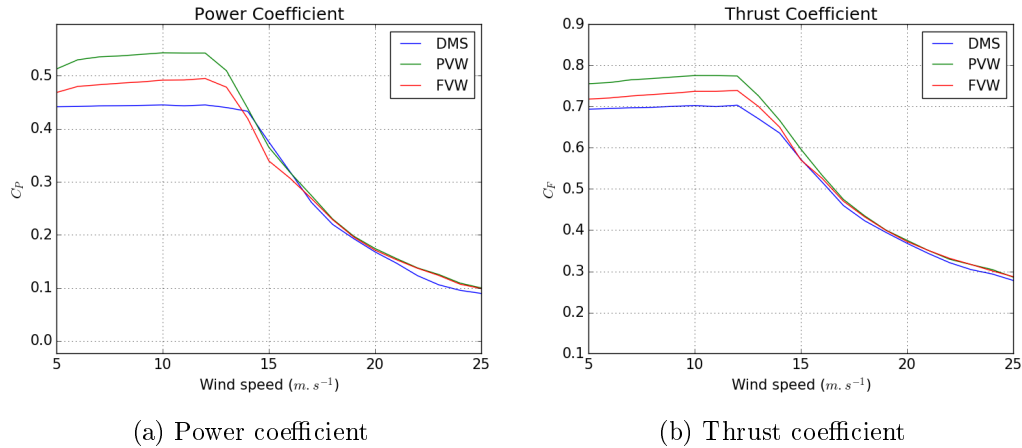
Figure 5.3 – Bottom-fixed VAWT: power and thrust coefficient

(a) Rotor speed

(b) TSR
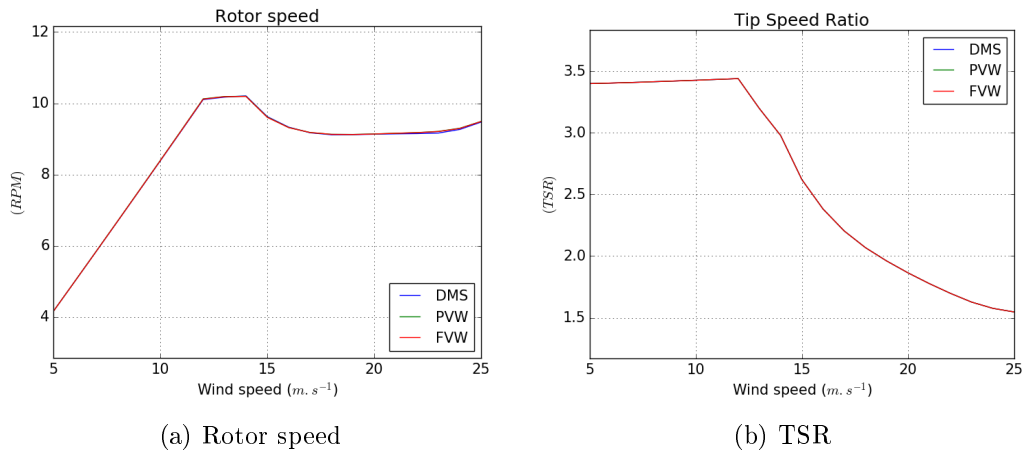
Figure 5.4 – Bottom-fixed VAWT: rotor speed and TSR

turbulence intensity. The wind profile is calculated with a power law. It is ensured that the computed rotor wake is sufficiently long on the PVW and FVW simulations. At $U_\infty = 12m.s^{-1}$, the wake length is 3 rotor diameters. It is equal to 2.5 rotor diameters at $U_\infty = 18m.s^{-1}$.

In the first place, the waves and the wind are collinear. The platform has 6 degrees of freedom and is moored as presented in section 5.2.2. The Leishman-Beddoes dynamic stall model is used in all models. Simulations are run for $5000s$ and the first $1200s$ are ignored in order to avoid any transient effects. The time series are processed into PSDs to see how the energy is distributed along the frequency range. Mean values and standard deviations are also computed in order to compare static and dynamic loadings on the different load cases. The presented analysis focuses on the platform roll and pitch as they are the two most relevant platform degrees of freedom. Similar conclusions are however obtained with other simulation outputs (other degrees of freedom, mooring line tension or generated power).

The roll and pitch PSDs are respectively presented in figure 5.5 and figure 5.6. In each following figure, the high TSR simulation ($U_\infty = 12m.s^{-1}$ wind speed) is shown on the left and the low TSR ($U_\infty = 18m.s^{-1}$ wind speed) is shown on the right.

The oscillating side thrust induces a substantial roll motion as can be seen in figure 5.5. The response is the highest at the roll natural frequency. One can see that the

(a) $U_\infty = 12m.s^{-1}$

(b) $U_\infty = 18m.s^{-1}$
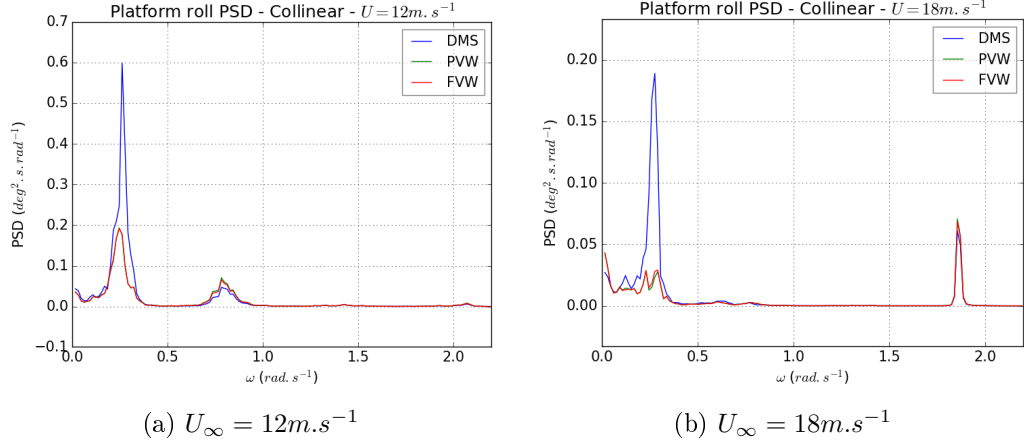
Figure 5.5 – Roll PSD in collinear wind and waves at high TSR (left) and low TSR (right)

(a) $U_\infty = 12m.s^{-1}$

(b) $U_\infty = 18m.s^{-1}$
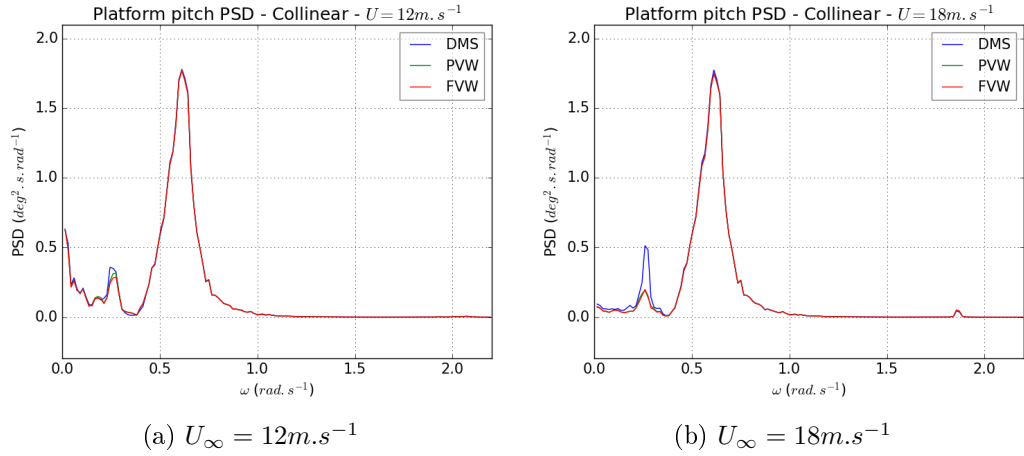
Figure 5.6 – Pitch PSD in collinear wind and waves at high TSR (left) and low TSR (right)

DMS solver shows a much higher resonance in roll at both wind speeds. The response is however higher at high TSR. The peak around $0.77rad.s^{-1}$ on the roll PSD results from a roll-yaw coupling. This coupling is not visible in the pitch PSD as the wave loads response is predominant at those frequencies. Also, a peak at the 2p frequency is visible in the roll PSD circa $1.8rad.s^{-1}$ when $U_\infty = 18m.s^{-1}$.

Surprisingly, the pitch PSDs of the different models in Figure 8 agree better at $U_\infty = 12m.s^{-1}$ than at $U_\infty = 18m.s^{-1}$ although unsteady phenomena are stronger at high TSR (higher rotor loading). The response at the pitch natural response at low TSR is higher with the DMS than with the vortex solvers. In terms of design in extreme conditions, the PSDs are extensively used. The DMS could hence lead to more conservative designs.

The mean values (colour bars) and standard deviations (error bars) for the platform roll and pitch motions are plotted at both wind speeds in figure 5.7. One can see that the agreement between the three aerodynamic solvers is better at low TSR. At high TSR, the mean pitch obtained with the DMS is substantially lower than that of the FVW solver (9% relative difference, against 4.4% at low TSR). This difference is explained by

(a) $U_\infty = 12m.s^{-1}$ (b) $U_\infty = 18m.s^{-1}$
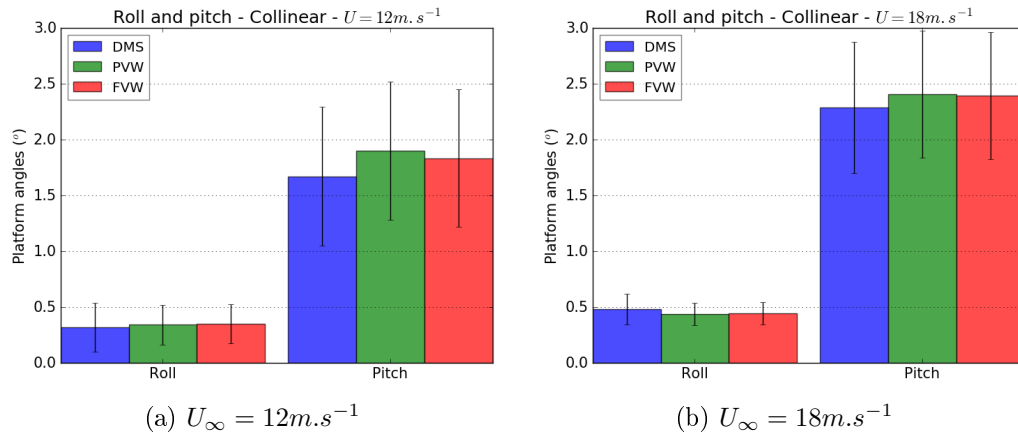
Figure 5.7 – Platform roll and pitch mean values and STDs in collinear wind and waves at high TSR (left) and low TSR (right)

the lower aerodynamic thrust observed at high TSR on the bottom-fixed case. Different mean tilt angles could lead to design issues, on the tower design for instance.

5.3.3 Turbine in imposed surge and pitch motions

5.3.3.1 Methodology

The aerodynamic forces acting on the turbine in imposed surge and pitch motions are compared in order to better explain the differences between the aerodynamic models. The objective is to compare the effects of the motions on the dynamic loads with the DMS, PVW and FVW models. The methodology presented in section 4.3.3 in chapter 4 is applied to determine imposed motions frequencies and amplitudes from the PSDs computed in section 5.3.2.

The turbine is considered with imposed surge and pitch motion. In pitch motion, the tower is rotating around the platform centre of mass. The rotor rotational speed is constant and set at the rated speed $\omega = 1.08 rad.s^{-1}$. The three aerodynamic solvers include Leishman-Beddoes dynamic stall model. Two constant wind velocities are considered: $U_\infty = 12$ and $18m.s^{-1}$. The platform pitch oscillates from 0 to $2 * A$, where A is the motion amplitude.

The imposed motion frequencies are described in table 5.3. Motion amplitudes for surge and pitch at the two studied wind speeds are presented in table 5.4. The low frequency motions are not compared because the motion amplitudes are too different between the respective wind speeds. The study focuses on the Natural Frequency (NF) and Wave Frequency (WF) motions in both surge and pitch. The surge motion impacts the relative wind velocity at the rotor, but the pitch motions impacts not only the velocity but also the skew angle of the rotor which induces aerodynamic stiffness.

The thrust acting on a bottom-fixed two-bladed VAWT is oscillating at its $2p$ frequency, p being the rotational frequency. For example, the thrust coefficient computed with the DMS solver in the case of a WF pitch motion is plotted for one motion period in figure 5.8. It is compared to the thrust acting on the bottom-fixed VAWT. The impact of the motion on the thrust is easily observed. With a sinusoidal imposed motion, an additional harmonic appears in the VAWT's thrust spectrum at the motion frequency. The thrust oscillations at the prescribed motion frequency in the three models are extracted using a Fourier transform and compared. This is convenient for observing the

Table 5.3 – Imposed motions: frequencies

Response	Frequencies ($rad.s^{-1}$)
Low frequency: LF	$\omega_{LF} = 0.03$
Pitch natural frequency: NF	$\omega_{NF} = 0.26$
Wave frequency: WF	$\omega_{WF} = 0.63$

Table 5.4 – Imposed motions: amplitudes

Surge (m)	$U_\infty = 12.0m.s^{-1}$	$U_\infty = 18.0m.s^{-1}$
LF	$A_{LF} = 2.32$	$A_{LF} = 1.15$
NF	$A_{NF} = 0.34$	$A_{NF} = 0.37$
WF	$A_{WF} = 1.46$	$A_{WF} = 1.45$
Pitch (^{o})		
LF	$A_{LF} = 0.27$	$A_{LF} = 0.13$
NF	$A_{NF} = 0.25$	$A_{NF} = 0.27$
WF	$A_{WF} = 0.77$	$A_{WF} = 0.76$
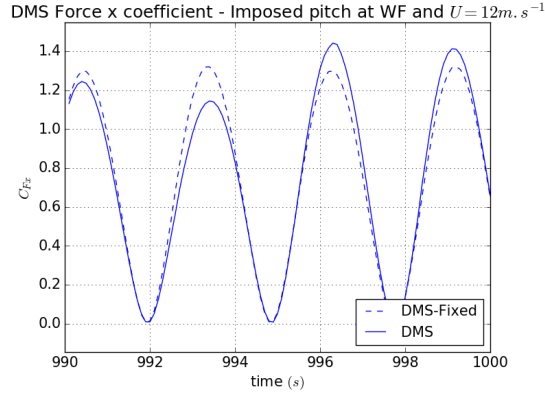
Figure 5.8 – Thrust coefficient on the 2-bladed VAWT with $U_\infty = 12m.s^{-1}$ in pitch imposed motion, compared to the bottom-fixed turbine (computed with the DMS solver)

direct impact of the motion of the turbine on the loads, but it does not capture the non-linear couplings between harmonics. Only the thrust in the direction of the wind is processed.

The thrust oscillation at the imposed motion frequency is then plotted as a function of the dynamic velocity at the equator of the VAWT (mid-height of the rotor) following the methodology presented in chapter 4 on a HAWT. In this representation of the oscillating thrust $\Delta Thrust = f(U_{dyn})$, the slope of the elliptic curve corresponds to the aerodynamic damping, in-phase with the velocity whereas the hysteresis area is correlated with quadrature-phase phenomena which are aerodynamic added mass and stiffness. However, the differences between mean loadings in the three different models cannot be represented following this methodology as only the dynamic loadings at the motion frequency are plotted.

5.3.3.2   Surge imposed motion

The pitch natural frequency and wave frequency imposed surge motions are respectively presented in figure 5.9 and figure 5.10. The damping coefficients obtained in the simu-

Table 5.5 – Damping coefficients in imposed surge motions (in $kN/(m.s^{-1})$), with relative differences to the FVW solver solution

U_∞ $(m.s^{-1})$	freq.	DMS	PVW	FVW
12	NF	45.8 (+19.1%)	35.5 (−7.7%)	38.5
18	NF	24.1 (+11.7%)	17.8 (−17.3%)	21.6
12	WF	44.9 (+21.9%)	38.6 (+4.8%)	36.9
18	WF	26.8 (+18.2%)	20.6 (−9.0%)	22.7

lations are given in table 5.5, with relative differences to the value computed with the FVW solver.

At natural frequency imposed motion, the aerodynamic damping (corresponding to the slope of the ellipses) is higher with the DMS method, and lower with the PVW solver. At $U_\infty = 12m.s^{-1}$, the damping computed by the DMS method is 19.1% larger than with the FVW method. The PVW solver computes a 7.7% smaller damping than the FVW. The quadratic effects (related to the area of the ellipses) are similar between PVW and DMS but slightly lower with the FVW. At lower TSR, when $U_\infty = 18m.s^{-1}$, this difference is increased. At low TSR the DMS computes a 11.7% larger damping than the FVW and the damping computed by the PVW is 17.3% smaller than that of the FVW. However, the NF imposed motion is very small and the induced loads are hence only near $2kN$ amplitude. It is then not enough to conclude.

On the WF motion, in figure 5.10, the motion is larger and the induced velocity at rotor mid-height reaches nearly the $1m.s^{-1}$ amplitude (respectively 8% and 6% of the inflow velocities). The higher aerodynamic damping in the DMS is again visible, at both wind speeds. However, the PVW and the FVW solvers are in better agreement than for the NF motion and seem to induce more important quadratic effects at this frequency. This may not be enough to alter the resonance frequency, but it can impact the amplitude of the motion response of the FWT. At $U_\infty = 18m.s^{-1}$, the PVW solver has the lowest aerodynamic damping.

5.3.3.3 Pitch imposed motions

The aerodynamic load variations at natural frequency and wave frequency imposed motions are respectively plotted in figure 5.11 and figure 5.12. The simulation at $U_\infty = 12m.s^{-1}$ is on the left and the simulation at $U_\infty = 18m.s^{-1}$ is on the right. The damping coefficients obtained in the simulations are given in table 5.6, with relative differences to the value computed with the FVW solver.

One can see a different behaviour in pitch at the natural frequency compared to the surge imposed motion in figure 5.11. The FVW solver computes a higher aerodynamic damping than the two other solvers at both wind speeds (12.7% higher than the DMS and 9.4% higher than the PVW at $U_\infty = 12m.s^{-1}$). Also, the FVW solver computes low quadratic effects at $U_\infty = 12m.s^{-1}$ while the PVW solver computes larger quadratic loads at $U_\infty = 18m.s^{-1}$. Here again, the motions at natural frequency have a low amplitude and the induced loads are low and it is difficult to conclude on trends followed by the induced loads. It can be highlighted that the skew angle of the rotor alters the induction. In particular, the unsteady and unequal distribution of the induction on the blade span, induced by the rotor skew angle and pitch motion, can cause complex wake dynamics in the FVW solver. Differences between the PVW and the FVW here come from different descriptions of this wake dynamics, particularly induced by the pitch

(a) $U_\infty = 12m.s^{-1}$ (b) $U_\infty = 18.0m.s^{-1}$
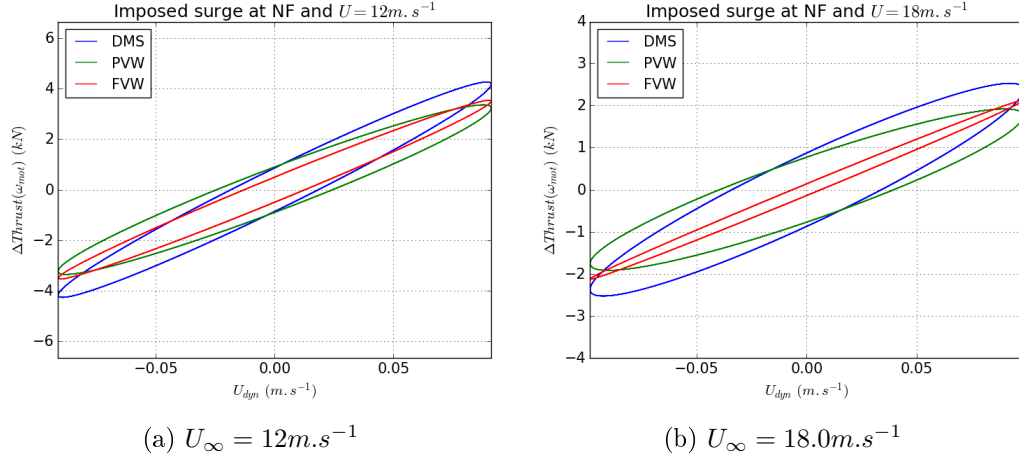
Figure 5.9 – Oscillating aerodynamic loading in natural frequency imposed surge motion

(a) $U_\infty = 12m.s^{-1}$ (b) $U_\infty = 18.0m.s^{-1}$
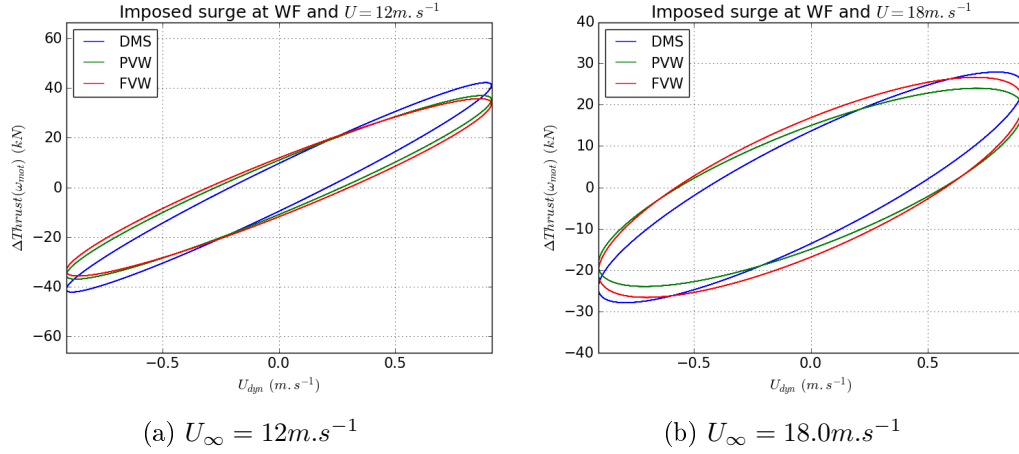
Figure 5.10 – Oscillating aerodynamic loading in wave frequency imposed surge motion

Table 5.6 – Damping coefficients in imposed pitch motions (in $kN/(m.s^{-1})$), with relative differences to the FVW solver solution

U_∞ $(m.s^{-1})$	freq.	DMS	PVW	FVW
12	NF	43.3 (-12.7%)	45.0 (-9.4%)	49.6
18	NF	25.2 (-16.8%)	28.4 (-6.2%)	30.2
12	WF	42.9 (-5.6%)	47.6 $(+4.8\%)$	45.4
18	WF	27.0 (-10.6%)	28.2 (-6.5%)	30.2

motion of the rotor.

At a higher frequency motion, in figure 5.12, the PVW solver computes a slightly higher aerodynamic damping at $U_\infty = 12m.s^{-1}$ than the FVW solver (4.8% relative difference). The FVW solver computes the highest damping and added mass and stiffness at $U_\infty = 18m.s^{-1}$ (10.6% higher that the DMS solver). Induced loads are here much higher as the motion velocity amplitude is above $1m.s^{-1}$

Differences observed in the aerodynamic forces acting on the rotor in imposed motions can alter the response of the FWT. For instance, the lower damping computed at low TSR by the DMS solver in pitch motions at pitch natural frequency (see figure 5.11)

(a) $U_\infty = 12m.s^{-1}$ (b) $U_\infty = 18.0m.s^{-1}$
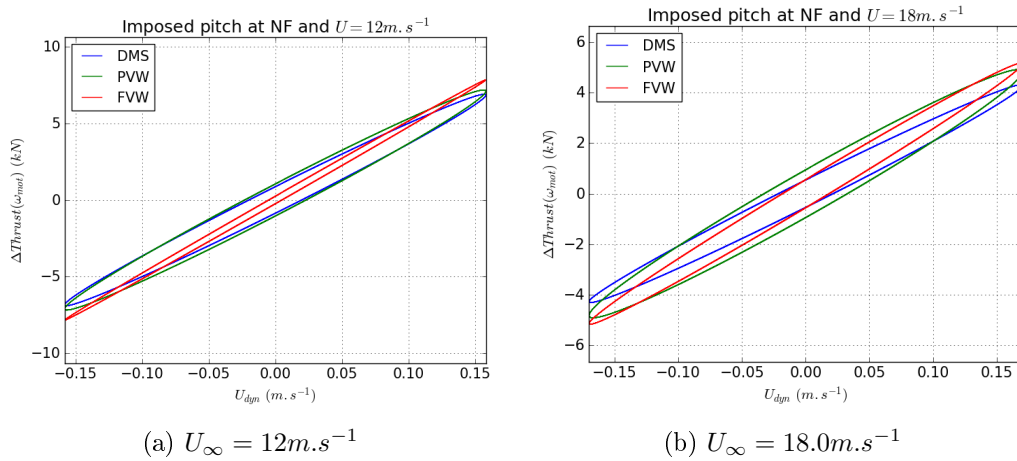
Figure 5.11 – Oscillating aerodynamic loading in natural frequency imposed pitch motion

(a) $U_\infty = 12m.s^{-1}$ (b) $U_\infty = 18.0m.s^{-1}$
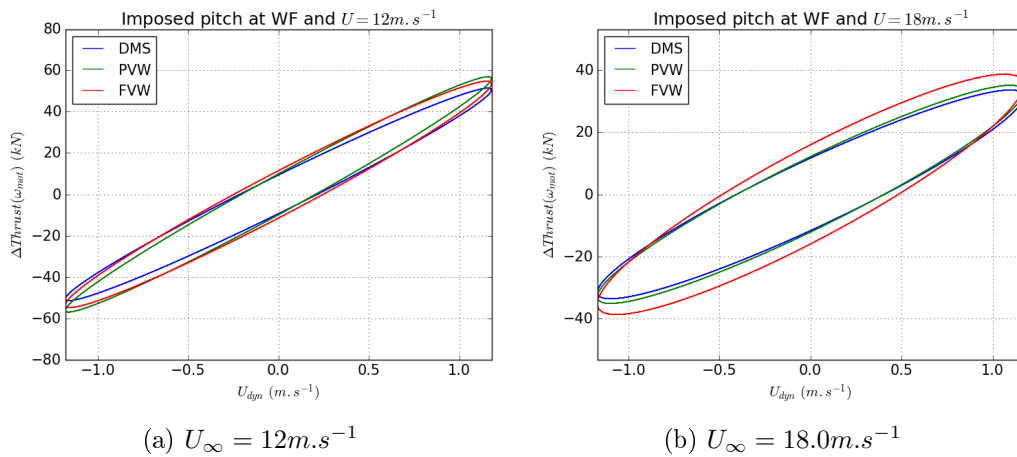
Figure 5.12 – Oscillating aerodynamic loading in wave frequency imposed pitch motion

could induce the higher pitch response observed in figure 5.6 in coupled simulations. But differences in aerodynamic damping at higher frequencies (including $2p$ frequency in particular) can also dissipate energy and alter the response of the FWT. Also, this study only considers the load harmonic induced at the motion frequency and ignores the non-linear couplings that could appear. Eventually, at wave frequency the loads induced by the waves are dominant, and differences between the aerodynamic models have only little impact at those frequency.

5.3.4 Coupled simulations: non-collinear wind and waves

In this section, the case of misaligned wind and waves is considered. The waves propagate along the x axis. The wind heading is $\theta_w = 45^o$. Thus, the turbine is pushed by the wind in mean thrust direction and pushed by the waves in the Ox direction. The FWT hence reaches a position at which the mooring loads are not symmetric. In the following, the surge is the translation in the waves heading direction (x axis) and the roll is the rotation around the x axis.

Platform roll PSDs are plotted in figure 5.13. In this case, the DMS solver induces

(a) $U_\infty = 12m.s^{-1}$ (b) $U_\infty = 18m.s^{-1}$
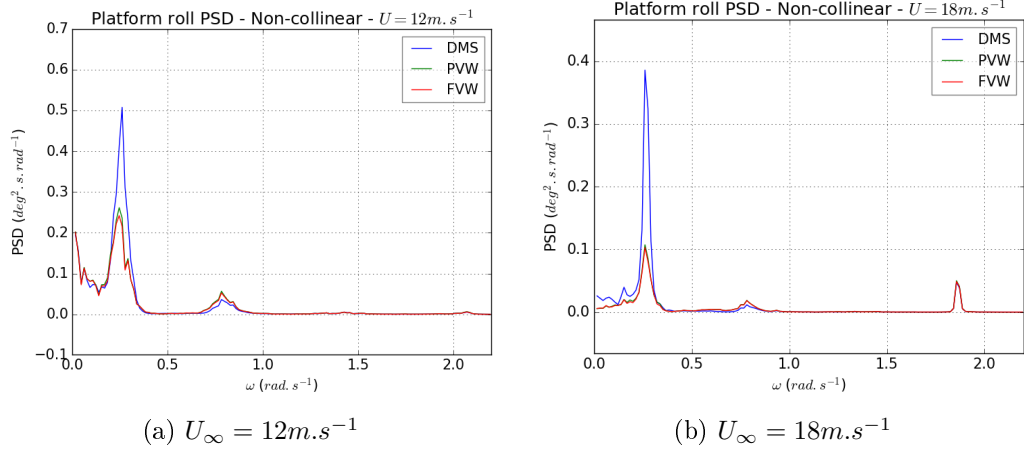
Figure 5.13 – Roll PSD in non-collinear wind and waves at high TSR (left) and low TSR (right) with $\theta_w = 45^o$

(a) $U_\infty = 12m.s^{-1}$ (b) $U_\infty = 18m.s^{-1}$
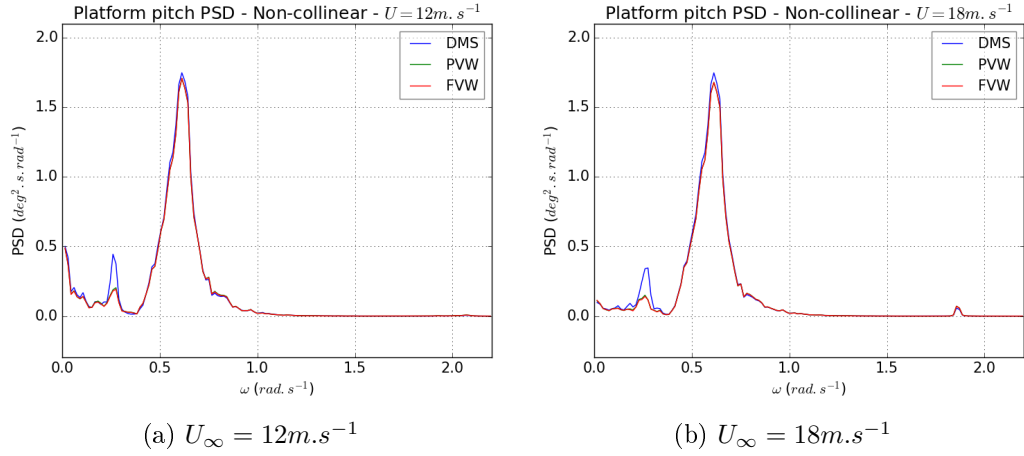
Figure 5.14 – Pitch PSD in non-collinear wind and waves at high TSR (left) and low TSR (right) with $\theta_w = 45^o$

more important oscillations at natural roll frequency, and the roll-yaw coupling is again visible around $0.77 rad.s^{-1}$. At low TSR, the $2p$ frequency peak is also more important.

The pitch PSDs are plotted in figure 5.14. The agreement between the models is poorer than in the collinear waves and wind case, especially at high TSR. The responses at the natural pitch frequency are higher in the DMS model at both TSRs. However, as seen previously, the response at low frequency (surge resonance frequency with excitation from wind turbulence) is in good agreement. In the wave frequency range, the wave loads are dominant and the agreement is very good.

Eventually, mean values and standard deviations in platform roll and pitch are plotted in figure 5.15. The wind mean thrust here induces a tilt composed of the mean platform roll and pitch. As seen in collinear wind and waves, the agreement between mean values and STDs is much better at low TSR. At high TSR, the DMS and the PVW seem to have differences induced by the wake induction and loads on the rotor. These are primarily induced by unsteady phenomena that are only accounted for in the PVW and FVW solvers. In particular, differences between the three solvers can be induced by complex wake dynamics and important tip vortices that can only be accounted or in

(a) $U_\infty = 12m.s^{-1}$ (b) $U_\infty = 18m.s^{-1}$
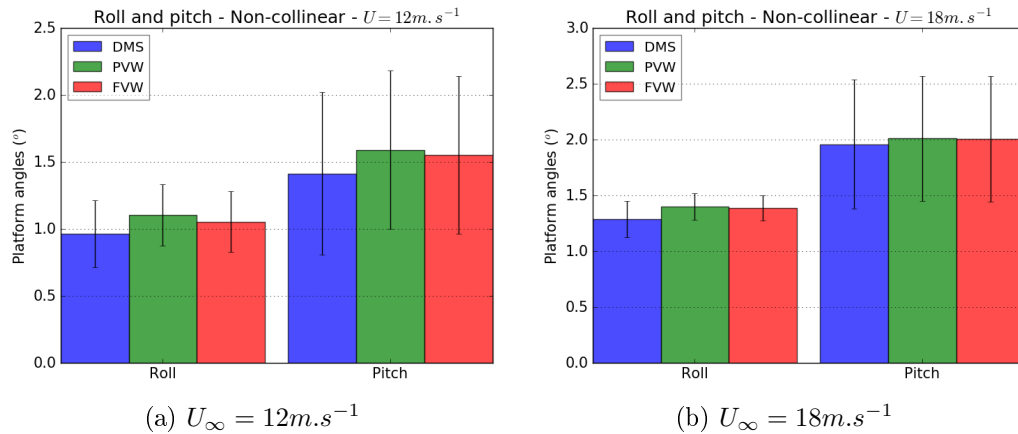
Figure 5.15 – Platform roll and pitch mean values and STDs in non-collinear wind and waves at high TSR (left) and low TSR (right)

the FVW solver. This affects the mean thrust acting on the turbine, and can also alter the dynamic response (i.e. the STDs).

Although pitch motion PSDs have a rather good agreement, mean values and standard deviations may be different from one model to the other. The PSDs describe the frequency distribution of the energy, but do not account neither for mean values nor for combination of several harmonics which depends on their phases.

5.3.5   Local blade loading

Additionally, the local blade loads are considered as they are important for the structural design of the blades. The tangential and normal forces on an equatorial blade element (at 80m height from the waterline) during a rotor revolution at both wind speeds are plotted in figure 5.16 and 5.17 for the case of collinear wind and waves, described in section 5.3.2. One can see large discrepancies between the vortex methods and the DMS at high TSR. At low TSR, the agreement is very good. Differences may come from unsteady aerodynamics that are accounted for in the vortex solvers (inherent dynamic inflow for instance). The little differences observed here between the PVW and the FVW models come essentially from the wake unsteady dynamics that are only accounted for in the FVW.

Differences in the local blade loads could have an impact on the blades response in a flexible turbine numerical model. The impact of the aerodynamic model is here very visible and follow-up studies should account for aero-elastic couplings. Such a study using aero-elastic coupled codes on a VAWT (momentum solvers and FVW solvers) and focusing on two TSRs led to similar conclusions [Blondel et al., 2018]: a good agreement was obtained at low TSR and differences between the solvers were visible at high TSR. In particular, the momentum models tended to over-estimate the blades bending moments at high TSR compared to vortex solvers.

5.4   Conclusion

A VAWT has been studied in several load cases: bottom-fixed, with imposed surge and pitch motions and floating in coupled hydro-aerodynamic simulations. Three aerodynamic models have been compared: a state of the art quasi-steady DMS solver, a PVW

(a) $U_\infty = 12m.s^{-1}$ (b) $U_\infty = 18m.s^{-1}$
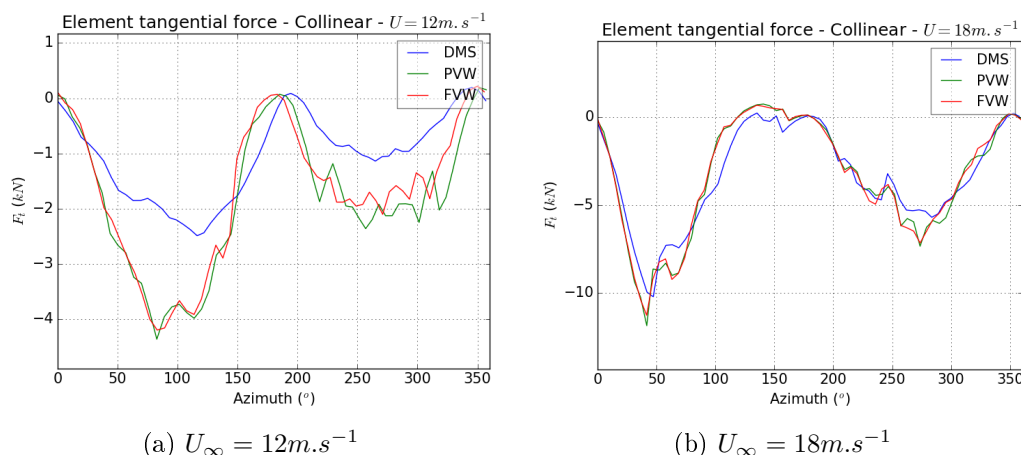
Figure 5.16 – Local tangential loads on a blade element in collinear wind and waves

(a) $U_\infty = 12m.s^{-1}$ (b) $U_\infty = 18m.s^{-1}$
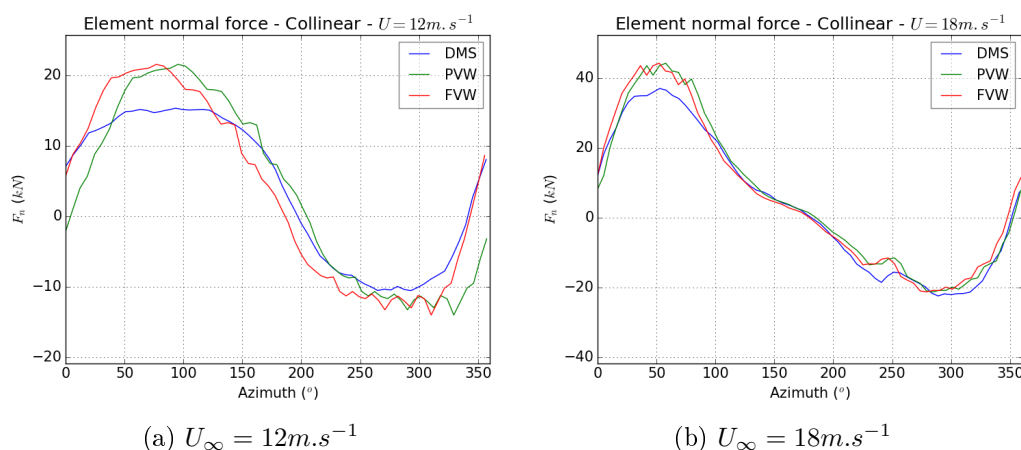
Figure 5.17 – Local normal loads on a blade element in collinear wind and waves

and a FVW solver. The methodology presented here allows for a better understanding of the aerodynamic loads and their impact on the motions of a FWT. Notably, the comparison of the aerodynamic loads on the turbine in imposed motions enables to isolate the damping term of the aerodynamic thrust induced by the turbine's motion. The differences between the damping loadings improve the understanding of the induced differences between the motions of the FWT computed by the three aerodynamic solvers in coupled simulations. However, this methodology ignores the non-linear couplings than can occur between harmonics, and particularly with the oscillation at $2p$ frequency.

The overall agreement between the three solvers in coupled simulations is good. The global behaviour of the floating VAWT is well modelled: resonance peaks are all located at the same frequencies in the motion PSDs and the responses at wave frequencies are very similar.

More precisely, the three codes show a good agreement at low TSR when the rotor is lightly loaded. However, at high TSR, unsteady aerodynamics seems to impact the motion of the turbine, especially at its natural frequencies. The differences are easily observed on the turbine's mean positions and their standard deviations. Differences might come primarily from unsteady phenomena that are inherently accounted for in the FVW model. Lower wind speeds have not been investigated because of too long

calculation times required by the FVW solver.

The fast DMS solver could hence be used in pre-design phases, in which computer efficiency is essential. The FVW solvers would then be too expensive for numerous calculations. Differences can however appear in the resonance peaks amplitudes, which could alter more accurate phases of the design of FWTs. As it has larger responses PSDs than the FVW, the DMS could lead to more conservative designs, which may induce higher costs of structures. Experimental validation would however be needed to state with certainty on the most accurate aerodynamic model to simulate the seakeeping of a floating VAWT.

Differences between the models were particularly observed at high TSR on the local blade loads. Firstly, high frequency damping loads can reduce the response of the turbine at lower frequencies. Secondly, errors on the local blade loads could lead to dramatic issues on the blade design. This aspect hence needs to be further investigated with flexible blades modelling.

Eventually, the impact of the aerodynamic model on the seakeeping of the VAWT needs to be investigated with other types of platforms (semi-submersible, TLP) for which the conclusions may be different.

Chapter 6

Comparison of seakeeping performance: HAWT vs. VAWT

Contents

Figure 6.1 – Artistic view of the Aerogenerator-X FVAWT ©2010 Wind Power Ltd and Grimshaw

6.1 Introduction

Floating Horizontal and Vertical Axis Wind Turbines can have a very different behaviour at sea. It is common to state, as in [Borg and Collu, 2015a] for instance, that floating VAWTs can have a lower centre of gravity and thrust, which enhances their stability and eases the installation and maintenance operations. Wind energy recovered with offshore floating VAWTs could then be cheaper than with HAWTs. However, the oscillating thrust on such turbines strongly increases at high wind speeds without dedicated blade pitch control laws. This could induce large amplitude motions and mooring loads and increase the cost of those structures.

[Borg and Collu, 2015a] presented a comparative study including the NREL 5MW HAWT [Jonkman et al., 2009] and the NOVA VAWT [Shires, 2013], presented in figure 6.1. The latest has an optimised geometry and very low centres of gravity and thrust. The study shows that the inclining moment of the VAWT is much lower than that of the HAWT, resulting in an enhanced stability and a lower cost of the substructure, either SPAR or semi-submersible platform. It is also denoted that the np frequency (n being the number of blades and p the rotational frequency) could alter the motions of the turbine for larger rotors with lower rotational speeds. In this first study, the dynamics of these FWTs is however studied in calm water. [Cheng et al., 2017d] presents a comparative study between the NREL 5MW HAWT and the DeepWind VAWT [Paulsen et al., 2014] supported by a SPAR platform. Here the vertical axis rotor is much taller, the centre of gravity is then higher and the turbine tends to have a lower pitch resonance frequency than the HAWT. Also, the thrust acting on the HAWT decreases at high wind speeds, whereas it strongly increases for the VAWT without an appropriate blade pitch control. This induces very high loads and motions in the VAWT response. With this rotor design, in which the centres of thrust and gravity are higher than with the NOVA rotor, the tower-base bending moment is much higher for the VAWT than for the HAWT at high wind speeds, resulting in higher costs for the turbine's structure.

This chapter presents a new comparison between floating HAWTs and VAWTs with the coupled tools developed in the context of this PhD thesis. It compares the NREL 5MW HAWT to the 5MW DeepWind VAWT based on the DeepCWind semi-

submersible platform defined in Phase II of the OC4 project [Robertson et al., 2014a].
The aim is to compare the two turbine concepts on the same platform in different
environmental conditions, including non-collinear wind and waves. The chapter first
introduces the studied wind turbines and their numerical models. Results are then
discussed, focusing on the motions of the platform and aerodynamic and mooring loads.
Also, a comparison of the power production of the two turbines is done.

It was shown in the chapters 4 and 5 that the quasi-steady aerodynamic model used
to model FWTs could have different results compared to unsteady models such as Free
Vortex Wake at high TSR when unsteady phenomena were substantial. Differences were
observed on the motion PSDs and on the mean motions and their STDs. Although the
quasi-steady models raise questions about their accuracy in unsteady conditions, they
are commonly used for preliminary design processes because they are able to describe
the inherent behaviour of the FWTs with a low CPU cost. The following study is hence
done using:

- *FAST* to study the FHAWT;

- *InWave-DMS* to study the FVAWT.

The study shows that the VAWT suffers from extreme aerodynamic loads in harsh
environmental conditions. The motions of the turbine are then very large which would
increase the cost of the turbine. Also, the side thrust and reaction yaw torque of the
VAWT induce unusual loads in the mooring lines. Eventually, the performance of the
HAWT is higher than that of the VAWT at above-rated wind speeds. Appropriate
blade pitch control would be required for the VAWT in order to keep a rated power
production while mitigating the aerodynamic loads.

This study has been done with the help of Elvire Katramiz, Master Student at Centrale Nantes which I supervised during a 5-months internship.

6.2 Description of the models

6.2.1 Semi-submersible platform and mooring system

The two FWTs are mounted on the DeepCWind semi-submersible platform. It is exhaustively described in [Robertson et al., 2014a]. A scheme of the platform is presented
in figure 6.2. It is composed of three large upper columns ($\phi 12m$) on the periphery
and a thinner main column ($\phi 6.50m$) on which the tower is installed. Heave plates are
installed at the bottom of the three large columns with a diameter $\phi 24m$ and a $6m$
thickness. The total draft is $20m$. All floaters are linked with braces ($\phi 1.60m$).

The water depth is 200m. The mooring system is composed of three identical
catenary lines installed at 120° from each other. Line 2 is in the main wave direction
(x axis) on the incident wave side. The layout is presented in figure 6.3.

Table 6.1 presents the main properties of the platform and mooring system. The
platform mass is slightly adapted for the VAWT in order to keep the same draft (see
section 6.2.2.2). It is chosen to keep the same platform dimensions for the two FWTs
to investigate the direct impact of the rotor concept on the seakeeping.
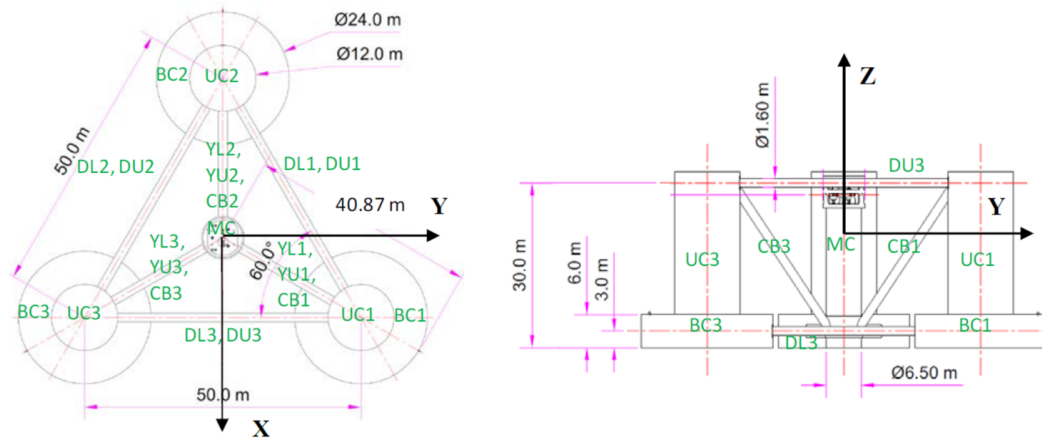
Figure 6.2 – Dimensions of the DeepCWind semi-submersible platform (from [Robertson et al., 2014a])
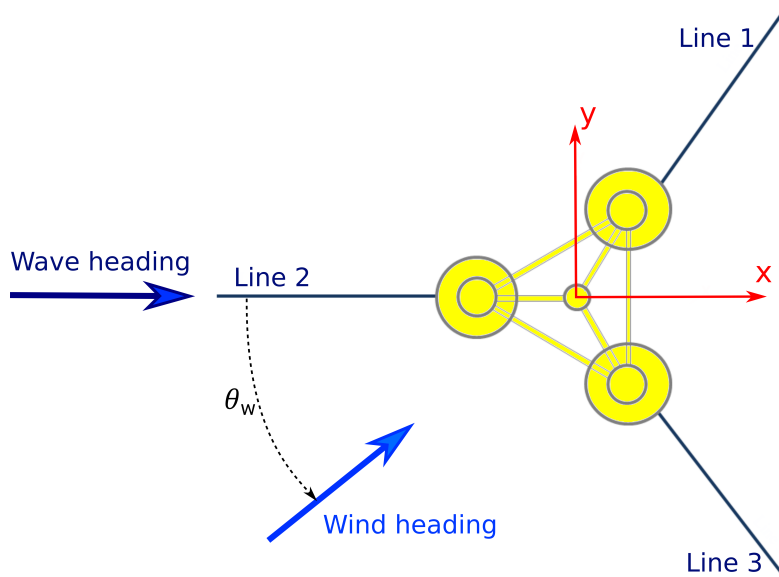
Figure 6.3 – Layout of the DeepCWind semi-submersible mooring system

Table 6.1 – Main properties of the DeepCWind floating platform and mooring system

Water depth	$200m$
Draft	$20m$
Main column diameter	$6.50m$
Upper column diameter	$12m$
Heave plates diameter	$26m$
Total columns height	$26m$
Heave plates height	$6m$
Braces diameter	$1.60m$
Platform mass, including ballast	$13500t$
Platform roll and pitch inertia about CM	$6.83E+09kg.m^2$
Platform yaw inertia about CM	$1.23E+10kg.m^2$
Fairleads depth (below water level)	$-14m$
Radius to anchors from platform centerline	$837.6m$
Radius to fairleads from platform centerline	$40.868m$
Unstretched line length	$835.35m$
Line linear mass in air	$113.35kg.m^{-1}$
Line diameter	$0.0766m$

Table 6.2 – FHAWT properties

Tower mass	$250t$
Nacelle mass	$240t$
Rotor radius	$63m$
Rotor mass	$110t$
Rotor inertia about its rotation axis	$3.89E+07kg.m^2$
Hub height	$90m$
Water clearance	$27m$
Shaft tilt	5°
Rated wind speed	$11.4m.s^{-1}$
Rated rotational speed	$12RPM$

6.2.2 Wind turbines supported by the DeepCWind semi-submersible platform

6.2.2.1 Horizontal Axis Wind Turbine

The HAWT is the reference NREL 5MW turbine described in table 6.2 and studied in chapter 4. The rotor is 3-bladed, 63m radius with a 90m hub height. A screenshot of an *InWave-FVW* simulation of the FHAWT is presented in figure 6.4.

6.2.2.2 Vertical Axis Wind Turbine

The VAWT uses the DeepWind rotor defined in [Vita et al., 2011] and [Paulsen et al., 2014]. The rotor is composed of the blades, tower and shaft. The root-to-root height of the troposkian 2-bladed rotor is 129.56m and its equatorial radius is 63.76m. The blades use a NACA0018 profile. Their polars C_L and C_D are computed with *Xfoil* [Drela, 1989]. The water clearance between the mean water level and the low root of the rotor is 15m. A view of the FVAWT is presented in figure 6.5.
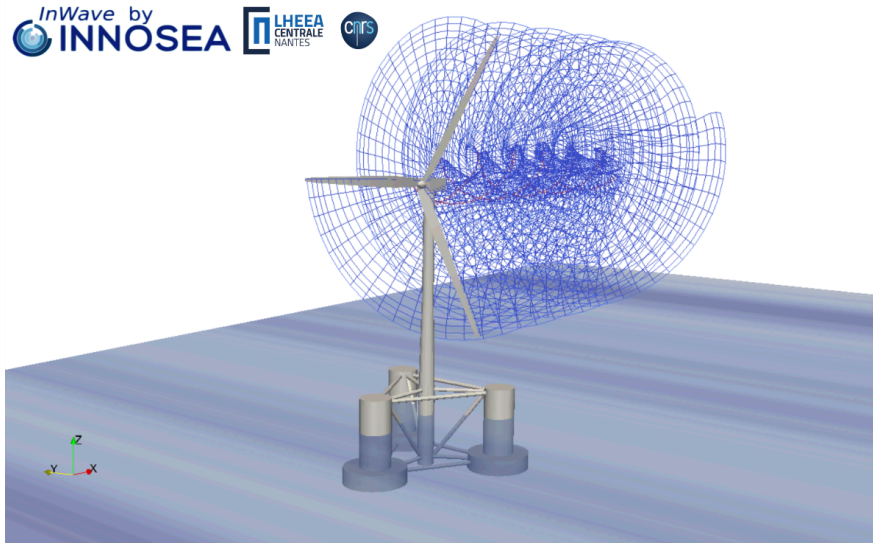
Figure 6.4 – The NREL 5MW HAWT mounted on the DeepCWind semi-submersible platform, simulation screenshot from *InWave-FVW*
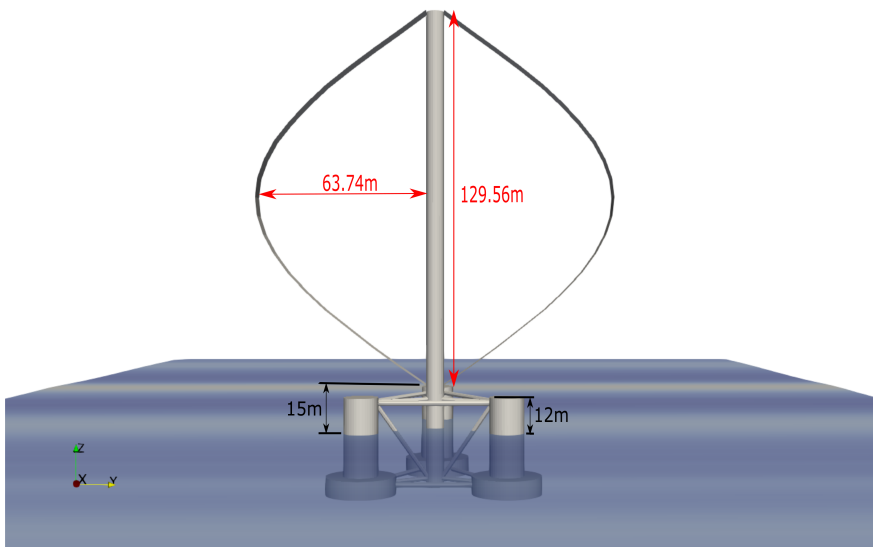
Figure 6.5 – DeepWind rotor mounted on the DeepCWind semi-submersible platform

The tower is a $6.30m$ diameter and $132.56m$ length hollow cylinder with a mass of $410t$ [Vita et al., 2011]. The shaft weights $38.6t$. Its diameter is $30cm$ and its height is $66.28m$. It is integrated inside the tower and there is no gearbox. The direct-driven generator is at the bottom of the tower, in the platform main column.

The ballast mass in the platform is adapted so that the draft of the platform supporting the VAWT is the same as for the HAWT (i.e. 20m). The total mass of the platform and its inertias are hence altered. The main properties of the FVAWT are presented in table 6.3.

Table 6.3 – FVAWT properties

Tower mass	$411t$
Rotor equatorial radius	$63.76m$
Rotor mass (blades + tower + shaft)	$754t$
Rotor inertia about its rotation axis	$5.59E + 08kg.m^2$
Rotor height (root-to-root)	$126.56m$
Water clearance	$15m$
Cut-in, rated, cut-out wind speed	$5, 14, 25m.s^{-1}$
Rated rotational speed	$5.26RPM$
Platform mass, including ballast	$13400t$
Platform roll and pitch inertia about CM	$6.74E + 09kg.m^2$
Platform yaw inertia about CM	$1.21E + 10kg.m^2$

6.2.3 Numerical models

6.2.3.1 Hydrodynamics

In *FAST*: *WAMIT* has been used to compute the hydrodynamic first-order loads used in *FAST*. The hydrodynamic mesh includes both large and slender parts of the platform. A viscous Morison drag force is however added on each part. The drag coefficients are the following (see figure 6.2 for the abbreviations):

- $C_d = 0.68$ for the Base Column BC and the heave plates;

- $C_d = 0.61$ for the Upper Column UC;

- $C_d = 0.56$ for the Main Column MC;

- $C_d = 0.63$ for the braces.

In *InWave*: only the large bodies have been modelled in the hydrodynamic mesh used for linear potential flow calculations run with *Nemoh*. Mesh convergence was performed prior to the simulations. The final mesh contains 2610 panels and is shown in figure 6.6. Viscous drag has also been considered on those large elements using the same drag coefficients as in *FAST*. The slender braces have been fully modelled through Morison equation. Their added mass coefficient C_a and drag coefficient C_d are both equal to 0.63.

Also, additional drag elements are considered on the heave plates in order to obtain the same hydrodynamic damping in heave and pitch as in *FAST*. *InWave*'s present version only computes viscous drag as a radial force on cylinders. Horizontal cylinders are then defined at the bottom of the heave plates, with an equivalent projected surface. Their drag coefficient is set equal to $C_d = 4.0$. The existence of these elements also induces a viscous force when the platform translates in sway or rotates in yaw. It for example has an impact on the yaw decay test as presented later.

An *InWave* model of the FHAWT is implemented. We perform decay tests with this model and compare them to results from *FAST* in order to validate the hydrodynamic model of the platform. Four decay tests (surge, heave, pitch and yaw) are plotted in figure 6.7. The initial positions in surge and heave are respectively $20m$ and $5m$ and the initial pitch and yaw angles are 10°. The agreement is good between *InWave* and *FAST*. The difference in damping is visible on the yaw motion but does not impact the
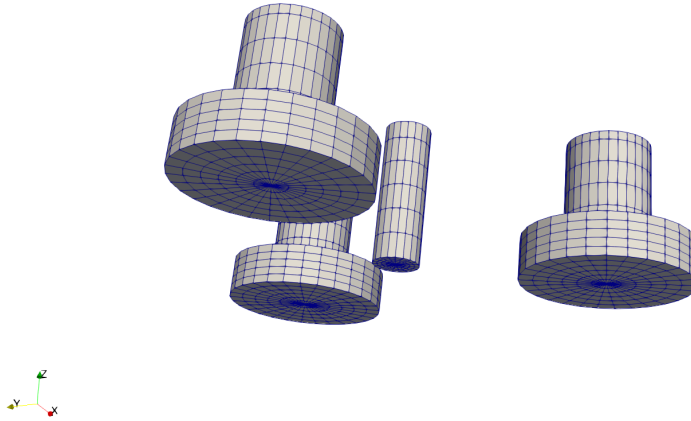
Figure 6.6 – Hydrodynamic mesh used in *Nemoh* for *InWave*'s model

Table 6.4 – Natural periods obtained with *FAST* and *InWave* during the decay tests of the FHAWT

DOF	*FAST*	*InWave*
Surge	$111.6s$	$112.1s$
Heave	$17.3s$	$16.8s$
Pitch	$25.5s$	$24.9s$
Yaw	$79.2s$	$80.3s$

other degrees of freedom. Natural periods show a good agreement and are given in table 6.4.

6.2.3.2   Aerodynamics

On the one hand, *FAST* uses the Blade Element Momentum theory to compute the aerodynamic forces acting on the HAWT, as presented in chapter 4. On the other hand, The DMS solver of *InWave* is used to compute the aerodynamics loads acting on the VAWT. Leishman-Beddoes dynamic stall model is used in both solvers.

Convergence of the aerodynamic models is ensured, following the methodology presented in section 4.2.2 (chapter 4).

6.2.3.3   Moorings

The moorings loads are calculated with the quasi-static mooring solver *MAP++* in both *FAST* and *InWave*.

6.2.3.4   Control

The control algorithm dedicated to the NREL 5MW [Jonkman et al., 2009] is used in *FAST*. This algorithm controls the generator torque and the blade pitch angle at over-rated wind speeds.

For the VAWT, the control algorithm presented in section 3.7.2 (chapter 3) and implemented in *InWave* is used. It only controls the generator torque. The blade pitch

(a) Surge decay test

(b) Heave decay test

(c) Pitch decay test
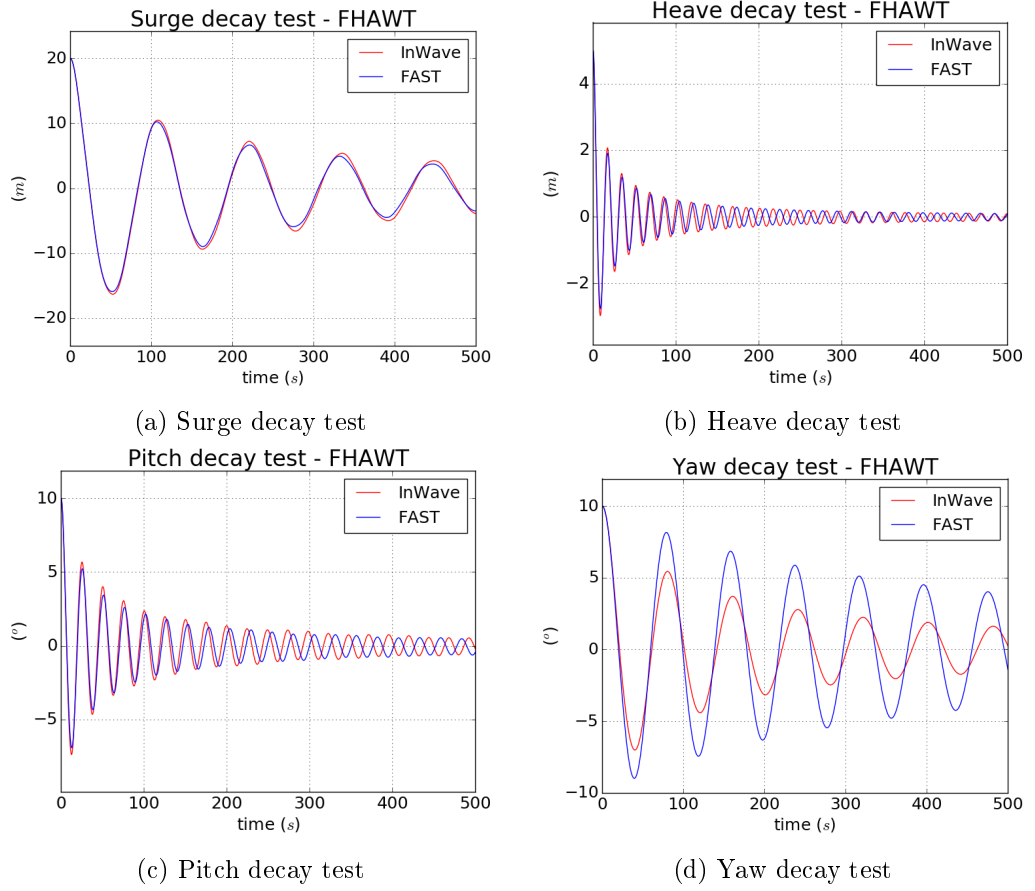
(d) Yaw decay test

Figure 6.7 – Decay tests performed with *InWave* and *FAST* on the FHAWT's model

angle stays constant (the chord is perpendicular to the rotor radius). The over-rated control law $\omega = f(U_\infty)$ is determined from the DeepWind rotor power curve.

6.2.4 Environmental conditions – Load cases

A set of realistic Dynamic Load Cases (DLCs) has been used in [Cheng et al., 2017d] for a SPAR-supported HAWT versus VAWT comparison. The same sea-states are considered in this study. They are presented in table 6.5. The sea states are generated using a JONSWAP spectrum with a $\gamma = 3.3$ peakness factor. The same free-surface elevation time series are used in both models, *FAST* and *InWave*.

The waves propagate along the x-axis but we consider several wind directions. The wind headings are (see figure 6.3 for orientation):

- $\theta_{w_1} = 0^o$ (aligned with the waves);

- $\theta_{w_2} = 30^o$;

- $\theta_{w_3} = 60^o$;

- $\theta_{w_4} = 90^o$ (along the y-axis).

The turbulent wind fields are the same for the two turbines. They are generated with *TurbSim* [Jonkman, 2009] using a Kaimal spectrum and a class C turbulence.

Table 6.5 – Dynamic load cases

	U_∞ $(m.s^{-1})$	H_s (m)	T_p (s)
DLC1	5	2.1	9.74
DLC2	10	2.88	9.98
DLC3	14	3.62	10.29
DLC4	18	4.44	10.66
DLC5	22	5.32	11.06
DLC6	25	6.02	11.38
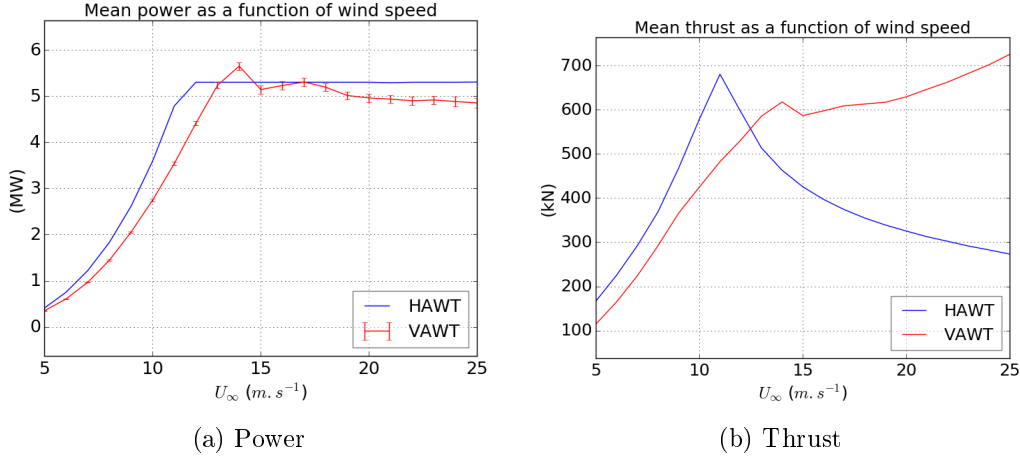
(a) Power   (b) Thrust

Figure 6.8 – Thrust and power comparison of the two turbines

The reference height for the wind speed measurement is $90m$ and the wind profile is calculated with a power law. The time steps are $0.1s$ in *InWave* and $0.0125s$ in *FAST*.

In the following, "$DLCi.j$" refers to DLC number i with the wind heading number j.

6.3 Results and discussion

6.3.1 Bottom-fixed wind turbines

The power and aerodynamic thrust on the bottom-fixed HAWT and VAWT are plotted in figure 6.8 for wind speeds from 5 to $25m.s^{-1}$. The STD of the generated power is also plotted for the VAWT. It is very small and demonstrates the efficiency of the control algorithm that filters the $2p$ frequency from the generator torque.

The generated power for low wind speeds ($U_\infty < 11.4m.s^{-1}$) is higher for the HAWT than for the VAWT as its optimal power coefficient is higher (see chapters 4 and 5). The control algorithm used for the VAWT is apparently less accurate at the rated wind speed ($U_\infty = 14m.s^{-1}$), as an over-rated power is observed. A more accurate tuning of the PID controller should be investigated but has not been studied in this PhD thesis. For over-rated wind speeds, the power is closer to the rated $5MW$.

The aerodynamic thrust on the VAWT is lower than on the HAWT for wind speeds below $12.5m.s^{-1}$. From $U_\infty = 11.4m.s^{-1}$, the blade pitch control of the HAWT is active which decreases the thrust while maintaining the rated output power. However, the thrust on the VAWT keeps increasing at over-rated wind speeds. For example, the thrust on the VAWT is twice as large as for the HAWT at $U_\infty = 20m.s^{-1}$.

(a) Surge decay test

(b) Heave decay test

(c) Pitch decay test
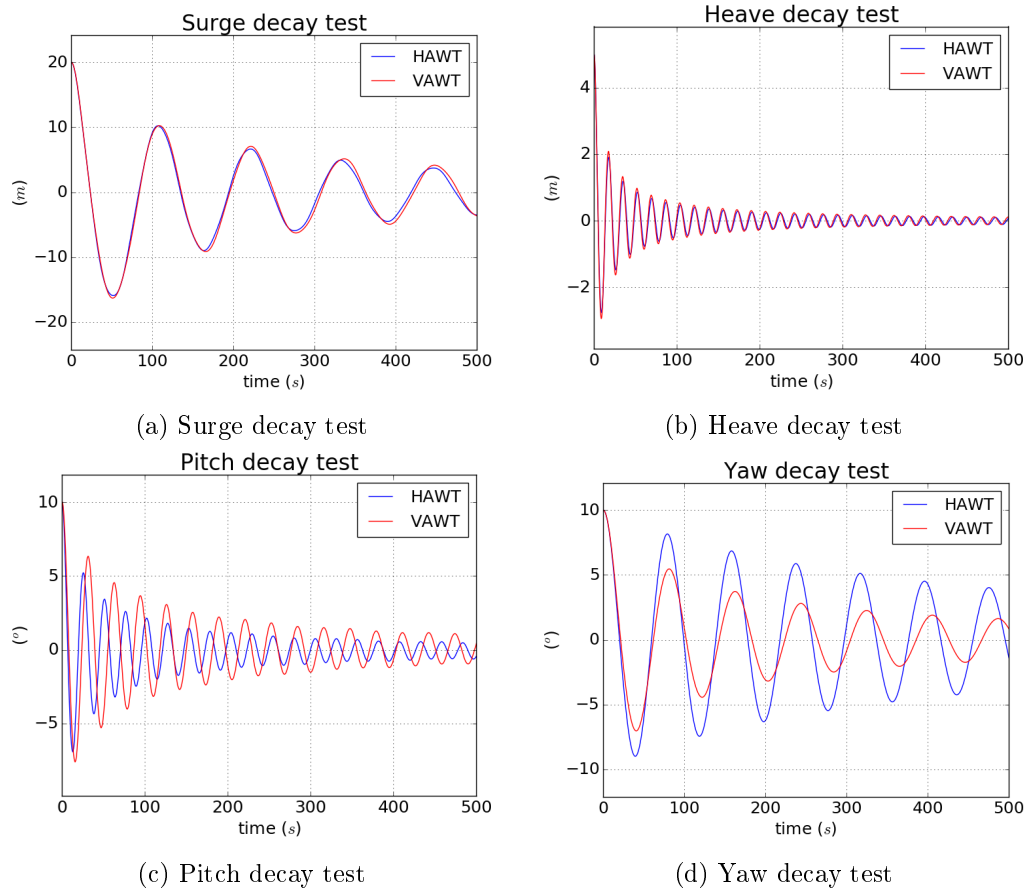
(d) Yaw decay test

Figure 6.9 – Decay tests of the floating HAWT and VAWT

Table 6.6 – Resonance periods of the FWTs

Degree of freedom	HAWT	VAWT
Surge	$111.6s$	$111.9s$
Heave	$17.3s$	$17.2s$
Pitch	$25.5s$	$31.6s$
Yaw	$79.2s$	$81.1s$

6.3.2 Floating wind turbines: Decay tests

Decay tests are performed in still water with the two FWTs. The rotation of the rotor is blocked during simulations and there is no aerodynamic forces. They are plotted in figure 6.9. Four degrees of freedom are investigated: surge, heave, pitch and yaw with the same initial positions as in section 6.2.3.1.

One can see that the large rotor of the VAWT induces larger natural periods in pitch and yaw than that of the HAWT. The important inertia of the rotor of the VAWT implies longer and larger oscillations. However, the natural periods in surge and heave are very similar between the two turbines. The important damping of the VAWT in yaw mostly comes from the hydrodynamic model used in *InWave*.
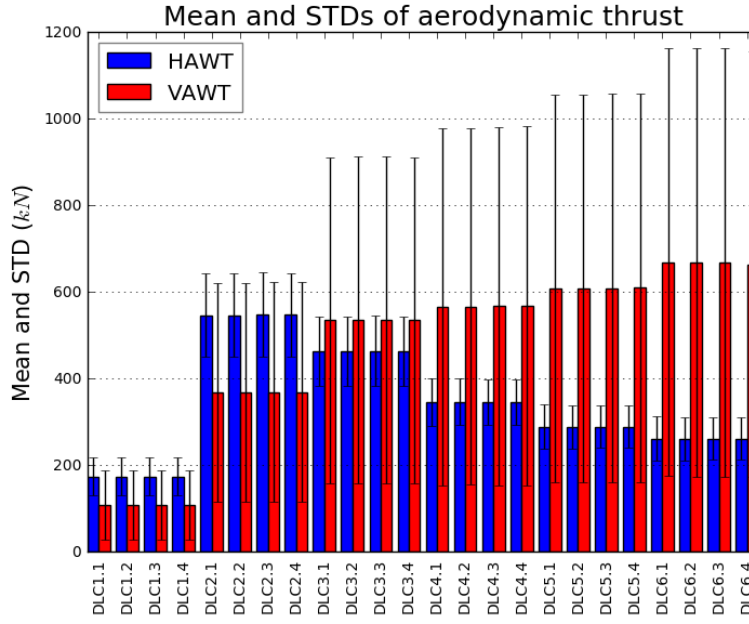
Figure 6.10 – Mean and STDs of the aerodynamic thrust in the wind direction

6.3.3 Coupled simulations

Simulations are run for 3600s with *FAST* for the HAWT and *InWave-DMS* for the VAWT. The first 1800s are removed in the analysis to avoid any transient effects.

6.3.3.1 Aerodynamic loads

The mean values and STDs of the aerodynamic thrust (in the wind direction) are plotted for all DLCs in figure 6.10. The DLC intensity increases from the left to the right and the wind orientation changes in each column. The shape of the bottom-fixed thrust curve presented in section 6.3.1 is recognised. The aerodynamic thrust follows the wind heading, and the wind-wave misalignment does not alter significantly the thrust amplitude. The impact of the platform motion on the aerodynamic loads is not predominant and only slightly alters the STDs. The thrust on the VAWT is as expected highly oscillating, and increasing up to more than $600kN$ at $U_\infty = 25m.s^{-1}$.

The thrust is also studied in time domain. A diagram representing the thrust vector on the VAWT in DLC6.1 in the xOy plane for 200s is plotted in figure 6.11. The side force F_y is plotted as a function of the wind-wise force F_x. The thrust force rotates counter-clockwise with time. The vector amplitude varies at each rotation because of the wind turbulence and turbine motions. The direction of the mean force is also plotted in black. It is not aligned with the wind but skewed with a -21° angle with respect to the wind direction. This angle is not the same in each DLC, it can vary with the TSR.

6.3.3.2 Platform motions

The platform motions computed in each DLC are processed and compared in this part. In each simulation and regardless of the wind direction, the surge motion is the translation along the x-axis, which is the wave propagation direction. Following the same convention, the pitch motion is the rotation about the y-axis.
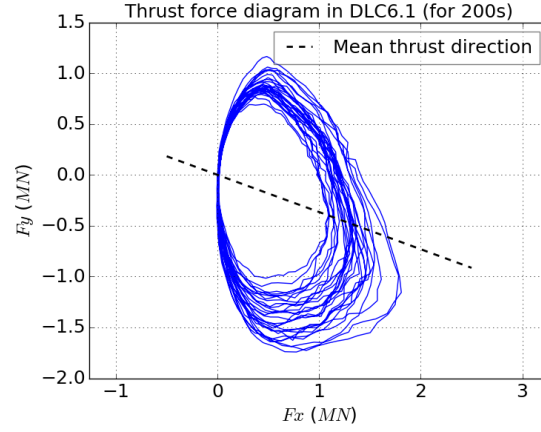
Figure 6.11 – Horizontal thrust force diagram on the VAWT in DLC6.1

(a) Mean surge and STD

(b) Mean pitch and STD
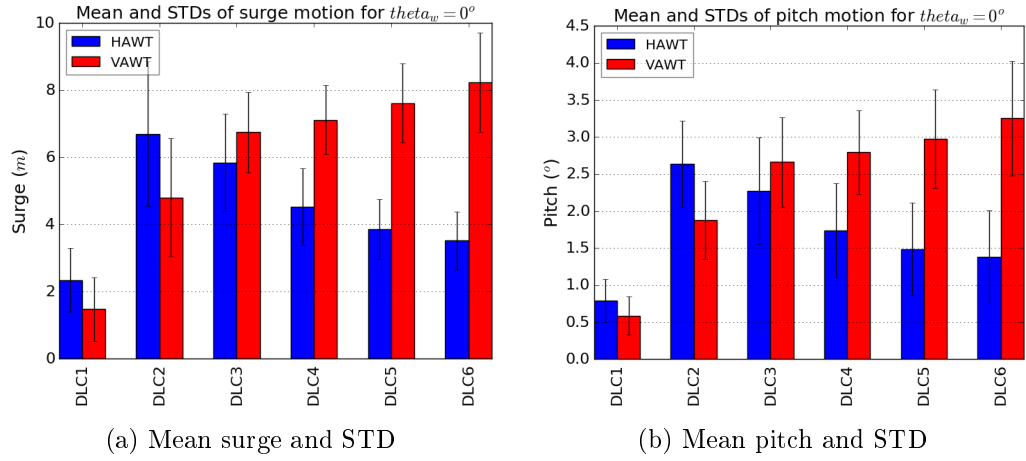
Figure 6.12 – Mean value and STD of platform motions in collinear wind and waves

First, the mean positions, standard deviation and maximum displacements are presented. For now, wind and waves are collinear ($\theta_w = 0^o$), and the mean surge and pitch motions are respectively presented in figure 6.12. The maximum displacements in surge and pitch are also presented in figure 6.13. The shape of the thrust curves in figure 6.8b are clearly recognised. At low wind speeds, the thrust acting on the HAWT is larger than on the VAWT which induces larger platform motions (mean values and STDs). The mean pitch of the HAWT is at its highest (2.6^o) at DLC2 ($U_\infty = 10 m.s^{-1}$). At over-rated wind speeds (DLCs higher than 2), the thrust on the HAWT decreases thanks to blade pitch control, and so do the surge and pitch. However the thrust on the VAWT keeps increasing at over-rated wind speeds which induces larger surge and pitch motions. In DLC6, the mean pitch of the VAWT is above 3° and the maximum reaches 5.7^o. The surge also increases: the mean surge of the VAWT reaches $8m$ with a $14m$ maximum excursion. This large excursion can be critical for the mooring system continuation. The STDs follow the same trend at over-rated wind speeds: they tend to decrease for the HAWT and increase for the VAWT.

If the wind direction varies, the motions of the turbines are impacted. As it could be instinctively thought, the pitch motion of the HAWT decreases and the roll increases when θ_w increases (see figure 6.3 for wind orientation). However, the VAWT has larger surge and pitch motions when $\theta_w = 30^o$. This is due to the skewed mean thrust force

(a) Maximum surge
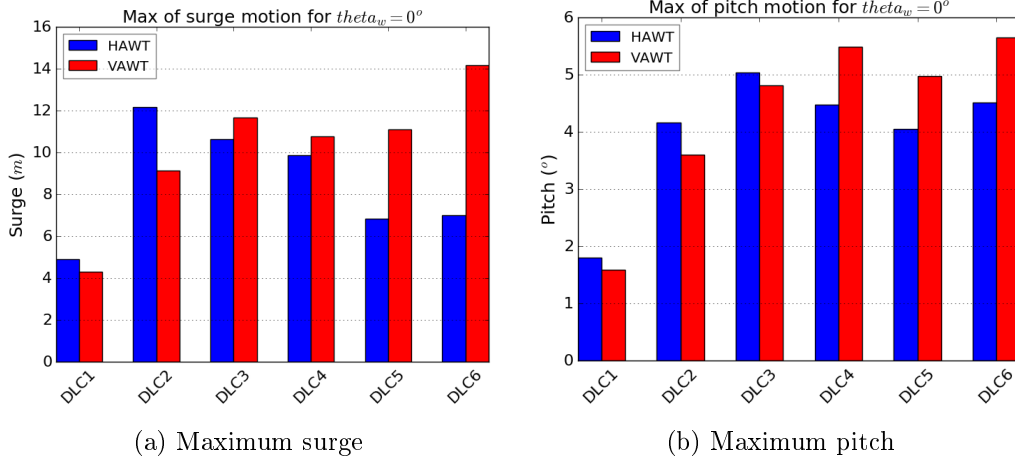
(b) Maximum pitch

Figure 6.13 – Maximum platform motions in collinear wind and waves

(a) Mean pitch
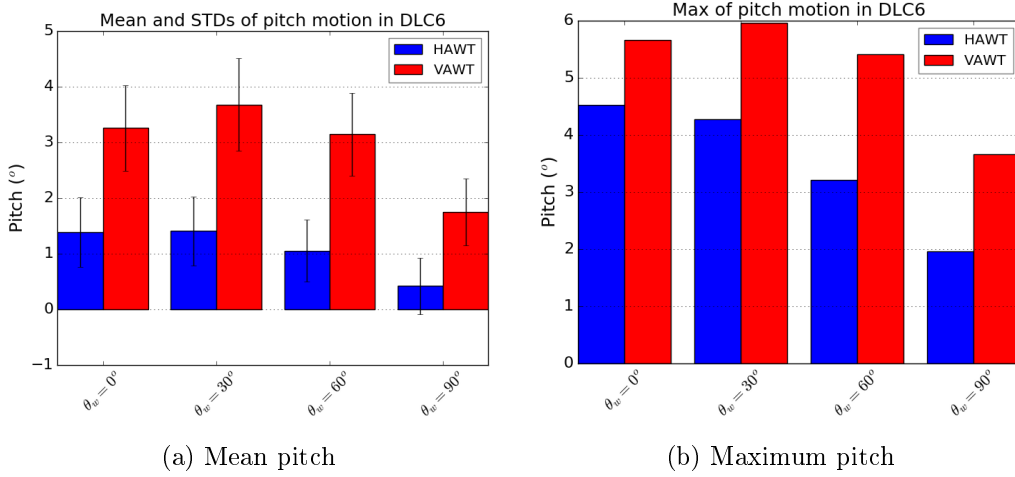
(b) Maximum pitch

Figure 6.14 – Platform motions in DLC6 as a function of wind and wave misalignment

acting on the VAWT with respect to the wind direction. For example, the mean pitch, standard deviation and maximum values obtained in DLC6 with various wind directions are plotted in figure 6.14. At DLC6.2, the maximum pitch of the VAWT reaches the value of 6° and the maximum surge is $14.7m$. The maximum pitch of the HAWT is 5° at DLC3.1 (see figure 6.13b). The maximum pitch is a critical design criterion for FWTs as it induces a large tower base bending moment, partly because of the weight and inertia of the superstructure (discussed in section 6.3.3.5).

Motion time-series are also processed into PSDs. The transient regime is ignored in the analysis. The pitch PSDs obtained in DLC2.1 and DLC5.1 (collinear wind and waves) are plotted in figure 6.15. The larger thrust acting on the HAWT at DLC2.1 induces larger low-frequency oscillations ($\omega < 0.3rad.s^{-1}$). The response at wave frequency ($\omega \in [0.4, 1.0]rad.s^{-1}$) is also higher for the HAWT. In DLC5.1, important response of the VAWT is observed at low frequencies, it is induced by the larger aerodynamic thrust. Also, the 2p frequency motion is visible at $\omega = 0.92rad.s^{-1}$. It is induced by the thrust oscillation at this frequency.

One intrinsic particularity of the VAWT is the generator reaction torque, which induces a yaw motion of the platform. The yaw of the turbines has been studied and is

(a) DLC2.1   (b) DLC5.1
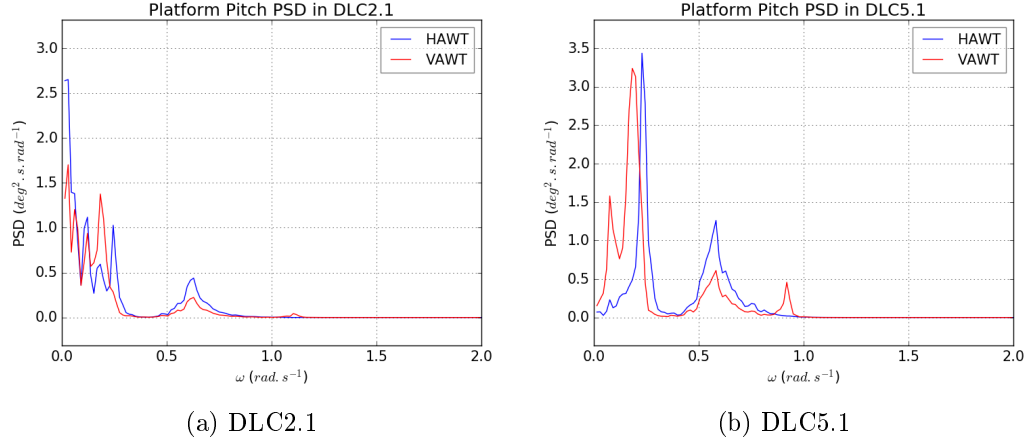
Figure 6.15 – Platform pitch PSDs in collinear wind and waves

(a) Mean yaw and STD in collinear wind and waves   (b) Maximum pitch
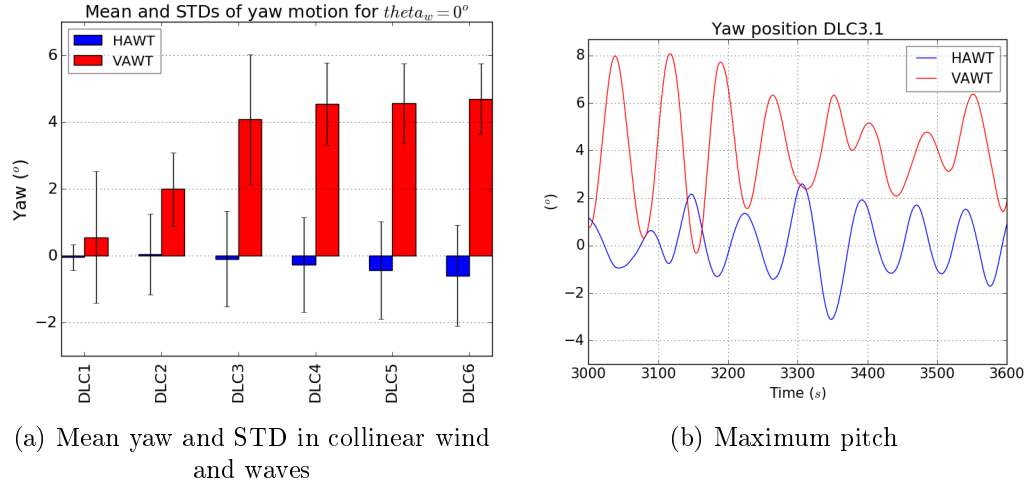
Figure 6.16 – Platform yaw motions in DLC3.1

plotted for each DLC in figure 6.16a (in collinear wind and waves). The wind heading does not significantly impact the yaw motion of the two turbines. An example of platform yaw time-series obtained in DLC3.1, with the largest yaw STD for the VAWT, is also plotted in 6.16b. A large offset is observed for the VAWT. At above-rated wind speeds, the mean yaw reaches 4.5^o. The maximum yaw of the VAWT is observed in DLC3.1 at 8.1^o.

The yaw motion of the HAWT can come from both DOF couplings and wind turbulence. The present model uses a collective blade pitch control. An individual blade pitch control could correct the asymmetric thrust on the rotor caused by turbulent wind. The yaw of the VAWT comes mostly from the reaction torque of the generator. It is also observed that the implemented control algorithm efficiently filters the 2p frequency of the aerodynamic torque: no 2p frequency harmonic is observed on the yaw time-series or PSDs.

6.3.3.3   Platform excursion

The mean surge and sway and their STDs are presented in the horizontal plane in figure 6.17. DLCs 1, 3 and 6 are plotted, with collinear wind and waves. The equilibrium
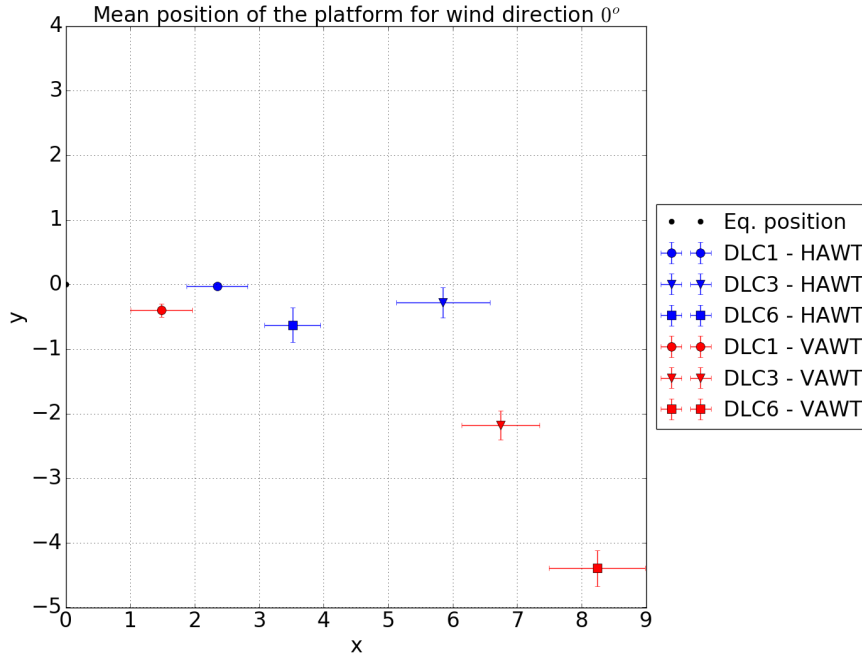
Figure 6.17 – Platform position in the horizontal plane in collinear wind and waves

position obtained without wind or waves is represented in $(0, 0)$. The drift is induced by the aerodynamic thrust and by the hydrodynamic Morison drag loads on the platform only.

The HAWT excursion occurs in the wind and waves direction. It is at its furthest position at DLC3 and then comes back towards its equilibrium position as the aerodynamic thrust decreases. A small offset is observed in the y direction. It might be induced by couplings between degrees of freedom as the rotor torque induces a roll motion to the platform. However, the VAWT excursion is skewed and keeps increasing with the DLC intensity.

For instance, the static position of the VAWT in DLC6.1 is $(x = 8.8, y = -4.4)$. The direction of the excursion from the equilibrium position then has an angle of about -28° with respect to the wind direction. Section 6.3.3.1 emphasized the skewed mean thrust on the VAWT. The measured skew angle was -21°.

At the equilibrium position, the mooring stiffness is the same on both x and y axes. In *FAST* and *InWave*, the mooring tensions are computed with a non-linear quasi-static mooring solver. The mooring stiffness thus changes when the platform moves. Given the mooring layout presented in figure 6.3, the mooring lines 1 and 3 become slack when the turbine is pushed in the x direction. This increases the stiffness in surge and decreases the stiffness in sway. The mean position in sway is reached when mooring restoring force equals the mean aerodynamic side force. A large sway is then induced to the VAWT by its aerodynamic side thrust, especially at high wind speeds.

6.3.3.4 Mooring loads

The tensions at the mooring lines fairleads are first studied in collinear wind and waves. The mooring model used in both models is quasi-static.

The time series of the tensions obtained in DLC3.1 are plotted in figure 6.18. This DLC leads to the maximum excursion of the HAWT, inducing a large mean tension
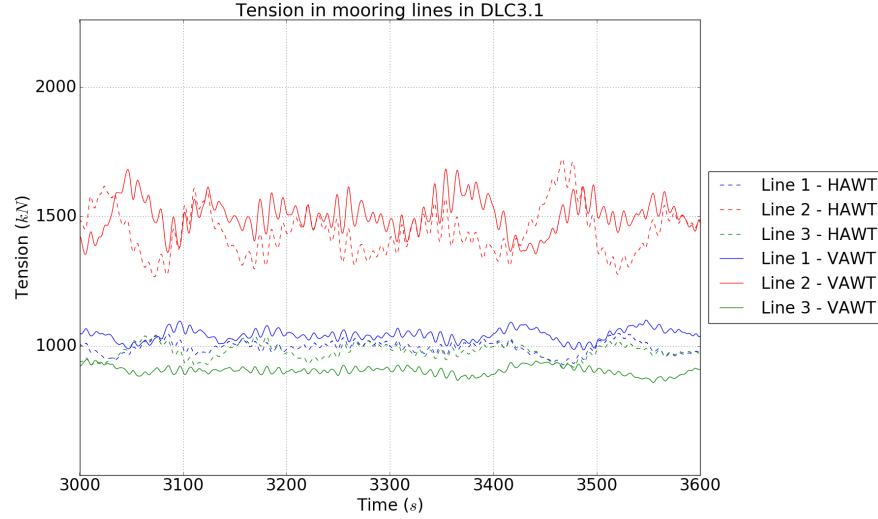
Figure 6.18 – Mooring tensions at fairleads time-series in DLC3.1
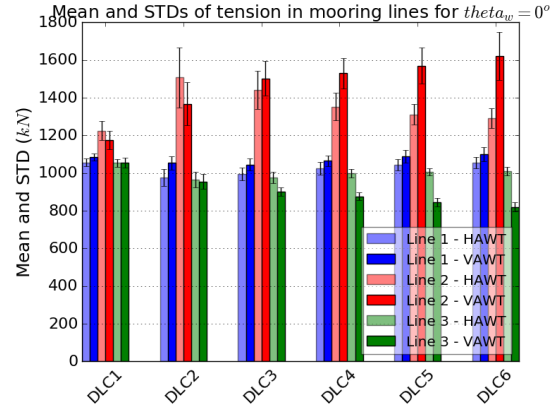
Figure 6.19 – Mooring tensions at fairleads in all DLCs with collinear wind and waves

difference between line 2 and lines 1 and 3 (see figure 6.3 for mooring layout). A phase shift is also observed between the tensions as a positive surge motion of the platform increases the tension in line 2 while reducing the tension in lines 1 and 3. For the HAWT, lines 1 and 3 experience the same tension, while line 1 is more loaded with the VAWT because of the sway offset and the positive yaw of the platform.

The mean tensions and STDs are plotted for each DLC in collinear wind and waves in figure 6.19. When looking at the tensions in line 2 for both the HAWT and the VAWT, one can see the same shape as the thrust curve previously studied. The mean tension in the line 2 of the VAWT is increasing until DLC6.1, reaching $1.6MN$, whereas the maximum mean tension for the HAWT is reached in DLC3.1 ($1.5MN$). For the HAWT, the difference between the tensions in lines 1 and 3 gets very large at severe DLCs (respectively $1300kN$ and $800kN$ in DLC6.1. The tension STD in line 2 follows the same trend: it is maximum in DLC3 for the HAWT and increases with DLC severity for the VAWT.

The mean tensions and STDs obtained in DLC3 with non-collinear wind and waves are plotted in figure 6.20. When the wind direction changes, the aerodynamic thrust rotates. The turbines excursions follow the wind orientation and the tensions in mooring lines 1 and 2 decrease and increase in line 3, on the wind inflow side. The mean tension
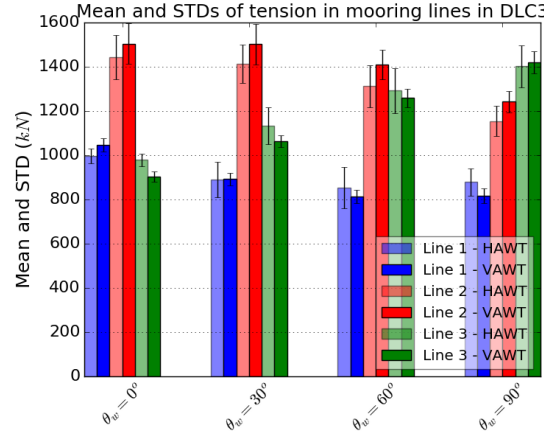
Figure 6.20 – Mooring tensions at fairleads in DLC3 for non-collinear wind and waves

(a) $\theta_w = 0^o$

(b) $\theta_w = 30^o$
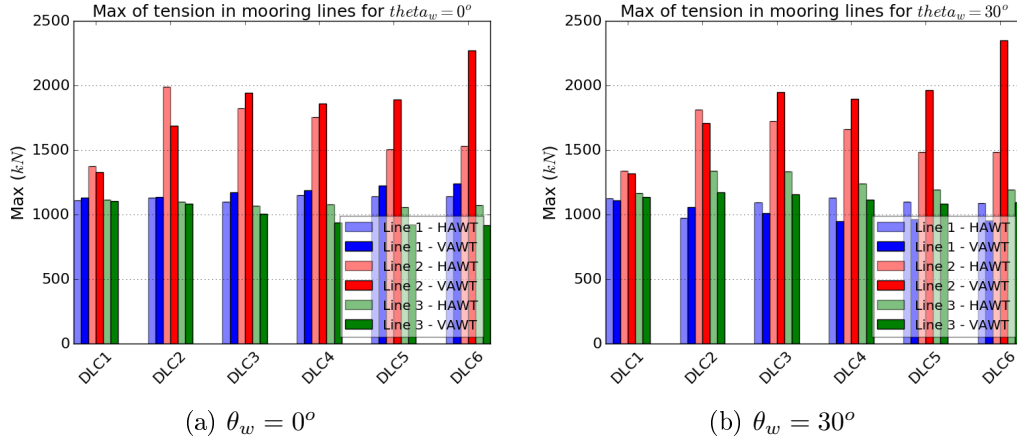
Figure 6.21 – Maximum mooring tensions in all DLCs for 2 wind headings

in line 2 of the VAWT reaches its maximum value when $\theta_w = 30^o$ because of the skewed aerodynamic thrust presented previously.

Finally, the maximum tensions in mooring lines are plotted for all DLCs with $\theta_w = 0^o$ and 30°. The former wind direction is the most critical for the HAWT and the latest is critical for the VAWT. In both cases, the VAWT mooring line 2 experiences larger extreme tension with $2.35 MN$ maximum tension in DLC6.2. The maximum tension in line 2 of the HAWT is $2MN$, obtained in DLC2.1.

It is important to mention that the mooring system was designed specifically for the floating HAWT, and used as it is for the VAWT.

Quasi-static mooring models can be accurate for mean tensions but errors might appear on the dynamic loads. A similar study should be done with a dynamic mooring solver to compute the dynamic and peak loads in the mooring lines more accurately.

6.3.3.5 Tower base bending moment

The tower base bending moment is a key design criterion for FWTs as the transition piece fixing the turbine tower to the platform can experience very large loads. In this study, the tower base loads torsor has been calculated as presented in section 4.3.5.1 of chapter 4.

(a) Mean values and STDs   (b) Maximum values
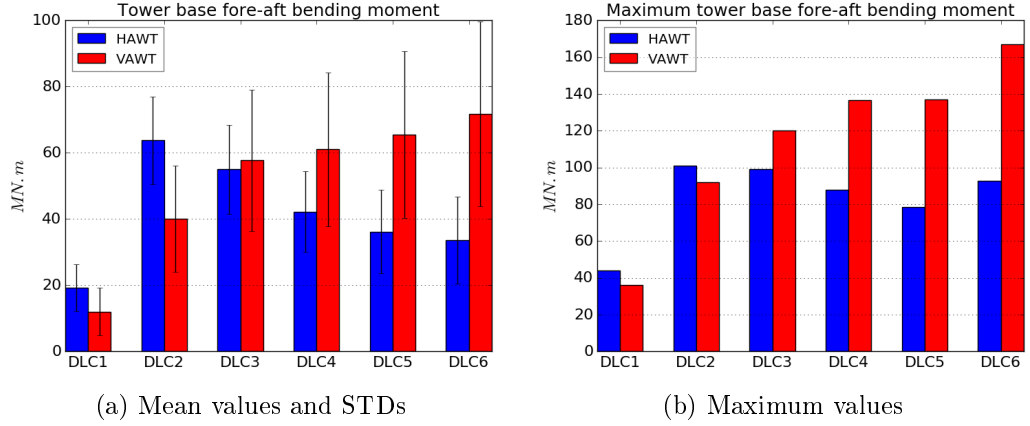
Figure 6.22 – Tower base bending moment in collinear wind and waves

For the HAWT, the centre of gravity of the top-side $\{rotor + nacelle + tower\}$ is higher than for the VAWT ($67.6m$ from the tower base for the HAWT and 63.9 for the VAWT), but the mass of the VAWT's $\{tower + rotor\}$ is higher.

The fore-aft tower base bending moment is computed for each DLC with collinear wind and waves. The mean values, STDs and the maximum values of the bending moment are plotted in figure 6.22.

The mean fore-aft tower base bending moment is maximum for the HAWT in DLC2, where it almost reaches $65MN.m$. The aerodynamic thrust is here maximal, the motions are important and the tilt angle of the platform reaches its maximum. At low wind speeds, the mean bending moment on the VAWT is much lower but the STDs are larger. Similar maximum values are hence reached with both turbines. At over-rated wind speeds however, the bending moment of the HAWT is slightly decreasing while highly increasing for the VAWT. The STDs get very large (twice as much for the VAWT than for the HAWT at DLC6) and the maximum value almost reaches $170MN.m$ in DLC6.

This analysis should be also done with flexible bodies, which could alter the bending moment.

These observations follow the comparison of the same rotors based on a SPAR platform and presented in [Cheng et al., 2017d].

6.3.3.6   Performances of the FWTs

Finally, the power production of the two turbines is studied. Only the DLCs with collinear wind and waves are here studied. The power curves of the floating wind turbines are plotted in figure 6.23. The bottom-fixed turbines power is also plotted for comparison. As studied in chapter 4, the controller of the HAWT allows to keep a fairly constant rated power at over rated wind speeds, equal to that of the bottom-fixed turbine. At below-rated wind speeds, the mean power is slightly lower with the FWTs. Larger differences can be observed with the VAWT and it generates less power. An improved generator control module could perhaps improve its performances. Also, the standard deviation is much larger for the VAWT. This is also partly due to the large motions of the VAWT at high wind speeds. The floating HAWT is always more productive than the VAWT.

Here, it is proposed to study the efficiency of the two turbine concepts. We chose to evaluate the ratio between the power coefficient and the thrust coefficient:
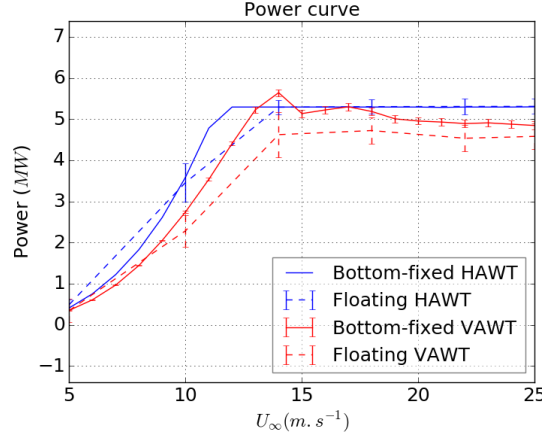
Figure 6.23 – Power curves of the Floating Wind Turbines
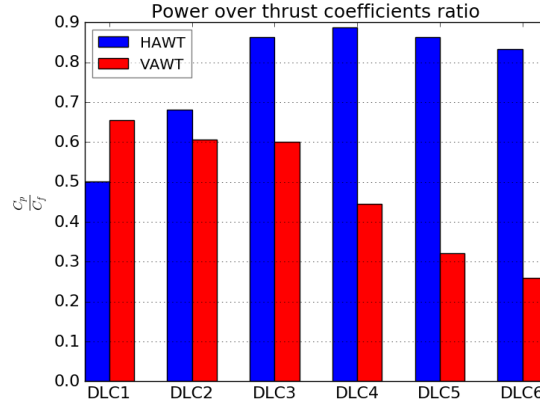
Figure 6.24 – C_P over C_F ratio, in collinear wind and waves

$$\xi = \frac{C_P}{C_F} \tag{6.1}$$

The power coefficient C_P represents the energy captured by the turbine, it is the gain of the system. Whereas the thrust relates to a cost as it dimensions the turbine (along with other types of loadings). This ratio ξ is plotted for collinear wind and waves in figure 6.24. The difference between the HAWT and the VAWT is large. At low wind speeds ($U_\infty = 5m.s^{-1}$), the ratio is higher for the VAWT. For all other DLCs, the HAWT is more efficient. The efficiency of the VAWTs decreases at high wind speeds, until the HAWT's efficiency is three times higher in DLC6.

6.4   Conclusion

Two Floating Wind Turbine concepts have been studied and compared in this chapter. A 5MW troposkian VAWT supported on a semi-submersible platform has been compared to a reference floating HAWT based on the same platform. *FAST* was used to model the HAWT and *InWave-DMS* was used for the VAWT. Free Vortex Wake simulations could not be run because of too high CPU costs. Previous studies presented in chapters 4 and 5 however showed that these quasi-steady aerodynamic solvers could describe the motions of FWTs with a sufficiently good accuracy for such a comparative study.

Complex sea states were used, including several levels of severity and of wind headings. The aerodynamic loads acting on the bottom-fixed turbines were studied and then used to analyse the motions and loads on the floating wind turbines.

Without blade pitch control for the VAWT, the aerodynamic thrust keeps increasing at high wind speeds, inducing very large loads on the turbine. For the HAWT, the control of the rotor drastically reduces the aerodynamic thrust while maintaining the rated power at over-rated wind speeds. Also, the mean thrust on the VAWT is skewed with respect to the wind heading.

The following conclusions can in particular be emphasized:

- At low wind speeds, the HAWT is more efficient thanks to a higher optimal power coefficient;

- The large thrust on the VAWT at high wind speeds induces very large platform motions in surge and pitch, leading to tilt angles above 5°. It also leads to large excursion of the turbine. Very high peak mooring tensions where then calculated with the VAWT;

- The skewed thrust on the VAWT implies a skewed excursion and asymmetric mooring line tensions which need to be accounted for in mooring design;

- The reaction torque of the generator induces a yaw motion to the VAWT's platform reaching a 4° mean yaw and more than 8° maximum yaw angle;

- The tower base bending moment on the VAWT is also very important and highly oscillating partly because of the 2P frequency in the aerodynamic thrust.

It is also important to mention that the platform, used as support structure for the two turbine concepts, was originally design for the HAWT. A VAWT optimised platform could diminish the motions, but this floater would be larger than that of the HAWT because of the large inclining moment.

This VAWT rotor design has a high center of gravity because of its massive tower. The centre of thrust is also high, and this increases the bending moment on the tower base. A comparison of the same rotors based on SPAR platform presented in [Cheng et al., 2017d] leads to the same conclusions. Another rotor design could have lower centres of gravity and thrust, lowering the inclining moment and loads. For example, different conclusions are obtained with H-shaped rotors [Cheng et al., 2017a], or the NOVA rotor presented in the introduction [Borg and Collu, 2015a].

From this study, it appears essential to develop new control strategies for such floating VAWTs in order to decrease the aerodynamic thrust at over-rated wind speeds. Blade pitch control laws should be investigated to improve the efficiency of the VAWTs. For troposkian rotors, the design of the actuators aimed at pitching the blades can be problematic, but jets could alternatively be used to control the lift and drag on the blades.

Chapter 7

Conclusion and perspectives

Contents

This PhD thesis addresses the numerical simulation of the seakeeping of both floating Horizontal and Vertical Axis Wind Turbines. It focuses on the dynamics of such systems in complex and realistic sea states and on the aerodynamic modelling, comparing quasi-steady with unsteady models. Time domain calculations have been completed with a coupled hydro-servo-aerodynamic solver and analysed. A comparison between floating HAWTs and VAWTs is finally done. This last chapter presents the conclusions of this work with recommendations for future works in this field.

7.1 Conclusions

Several questions have been addressed in this PhD thesis. The main contributions can be emphasized as follows.

Coupling between a seakeeping solver and an unsteady aerodynamic solver for numerical simulation of Floating Wind Turbines. An innovative simulation tool for FWTs was developed coupling the seakeeping solver *InWave*, developed at INNOSEA and Centrale Nantes (France), to the unsteady aerodynamic solver *CACTUS*, developed at Sandia National Laboratories (USA), based on Free Vortex Wake theory. The coupling was presented in chapter 3. A verification was first performed on the NREL 5MW HAWT, supported by the OC3 Hywind SPAR platform [Jonkman, 2010] and presented in chapter 4. Servo-hydro-aerodynamic simulations were compared to the reference *FAST* [Jonkman and Buhl, 2005] FWT design tool, showing a good agreement in several load cases. Differences were however observed when the rotor is highly loaded. They are discussed in the following.

Development of a simulation tool for floating Vertical Axis Wind Turbines. The unsteady aerodynamic solver coupled to *InWave* is adapted for simulation of both horizontal and vertical axis lift-driven rotors. An additional quasi-steady aerodynamic solver based on the Double Multiple Streamtube theory was developed during this PhD thesis and coupled to *InWave*. Also, an algorithm was implemented to control the generator torque, following [Merz and Svendsen, 2013] and [Cheng, 2016]. Various validations have been completed with comparison to experimental data, including a bottom-fixed VAWT in real conditions and a tilted small-scale VAWT. Simulations of a floating VAWT have been performed in various environmental conditions with both the DMS and the FVW solvers. Results show a good agreement but, as discussed later, differences are visible when the rotor is highly loaded.

How to quantify the impact of unsteady aerodynamics on FWTs simulations? An innovative methodology has been proposed for HAWTs and VAWTs. It consists in the following steps:

1. Analysis of the aerodynamic loads acting on the bottom-fixed turbine;

2. Coupled simulations of the FWTs;

3. Motion analysis and decomposition of the coupled response: identification of significant harmonic motions at resonance and wave frequencies;

4. Simulations of the rotors in significant prescribed motions.

In the last phase, it is possible to discriminate the loads in-phase with the motion (corresponding to aerodynamic damping) and loads in quadrature (i.e. stiffness and added mass). The differences obtained between the aerodynamic damping computed by the two models can then be correlated to previously simulated coupled responses, especially if the aerodynamic loads are predominant.

To what extent do unsteady aerodynamic loads alter the simulation of the seakeeping of FWTs? The above methodology has been applied separately to a floating HAWT (chapter 4) and to a floating VAWT (chapter 5). The study was performed with a SPAR platform, which may induce smaller motions than other types of platforms such as barges or semi-submersible floaters. The results show that quasi-steady (BEM or DMS) and unsteady (FVW) aerodynamic models have globally similar results. The behaviour of the FWTs is well captured with both models. In particular, very similar results are obtained at low Tip Speed Ratio when the rotor is lightly loaded, typically at over-rated wind speeds. Unsteady aerodynamic phenomena such as strong rotor-wake interactions are then unlikely to be of importance and to impact the motion of the turbine. However, differences appear between the resonance peak amplitudes or position mean values and standard deviations when the rotor is highly loaded at high TSR. The motion of the platform then makes the rotor operate in its own wake and/or strongly interact with it. This alters the aerodynamic loads and particularly the aerodynamic damping.

Which aerodynamic model is the most appropriate to simulate the behaviour of FWTs in complex environmental conditions? Following what has been discussed previously, the choice of an aerodynamic model highly depends on the concerned design stage. In early design stages, quasi-steady solvers which offer a very low computational cost are very suitable for numerous simulations. For more accurate design phases, unsteady simulations should be considered, especially at high TSR. For example, local blade aerodynamic loads could be very different between a FVW solver and DMS solver in the case of a VAWT. These differences might be more pronounced for larger wind turbines with substantial aero-elastic effects.

How does a floating VAWT behave at sea compared to a HAWT? A comparative study has been completed between HAWTs and VAWTs supported by a similar semi-submersible platform. A set of realistic sea-states have been tested, including non-collinear wind and waves. The reaction torque of the generator induces large yaw motions of the platform of the VAWT. In particular, the mean yaw of the platform is increased up to more than 4°. This is completely inherent to the VAWT concept. However, the VAWT's generator control filters the $2p$ frequency torque oscillation, annihilating yaw oscillations at this frequency. The yaw motion of the turbine impacts the mooring line tensions. It thus needs to be accounted when designing the mooring system of the floating VAWT.

At large wind speeds, the blade pitch control of the horizontal axis rotor mitigates the aerodynamic thrust while keeping a constant rated power. The studied troposkian VAWT does not have such a feature, and the aerodynamic thrust acting on it keeps increasing at high wind speeds. It also has high centres of thrust and gravity. This induces large surge and pitch motions. The excursion is very large at high wind speeds (more than $8m$) and the tower tilt exceeds 5°. Also, the skewed thrust on the rotor induces a large sway excursion and oscillations in sway and roll.

What are the performances and loads and motions of a floating VAWT compared to a HAWT? At low wind speeds, the power generated by the VAWT is lower than that of the HAWT because of a lower optimal power coefficient. The loads on the VAWT are however lower, leading to an equivalent balance between power and loads.

The loads acting on the VAWT get very large at over-rated wind speeds and significantly exceed the loads acting on the HAWT. The large excursion of the VAWT induces very large mooring tensions which can lead to an additional cost for the VAWT mooring system. The large tilt of the platform induces large tower base bending moment (twice higher than that of the HAWT). In that case, the performances of the VAWT are less interesting than those of the HAWT. The studied VAWT did not use blade pitch control, which appears to be a key feature at over-rated wind speeds. It could allow to keep the rated power while mitigating the loads on the turbine and thus decreasing the extreme loads and excursion of the platform. It could eventually lower the cost of such systems. Also, it may be interesting to lower the projected area of the turbine. H-shaped rotors, for instance, have lower centres of thrust and gravity, leading to lower tower base bending moments as presented in [Cheng et al., 2017a]. The number of blades can also be determinant as it has a strong impact on the tower base bending moment STD [Cheng et al., 2017a].

7.2 Perspectives

7.2.1 Numerical modelling improvements

7.2.1.1 Aerodynamics

This PhD thesis emphasizes the need for improvements of the state of the art numerical models. In particular, quasi-steady aerodynamic models seem to miss essential unsteady effects when the rotor is highly loaded. Floating Wind Turbines operate most of the time at optimal TSR at below-rated wind speeds. Few calculations were however completed in this region because of the high CPU cost of Free Vortex Wake calculations. The first priority would then be to accelerate these solvers. *CACTUS* was parallelized during this PhD thesis but the scalability of the solver has not been evaluated and the solver architecture can still be optimised.

At high TSR, the time-steps need to be small and the wake needs to be sufficiently long (about 4 to 5 rotor diameters). In low TSR simulations, the modelled wake length can be much shorter, which significantly reduces the CPU cost. For example, with the HAWT presented in chapter 4, a 3600s simulation with *InWave-FVW* running on 10 threads of a desktop computed lasted:

- 24h for $U_\infty = 18m.s^{-1}$

- 2.5 weeks for $U_\infty = 8m.s^{-1}$

General-Purpose Graphic Processing Units (GPGPUs) can be very interesting for massively parallel calculations. FVW solvers can have a high scalability when calculating the induced velocities and GPGPU seems very suitable for this application. A very important gain in CPU cost could be obtained. Other possibilities are being investigated for accelerations of FVW solvers. For example, [Boorsma et al., 2018] suggests wake simplifications at a given distance from the rotor. The method consists in skipping vortices in the Biot-Savart calculations in the far wake of the turbine. This allows 60%

to 90% CPU time reductions while maintaining a good accuracy. Another strategy is chosen in the FVW solver *QBlade* [Marten et al., 2015]: trailing vortices are merged in single and stronger vortices in the mid to far wake. This allows a substantial reduction in the CPU cost. Such strategies have been studied for HAWTs but need to be investigated and adapted for the complex wakes of VAWTs.

A large uncertainty of lifting line and blade element models is the aerodynamic polars C_L and C_D. Also, inviscid models need to use dynamic stall models, which are highly sensitive to these polars. This PhD thesis uses polars computed with potential solvers such as *Xfoil* [Drela, 1989]. The use of polars computed with inviscid high fidelity solvers, or measured through experimental testing should be considered. [Wendler et al., 2016] suggests the hybrid use of fully attached flow and fully separated flow aerodynamic coefficients when computing instantaneous aerodynamic loads in the FVW solver *QBlade*, showing good solver performances.

Eventually, the implementation of a BEM solver in *InWave* would be very valuable for this new Floating Wind Turbine simulation tool.

7.2.1.2 Hydrodynamics

The hydrodynamic model used in this PhD thesis combines linear potential flow theory for the large bodies and Morison formulation for slender bodies. As seen in chapter 6, *InWave*'s model of the heave plates viscous drag, computed with Morison formula, needs to be improved. *InWave* also uses *Nemoh* [Babarit and Delhommeau, 2015] as potential flow solver, which only computes the first order hydrodynamic coefficients. *InWave* should however be adapted to account for second order loads through Quadratic Transfer Functions (QTFs). This hydrodynamic database could be computed with an third-party solver such as *WAMIT* [Lee, 1995], for instance. Second-order hydrodynamic loads can cause both high frequency and low frequency differences in the hydrodynamic loads on the platform, especially in steep waves. It could notably alter the excursion of the turbine and hence increase the tensions in the mooring lines.

Another hydrodynamic theory could also be used. Pierre-Yves Wuillaume (LHEEA Lab. of Centrale Nantes and INNOSEA) has for example been working in parallel with this PhD on the tight coupling of *InWave*'s multi-body algorithm with a hydrodynamic Weak-Scatterer theory-based solver [Wuillaume et al., 2017]. The solver is based on a weakly non-linear potential flow theory using the weak-scatterer approximation. It allows the computation of the unsteady hydrodynamic loads without being limited by the classical hypotheses of the linear potential flow theory, improving the accuracy of the simulations where severe sea states are considered.

Finally, *FAST* and *InWave* respectively use linear and non-linear hydrostatics. No difference induced by hydrostatics modelling was noticed in large motions in decay tests, for instance, meaning linear modelling may be accurate enough. Non-linear hydrostatics necessitate to integrate the hydrostatic pressure on the wetted mesh of the platform, which considerably increases the computational cost.

7.2.1.3 Mooring loads

The present study only uses the quasi-static mooring solver *MAP++* [Masciola et al., 2013a]. This theory can compute an accurate mean tension of the mooring lines, but misses the dynamic behaviour of the mooring such as snap loads, for example. Using a finite-element solver or a lumped-mass mooring solver, for example (presented in section 2.3.3 of chapter 2) could include those effects. Differences induced by the mooring

modelling on the numerical simulations of FWTs have for example been presented in [Cevasco et al., 2017]. Dynamic mooring modelling could for instance improve the accuracy of the computed pitch motion, highly critical for the design of FWTs. Also, it would improve the comparative analysis between HAWTs and VAWTs.

7.2.1.4   Structural dynamics

The simulations performed with *InWave* assume rigid bodies as structural dynamics cannot be accounted for. Large aero-elastic effects are nonetheless observed on wind turbines blades or towers, with either HAWTs ([Harrison et al., 2018], for example) or VAWTs ([Wang et al., 2016], for example). As offshore structures get larger, platform deformations in severe sea states could also be included in numerical simulations as performed in [Borg et al., 2016]. The bending of a SPAR platform in large pitch motions can for example be a crucial issue. It is hence essential to improve the solvers and to perform hydro-aero-elastic simulations. The effects of unsteady aerodynamic loading on local internal blade loads could then be investigated, for example.

David Ogden (University of Edinburgh (Scotland, UK) and INNOSEA) has recently focused on the coupling of *InWave* to a third party multi-body dynamics code, *HOTINT* [Gerstmayr, 2009]. This should open new features to *InWave*: complex links between bodies (friction, for instance), closed mechanical loops, ropes... But also the modelling of structural dynamics of the bodies, including blades, tower and platform.

A more profound study on FWTs could include these effects with an appropriate hydrodynamic solver. It would allow to more accurately predict the behaviour and long time service of FWTs, including extreme and fatigue loadings.

7.2.1.5   Control

Chapter 6 emphasized the need for new control strategies for a troposkian floating VAWT. Blade pitch control would allow to keep an optimal power production while reducing the thrust on the rotor at over-rated wind speeds as presented in [Kumar et al., 2018], for example. Blade pitch control on VAWTs is challenging as actuators have to be installed on the blades. If H-shaped rotors are suitable for such systems, it can be harder to design troposkian blades with pitch actuators. Fluidic lift and drag control through air jets is however possible as experimented in [Baleriola et al., 2018]. These strategies still need to be developed and their efficiency on VAWTs or large scale turbines needs to be proven.

7.2.2   Experimental validation

The need for experimental validation of FWTs simulation tools has often been evoked in this PhD thesis. Indeed, many uncertainties remain on the validity of the developed models.

Small scale testing could be performed, notably using hybrid testing strategies (presented in section 2.6.3 of chapter 2) to validate either the aerodynamic or hydrodynamic models with FWTs. Such validations should be performed with several types of floater designs (spar, TLP, semi-submersible, barge). Indeed, the nature of the floaters and mooring systems could influence the results and accuracy of the numerical aerodynamic models. Full-scale FWTs have also been installed recently, which could help validating simulation tools.

Such validations are essential to evaluate the uncertainties of the solvers and the safety factors that should be used in design phases of the FWTs.

7.2.3 Further investigations on Floating Wind Turbines

A coupled unsteady aerodynamic solver could be used to study several topics on the dynamic analysis of Floating Wind Turbines. It would for example allow to account for strong rotor/wake aerodynamic interaction and to improve blade pitch control laws used to avoid platform pitch instability issues, studied in [Larsen and Hanson, 2007] for instance.

Vertical Axis Wind Turbines are still emerging and plenty of designs are still being studied. For example, twin counter-rotating rotors are being designed as they allow an enhanced power coefficient. The FVW theory could probably be an accurate design tool for such turbines as the rotors and wakes interaction would inherently be included in the computations. *InWave-FVW* cannot simulate such rotors for now. It should be adapted and optimised for such configurations.

The present PhD thesis also emphasizes the very high loads acting on a large troposkian VAWT in chapter 6. Rotors with other topologies and lowered centres of thrust or various number of blades should also be studied. This could maybe help the VAWT designs to converge towards more efficient concepts with cheaper substructures and mooring systems. This may finally help the offshore wind energy sector to develop and decarbonise our energy supply.

References

[Akins et al., 1986] Akins, R. E., Berg, D. E., and Cyrus, W. T. (1986). Measurements and calculations of aerodynamic torques for a vertical axis wind turbine. sand86-2164. Technical report, Sandia National Laboratories. xviii, 59, 60

[Allet and Paraschivoiu, 1995] Allet, A. and Paraschivoiu, I. (1995). Viscous flow and dynamic stall effects on vertical-axis wind turbines. *International Journal of Rotating Machinery*, 2(1):1–14. 59

[Aubrun et al., 2017] Aubrun, S., Leroy, A., and Devinant, P. (2017). A review of wind turbine-oriented active flow control strategies. *Experiments in Fluids*, 58(10):134. 36

[Babarit and Delhommeau, 2015] Babarit, A. and Delhommeau, G. (2015). Theoretical and numerical aspects of the open source bem solver nemoh. In *Proceedings of the 11th European Wave and Tidal Energy Conference 6-11th Sept 2015, Nantes, France*. 29, 44, 135

[Baleriola et al., 2018] Baleriola, S., Leroy, A., Loyer, S., Devinaut, P., and Aubrun, S. (2018). Experimental lift control using uidic jets on a model wind turbine. *Journal of Physics: Conference Series*, 1037:022014. 136

[Bayati et al., 2016] Bayati, I., Belloli, M., Bernini, L., and Zasso, A. (2016). Wind tunnel validation of aerodyn within lifes50+ project: imposed surge and pitch tests. *Journal of Physics: Conference Series*, 753:092001. 25, 38, 66, 79

[Bayati et al., 2018] Bayati, I., Foletti, S., Tarsitano, D., and Belloli, M. (2018). A reference open data vertical axis wind turbine, with individual pitch control, for code validation purposes. *Renewable Energy*, 115:711–720. 36

[Blondel et al., 2016] Blondel, F., Boisard, R., Milekovic, M., Ferrer, G., Lienard, C., and Teixeira, D. (2016). Validation and comparison of aerodynamic modelling approaches for wind turbines. *Journal of Physics: Conference Series*, 753:022029. 24

[Blondel and Cathelain, 2017] Blondel, F. and Cathelain, M. (2017). Benchmarking activities (code to code comparison) on the rigid 1hs 3-bladed vawt. Technical report, IPF Energies Nouvelles. 25

[Blondel et al., 2017] Blondel, F., Ferrer, G., Cathelain, M., and Teixeira, D. (2017). Improving a bem yaw model based on newmexico experimental data and vortex/cfd simulations. In *Actes du 23ème Congrès Français de Mécanique, 28 Août au 1er Septembre, Lille, France*. 24

[Blondel et al., 2018] Blondel, F., Galinos, C., Paulsen, U. S., Bozonnet, P., Cathelain, M., Ferrer, G., Madsen, H. A., Pirrung, G., and Silvert, F. (2018). Comparison of

aero-elastic simulations and measurements performed on nenuphar's 600kw vertical axis wind turbine: impact of the aerodynamic modelling methods. *Journal of Physics: Conference Series*, 1037:022010. 106

[Boorsma et al., 2018] Boorsma, K., Greco, L., and Bedon, G. (2018). Rotor wake engineering models for aeroelastic applications. *Journal of Physics: Conference Series*, 1037:062013. 49, 134

[Borg and Collu, 2014] Borg, M. and Collu, M. (2014). A comparison on the dynamics of a floating vertical axis wind turbine on three different floating support structures. *Energy Procedia*, 53:268–279. 11

[Borg and Collu, 2015a] Borg, M. and Collu, M. (2015a). A comparison between the dynamics of horizontal and vertical axis offshore floating wind turbines. *Philosophical Transactions of the Royal Society of London*, 373:20140076. xvii, 4, 11, 110, 129

[Borg and Collu, 2015b] Borg, M. and Collu, M. (2015b). Offshore floating vertical axis wind turbines, dynamics modelling state of the art. part iii : Hydrodynamics and coupled modelling approaches. *Renewable and Sustainable Energy Reviews*, 46:296–310. 11

[Borg et al., 2014a] Borg, M., Collu, M., and Kolios, A. (2014a). Offshore floating vertical axis wind turbines, dynamics modelling state of the art. part ii : Mooring line and structural dynamics. *Renewable and Sustainable Energy Reviews*, 39:1226–1234. 11

[Borg et al., 2016] Borg, M., Hansen, A. M., and Bredmose, H. (2016). Floating substructure flexibility of large-volume 10mw oshore wind turbine platforms in dynamic calculation. *Journal of Physics: Conference Series*, 753:082024. 136

[Borg et al., 2014b] Borg, M., Shires, A., and Collu, M. (2014b). Offshore floating vertical axis wind turbines, dynamics modelling state of the art. part i : Aerodynamics. *Renewable and Sustainable Energy Reviews*, 39:1214–1225. iii, xvii, 5, 11, 22

[Burton et al., 2001] Burton, T., Sharpe, D., Jenkins, N., and Bossanyi, E. (2001). *Wind Energy Handbook*. Wiley. 52

[Cevasco et al., 2017] Cevasco, D., Collu, M., Hall, M., and Rizzo, C. M. (2017). On the comparison of the dynamic response of an offshore floating vawt system when adopting two different mooring model of dynamics: quasi-static vs lumped mass approach. omae2017-61450. In *Proceedings of the ASME 2017 36th International Conference on Ocean, Offshore and Arctic Engineering, OMAE2017, June 25-30, 2017, Trondheim, Norway*. 34, 136

[Cevasco et al., 2018] Cevasco, D., Collu, M., Rizzo, C. M., and Hall, M. (2018). On mooring line tension and fatigue prediction for offshore vertical axis wind turbines: a comparison of lumped mass and quasi-static approaches. *Wind Engineering*, 42(2):97–107. 34

[Chabaud, 2016] Chabaud, V. (2016). *Real-time hybrid model testing of floating wind turbines*. PhD thesis, Norwegian University of Science and Technology (NTNU). 39

[Cheng, 2016] Cheng, Z. (2016). *Integrated Dynamic Analysis of Floating Vertical Axis Wind Turbines*. PhD thesis, Norwegian University of Science and Technology (NTNU). xviii, 5, 12, 21, 57, 58, 84, 95, 132, 152, 155

[Cheng et al., 2017a] Cheng, Z., Madsen, H. A., Chai, W., Gao, Z., and Moan, T. (2017a). A comparison of extreme structural responses and fatigue damage of semi-submersible type floating horizontal and vertical axis wind turbines. *Renewable Energy*, 108:207–219. 129, 134

[Cheng et al., 2016] Cheng, Z., Madsen, H. A., Gao, Z., and Moan, T. (2016). Aerodynamic modeling of floating vertical axis wind turbines using the actuator cylinder flow method. *Energy Procedia*, 94:531–543. 154, 155

[Cheng et al., 2017b] Cheng, Z., Madsen, H. A., Gao, Z., and Moan, T. (2017b). Effect of the number of blades on the dynamics of floating straight-bladed vertical axis wind turbines. *Renewable Energy*, 101:1285–1298. 12

[Cheng et al., 2017c] Cheng, Z., Madsen, H. A., Gao, Z., and Moan, T. (2017c). A fully coupled method for numerical modeling and dynamic analysis of floating vertical axis wind turbines. *Renewable Energy*, 107:604–619. 95

[Cheng et al., 2015] Cheng, Z., Wang, K., Gao, Z., and Moan, T. (2015). Dynamic response analysis of three floating wind turbine concepts with a two-bladed darrieus rotor. *Journal of Ocean and Wind Energy*, 2(4):213–222. 12

[Cheng et al., 2017d] Cheng, Z., Wang, K., Gao, Z., and Moan, T. (2017d). A comparative study on dynamic responses of spar-type floating horizontal and vertical axis wind turbines. *Wind Energy*, 20:305–323. 110, 117, 127, 129

[Collu et al., 2013] Collu, M., Borg, M., Shires, A., and Brennan, F. P. (2013). Flovawt : Progress on the development of a coupled model of dynamics for floating offshore vertical axis wind turbines. omae2013-10717. In *Proceedings of the ASME 2013 32nd International Conference on Ocean, Offshore and Arctic Engineering, OMAE2013, June 9-14, 2013, Nantes, France*. 11, 38

[Combourieu et al., 2015] Combourieu, A., Philippe, M., Larivain, A., and Espedal, J. (2015). Experimental validation of inwave, a numerical design tool for wecs. In *Proceedings of the 11th European Wave and Tidal Energy Conference (EWTEC) 6-11th Sept 2015, Nantes, France ISSN 2309*. 58

[Combourieu et al., 2014] Combourieu, A., Philippe, M., Rongère, F., and Babarit, A. (2014). Inwave: a new flexible tool dedicated to wave energy converters. omae2014-24564. In *Proceedings of the ASME 2014 33rd International Conference on Ocean, Offshore and Arctic Engineering, OMAE2014, June 8-13, 2014, San Francisco, California, USA*. iv, 12, 43, 58

[Cordle and Jonkman, 2011] Cordle, A. and Jonkman, J. (2011). State of the art in floating wind turbine design tool. In *Proceedings of International Offshore and Polar Engineering conference*. 10, 66

[Courbois, 2013] Courbois, A. (2013). *Etude expérimentale du comportement dynamique d'une éolienne offshore ottante soumise à l'action conjuguée de la houle et du vent*. PhD thesis, Ecole Centrale de Nantes. xvii, 10, 38, 39

[Cummins, 1962] Cummins, W. E. (1962). The impulse response functin and ship motions. Technical Report DTMB-1661, David Taylor Model Basin Washington DC. 29

[Darrieus, 1931] Darrieus, G. J. M. (1931). Turbine having its rotating shaft transverse to the flow of the current. *U.S. Patent No 1,835,018, 8 déc.* xvii, 5, 6

[DNV, 2013a] DNV (2013a). Dnv-os-e301: Position mooring. Technical report, Det Norske Veritas. 32

[DNV, 2013b] DNV (2013b). Dnv-os-j103: Design of floating wind turbine structures. Technical report, Det Norske Veritas. 32

[Drela, 1989] Drela, M. (1989). Xfoil: An analysis and design system for low reynolds number airfoils. In *Conference on Low Reynolds Number Airfoil Aerodynamics, University of Notre Dame, June.* 21, 69, 95, 113, 135

[Driscoll et al., 2016] Driscoll, F., Jonkman, J., Robertson, A., Sirnivas, S., Skaare, B., and Nielsen, F. G. (2016). Validation of a fast model of the statoil-hywind demo floating wind turbine. *Energy Procedia*, 94:3–19. 66

[Faltinsen, 1990] Faltinsen, O. M. (1990). *Sea loads on ships and offshore structures.* Cambridge University Press. xvii, 25, 28, 31, 33

[Ferreira, 2009] Ferreira, C. S. (2009). *The near wake of the VAWT.* PhD thesis, TU Delft. 22

[Fraile and Mbistrova, 2018] Fraile, D. and Mbistrova, A. (2018). Wind in power 2017 - annual combined onshore and offshore wind energy statistics. Technical report, Wind Europe. xvii, 2

[Fried, 2017] Fried, L. (2017). Global wind statistics. Technical report, Global Wind Energy Council (GWEC). 2

[Gerstmayr, 2009] Gerstmayr, J. (2009). Hotint − a c++ environment for the simulation of multibody dynamics systems and finite elements. In *Proceedings of the Multibody Dynamics 2009 Eccomas Thematic Conference, K. Arczewski, J. Frączek, M. Wojtyra (eds.), 29 June − 2 July, pp. 1-20.* 136

[Hall, 2017] Hall, M. (2017). Moordyn user's guide. Technical report, School of Sustainable Design Engineering, University of Prince Edward Island. 37, 38

[Harrison et al., 2018] Harrison, M., Kloosterman, M., and Urbano, R. B. (2018). Aerodynamic modelling of wind turbine blade loads during extreme deflection events. *Journal of Physics: Conference Series*, 1037:062022. 136

[Islam et al., 2013] Islam, M. R., Mekhilef, S., and Saidur, R. (2013). Progress and recent trends of wind energy technology. *Renewable and Sustainable Energy Reviews*, 21:456–468. 2

[Jeon et al., 2014] Jeon, M., Lee, S., and Lee, S. (2014). Unsteady aerodynamics of offshore floating wind turbines in platform pitching motion using vortex lattice method. *Renewable Energy*, 65:207–212. iii, 11, 24, 91

[Jonkman, 2009] Jonkman, B. J. (2009). Turbsim user's guide: Version 1.50. nrel/tp-500-46198. Technical report, National Renewable Energy Laboratory. 37, 50, 76, 97, 117

[Jonkman, 2010] Jonkman, J. (2010). Definition of the floating system for phase iv of oc3. nrel/tp-500-47535. Technical report, National Renewable Energy Laboratory. 13, 66, 67, 71, 95, 132

[Jonkman and Buhl, 2005] Jonkman, J. and Buhl, M. L. (2005). Fast user's guide v.7. nrel/el-500-38230. Technical report, National Renewable Energy Laboratory. iv, 10, 13, 20, 30, 36, 37, 66, 132

[Jonkman et al., 2009] Jonkman, J., Butterfield, S., Musial, W., and Scott, G. (2009). Definition of a 5-mw reference wind turbine for offshore system development. nrel/tp-500-39060. Technical report, National Renewable Energy Laboratory. 35, 36, 57, 66, 67, 73, 79, 110, 116

[Jonkman and Musial, 2010] Jonkman, J. and Musial, W. (2010). Offshore code comparison collaboration (oc3) for iea task 23 offshore wind technology and deployment. nrel/tp-5000-48191. Technical report, National Renewable Energy Laboratory. 10, 66, 67, 71

[Jonkman et al., 2016] Jonkman, J. M., Hayman, G. J., Jonkman, B. J., and Damiani, R. R. (2016). Aerodyn v15 user's guide and theory manual (draft report). Technical report, National Renewable Energy Laboratory. 37, 69

[Jonkman et al., 2014] Jonkman, J. M., Robertson, A., and Hayman, G. J. (2014). Hydrodyn user's guide and theory manual (draft report). Technical report, National Renewable Energy Laboratory. 30, 37

[Jumper et al., 1987] Jumper, E. J., Schreck, S. J., and Dimmick, R. L. (1987). Lift-curve characteristics for an airfoil pitching at constant rate. *Journal of Aircraft*, 24(10):680–687. 23

[Katz and Plotkin, 1991] Katz, J. and Plotkin, A. (1991). *Low speed aerodynamics: from wing theory to panel methods*. McGraw-Hill series in aeronautical and aerospace engineering. 48

[Koppenol et al., 2017] Koppenol, B., Cheng, Z., Gao, Z., Ferreira, C. S., and Moan, T. (2017). A comparison of two fully coupled codes for integrated dynamic analysis of floating vertical axis wind tubines. *Energy Procedia*, 137:282–290. 38

[Kulunk, 2011] Kulunk, E. (2011). *Fundamental and Advanced Topics in Wind Power*, chapter Aerodynamics of Wind Turbines, pages pages 3–18. InTech. xvii, xix, 19, 20, 151

[Kumar et al., 2018] Kumar, V., Savenije, F. J., and van Wingerden, J. W. (2018). Repetitive pitch control for vertical axis wind turbine. *Journal of Physics: Conference Series*, 1037:032030. 136

[Larsen and Hansen, 2013] Larsen, T. J. and Hansen, A. M. (2013). How 2 hawc2, the user's manual. Technical report, Riso National Laboratory, Technical University of Denmark: Roskilde, Denmark. 37

[Larsen and Hanson, 2007] Larsen, T. J. and Hanson, T. D. (2007). A method to avoid negative damped low frequent tower vibrations for a floating, pitch controlled wind turbine. *Journal of Physics: Conference Series*, 75:012073. 137

[Le Cunff et al., 2013] Le Cunff, C., Heurtier, J.-M., Piriou, L., Berhault, C., T., P., Teixeira, D., Ferrer, G., and Gilloteaux, J.-C. (2013). Fully coupled floating wind turbine simulator based on nonlinear finite element method - part i: Methodology. In *Proceedings of the ASME 2013 32nd International Conference on Ocean, Offshore and Arctic Engineering, OMAE2013, June 9-14, Nantes, France.* 38

[Lee, 1995] Lee, C. H. (1995). Wamit theory manual. Technical report, Massachusetts Institute of Technology, Department of Ocean Engineering. 29, 135

[Lei et al., 2017a] Lei, H., Zhou, D., Bao, Y., Chen, C., Ma, N., and Han, Z. (2017a). Numerical simulations of the unsteady aerodynamics of a floating vertical axis wind turbine in surge motion. *Energy*, 127:1–17. 94

[Lei et al., 2017b] Lei, H., Zhou, D., Lu, J., Chen, C., Han, Z., and Bao, Y. (2017b). The impact of pitch motion of a platform on the aerodynamic performance of a floating vertical axis wind turbine. *Energy*, 119:369–383. 94

[Leishman and Beddoes, 1989] Leishman, J. G. and Beddoes, T. S. (1989). A semi-empirical model for dynamic stall. *Journal of the American Helicopter Society*, 34(3):3–17. 24

[Leroy et al., 2014] Leroy, V., Combourieu, A., Philippe, M., Babarit, A., and Rongère, F. (2014). Benchmarking of the new design tool inwave on a selection of wave energy converters from numwec project. In *Proceedings of 2nd Asian Wave and Tidal Energy Conference, Jul 28-30, 2014, Tokyo, Japan.* 58

[Leroy et al., 2018] Leroy, V., Gilloteaux, J.-C., Combourieu, A., Babarit, A., and Ferrant, P. (2018). Impact of the aerodynamic model on the modelling of the behaviour of a floating vertical axis wind turbine. *Journal of Physics: Conference Series*, 1104:012001. 94

[Leroy et al., 2017] Leroy, V., Gilloteaux, J.-C., Philippe, M., Babarit, A., and Ferrant, P. (2017). Development of a simulation tool coupling hydrodynamics and unsteady aerodynamics to study floating wind turbines. omae2017-61203. In *Proceedings of the ASME 2017 36th International Conference on Ocean, Offshore and Arctic Engineering, OMAE2017, June 25-30, 2017, Trondheim, Norway.* 77

[Madsen, 1982] Madsen, H. A. (1982). *The actuator cylinder - A flow model for vertical axis wind turbines.* PhD thesis, Institute of Industrial Constructions and Energy Technology, Aalborg University Centre, Denmark. xvii, xix, 21, 94, 95, 152, 153, 154, 155

[Madsen et al., 2013] Madsen, H. A., Larsen, T. J., Vita, L., and Paulsen, U. S. (2013). Implementation of the actuator cylinder flow model in the hawc2 code for aeroelastic simulations on vertical axis wind turbines. aiaa 2013-0913. In *Proceedings of the 51st AIAA Aerospace Sciences Meeting including the New Horizons Forum and Aerospace Exposition.* 38

[Maries et al., 2012] Maries, A., Haque, M. A., Yilmaz, S. L., Nik, M. B., and Marai, G. E. (2012). Interactive exploration of stress tensors used in computational turbulent combustion. In *New Developments in the Visualization and Processing of Tensor Fields, Springer, pp. 137-156.* 23

[Marten et al., 2017] Marten, D., Bianchini, A., Pechlivanoglou, G., Balduzzi, F., Nayeri, C. N., Ferrara, G., Paschereit, C. O., and Ferrari, L. (2017). Effects of airfoil's polar data in the stall region on the estimation of darrieus wind turbine performance. *Journal of Engineering for Gas Turbines and Power*, 139:022606. 21, 61

[Marten et al., 2015] Marten, D., Lennie, M., Pechlivanoglou, G., Nayeri, C. N., and Paschereit, C. O. (2015). Implementation, optimization and validation of a nonlinear lifting line free vortex wake module within the wind turbine simulation code qblade. *Journal of Engineering for Gas Turbines and Power*, 138(7):072601. 38, 135

[Masciola et al., 2013a] Masciola, M., Jonkman, J., and Robertson, A. (2013a). Implementation of a multisegmented, quasi-static cable model. In *Proceedings of the 23rd International Ocean, Offshore and Polar Engineering Conference – ISOPE 2013, Anchorage, Alaska.* 37, 38, 45, 135

[Masciola et al., 2014] Masciola, M., Jonkman, J., and Robertson, A. (2014). Extending the capabilities of the mooring analysis program a survey of dynamic mooring line theories for integration into fast. omae2014-23508. In *33rd International Conference on Ocean, Offshore and Arctic Engineering, OMAE 2014.* xvii, 33, 34

[Masciola et al., 2013b] Masciola, M., Robertson, A., Jonkman, J., Coulling, A., and Goupee, A. (2013b). Assessment of the importance of mooring dynamics on the global response of the deepcwind floating semisubmersible offshore wind turbine. In *Proceedings of the 23rd International Ocean, Offshore and Polar Engineering Conference – ISOPE 2013, Anchorage, Alaska.* 34

[Matha et al., 2011] Matha, D., Schlipf, M., Cordle, A., Pereira, R., and Jonkman, J. (2011). Challenges in simulation of aerodynamics, hydrodynamics and mooring-line dynamics of floating offshore wind turbines. In *Proceedings of the 21st Offshore and Polar Engineering Conference, Maui, Hawaii, June 19-24.* 9

[Mertens et al., 2003] Mertens, S., Van Kuik, G., and Van Bussel, G. (2003). Performance of an h-darrieus in the skewed flow on a roof. *Journal of Solar Energy Engineering*, 125:433–440. 55, 61

[Merz, 2012] Merz, K. O. (2012). A method for analysis of vawt aerodynamic loads under turbulent wind and platform motion. *Energy Procedia*, 24:44–51. 94

[Merz and Svendsen, 2013] Merz, K. O. and Svendsen, H. G. (2013). A control algorithm for the deepwind floating vertical-axis wind turbine. *Journal of Renewable and Sustainable Energy*, 5:063136. 35, 57, 132

[Michelen et al., 2014] Michelen, C., Neary, V. S., Murray, J. C., and Barone, M. (2014). Cactus open source code for hydrokinetic turbine design and analysis: model performance evaluation. In *Proceedings of the 2nd Marine Energy Technology Symposium, METS2014, April 15-18-2014, Seattle, WA.* 50

[Molin, 2002] Molin, B. (2002). *Hydrodynamique des structures offshores.* TECHNIP. 28, 30

[Moné et al., 2015] Moné, C., Smith, A., Maples, B., and Hand, M. (2015). 2013 cost of wind energy review. nrel/tp-5000-63267. Technical report, National Renewable Energy Laboratory. 2

[Montgomerie, 2004] Montgomerie, B. (2004). Methods for root effects, tip effects and extending the angle of attack range to +-100deg, with application to aerodynamics for blades on wind turbines and propellers. Technical report, FOI Swedish Defence Research Agency, Scientific Report FOI-R-1035-SE. 20

[Moriarty and Hansen, 2005] Moriarty, P. J. and Hansen, A. C. (2005). Aerodyn theory manual. nrel/tp-500-36881. Technical report, National Renewable Energy Laboratory. 18, 20, 37, 38, 69

[Murray and Barone, 2011] Murray, J. C. and Barone, M. (2011). The development of cactus, a wind and marine turbine performance simulation code. In *Proceedings of the 49th AIAA Aerospace Sciences Meeting including the New Horizons Forum and Aerospace Exposition, AIAA2011, 4 - 7 January 2011, Orlando, Florida*. iv, 13, 46, 47, 49, 50, 61

[Ormberg and Bachynski, 2012] Ormberg, H. and Bachynski, E. (2012). Global analysis of oating wind turbines: Code development, model sensitivity and benchmark study. In *Proceedings of the 22th International Oshore and Polar Engineering Conference, Rhodes, Greece*. 37

[Paraschivoiu, 2002] Paraschivoiu, I. (2002). *Wind Turbine Design: With Emphasis on Darrieus Concept*. Presses Internationales Polytechniques. iv, 20, 23, 50, 94

[Paraschivoiu et al., 2009] Paraschivoiu, I., Trifu, O., and Saeed, F. (2009). H-darrieuswind turbine with blade pitch control. *International Journal of Rotating Machinery*, 2009:505343. 36

[Paulsen et al., 2014] Paulsen, U. S., Madsen, H. A., Kragh, K. A., Nielsen, P. H., Baran, I., Hattel, J., Ritchie, E., Leban, K., Svendsen, H. G., and Berthelsen, P. A. (2014). Deepwind-from idea to 5 mw concept. *Energy Procedia*, 53:23–33. 5, 57, 110, 113

[Perdrizet et al., 2013] Perdrizet, T., Gilloteaux, J.-C., Teixeira, D., Ferrer, G., Piriou, L., Cadiou, D., Heurtier, J.-M., and Le Cunff, C. (2013). Fully coupled floating wind turbine simulator based on nonlinear finite element method - part ii: Validation results. In *Proceedings of the ASME 2013 32nd International Conference on Ocean, Offshore and Arctic Engineering, OMAE2013, June 9-14, Nantes, France*. 38

[Philippe, 2012] Philippe, M. (2012). *Couplage aéro-hydrodynamique pour l'étude de la tenue à la mer des éoliennes offshore flottantes*. PhD thesis, Ecole Centrale de Nantes, Nantes, France. 10, 28, 30

[Philippe et al., 2013] Philippe, M., Courbois, A., Babarit, A., Bonnefoy, F., Rousset, J.-M., and Ferrant, P. (2013). Comparison of simulation and tank test results of a semi-submersible floating wind turbine under wind and wave loads. omae2013-11271. In *Proceedings of the ASME 2013 32nd International Conference on Ocean, Offshore and Arctic Engineering OMAE2013 June 9-14, 2013, Nantes, France*. 10, 38

[Pitt and Peters, 1980] Pitt, D. M. and Peters, D. A. (1980). Theoretical prediction of dynamic-inflow derivatives. In *6th European Rotorcraft and Powered Lift Aircraft Forum, Bristol, England*. 75

[Quallen and Xing, 2016] Quallen, S. and Xing, T. (2016). Cfd simulation of a floating offshore wind turbine system using a variable-speed generator-torque controller. *Renewable Energy*, 97:230–242. 22

[Rapin and Noël, 2010] Rapin, M. and Noël, J.-M. (2010). *Energies Eolienne*. DUNOD. 2

[Robertson, 2017] Robertson, A. (2017). Uncertainty analysis of oc5-deepcwind floating semisubmersible offshore wind test campaign. In *Proceedings of the International Society of Offshore and Polar Engineers' International Ocean and Polar Engineering Conference, San Francisco, California, June 25–30*. 9, 11, 66

[Robertson et al., 2014a] Robertson, A., Jonkman, J., Masciola, M., and Song, H. (2014a). Definition of the semisubmersible floating system for phase ii of oc4. nrel/tp-5000-60601. Technical report, National Renewable Energy Laboratory. xix, 13, 30, 111, 112

[Robertson et al., 2014b] Robertson, A., Jonkman, J., Vorpahl, F., Popko, W., Qvist, J., Frøyd, L., Chen, X., Azcona, J., Uzunoglu, E., Guedes Soares, C., Luan, C., Yutong, H., Pengcheng, F., Yde, A., Larsen, T., Nichols, J., Buils, R., Lei, L., Anders Nygard, T., Manolas, D., Heege, A., Ringdalen Vatne, S., Ormberg, H., Duarte, T., Godreau, C., Fabricius Hansen, H., Wedel Nielsen, A., Riber, H., C., L. C., Abele, R., Beyer, F., Yamaguchi, A., K., J. J., Shin, H., Shi, W., Park, H., Alves, M., and Guérinel, M. (2014b). Offshore code comparison collaboration continuation within iea wind task 30: phase ii results regarding a floating semisubmersible wind system. In *Proceedings of the ASME 2014 33rd International Conference on Ocean, Offshore and Arctic Engineering. American Society of Mechanical Engineers*. 10, 66

[Robertson et al., 2017] Robertson, A. N., Wendt, F., Jonkman, J. M., Popko, W., Dagher, H., Gueydon, S., Qvist, J., Vittori, F., Azcona, J., Uzunoglu, E., Guedes Soares, C., Harries, R., Yde, A., Galinos, C., Hermans, K., Bernadus de Vaal, J., Bozonnet, P., Bouy, L., Bayati, I., Bergua, R., Galvan, J., Mendikoa, I., Barrera Sanchez, C., Shin, H., Oh, S., Molins, C., and Debruyne, Y. (2017). Oc5 project phase ii: validation of global loads of the deepcwind floating semisubmersible wind turbine. *Energy Procedia*, 137:38–57. 11, 66

[Roddier et al., 2017] Roddier, D., Cermelli, C., A., A., and Peiffer, A. (2017). Summary and conclusions of the full life-cycle of the windfloat fowt prototype project. omae2017-62561. In *Proceedings of the ASME 2017 36th International Conference on Ocean, Offshore and Arctic Engineering, OMAE2017, June 25-30, 2017, Trondheim, Norway*. xvii, 39, 40

[Rongère and Clément, 2013] Rongère, F. and Clément, A. H. (2013). Systematic dynamic modeling and simulation of multibody offshore structures: application to wave energy converters. omae2013-11370. In *Proceedings of the ASME 2013 32nd International Conference on Ocean, Offshore and Artic Engineering, OMAE2013, June 9-14, 2013, Nantes, France*. 43

[Schepers, 2012] Schepers, J. G. (2012). *Engineering models in wind energy aerodynamics*. PhD thesis, Aerospace Engineering. Delft University of Technology. xvii, 10, 23, 24

[Sebastian and Lackner, 2013] Sebastian, T. and Lackner, M. A. (2013). Characterization of the unsteady aerodynamics of offshore floating wind turbines. *Wind Energy*, 16:339–352. iii, 11, 24

[Shen et al., 2018a] Shen, X., Chen, J., Zhu, X., and Du, Z. (2018a). Study of the unsteady aerodynamics of floating wind turbines. *Energy*, 145:793–809. 22

[Shen et al., 2018b] Shen, X., Hu, P., Chen, J., Zhu, X., and Du, Z. (2018b). The unsteady aerodynamics of floating wind turbine under platform pitch motion. In *Proceedings of the Institution of Mechanical Engineers, Part A: Journal of Power and Energy*, page 0957650918766606. 11, 22, 25, 82, 91

[Shires, 2013] Shires, A. (2013). Design optimisation of an offshore vertical axis wind turbine. *Proceedings of the ICE-Energy*, 166(EN1):7–18. 110

[Sørensen and Shen, 2002] Sørensen, J. N. and Shen, W. Z. (2002). Numerical modeling of wind turbine wakes. *Journal of Fluids Engineering*, 124:393–399. 21

[Strickland, 1975] Strickland, J. H. (1975). The darrieus turbine: a performance prediction model using multiple streamtubes. Technical report, Sandia National Laboratories. 94

[Strickland et al., 1979] Strickland, J. H., Webster, B. T., and Nguyen, T. (1979). A vortex model of the darrieus turbine: an analytical and experimental study. *Journal of Fluids Engineering*, 101(4):500–505. 21

[Sutherland et al., 2012] Sutherland, H. J., Berg, D. E., and Ashwill, T. D. (2012). A retrospective of vawt technology. sand2012-0304. Technical report, Sandia National Laboratories. 5

[Svendsen and Merz, 2013] Svendsen, H. G. and Merz, K. O. (2013). Control system for start-up and shut-down of a floating vertical axis wind turbine. *Energy Procedia*, 35:33–42. 35

[T. and Mbistrova, 2018] T., R. and Mbistrova, A. (2018). Offshore wind in europe - key trends and statistics 2017. Technical report, Wind Europe. 2

[Tran and Kim, 2015] Tran, T. T. and Kim, D. H. (2015). The aerodynamic interference effects of a floating offshore wind turbine experiencing platform pitching and yawing motions. *Journal of Mechanical Science and Technology*, 29(2):549–561. 25, 82

[Van Kuik, 2018] Van Kuik, G. (2018). *The Fluid Dynamic Basis for Actuator Disc and Rotor Theories*. IOS Press. 18

[Vita et al., 2011] Vita, L., Pedersen, T. F., and Madsen, H. A. (2011). *Offshore Vertical Axis Wind Turbine with Floating and Rotating Foundation*. PhD thesis, DTU Wind Energy. xvii, 8, 11, 113, 114

[Viterna and Corrigan, 1982] Viterna, L. A. and Corrigan, R. D. (1982). Fixed pitch rotor performance of large horizontal axis wind turbines. Technical report, NASA Lewis Research Center, Cleveland, Ohio. 20

[Wang, 2015] Wang, K. (2015). *Modelling and dynamic analysis of a semi-submersible floating Vertical Axis Wind Turbine.* PhD thesis, Norwegian University of Science and Technology (NTNU). xvii, 11, 38, 50, 51, 52

[Wang et al., 2016] Wang, K., Moan, T., and Hansen, M. O. L. (2016). Stochastic dynamic response analysis of a floating vertical axis wind turbine with a semi-submersible floater. *Wind Energy*, 19:1853–1870. 37, 136

[Wayman, 2006] Wayman, E. (2006). Coupled dynamics and economic analysis of floating wind turbine systems. Master's thesis, Massachusetts Institute of Technology. 4

[Wendler et al., 2016] Wendler, J., Marten, D., Pechlivanoglou, G., Nayeri, C. N., and Paschereit, C. O. (2016). An unsteady aerodynamics model for lifting line free vortex wake simulations of hawt and vawt in qblade. In *Proceedings of ASME Turbo Expo 2016: Turbomachinery Technical Conference and Exposition, GT2016, June 13 – 17, 2016, Seoul, South Korea.* 135

[Wuillaume et al., 2017] Wuillaume, P.-Y., Rongère, F., Babarit, A., Philippe, M., and Ferrant, P. (2017). Development and adaptation of the composite rigid body algorithm and the weak-scatterer approach in view of the modeling of marine operations. In *Actes du 23ème Congrès Français de Mécanique, 28 Août au 1er Septembre, Lille, France.* 135

[Yan et al., 2016] Yan, J., Korobenko, A., Deng, X., and Bazilevs, Y. (2016). Computational free-surface fluid–structure interaction with application to floating offshore wind turbines. *Computers and Fluids*, 141:155–174. 22, 23

Appendix A

Aerodynamic models

A.1 Froude-Rankine Actuator Disk

The equations presented here can also be found in [Kulunk, 2011].

Froude-Rankine's Actuator Disk theory considers an inviscid, incompressible, axial and steady flow in a streamtube. The flow goes through an actuator disk as presented in figure A.1. The inflow velocity is U_∞, the pressure at the undisturbed inflow and far wake is p_0. As it goes through the actuator disk at the velocity U_R, the flow experiences a pressure drop from p_u to p_d. The far wake velocity is noted U_w. The streamtube sections at inflow, disk and far wake are respectively A_∞, A (surface of the disk) and A_w. Let also call U_2 and U_3 the velocities at the upwind and downwind boundaries of the disk. The disk being infinitely thin, the axial velocity is continuous through the disk as written in equation A.1.

$$U_R = U_2 = U_3 \tag{A.1}$$

ρ being the volumetric mass of the fluid, the conservation of mass gives:

$$\dot{m} = \rho A_\infty U_\infty = \rho A U_R = \rho A_w U_w \tag{A.2}$$

The flow being inviscid, impressible and steady, it is possible to write the equation of Bernoulli in two separate regions: upwind region (from 1 to 2) and downwind region (3 to 4):

$$\begin{cases} \frac{1}{2}\rho U_\infty^2 + p_0 = \frac{1}{2}\rho U_R^2 + p_u \\ \frac{1}{2}\rho U_R^2 + p_d = \frac{1}{2}\rho U_w^2 + p_0 \end{cases} \tag{A.3}$$
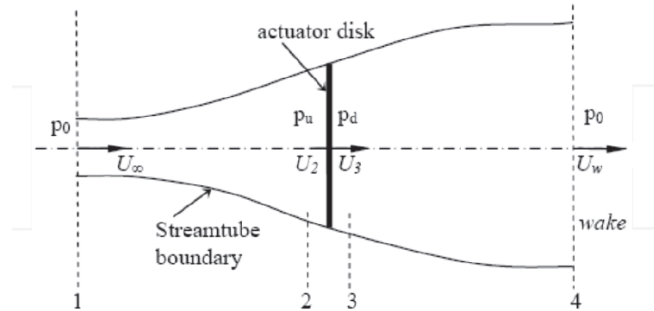

Figure A.1 – Froude-Rankine Actuator Disk in a streamtube (from [Kulunk, 2011])

Combining these two equations, one can obtain the pressure drop between regions 2 and 3:

$$\Delta p = p_u - p_d = \frac{1}{2}\rho(U_\infty^2 - U_w^2) \tag{A.4}$$

The thrust F on the actuator disk is then:

$$F = \Delta p A = \frac{1}{2}\rho A(U_\infty^2 - U_w^2) \tag{A.5}$$

Applying the conservation of momentum from the far inflow (region 1) to the far wake (region 4), one obtains:

$$\dot{m}(U_\infty - U_w) = F \tag{A.6}$$

Or:

$$\rho A U_R(U_\infty - U_w) = \frac{1}{2}\rho A(U_\infty^2 - U_w^2) \tag{A.7}$$

Let a be the induction factor, defined as: $a = \frac{U_\infty - U_R}{U_\infty}$. The velocity at the disk is thus:

$$U_R = U_\infty(1 - a) \tag{A.8}$$

Equation A.7 then becomes:

$$\rho A U_\infty(1 - a)(U_\infty - U_w) = \frac{1}{2}\rho A(U_\infty^2 - U_w^2) \tag{A.9}$$

And, eventually, the wake velocity becomes:

$$U_w = U_\infty(1 - 2a) \tag{A.10}$$

Finally, the thrust force F and the power extracted by the actuator disk P are respectively given as follows:

$$F = 2\rho A a(a - 1)U_\infty^2 \tag{A.11}$$

$$P = F * U_R = 2\rho A a(a - 1)^2 U_\infty^3 \tag{A.12}$$

The thrust and power coefficients are respectively given as follows:

$$C_T = \frac{F}{\frac{1}{2}\rho A U_\infty^2} = 4a(1 - a) \tag{A.13}$$

$$C_P = \frac{P}{\frac{1}{2}\rho A U_\infty^3} = 4a(1 - a)^2 \tag{A.14}$$

A.2 Actuator Cylinder theory

The Actuator Cylinder (AC) theory is an extension of the Actuator Disk theory, but applied on a cylindrical surface describing the total surface swept by the blades of a VAWT as shown in figure A.2. The theory as originally been introduced in [Madsen, 1982] and was improved in [Cheng, 2016].

The method assume a steady, inviscid and incompressible flow. It lies on the conservation of mass and Euler equations. Euler's momentum conservation equation is written as follows if v is the flow velocity:

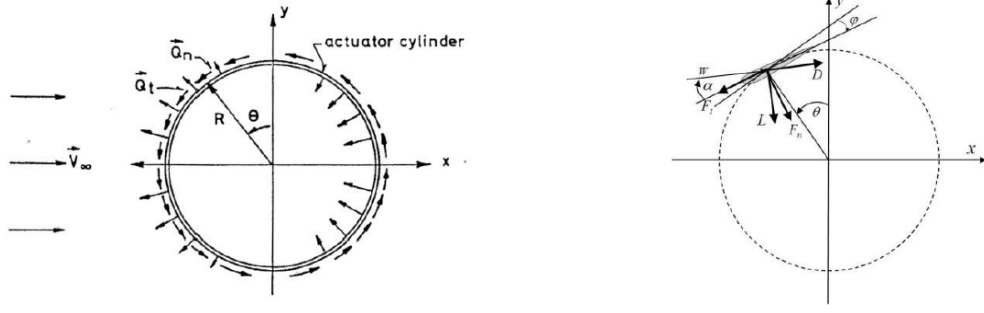$$\rho v \cdot \nabla v = -\nabla p + F_{vol} \tag{A.15}$$

Figure A.2 – Actuator Cylinder representation (from [Madsen, 1982])

Where F_{vol} contains the volume forces.

For simplification, it is written in 2D in the following. If θ is the azimuthal position of a blade segment, let $Q_n(\theta)$ and $Q_t(\theta)$ be the reactions of the normal and tangential blade forces $F_n(\theta)$ and $F_t(\theta)$. Those forces are computed through Blade Element theory using tabulated aerodynamic data and applied as volume forces perpendicular and tangential to the rotor surface. The reactions are given as follows:

$$\begin{cases} Q_n(\theta) = \frac{BF_n(\theta)}{2\pi R\rho U_\infty} \\ Q_t(\theta) = -\frac{BF_t(\theta)}{2\pi R\rho U_\infty} \end{cases} \tag{A.16}$$

B being the number of blades and R the rotor radius.

The following equations are non-dimensional. The fluid velocity in the domain is written as a function of velocity perturbations w_x and w_y on both x and y axes:

$$\begin{cases} v_x = 1 + w_x \\ v_y = w_y \end{cases} \tag{A.17}$$

The steady Euler equation then takes the form:

$$\begin{cases} \frac{\partial w_x}{\partial x} + w_x \frac{\partial w_x}{\partial x} + w_y \frac{\partial w_x}{\partial y} = -\frac{\partial p}{\partial x} + f_x \\ \frac{\partial w_y}{\partial x} + w_x \frac{\partial w_y}{\partial x} + w_y \frac{\partial w_y}{\partial y} = -\frac{\partial p}{\partial y} + f_y \end{cases} \tag{A.18}$$

And the equation of conservation of mass:

$$\frac{\partial w_x}{\partial x} + \frac{\partial w_y}{\partial y} = 0 \tag{A.19}$$

Euler equations A.18 can also be written as follows:

$$\begin{cases} \frac{\partial w_x}{\partial x} = -\frac{\partial p}{\partial x} + f_x + g_x \\ \frac{\partial w_y}{\partial x} = -\frac{\partial p}{\partial y} + f_y + g_y \end{cases} \tag{A.20}$$

Where the second order forces g_x and g_y are expressed as:

$$\begin{cases} g_x = -(w_x \frac{\partial w_x}{\partial x} + w_y \frac{\partial w_x}{\partial y}) \\ g_y = -(w_x \frac{\partial w_y}{\partial x} + w_y \frac{\partial w_y}{\partial y}) \end{cases} \tag{A.21}$$

By deriving respectively the obtained equations with x and y, one shall obtain the Poisson equation:

$$\frac{\partial^2 p}{\partial x^2} + \frac{\partial^2 p}{\partial y^2} = \left(\frac{\partial f_x}{\partial x} + \frac{\partial f_y}{\partial y}\right) + \left(\frac{\partial g_x}{\partial x} + \frac{\partial g_y}{\partial y}\right) \tag{A.22}$$

With the condition $p \to 0$ far from the cylinder, the solution of this equation shall be:

$$p(f) = \frac{1}{2\pi} \int \int \frac{f_x(x-\xi) + f_y(y-\eta)}{(x-\xi)^2 + (y-\eta)^2} d\xi d\eta \tag{A.23}$$

And:

$$p(g) = \frac{1}{2\pi} \int \int \frac{g_x(x-\xi) + g_y(y-\eta)}{(x-\xi)^2 + (y-\eta)^2} d\xi d\eta \tag{A.24}$$

Those integrals shall be computed in the region where the volume forces are different from 0. The velocities are obtained after integration of equation A.20 once the pressure fields are known:

$$\begin{cases} w_x = -p(f) + I(f_x) - p(g) + I(g_x) = w_x(f) + w_x(g) \\ w_y = -\int_{-\infty}^{x} \frac{\partial}{\partial y} p(f) dx' + I(f_y) - \int_{-\infty}^{x} \frac{\partial}{\partial y} p(g) dx' + I(g_y) = w_y(f) + w_y(g) \end{cases} \tag{A.25}$$

Where the integrals $I(f_x)$, $I(f_y)$, $I(g_x)$ and $I(g_y)$ are computed as follows:

$$I(h) = \int_{-\infty}^{x} h dx' \tag{A.26}$$

As it can be seen in equation A.25, the final solution is the sum of a linear part, which depends on the prescribed forces f, and of a non-linear part that depends on the induced or second-order forces.

Linear solution: As explained in [Madsen, 1982], the prescribed forces f are only applied on the cylindrical surface representing the rotor so p(f) is a solution of the Laplace equation in two connected regions: outside and inside the cylinder. It can be analytically computed using:

- Blade Element theory to compute Q_n and Q_t

- The assumption of piecewise constant loads on the blade path

The linear solution is here given as follows:

$$\begin{aligned} w_x = {} & \frac{1}{2\pi} \int_0^{2\pi} Q_n(\theta) \frac{-(x + \sin\theta)\sin\theta + (y - \cos\theta)\cos\theta}{(x + \sin\theta)^2 + (y - \cos\theta^2)} d\theta \\ & - \frac{1}{2\pi} \int_0^{2\pi} Q_t(\theta) \frac{-(x + \sin\theta)\cos\theta - (y - \cos\theta)\sin\theta}{(x + \sin\theta)^2 + (y - \cos\theta^2)} d\theta \\ & - (Q_n(\cos^{-1} y)^* + (Q_n(-\cos^{-1} y))^{**} \\ & + (Q_t(\cos^{-1} y \frac{y}{\sqrt{1-y^2}}))^* - (Q_t(\cos^{-1} y \frac{y}{\sqrt{1-y^2}}))^{**} \end{aligned} \tag{A.27}$$

$$\begin{aligned} w_y = {} & - \frac{1}{2\pi} \int_0^{2\pi} Q_n(\theta) \frac{-(x + \sin\theta)\cos\theta - (y - \cos\theta)\sin\theta}{(x + \sin\theta)^2 + (y - \cos\theta^2)} d\theta \\ & - \frac{1}{2\pi} \int_0^{2\pi} Q_t(\theta) \frac{(x + \sin\theta)\sin\theta - (y - \cos\theta)\cos\theta}{(x + \sin\theta)^2 + (y - \cos\theta^2)} d\theta \end{aligned} \tag{A.28}$$

Where terms marked with $*$ are added only inside the cylinder area, while the terms marked with $*$ and $**$ are added in the area behind the cylinder.

More details on the equations can be found in [Cheng et al., 2016].

Non-linear solution: The process to obtain the non-linear solution is different as it requires an iterative process. Once the linear solution is obtained, the full solution can be written as follows:

$$\begin{cases} w_x^n = w_x(f) - p(g^{n-1}) + I(g_x^{n-1}) = w_x(f) + w_x(f) + w_x(g^{n-1}) \\ w_y^n = w_y(f) - \int_{-\infty}^{x} \frac{\partial}{\partial y} p(g^{n-1}) dx' + I(g_y^{n-1}) = w_y(f) + w_y(g^{n-1}) \end{cases} \tag{A.29}$$

Where w^n is the result of the nth iteration. Equation A.24 is differentiated with respect to y and integrated with respect to x to obtain w_y^n but this process requires to mesh the fluid domain into a certain number of elements and to compute integrals over the whole domain. It is thus very time-consuming compared to the analytic linear solution (see [Madsen, 1982] for more details).

Modified linear solution to by-pass the calculation of the non-linear solution: It is proposed in [Madsen, 1982] to mitigate the linear solution in order to reach a better agreement with the fully non-linear solution, without computing the time-consuming non-linear part. A simple multiplication factor is added to the linear solution. This factor is determined with empirical data and is a function of the induction factor and of the thrust coefficient. The value of this multiplication factor is improved in [Cheng et al., 2016] to better account for rotor induction phenomena. This method has shown a good accuracy on fixed turbines as shown in [Cheng et al., 2016] and [Cheng, 2016].

Titre : Aérodynamique instationnaire pour l'analyse de la tenue à la mer des éoliennes flottantes

Mots clés : Eolien flottant, simulation numérique, aérodynamique, hydrodynamique, couplage

Résumé : La simulation numérique des éoliennes flottantes est essentielle pour le développement des Energies Marines Renouvelables. Les outils de simulation classiquement utilisés supposent un écoulement stationnaire sur les rotors. Ces théories sont généralement assez précises pour calculer les forces aérodynamiques et dimensionner les éoliennes fixes (à terre ou en mer) mais les mouvements de la plateforme d'une éolienne flottante peuvent induire des effets instationnaires conséquents. Ceux-ci peuvent par exemple impacter la force de poussée sur le rotor. Cette thèse de doctorat cherche à comprendre et à quantifier les effets de l'aérodynamique instationnaire sur la tenue à la mer des éoliennes flottantes, dans différentes conditions de fonctionnement.

L'étude montre que les forces aérodynamiques instationnaires impactent les mouvements de la plateforme lorsque le rotor est fortement chargé. Les modèles quasi-stationnaires arrivent néanmoins à capturer la dynamique des éoliennes flottantes avec une précision suffisante pour des phases de design amont.
Les éoliennes flottantes à axe vertical sont elles aussi étudiées pour des projets offshore puisqu'elles pourraient nécessiter des coûts d'infrastructure réduits. Après avoir étudié l'influence de l'aérodynamique instationnaire sur la tenue à la mer de ces éoliennes, une comparaison est menée entre éoliennes flottantes à axe horizontal et à axe vertical. Cette dernière subit une importante poussée aérodynamique par vents forts, induisant de très grands déplacements et chargements.

Title: Unsteady aerodynamic modelling for seakeeping analysis of Floating Offshore Wind Turbines

Keywords: Floating Wind Turbines, numerical simulation, aerodynamics, hydrodynamics, coupling

Abstract: Accurate numerical simulation of the seakeeping of Floating Wind turbines (FWTs) is essential for the development of Marine Renewable Energy. State-of-the-art simulation tools assume a steady flow on the rotor. The accuracy of such models has been proven for bottom-fixed turbines, but has not been demonstrated yet for FWTs with substantial platform motions. This PhD thesis focuses on the impact of unsteady aerodynamics on the seakeeping of FWTs. This study is done by comparing quasi-steady to fully unsteady models with a coupled hydro-aerodynamic simulation tool. It shows that unsteady loads have a substantial effect on the platform motion when the rotor is highly loaded. The choice of a numerical model for example induces differences in tower base bending moments. The study also shows that state of the art

quasi-steady aerodynamic models can show rather good accuracy when studying the global motion of the FWTs.
Vertical Axis Wind Turbines (VAWTs) could lower infrastructure costs and are hence studied today for offshore wind projects. Unsteady aerodynamics for floating VAWTs and its effects on the seakeeping modelling have been studied during the PhD thesis, leading to similar conclusions than for traditional floating Horizontal Axis Wind Turbines (HAWTs). Those turbines have been compared to HAWTs. The study concludes that, without blade pitch control strategy, VAWTs suffer from very high wind thrust at over-rated wind speeds, leading to excessive displacements and loads. More developments are hence needed to improve the performance of such floating systems.